UNIVERSIDAD COMPLUTENSE DE MADRID

FACULTAD DE FARMACIA
Departamento de Química-Física II

TESIS DOCTORAL

Síntesis de nanomateriales híbridos coloidales biocompatibles para sistemas avanzados de encapsulación y liberación de fármacos, y biosensores

Synthesis of biocompatible colloidal hybrid nanomateriales for advanced drug encapsulation and release systems, and biosensors

MEMORIA PARA OPTAR AL GRADO DE DOCTOR

PRESENTADA POR

Paulino Alonso Cristóbal

Directores

Enrique López Cabarcos
Jorge Rubio Retama

Madrid, 2016

© **Paulino Alonso Cristóbal, 2015**

UNIVERSIDAD COMPLUTENSE DE MADRID

FACULTAD DE FARMACIA

Departamento de Química-Física II

SÍNTESIS DE NANOMATERIALES HÍBRIDOS COLOIDALES BIOCOMPATIBLES PARA SISTEMAS AVANZADOS DE ENCAPSULACIÓN Y LIBERACIÓN DE FÁRMACOS, Y BIOSENSORES

MEMORIA PRESENTADA PARA OPTAR AL GRADO DE DOCTOR

PAULINO ALONSO CRISTÓBAL

TESIS DIRIGIDA POR

Prof. Dr. D. ENRIQUE LÓPEZ CABARCOS

Prof. Dr. D. JORGE RUBIO RETAMA

Madrid 2015

COMPLUTENSE UNIVERSITY OF MADRID

FACULTY OF PHARMACY

Department of Physical-Chemistry II

SYNTHESIS OF BIOCOMPATIBLE COLLOIDAL HYBRID NANOMATERIALS FOR ADVANCED DRUG ENCAPSULATION AND RELEASE SYSTEMS, AND BIOSENSORS.

PhD thesis

PAULINO ALONSO CRISTÓBAL

Thesis supervised by:

Prof. Dr. D. ENRIQUE LÓPEZ CABARCOS

Prof. Dr. D. JORGE RUBIO RETAMA

Madrid 2015

A mis padres

A mi familia

A mis amigos

Agradecimientos

Una tesis es un trabajo que lleva mucho tiempo y que involucra directa e indirectamente a muchas personas de ámbitos muy distintos y merecen un sincero agradecimiento:

En primer lugar quiero agradecer a mis directores de tesis, los profesores Enrique López Cabarcos y Jorge Rubio Retama la oportunidad de trabajar con ellos.

Enrique me has enseñado muchísimo no sólo en el aspecto puramente científico sino también como persona. Para mi eres un referente en ese aspecto.

Jorge ya hemos pasado 5 años juntos y tengo que decirte que es un orgullo para mí haber trabajado contigo. Eres a la vez mi jefe y mi amigo, y sin duda el gran responsable del trabajo que se presenta en esta tesis. He podido aprender mucho de ti, de tus ideas y de tu forma de pensar.

Quiero agradecer también a todos los compañeros del grupo de investigación, ellos son el motivo de que los resultados de esta tesis estén escritos en primera persona del plural:

Marco, si Jorge es mi padre científico, tú eres mi padrino. Te agradezco muchísimo por todo lo que me has enseñado y ayudado, sobre todo al principio que es cuando más falta hace. Además de un buen compañero eres un gran amigo.

A David por todos los buenos momentos y grandes consejos.

A Diego, por tu paciencia casi infinita y esas charlas cuasi-filosóficas que hemos tenido… he aprendido mucho de ti, y te deseo de corazón mucha suerte con tu tesis! Que las nanopartículas son muy caprichosas ya lo sabes.

A Yousof, porque eres una gran persona, y aunque tengamos puntos de vista muy distintos sobre algunos temas es siempre un placer charlar contigo.

A Ana, porque aunque hemos coincidido durante relativamente poco tiempo, me has demostrado que eres única. Consigues que un día malo se convierta

en bueno y que uno bueno se convierta en mejor, y eso no está al alcance de cualquiera. No me olvido de toda la gente que he conocido en el grupo y que también merecen que se les agradezca su aportación tanto en el terreno profesional como en el personal: Abdullah, Julia, Jatsue, Ana, Fernando, Olalla, Jose, Mohammad y Monte. A todos vosotros, gracias.

No me quiero dejar a una persona que ha sido clave para que me incorporase al grupo, el Prof. Gregorio Carcedo. Muchas gracias por llevarme de la mano al grupo de investigación.

Tampoco quiero dejar de mencionar a Jose: A pesar de los cafés “bomba” que me pones, eres el principal responsable de que algunos días haya sido capaz de abrir los ojos. Además eres una gran persona y un gran amigo.

A todos los miembros del departamento de Química-Física II de la Facultad de Farmacia de la UCM, porque con vuestros consejos y vuestras ayudas habéis facilitado la realización de este trabajo.

Quiero también reconocer y agradecer el trabajo y el apoyo de los miembros de los Centros de Apoyo a la Investigación de la Complutense, con mención especial a Agustín Fernández y Marisa García del CAI de Microscopía Electrónica.

Of course, I will never forget my stay in Southampton. I want to thank first to Prof. Antonios Kanaras for accepting me in the group, and for all the help and advices that you gave me. I learned a lot of things in a short time and you are responsible for that. Thank you!

However, all that time wouldn’t have been so fantastic without the people that I met there: Amelie, Patrick, Johanna, Pascal and Erika, I really thank you for all you did. You are amazing people and I will always consider you good friends! Thanks to the bbq-crew for being sooooo cooool! Who said that it was impossible to prepare a barbecue in winter in the UK?

I would like to thank also the help that I received from Otto, Jordi and Mauro, which was of key relevance for my work there. My most sincere thank you for all of you, Southamptoners!

Por último pero no por ello menos importante, quiero agradecer a mi familia y a mis amigos todo su apoyo. Cuando te preguntan el “cómo va la tesis?” o “de qué va tu investigación?” y te escuchan y atienden a pesar de que realmente les estás hablando en “chino”. Loreto, muchísimas gracias por todo tu apoyo y porque si realmente se puede sacar una conclusión después de todo este tiempo, es que tu paciencia es infinita. Has sido sin duda alguna una pieza clave para la estabilidad y la continuidad del trabajo que se presenta en esta tesis y mereces el reconocimiento. Además que me has ayudado un montón con las correcciones del inglés.

Quiero agradecer al Ministerio de Educación la beca FPU AP2010-1163 que he disfrutado durante la realización de este trabajo, al Ministerio de Ciencia el proyecto MAT2010-15349 por la financiación del material y otros recursos necesarios, y a los proyectos europeos COST Action D43 y CM1101 por la financiación para la divulgación de la investigación.

“The definition of insanity is doing the same thing over and over again and expecting different results”

Albert Einstein

INDEX

ABSTRACT

Nanotechnology offers the possibility of combining materials with different properties to create advanced functional materials with applications in many fields. Biomedicine requires new materials that can overcome current problems; for example improving the efficacy of drugs while reducing the side effects, the sensitivity of sensors, or enhancing the quality of *in vivo* imaging, etc. The fabrication of a selective system for biomedical applications is a complex task and it requires a lot of investigation before a final product reaches the market.

This PhD thesis is focused on the development of new nanomaterials with enhanced properties that could be applied in biomedicine and are composed by multiple components, assembled in the nanoscale. To achieve this, the processes begin with the synthesis and characterization of each component. Next, the combination and nanoengineering of all the moieties is carefully realized and characterized, ending up with the application of the nanotechnology-based materials.

This thesis is organized according to the learning process followed for the production of hybrid multifunctional nanomaterials. We started preparing organic nanoparticles with a core-shell structure based on biocompatible polymers. The inorganic nanoparticles provided additional functionalities to the nanosystems. We synthesized iron oxide (Fe_3O_4) and gold (Au) nanoparticles to provide magnetic and optical properties. To improve stability and dispersion of inorganic nanoparticles in aqueous media, and also to give them additional properties it is necessary to functionalize their surface with various moieties which is not a trivial process. Silica coating of inorganic nanoparticles has demonstrated to be an adequate method to solve these problems. We proved that the method works with two examples: i) by functionalizing upconversion nanoparticles ($NaYF_4$:Yb,Er) with single strands of DNA with the aim to prepare a highly sensitive DNA sensor; ii) by functionalizing upconversion nanoparticles ($NaYF_4$:Yb,Tm) with a photodegradable ortho-nitrobenzyl alcohol derivate which released the attached doxorubicin after the exposure to NIR light.

In the first chapter of this work, we pretend to enhance the solubility in water of highly hydrophobic anticancer drugs by means of amphiphilic star shaped block copolymers, based on biocompatible components. These macromolecules were synthesized using branched poly(ε-caprolactone) as hydrophobic core and branched poly(ethyleneglycol) as hydrophilic corona. The structure of this macromolecule, based on two well differentiated blocks, conferred amphiphilic behavior to the whole system that acted as driving force for its self-assembling in aqueous media. Depending on the polymer concentration, it was possible to obtain different architectures. The TEM micrographs permitted to follow the evolution of the system from single vesicles toward necklace entanglements. In addition, the proposed star shaped block copolymer presented good solubilizing properties that were used to disperse in aqueous solution the insoluble chlorine-carbazole derivate molecule. The amphiphilic star shaped block copolymer was used as drug nano-carrier, proving the suitability of the self-assembled nanostructures for encapsulating hydrophobic molecules within the hydrophobic core while the hydrophilic shell stabilizes the whole system.

In the second chapter, we developed a theranostic system based on Fe_3O_4@Au nanoparticles encapsulated within star-shaped block copolymers. For that, we produced Fe_3O_4@Au nanoparticles by using a two-step solvothermal route that employed Fe_3O_4 nanoparticles as seeds for the Au deposition. Although this protocol leads to highly monodisperse and reproducible Fe_3O_4@Au nanoparticles it was necessary to perform a systematic study in order to improve the yield and to obtain a tunable Au shell thickness that would provide different SPR absorption. We demonstrated that the Au:Fe_3O_4 ratio is a key parameter that, contrary to what could be expected, does not influence the Au shell thickness. However, this parameter should be optimized because it strongly influences the yield. When the Au:Fe_3O_4 ratio was low, there were plenty of uncoated Fe_3O_4 nanoparticles, whereas when the Au:Fe_3O_4 ratio was high, there were pure Au nanoparticles together with the desired Fe_3O_4@Au nanoparticles. Furthermore we demonstrated that the Au shell thickness could be tuned by varying the reaction temperature. The as synthesized Fe_3O_4@Au nanoparticles were successfully transferred to aqueous

solution using the star shaped amphiphilic block copolymer, which yielded a nano-assembled multifunctional hybrid material: The Fe_3O_4@Au nanoparticles could serve as contrast agent for multimodal MRI/CT imaging and the amphiphilic star shaped block copolymer would stabilize the whole system. This system could also serve as a theranostic tool by exploiting the photothermal effect of the Au nanoshell, releasing the drug upon an external stimulus.

In the third chapter of this thesis, we boarded the fabrication of a synthetic tool that can be used to create multifunctional materials with nanometric architecture. Herewith, we performed a parametric study of a silica coating technique that permits to cover single inorganic nanoparticles with a nanometric control of the shell. The silica coating permitted to co-encapsulate water soluble molecules within the silica shell, leading to multifunctional hybrid materials. In addition, we demonstrate that this methodology can be applied with inorganic nanoparticles of different nature, such as iron oxide, gold, silver, quantum-dots and upconversion nanoparticles. The silica coating provides aqueous-solubility, cytocompatibility and stability to the inorganic nanoparticles, but it also provides an excellent platform for surface functionalization. The chemistry on the silica shell permits to introduce almost any type of functional group in the surface of the nanoparticles, which opens the possibility to anchor molecules such as enzymes, vitamins, DNA or other functional and specific molecules such as polymers, photoactive molecules or drugs. By combining the inner properties of inorganic nanoparticles and the possibilities that offer the silica as the coating material it is possible to create nanoengineered materials with a remarkable homogeneity that can be employed in very different applications, depending on their surface functionalization. In this thesis, this colloidal chemistry for the modification of the surface, has been studied with folic acid, poly(ethylene glycol), DNA and a doxorubicin-photoactive molecule, over silica coated inorganic nanoparticles. The resulting hybrid nanomaterials were tested for different applications in further studies.

In the fourth chapter we present a DNA biosensor based on the fluorescence resonance energy transfer (FRET) between silica coated upconversion nanoparticles and graphene oxide (GO). This biosensor was constituted by monodisperse β-$NaYF_4$:Yb,Er nanoparticles with a mean

diameter of 29.1 ± 2.2 nm were synthesized and coated with a SiO_2 shell of 11 nm and subsequently grafted with single strands of DNA. When these DNA-functionalized $NaYF_4$:Yb,Er@SiO_2 nanoparticles were in the proximity of the GO surface, the $\pi-\pi$ stacking interaction between the nucleobases of the DNA and the sp^2 carbons of the GO induced a FRET fluorescence quenching due to the overlap of the fluorescence emission of the β-$NaYF_4$:Yb,Er@SiO_2 and the absorption spectrum of GO. By contrast, in the presence of the complementary DNA strands, the hybridization led to double-stranded DNA that did not interact with the GO surface, and thus the β-$NaYF_4$:Yb,Er@SiO_2 nanoparticles remained unquenched and fluorescent. The high sensitivity and specificity of this sensor introduces a new method for the detection of DNA with a detection limit of 5 pM. In addition to the low detection limit, these biosensors were highly specific due to the selectivity of the DNA base pairing rules. The characteristics of the upconversion emission provide a high signal-to-noise ratio and avoid photobleaching and blinking effects, rendering a robust and reproducible biosensor.

In chapter five we present another interesting application of the surface chemistry carried out on the silica coatings, which was to release drugs upon an external activation. In this work, we present a stimuli responsive drug delivery system, which is able to release the anticancer drug Doxorubicin when exposed to a NIR-light stimulus. The proposed system is based on upconversion fluorescence nanoparticles of β-$NaYF_4$:Yb,Tm@SiO_2 with a mean diameter of 52 ± 2.5 nm that absorb the NIR light and emit UV light. The UV emission initiates the photodegradation of the light sensitive ortho-nitrobenzyl alcohol molecules attached on the surface of the nanoparticles, which act as linkers for the attachment of the Doxorubicin. The photodegradation triggers the drug release, rendering a NIR light dependent drug delivery system. The system was tested *in vitro* with HeLa cells and showed great potential for biomedical applications, where it is crucial to deliver the drug in a specific tissue with a remote activation. We demonstrated that the NIR-light stimulus as well as the upconverted UV emission did not show any reduction in the cell viability. In addition, the Doxorubicin-loaded β-$NaYF_4$:Yb,Tm@SiO_2 nanoparticles did not show a significant cytotoxic effect without the NIR-light stimulus, whereas the

same particles provoked a concentration dependent cytotoxicity, comparable to that of free Doxorubicin. This effective NIR-light responsive drug delivery system could be very useful for administering highly toxic drugs, since the side effects would be importantly reduced.

Keywords: Nanoparticles, Star shaped block copolymer, core@shell, biocompatible, self-assembling, multifunctional, Fe_3O_4@Au, hybrid material, silica coating, surface functionalization, DNA biosensor, upconversion, graphene oxide, FRET, NIR light responsive, phototriggered drug release, Doxorubicin.

RESUMEN

La nanotecnología ofrece la posibilidad de combinar diferentes materiales con distintas propiedades para crear materiales funcionales avanzados, con aplicaciones en distintos campos. La biomedicina requiere de nuevos materiales que sean capaces de solventar problemas actuales, por ejemplo la mejora de la eficacia de tratamientos con fármacos junto a la reducción de los efectos secundarios, el aumento de la sensibilidad de los sensores, la mejora de la calidad de las imágenes *in vivo* para diagnóstico, etc. La fabricación de un sistema específico de aplicación en biomedicina es una tarea compleja y requiere de mucha investigación antes de que el producto final alcance el mercado.

Esta tesis doctoral se centra en el desarrollo de nuevos nanomateriales con propiedades mejoradas que podrían ser aplicados en biomedicina y que están compuestos por varios componentes, ensamblados de forma específica a escala nanométrica. Para lograr esto, el proceso comienza con la síntesis y caracterización de cada componente. Posteriormente, se realiza la combinación y la nano-ingeniería de todas estas partes y se analiza con detalle, para terminar con la aplicación de estos materiales basados en la nanotecnología.

Esta tesis se organiza en base al proceso de aprendizaje llevado a cabo para la producción de nanomateriales híbridos multifuncionales. Empezamos preparando nanopartículas orgánicas con estructura tipo núcleo-corteza basadas en polímeros biocompatibles. Las nanopartículas inorgánicas dotaban a los nanosistemas con propiedades adicionales. Sintentizamos nanopartículas de óxido de hierro (Fe_3O_4) y oro (Au) para dotar a los sistemas de propiedades magnéticas y ópticas. Para mejorar la estabilidad coloidal de las dispersiones de nanopartículas inorgánicas en medios acuosos, y también para dotar de propiedades adicionales es necesario funcionalizar la superficie de dichas nanopartículas con distintas subunidades lo cual no es un proceso sencillo. El recubrimiento con sílice de nanopartículas inorgánicas ha demostrado ser un

método adecuado para solucionar estos problemas. Demostramos que el método es útil con dos ejemplos: i) mediante la funcionalización de nanopartículas de upconversion ($NaYF_4$:Yb,Er) con cadenas de hebra simple de ADN con el objetivo de preparar un sensor altamente sensible de ADN; ii) mediante la funcionalización de nanopartículas de upconversion ($NaYF_4$:Yb,Tm) con una molécula fotodegradable basada en un derivado del orto-nitrobencil alcohol que liberaba la doxorrubicina anclada tras la exposición a luz en el infrarrojo cercano (NIR).

En el primer capítulo de este trabajo, pretendemos aumentar la solubilidad en medios acuosos de principios activos antitumorales altamente hidrofóbicos por medio de copolímeros anfifílicos estructurados en forma de estrella. Estas moléculas se han sintetizado utilizando poli(ε-caprolactona) ramificada como núcleo hidrofóbico y poli(etilén glicol) ramificado como corteza hidrofílica. La composición de esta macromolécula, basada en dos bloques bien diferenciados, dota de carácter anfifílico al sistema lo cual actúa como fuerza impulsora para su auto-ensamblado en medios acuosos. Dependiendo de la concentración de polímero ha sido posible obtener distintas estructuras en las partículas resultantes. Las fotografías de microscopía electrónica de transmisión permitieron hacer el seguimiento de la evolución del sistema desde vesículas sencillas hasta macroestructuras en forma de collar de perlas. Además, el copolímero en forma de estrella que se propone ha mostrado buenas propiedades solubilizantes que se emplearon para dispersar en medio acuoso un derivado insoluble de cloro-carbazol. Así, el copolímero anfifílico en forma de estrella fue usado como un nano-transportador de fármacos, demostrando la capacidad de las estructuras auto-ensambladas para encapsular sustancias hidrofóbicas en su núcleo hidrofóbico, mientras que la corteza hidrofílica es capaz de estabilizar todo el sistema.

En el segundo capítulo, hemos desarrollado un sistema teranóstico basado en nanopartículas de Fe_3O_4@Au encapsuladas en el copolímero anfifílico en forma de estrella. Para ello, producimos nanopartículas de Fe_3O_4@Au por medio de una ruta solvo-termal realizada en dos pasos que emplea nanopartículas de Fe_3O_4 como semillas para que se produzca la deposición de una capa de Au. Aunque este método produce nanopartículas de Fe_3O_4@Au

muy monodispersas y de forma muy reproducible, era necesario realizar un estudio sistemático del proceso para aumentar el rendimiento y tener un mejor entendimiento del proceso, lo que permitiría modificar el espesor de la capa de Au permitiendo así modular las propiedades ópticas del conjunto. Demostramos que el ratio entre precursor de oro y nanopartículas de óxido de hierro (ratio Au:Fe_3O_4) es un parámetro clave que, al contrario de lo que cabría esperar, no tiene ninguna influencia sobre el grosor de la capa de oro que se deposita. Sin embargo, este parámetro debe ser optimizado porque afecta enormemente al rendimiento de la síntesis: Cuando el ratio Au:Fe_3O_4 empleado fue bajo se encontraron muchas nanopartículas de Fe_3O_4 sin recubrir, mientras que cuando el ratio Au:Fe_3O_4 empleado fue alto se encontraron nanopartículas de Au puras, sin núcleo magnético, junto a las nanopartículas de Fe_3O_4@Au deseadas. Además, demostramos que el grosor de la corteza de Au puede ser modificado mediante el control de la temperatura de reacción. Las nanopartículas de Fe_3O_4@Au fueron transferidas con éxito a medio acuoso mediante la combinación con el copolímero anfifílico en estrella, creando así un material híbrido nano-ensamblado y multifuncional con aplicación potencial en biomedicina: las nanopartículas de Fe_3O_4@Au estabilizadas en medio acuoso podrían ser utilizadas como agentes de contraste de imagen multimodal MRI/CT basados en resonancia magnética de (MRI) y tomografía computarizada (CT). Este sistema podría ser útil también como herramienta teranóstica, explotando el efecto fototérmico de la nanocorteza de Au para liberar principio activo en respuesta a un estímulo externo.

En el tercer capítulo de esta tesis, estudiamos la fabricación de una herramienta de síntesis que puede ser empleada para crear materiales multifuncionales con estructuración nanométrica. Realizamos un estudio paramétrico de la técnica de recubrimiento con sílice que permite recubrir de forma individualizada nanopartículas inorgánicas permitiendo un ajuste preciso a nivel nanométrico del espesor de la corteza de sílice. El recubrimiento con sílice permitió co-encapsular moléculas solubles en agua dentro de la capa de sílice, dando lugar a materiales híbridos multifuncionales. Además, demostramos que este método puede ser empleado con nanopartículas inorgánicas de distinta naturaleza, tales como óxido de hierro, oro, plata,

quantum-dots y nanopartículas de upconversion. El recubrimiento con sílice dota al sistema de solubilidad en medio acuoso, citocompatibilidad, y la estabilidad coloidal a las nanopartículas inorgánicas, pero además la sílice es una plataforma ideal para la funcionalización en superficie. La química sobre la capa de sílice permite introducir prácticamente cualquier tipo de grupo funcional en la superficie de las nanopartículas, lo cual abre la posibilidad de anclar moléculas como enzimas, vitaminas, ADN u otros grupos funcionales más específicos como polímeros, moléculas fotoactivas o principios activos. Mediante la combinación de las propiedades inherentes a las nanopartículas inorgánicas y las posibilidades que ofrece la sílice como material de recubrimiento es posible crear materiales ensamblados en la nanoescala con una alta homogeneidad que pueden ser empleados en distintas aplicaciones, dependiendo de la funcionalización en superficie. En esta tesis, los procesos de química coloidal para la funcionalización en superficie de nanopartículas inorgánicas recubiertas con sílice se han estudiado con el anclaje de moléculas tales como ácido fólico, poli(etilenglicol), ADN y una molécula fotoactiva anclada a su vez a doxorrubicina. Los nanomateriales híbridos resultantes fueron estudiados para diferentes aplicaciones en estudios posteriores.

En el cuarto capítulo presentamos un sensor de ADN basado en el fenómeno de transferencia de energía por resonancia de fluorescencia (FRET) entre nanopartículas de $NaYF_4$:Yb,Er y óxido de grafeno (GO). Se sintetizaron nanopartículas monodispersas de $NaYF_4$:Yb,Er con un diámetro medio de 29.1 $\pm$ 2.2 nm y se recubrieron con una capa de sílice de 11 nm, que permitió el anclaje de cadenas de ADN monocatenarias, es decir, de hebra simple (ssDNA). Cuando estas nanopartículas $NaYF_4$:Yb,Er@SiO_2 funcionalizadas con ssDNA se encuentran próximas a la superficie del GO, las interacciones de apilamiento tipo π-π entre las bases nitrogenadas del ADN y los carbonos sp^2 del GO inducen la amortiguación de fluorescencia por FRET debido a la superposición entre la emisión de fluorescencia de las nanopartículas de $NaYF_4$:Yb,Er@SiO_2 y la absorción del GO. Por el contrario, en presencia de hebras de ADN complementarias se produce el proceso de hibridación que da lugar a la doble hebra de ADN (dsDNA) en la superficie de las nanopartículas, que no interacciona con la superficie del GO y por tanto las nanopartículas de

$NaYF_4$:Yb,Er@SiO_2 mantienen su fluorescencia sin amortiguación. La alta sensibilidad y especificidad es este sensor introduce un nuevo método de detección de ADN con un límite de detección de 5 pM. Además de esto, este tipo de sensores son altamente específicos debido a las normas de hibridación entre las bases nitrogenadas del ADN. Las características de la emisión de fluorescencia por conversión ascendente permiten que exista una relación señal/ruido excelente, que no haya pérdida de fluorescencia por fotoblanqueo ni efectos de intermitencia en la emisión (conocidos como parpadeo, “blinking”), lo cual provee al sensor de una gran reproducibilidad y fiabilidad.

En el capítulo cinco se presenta otra interesante aplicación de la química en superficie realizada sobre los recubrimientos de sílice, que consiste en la liberación de un principio activo en respuesta a un estímulo externo. En este trabajo se presenta un sistema de liberación de fármacos capaz de responder a estímulos externos, que permite liberar doxorrubicina cuando se estimula con luz en el infrarrojo cercano (NIR). El sistema se basa en nanopartículas de β-$NaYF_4$:Yb,Tm@SiO_2 con fluorescencia de conversión ascendente con un diámetro medio de 52 $\pm$ 2.5 nm que son capaces de absorber luz NIR y emitir luz ultravioleta (UV). La emisión de fotones con longitud de onda correspondiente al UV provoca la fotodegradación de las moléculas fotosensibles basadas en derivados del orto-nitrobencilalcohol ancladas en la superficie de las nanopartículas por un lado y al principio activo doxorrubicina por otro. La fotodegradación dispara la liberación del fármaco, dando lugar a un sistema de liberación dependiente de luz NIR. Este sistema fue probado *in vitro* con células HeLa y demostró un gran potencial para su aplicación en biomedicina, donde sería importante poder liberar un fármaco en un tejido concreto activado de forma externa. Se demuestra que ni el estímulo con luz NIR, ni la emisión de fotones UV de las partículas provocaron una reducción significativa de la viabilidad celular. Además, las nanopartículas de β-$NaYF_4$:Yb,Tm@SiO_2 cargadas con doxorrubicina tampoco mostraron una reducción de la viabilidad celular en ausencia del estímulo de luz NIR, mientras que este mismo sistema mostró una toxicidad celular importante en presencia del estímulo de luz NIR. La actividad citotóxica mostrada por el sistema fue dependiente de la concentración y similar a la producida por la doxorrubicina

libre. Este sistema de liberación de fármaco en función de un estímulo de luz NIR ha demostrado ser efectivo y podría ser muy útil para la administración de principios activos altamente tóxicos, ya que los efectos secundarios derivados de su uso se reducirían de forma notable.

Palabras clave: Nanopartículas, copolímero dibloque en estrella, núcleo@corteza, biocompatible, auto-ensamblado, multifuncional, Fe_3O_4@Au, material híbrido, recubrimiento con sílice, funcionalización superficial, biosensor de ADN, fluorescencia de conversión ascendente, óxido de grafeno, FRET, respuesta a luz NIR, liberación de fármaco disparada por estímulo lumínico, Doxorrubicina.

WORK HYPOTHESIS

The hypothesis of this work is that it is possible to control at the nanoscale level the assembly of several components and the formation of structures. This structuring would permit the development of novel functional materials with enhanced properties that would be useful in the biomedical field for the production of drug nanocarriers, multifunctional materials, biosensors and stimuli responsive drug release systems.

HIPÓTESIS DE TRABAJO

La hipótesis de este trabajo es que es posible controlar el ensamblado de varios componentes a escala nanométrica y la formación de estructuras. Dicha estructuración permitiría la creación de nuevos materiales funcionales con propiedades mejoradas que podrían ser de utilidad en el campo de la biomedicina para la fabricación de nano-transportadores de fármacos, materiales multifuncionales, biosensores y sistemas de liberación de fármacos en respuesta a estímulos.

1. INTRODUCTION

"There is plenty of room at the bottom" said Richard Feynman at an American Physical Society meeting in 1959[1]. Today we can say: "There is still space at the bottom". Feynman referred to the possibility of developing new materials by manipulating the pieces at the molecular or atomic level, and was unnoticed until 1980 when Erik Drexler published a work in the Journal *Proceedings of the National Academy of Sciences* entitled: *Molecular Engineering: An approach to the development of general capabilities for molecular manipulation*[2]. In this work, Drexler theorized the idea of manipulating individual molecules to create nanoscale assemblies. Few years later, the invention of the scanning tunneling microscope, the discovery of the fullerenes in 1985 and the publication of the book of Erik Drexler in 1986 entitled: *Engines of Creation: The Coming Era of Nanotechnology*[3], which cited Feynman, provoked the birth of Nanotechnology as a complete research field. Today Nanotechnology is a broad interdisciplinary field that has attracted tremendous attention. This has boosted the fundamental knowledge, the chemical synthesis and the practical applications as well as the manufacturing of nanomaterials.

The term "nanoscale" is generally referred to a scale between 1 and 100 nm. In this length range the dominating forces over the system are different from the bulk materials, even at the microscale. For example, the influence of gravity is drastically reduced whereas the interfacial tension and van der Waals attraction become dominant. New phenomena can occur in nanomaterials because quantum mechanical effects dominate material properties at this scale. One example is quantum confinement where the electronic properties of solids are different with great reductions in particle size[4]. The optical properties of nanoparticles, e.g. localized surface plasmon resonance in gold nanoparticles, also become a function of the particle diameter. This effect does not come into play by going from macroscopic to micrometer dimensions, but becomes pronounced when the nanometer scale is reached.

The creation of materials with new, different, or enhanced properties has been a major research topic since nanotechnology emerged. Materials with structure in the nanoscale often present unique properties because the combination of several materials in a hierarchical manner provides multiple properties. Concretely, the biomedical field has been highly influenced by this boost of nanomaterials with new properties. The size of nanomaterials is similar to that of most biological molecules and structures and therefore nanomaterials can be useful for both in vivo and in vitro biomedical research and applications. The rise of these nanomaterials evolved rapidly toward applications as multiresponsive smart drug delivery systems; advanced contrast imaging and dual-mode imaging; theranostics that combines in one therapeutic and diagnostic capacity, etc. All these promising applications are included in the research field called Nanomedicine, which seeks to deliver a valuable set of research tools and clinically useful devices in the near future[5,6].

The manipulation of different materials at the nanoscale is totally different from the one used at the micro and the macro-scales. As result, the production of ordered nanostructured materials requires new tools that can act at the molecular level. Chemical reactions, physical-chemical processes and intermolecular forces provide the fundamental knowledge that permits the rational design of functional materials.

This thesis covers the synthesis and characterization of different nanomaterials for biomedical applications. In this work there is an extensive study about synthetic and manipulation methods for the creation of advanced functional materials.

1.1 Polymers

A polymer is a macromolecule composed by many repeated subunits, known as monomers. There are many different polymers with many different properties and applications, ranging from natural polymers such as proteins or DNA to synthetic polymers such as plastics. In this work we focus on synthetic polymers with application in biomedicine. Inside this group, poly(ε-caprolactone) (PCL) and polyethylene glycol (PEG) stand out as hydrophobic and hydrophilic polymers respectively, and both are considered biocompatible[7].

More specifically, PCL is a semi-crystalline biodegradable polyester with a low melting point that is synthesized by ring opening polymerization[8]. See scheme 1.1

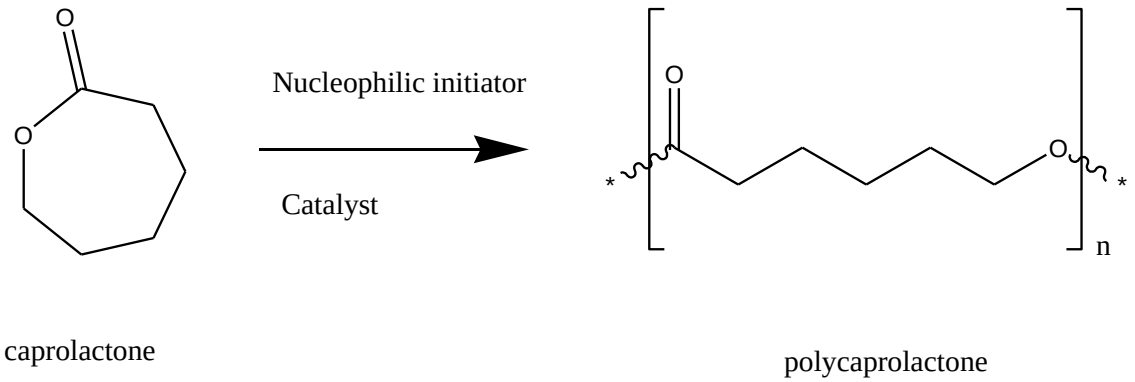

caprolactone

polycaprolactone

Scheme 1.1. Typical polymerization reaction of ε-caprolactone

PCL can be degraded in physiological conditions by the hydrolysis of the ester bonds and therefore is considered a biodegradable polymer[9]. This is reason why PCL has attracted tremendous interest for its use in implantable devices. The biocompatible character of the PCL has been highlighted since the Food and Drug Administration (FDA) has approved the use of PCL in specific applications in human body like surgical suture threads, drug delivery or adhesion barriers[10].

On the other hand, PEG is a polyether with many applications from industrial manufacturing to medicine. PEG is usually synthesized by anionic polymerization.

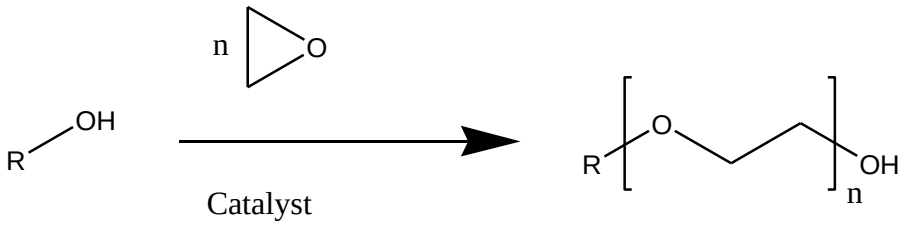

Scheme 1.2. Typical polymerization reaction of ethylene glycol

PEG is referred to low molecular weight polymers or oligomers, while polyethylene oxide (PEO) is used to refer to high molecular weight polymers (>20 kDa).

PEG is a non ionic hydrophilic polymer which is recognized to be biocompatible, since it has been extensively used in the pharmaceutical industry: PEG is present in laxatives, lubricants, eye drops, etc. In addition, when PEG is attached to proteins the clearance from bloodstream is decreased, and many protein-based drugs are being administered with PEG (e.g. pegylated α-TNF in the hepatitis therapy). The pegylation process provides enhanced solubility, increases biological half-life and reduces the allergenic response to the drug without decreasing the therapeutic efficacy[11].

The combination of two polymers of different nature in one macromolecule is referred as copolymer. When the two polymers present different solubility, the resulting macromolecule is an amphiphilic copolymer, which has a potential application in biomedicine as solubilizing agents for highly aqueous insoluble drugs. When an amphiphilic molecule is dispersed in water the system will tend to minimize the interfacial tension and will evolve toward the formation of micelles when a certain concentration is reached. This concentration is known as critical micelle concentration (CMC) that is characteristic for a certain surfactant, at fixed conditions of temperature and pressure and without considering other surface active molecules or electrolytes. The CMC represents a dynamic system in which the micelles are continuously exchanging molecules between the structure and the media:

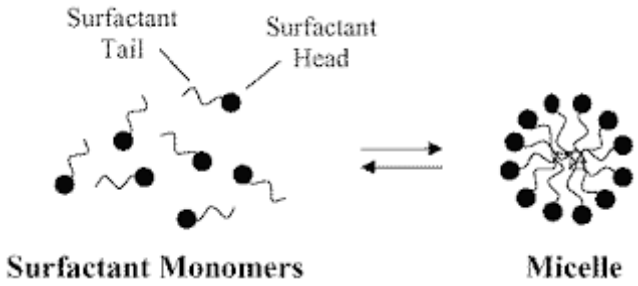

Scheme 1.3. Mechanism of the formation of micelles when the concentration of surfactant is above the CMC.

The amphiphilic copolymers are macromolecules with higher molecular weight than the classical surfactants. When they are dispersed in the appropriate media they can form supramolecular assemblies with different architectures, which are generally recognized as polymersomes, polymeric micelles and polymeric nanoparticles in the literature[12,13]. The minimum concentration of polymer to form these structures is known as critical aggregation concentration (CAC). The CAC is generally lower than the CMC of the classical surfactants, and represents a dynamic equilibrium that is highly displaced to the right[14], as represented in Scheme 1.4.

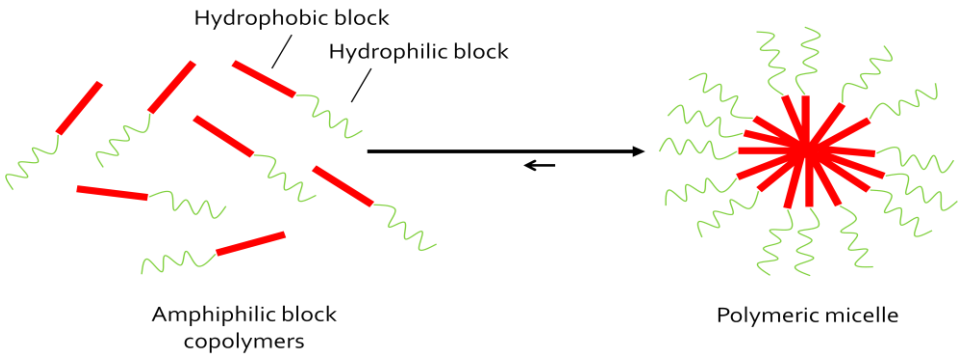

Scheme 1.4. Representation of the formation of polymeric micelles.

The polymeric micelles present a very slow rate of disassembly that provides high stability in solution, which is a major advantage for its use as drug carriers. This stability would be maximum for polymeric micelles formed by a unique high molecular weight amphiphilic molecule[15]. The low CAC value of the polymeric surfactants permits to have stable structures under diluted conditions, reducing the amount of surfactant in pharmaceutical formulations[16]. For this reason the polymeric micelles are of great scientific interest as drug nanocarriers.

The encapsulation of highly water insoluble drugs within polymeric micelles of a given nature depends on the relative weight ratio between the hydrophobic and the hydrophilic blocks of the polymer:

$$ratio(w/w) = \frac{Mw_l}{Mw_h}$$

Where Mw_l is the total molecular weight of the hydrophobic block and Mw_h is the total molecular weight of the hydrophilic block. For nonlinear amphiphilic structures, the Mw_l and the Mw_h should be calculated as the sum of all the individual blocks in the molecule[17].

A high value of this relative ratio would permit the encapsulation of lipophilic drugs inside the structure. However, the aqueous stability of the whole system can be affected. For this reason, it is of key relevance to find the appropriate balance that permits encapsulating a reasonable amount of drug and maintaining the stability of the whole system[18].

The amphiphilic block copolymers composed by biocompatible components with a biodegradable core could be used for the administration of highly insoluble drugs in formulations that would have less quantity of surfactant and would require a less frequent administration of the dose. All these features could be of great interest in cancer therapy.

1.2 Inorganic Nanoparticles

Materials often exhibit novel physical, chemical, electrical and optical properties as their size approaches the nanometer scale. At this scale, quantum effects dominate properties of materials, many of which are related with the discreteness of energy, the wave-particle duality of light and matter, quantum tunneling and uncertainty of measurements. These new properties open new applications in catalysis, energy, analytical chemistry and electronics.

Furthermore, nanoparticles have a very high surface to volume ratio, which provokes that large quantities of atoms are exposed to interactions with the medium. This increases the surface tension, which would lead to a final aggregation of the system. For this reason, the nanoparticles require a stabilizing agent. Depending on the synthetic conditions and the dispersion medium, there are basically two stabilization methods: electrostatic repulsion (DLVO theory) and steric hindrance (Vold and Vincent theory)[19].

The electrostatic repulsion consists in the coating of the nanoparticles with charged molecules (either negatively or positively charged) that prevent the aggregation. In summary the DLVO theory states that the colloidal stability is determined by the potential energy of the particles (V_T), which accounts for the potential energy of the attractive interaction due to van der Waals forces (V_A) and potential energy of the repulsive electrostatic interactions (V_R).

$$V_T = V_A + V_R$$

The van der Waals potential for two surfaces can be calculated as:

$$V_A = -\frac{H}{12\pi x^2}$$

For two spheres:

$$V_A = -\frac{H}{6x}\frac{R_1 R_2}{(R_1 + R_2)}$$

Where H is the Hamaker constant, x is the distance between the particles and R_1 and R_2 the radius of the two interacting particles.

The Hamaker constant H is given by the equation:

$$H = \pi^2 C \rho_1 \rho_2$$

Where ρ_1 and ρ_2 are the number of atoms per volume unit in two interacting bodies and C is a constant for the interaction energy in the particle-particle pair.

The electrostatic repulsion free energy for two planar surfaces is given by:

$$V_R = \frac{64 k_B T \rho_\infty \gamma^2}{\kappa} e^{-\kappa x}$$

Whereas for two spheres with radius R is given by:

$$V_R = \frac{64 \pi k_B T R \rho_\infty \gamma^2}{\kappa^2} e^{-\kappa x}$$

Where: k_B is the Boltzmann constant, ρ_∞ is the number density of atoms in the bulk solution, κ is related to the thickness of the diffuse electric double layer that is also referred as the Debye screening length $1/\kappa$ and γ is the reduced surface potential.

The reduced surface potential γ is shown as:

$$\gamma = \tanh \frac{Ze\psi_0}{4kT}$$

Where Z is the valence of the ion and ψ_0 is the potential on the surface.

The inverse of the Debye screening length κ is given by:

$$\kappa = \left(\frac{\sum_i \rho_\infty e^2 Z^2}{\varepsilon_r \varepsilon_0 k_B T} \right)^{\frac{1}{2}}$$

Where ε_r is the relative permittivity, ε_0 is the vacuum permittivity and ρ_∞ is the number density of ion “i” in the bulk solution.

By contrast, for those particles that are coated, the colloidal interactions are governed by two terms, van der Waals and steric forces. The effect of the van der Waals attractive interaction between particles coated with polymers was initially described by Vold and Vincent and gave as result an attractive effect, which can be enhanced as result of the nature of the polymer layer that decorates the particles. In the case of the steric term, this can be attractive or repulsive and thereby it can induce the flocculation of the samples or to provide thermodynamic stability. The main governing parameter, which dictates the sign of the steric interaction, is the affinity between the solvent and the tethered chains, which has been described by Napper[20]. In this approximation, the steric interaction potential is divided into two terms: the mixing osmotic contribution ΔG_{mix}, arising from the intimate mixing of the chain segments from two different particles (in the interpenetration zone) and elastic contribution, which accounts for the entropy loss due to the constriction of the polymer chains between the rigid particle surfaces.

$$V_{steric} = \Delta G_{mix} + \Delta G_{elas}$$

The particle destabilization begins in the interpenetration zone, and here the steric interaction between two identical particles is as follows[21]:

$$V_{steric} = k_B T \left[\frac{4\pi R}{v_m} \varphi^{av} \left(L - \frac{x}{2} \right)^2 \right] \left(\frac{1}{2} - \chi \right)$$

Where R is the particle radius, k_B is the Boltzmann constant, T is the absolute temperature, v_m is the volume of a solvent molecule, L is the length of the polymer chains, x is the distance between particles, χ is the Flory-Huggins interaction parameter that represents the solvency of the medium for the chains and the term φ^{av} is the average volume fraction of the segment in the grafted layer. It is evident from the equation that the sign of V_{steric} depends on the value of χ parameter, since the expression within the brackets is always positive. Thus, to stabilize the particles (positive V_{steric}) the medium must be good for the chains on the outer layer, that is, $\chi < 1/2$. On the contrary, chains with poor interaction with the solvent lead to attractive interactions (negative V_{steric}).

The steric hindrance has proved to be an efficient method for stabilizing nanoparticles, although the most used molecules (surfactants) might limit the final application of the nanoparticles[22]. A novel approach is to stabilize the nanoparticles with inert inorganic coatings within complex nanostructures such as core@shell nanoparticles. This could preserve the original properties of the nanoparticles and at the same time provide a stable environment and facilitate the functionalization of the nanoparticles[23].

The syntheses of inorganic nanoparticles require a controlled environment that contains 1) the inorganic precursor, 2) the reagents such as reducing agents, and 3) the stabilizing agents. There are several synthetic techniques for the production of nanoparticles of different nature, size and shape. However most of the synthetic protocols follow the nucleation theory of LaMer[24] summarized in Figure 1.1.

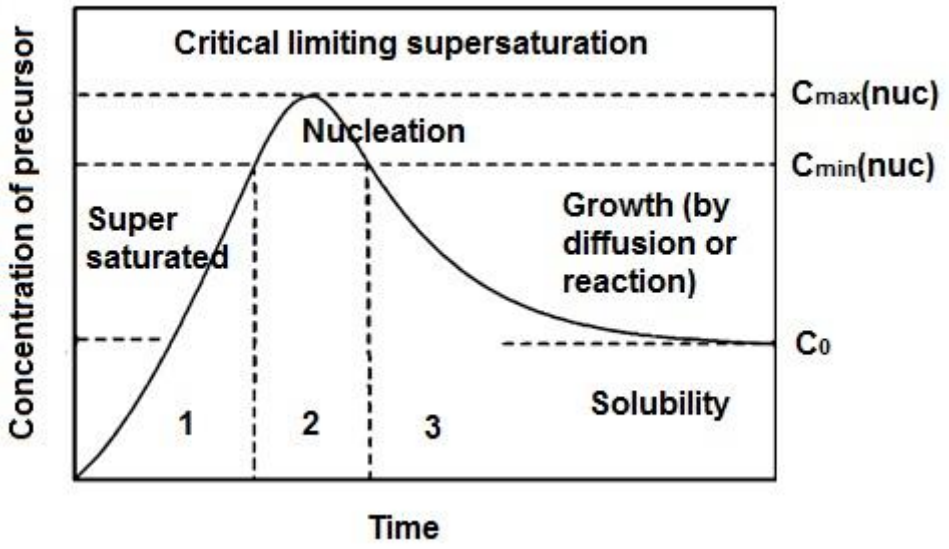

Figure 1.1. LaMer diagram with the time separation between the nucleation, growth and saturation stages in the synthesis of nanoparticles.

The LaMer diagram states that the synthesis of nanoparticles should follow three steps: In the first step, the concentration of the precursors (salts, complexes, etc.) and reagents increase to reach the necessary concentration for nucleation. The second step is the nucleation, in which the precursors produce small nuclei of nanoparticles, which is concomitant with a reduction of the concentration of the precursors. The third step consists in the growth of

these nuclei, by the passive diffusion of the remaining precursors. This basic diagram can explain several synthetic techniques like the seed mediated growth, the heating up and hot-injection processes[25].

When the concentration of a solute in a solvent exceeds its solubility a new phase appears. In the case of homogeneous nucleation a solid phase nucleates from a supersaturared solution. The Gibbs free energy of the supersaturated solution is higher than that of a solution below saturation and can be reduced by the nucleation of particles. This reduction of Gibbs free energy is the driving force for both nucleation and growth. The change of Gibbs free energy per unit of volume of the solid phase, ΔG_v, is given by:

$$\Delta G_v = -\frac{k_B T}{a} \ln(1+\sigma)$$

Where a is the atomic volume, k_B the Boltzmann constant, T the temperature and σ is the supersaturation, defined by:

$$\sigma = \frac{C - C_0}{C_0}$$

Where C is the concentration of solute and C_0 is the solubility.

At supersaturation (ΔG_v=0) and below (ΔG_v>0) no nucleation would occur. When C > C_0, ΔG_v is negative and nucleation occurs spontaneously. Assuming that a spherical nucleus with a radius R is formed, the change of Gibbs free energy or volume energy is given by:

$$\Delta \mu_v = \frac{4}{3} \pi R^3 \Delta G_v$$

This energy reduction is counter balanced by the gain of surface energy which accompanied the formation of the spherical particles, and is given by:

$$\Delta \mu_s = 4\pi R^2 \gamma$$

Where γ is the surface energy per unit area. The total free energy change for the formation of the nucleus, ΔG, is given by:

$$\Delta G = \Delta\mu_v + \Delta\mu_s = \frac{4}{3}\pi R^3 \Delta G_v + 4\pi R^2 \gamma$$

The new formed nucleus is stable only when its radius exceeds a critical size R*. A nucleus smaller than R* will dissolve whereas a nucleus larger than R* is stable and continues to grow. The critical size R* is obtained by the condition:

$$\frac{d\Delta G}{dR} = 0$$

and is given by:

$$R^* = -\frac{2\gamma}{\Delta G_v}$$

Figure 1.2 represents the nucleation and growth process when R $\geq$ R*

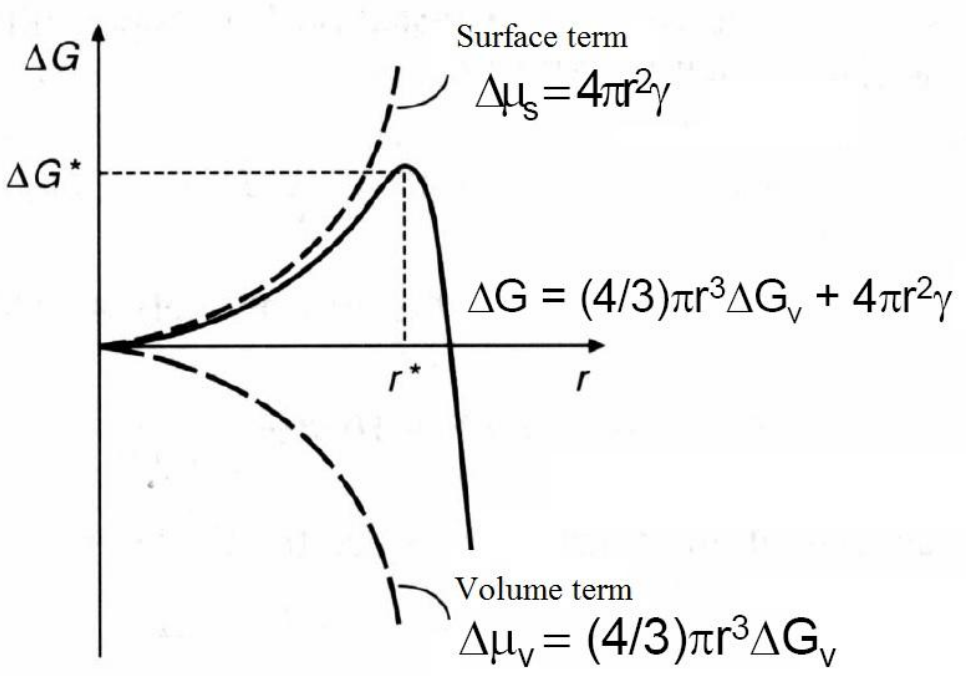

Figure 1.2. Representation of the free energy as a function of two terms: the surface term and the volume term. Nucleation occurs when R is equal or higher than R*.

Ideally, monodisperse nanoparticles could be obtained by separating in time the nucleation and growth steps. Polydisperse samples are obtained when the nucleation process is long or there are multiple moments of nucleation within the synthesis.

1.2.1 SuperParamagnetic Iron Oxide Nanoparticles (SPIONs)

Iron oxide nanoparticles are crystals of Fe^{3+} and/or Fe^{2+} with O^{2-} with a size between 1 and 100 nm of diameter, generally with spherical or cubic shape. The two main forms are magnetite (Fe_3O_4) and its oxidized form maghemite (γ-Fe_2O_3)[26]. The iron oxide nanoparticles are characteristic due to their superparamagnetic behavior when the size is below 30 nm of diameter[27].

The SPIONs can be synthesized by different procedures, but the best results in terms of yield and sample size distribution is generally obtained by three[22]: the coprecipitation, the solvothermal and the thermal decomposition methods.

Coprecipitation method: Consists in mixing stoichometric mixtures of Fe^{2+} and Fe^{3+} ions, generally as chloride salts, in an aqueous solution at basic pH. This synthesis is often referred as the Massart[28] method and yields spherical iron oxide nanoparticles of approximately 5-10 nm in size, relatively monodisperse. The nanoparticles are stabilized only by the surface charges, which often leads to the aggregation of the sample when the pH of the media tends to 7. A variant of this method consists in the reaction of Fe^{2+} salts, generally sulfates, with nitrate ions at elevated pH. This synthesis is known as the Sugimoto and Matijevic[29] method, and yields spherical or cubic iron oxide nanoparticles, depending on the synthetic conditions, with a size distribution between 30 and 100 nm. The sample size distribution is generally high, with polydisperse samples. The nanoparticles are stabilized by electrostatic repulsion due to the surface charges and they have a strong tendency to aggregate. Both syntheses yield highly crystalline structures with a strong magnetic response.

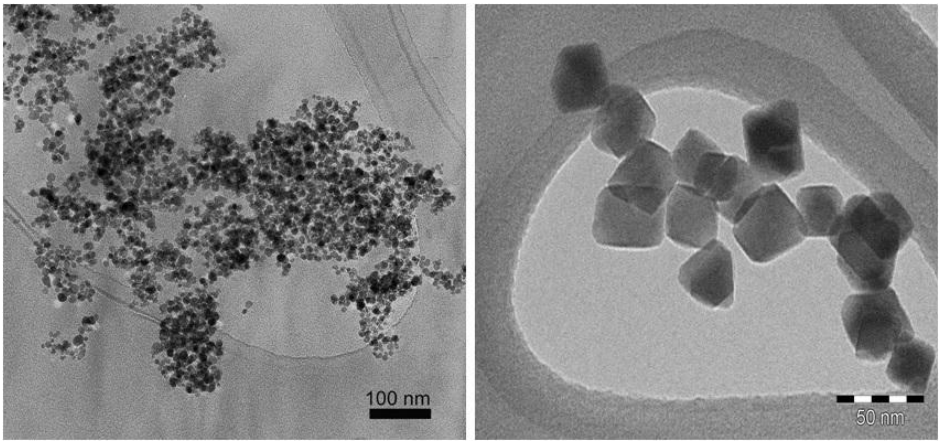

Figure 1.3. TEM images of: Left: Iron oxide nanoparticles obtained by the Massart method. Right: Iron oxide nanoparticles obtained by the Sugimoto and Matijevic method.

Solvothermal method: This method, also known as sol-gel method, consists in the reaction of Fe^{2+} and Fe^{3+} in a basic environment in a mixture of surfactants such as sodium oleate and ethylene glycol[30]. The mixture is heated in a stainless steel autoclave and yields spherical structures of tunable size from 80 to 400 nm. The structures are composed by small iron oxide nanoparticles with a pomegranate like aggregation. The stabilization is based on the surfactants that are surrounding the structure that avoids the aggregation by direct steric hindrance between the nanoparticles. Therefore, the samples are fairly stable, monodisperse and the high crystallinity provides a strong magnetic response.

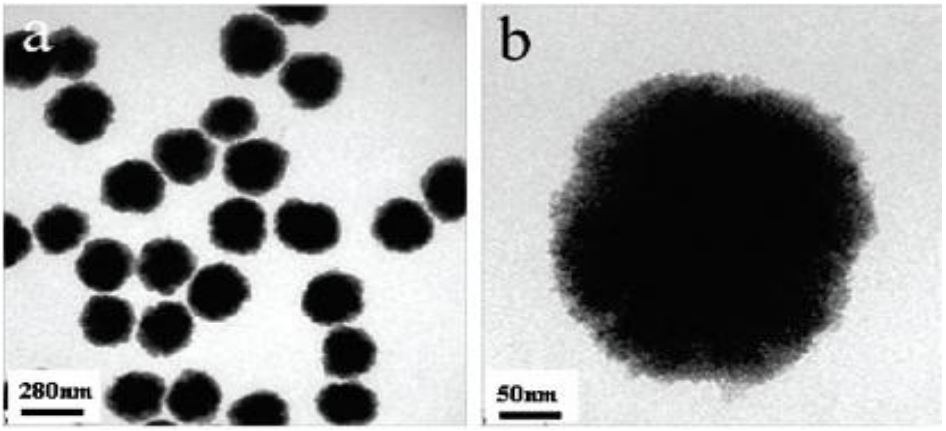

Figure 1.4. a) TEM image of iron oxide nanoparticles obtained by the solvothermal method and b) magnification of one particle.

Thermal decomposition method: Consists in the reaction at elevated temperature of organic iron complexes such as iron (III) oleate, iron (III) acetylacetonate, iron (0) pentacarbonyl... etc, in a mixture of surfactants like oleic acid, oleylamine, trioctylphosphine oxide... etc, dissolved in a non-coordinating high boiling point solvent such as 1-octadecene, diphenylether, tetracosane... etc. Depending on the reaction parameters and reagents, it is possible to obtain extremely monodisperse spherical[31] or cubic[32] iron oxide nanoparticles with tunable size between 2 and 40 nm. The resulting iron oxide nanoparticles are stabilized with the surfactants on their surface, which provides a high stability due to the steric hindrance. The nanoparticles obtained by this method are individual and remain stable and separated for several months despite their small size. The nanoparticles possess good crystallinity and can be readily dispersed in organic solvents such as hexane, toluene, chloroform, etc.

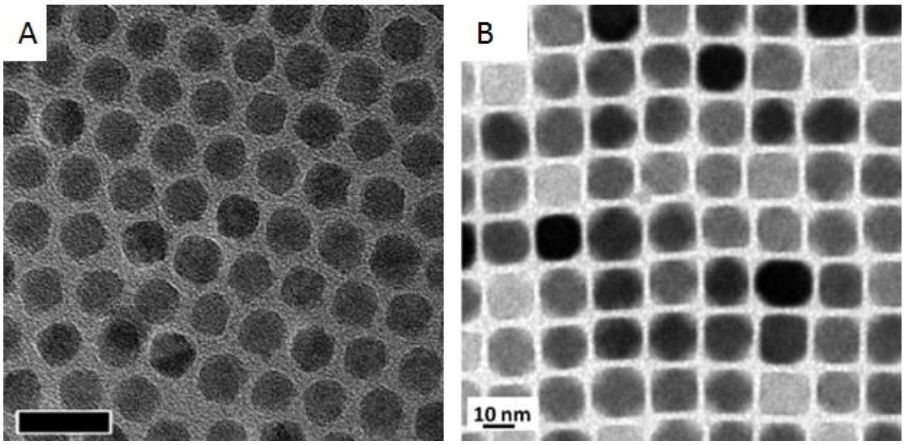

Figure 1.5. A) TEM image of spherical iron oxide nanoparticles synthesized by thermal decomposition of iron (III) oleate. Scale bar is 15 nm. B) TEM image of cubic iron oxide nanoparticles synthesized by thermal decomposition of iron (III) acetylacetonate.

The main characteristic of the iron oxide nanoparticles is their “magnetism”. The colloquial sentence that says “magnetic nanoparticles” often refers to their magnetic interaction with an external magnetic field. However, it is important to differentiate the different types of magnetism, which are basically four:

Diamagnetic materials: These materials create an induced magnetic field that opposes to an external magnetic field, and therefore they are repelled by a magnet. The diamagnetism is a property of all materials, but in the presence of other forms of magnetism, it becomes negligible. Examples of diamagnetic materials are water, wood, many organic compounds, mercury, bismuth, pyrolytic carbon…

Ferromagnetic materials: These materials have intrinsic magnetic moment with a random orientation of their magnetic domains. In the presence of an external magnetic field, all the magnetic domains will align with the field, and therefore they are attracted by a magnet. When the external magnetic field is removed, the magnetic domains of ferromagnetic materials keep their orientation. In this way, the ferromagnetic material shows intrinsic magnetism and becomes a permanent magnet. The ferromagnetic materials can be demagnetized at the Curie temperature. Examples of ferromagnetic materials are iron, nickel, cobalt…

Paramagnetic materials: These materials have intrinsic magnetic moment with a random orientation of their magnetic domains. In the presence of an external magnetic field, all the magnetic domains will align with the field, and therefore they are attracted by a magnet. When the external magnetic field is removed, the magnetic domains can interact between them. This provokes that the paramagnetic materials remain the magnetization for a period of time after the external field is removed. However, when these interactions between the magnetic domains disappear, the paramagnetic materials lose the magnetization. Examples of paramagnetic materials are tungsten, aluminum, and some transition metal complexes.

Superparamagnetic materials: Superparamagnetism occurs when ferromagnetic materials reduce their size to a point in which the magnetic domains are reduced to just one. In the nanoscale it is considered that each nanoparticle possess a single magnetic domain. Under this scenario, the magnetization can randomly flip direction under the influence of temperature. As consequence, the magnetization of a sample containing the nanoparticles appears to be in average zero. In the presence of an external magnetic field,

the magnetic domains of the nanoparticles will align with the field, and therefore they are attracted by the magnet. However, when the external magnetic field is removed, the magnetic domains flip with the temperature and therefore the overall magnetization is averaged to zero again. The temperature required to flip is under the Curie temperature, which is the main difference with the ferromagnetic materials. The mean time between two flips is the Néel relaxation time τ_n given by the Néel-Arrhenius equation:

$$\tau_n = \tau_0 \exp\left(\frac{KV}{k_B T}\right)$$

Where τ_n is the average time it takes for the nanoparticles magnetization to flip due to the thermal fluctuation, τ_0 is a time characteristic of the material also known as attempt period, K is the magnetic anisotropy energy density of the nanoparticles, V is the volume of the nanoparticles, k_B is the Boltzmann constant and T the temperature.

The superparamagnetic nanoparticles show a high magnetic susceptibility but the overall magnetic moment of a sample containing the nanoparticles is zero in the absence of an external magnetic field. This behavior is typically demonstrated by the narrow hysteresis loop in SQUID magnetization measurements.

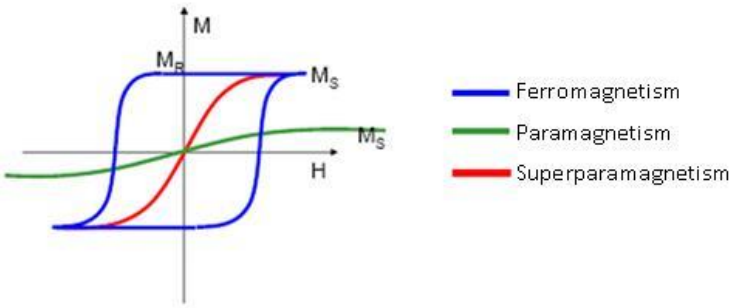

Figure 1.6. Schematic representation curves obtained in SQUID magnetization measurements for each type of magnetism behavior.

SPIONs have potential to be applied in biomedicine[33] because magnetite and maghemite are biocompatible, non-toxic and biodegradable[34], which makes

them ideal for in vivo applications[35]. In addition, the superparamagnetic behavior of the iron oxide nanoparticles prevents the aggregation after the response to an external magnetic field[36].

Magnetic Resonance Imaging: The SPIONs can be used as contrast agents in Magnetic Resonance Imaging (MRI). MRI is a medical imaging technique used in radiology to investigate the anatomy and physiology of the body in both health and disease by a non invasive methodology[37]. MRI scanners use magnetic fields and radio waves that are not harmful for health. For these reasons MRI is widely used in hospitals as diagnostic tool. The MRI is based on the ^{1}H nuclear magnetic resonance of the water molecules of the tissues in the presence of an external magnetic field and the radiofrequency pulse excitation. The different environments of the tissues provoke a different rate at which excited atoms return to the equilibrium state, which renders the contrast between the tissues. There are two types of possible contrast in MRI[38]: The spin-lattice relaxation that leads to the so called T_1-weighted MRI contrast and the spin-spin relaxation that leads the T_2-weighted MRI contrast. The superparamagnetic iron oxide nanoparticles reduce the T_2 signals by the alteration of the proton relaxation in the tissue microenvironment. Therefore can be used as contrast agents in T_2-weighted MRI, which could be useful for example in the detection of tumors.

Drug delivery: The SPIONs can also find application in targeted drug delivery due to the magnetic responsiveness to external magnetic fields. Although this idea has been around for many years with limited success, the potential of the SPIONs as targeted drug delivery vehicles is still very exciting[39]. The basic idea was to administer drug loaded iron oxide nanoparticles, and magnetically arrest them with an external magnetic field. Despite the difficulties, novel approaches combine the superparamagnetic nanoparticles with other alternatives such as active targeting[40], magnetic field gradients with implanted magnetic grids[41], and other drug release mechanisms like pH or temperature responsive materials[42]. The magnetic targeted drug delivery is still a major research topic in cancer therapy[43].

Magnetic hyperthermia: This process consists in the application of a magnetic field that alternates the direction with a specific frequency. When the SPIONs are exposed to the alternating magnetic field, they generate heat that locally increases the temperature[44]. This can be applied to tumor tissues and bacterial infections, in which an increment of temperature to 44 ºC will cause cell death. The mechanism involved in the heat generation relies on the continuous relaxation and orientation of the easy axis of the magnetic spin of the nanoparticles. The magnetic hyperthermia is a promising tool in cancer therapy, for which has entered in phase II clinical trials in Europe.

1.2.2 Metal nanoparticles

Noble metal nanoparticles have been extensively studied within the past years due to their prominent optical resonance in the visible range and their sensitivity to environmental changes. The most employed materials for developing metal nanoparticles for biomedical applications are gold (Au NPs) and silver (Ag NPs). The main characteristic of these nanoparticles is their optical properties due to the localized surface plasmon resonance (LSPR)[45].

The metal nanoparticles can be synthesized by different procedures that have a strong influence on the final product because the optical properties are different depending on the size and shape of the nanoparticles. The colloidal stability of the nanoparticles requires a surfactant or stabilizing agent in solution. The most employed methods are the organic phase synthesis involving a two phase process (known as Brust method[46]), or the single phase water based reduction of a gold or silver salt by citrate (known as Turkevich method[47]). The cetyl trimethylammonium bromide (CTAB) is used as surfactant for seed mediated growth of Au and Ag NPs that permits a good control over the size and the shape of the product. In this method, the first step is the synthesis of small uniform spherical nanoparticles known as seeds. These seeds are used as templates for the addition of more precursors under mild conditions[48].

Colloidal solutions of metal nanoparticles exhibit intense color due to the localized surface plasmon resonance, which occurs when the size of the nanoparticle is smaller than the wavelength of light. For example, bulk gold has a characteristic yellow color, caused by a reduction in reflectivity for light at the

end of the spectrum whereas a solution containing spherical gold nanoparticles of 12 nm presents an intense deep red color caused by an intense absorption at 520 nm, which corresponds to the green light. The color of a colloidal solution with metal nanoparticles depends on the resonance frequency of the nanoparticles, which can vary due to the nature of the material, the size and the shape[49]. See Figure 1.7.

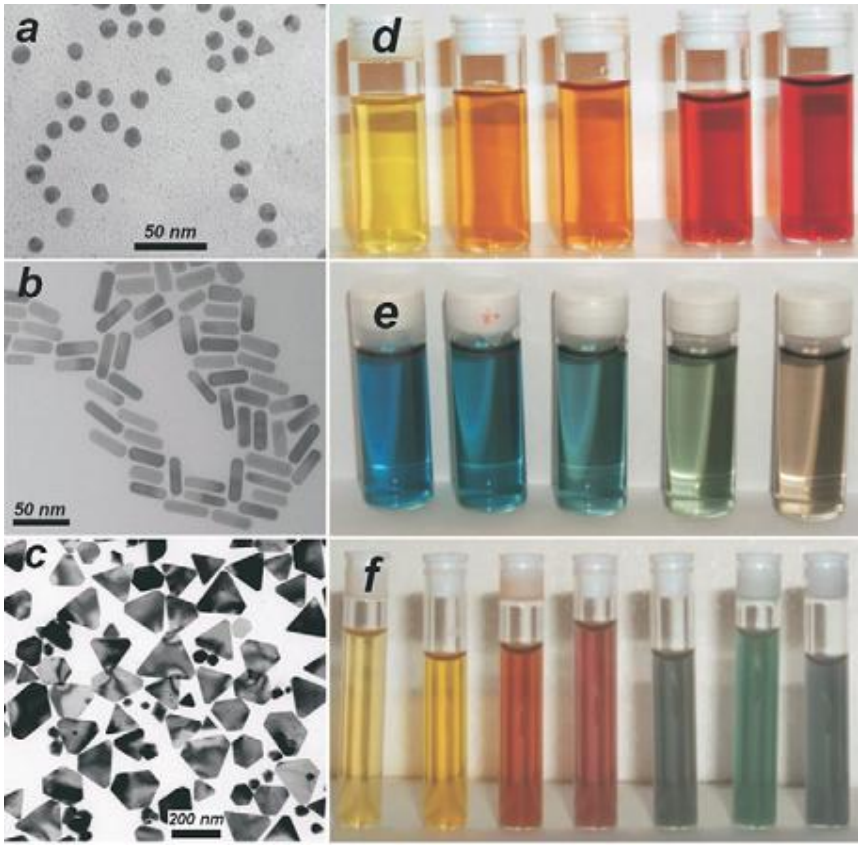

Figure 1.7. Left: TEM micrographs of Au nanospheres and nanorods (a,b) and Ag nanoprisms (c). Right: Pictures taken from colloidal dispersions of AuAg alloy nanoparticles with increasing Au concentration (d), Au nanorods with increasing aspect ratio (e) and Ag nanoprisms with increasing lateral size (f)[49].

The LSPR was theoretically explained by Mie[50], who could solve the Maxwell's equation for metallic spheres with a size smaller than the wavelength of visible light and gave the explanation for the red color of gold nanoparticles in solution. The physical origin of the light absorption by metal nanoparticles is the coherent oscillation of the electrons in the conduction band, induced by the interacting electromagnetic field.

The electromagnetic waves can propagate along the surface of the nanoparticles along the interface between conducting and dielectric materials over a broad range of frequencies[51]. Oscillation modes comprise an electromagnetic field coupled to the oscillations of electrons in the conduction bands are called surface plasmons. They are characterized by a strong field enhancement at the interface that decays exponentially with the distance[52]. When the dimension of the conductor are reduced, boundary and surface effects become dominant, and for this reason the optical properties of metal nanoparticles are dominated by collective oscillation of conduction electrons[53]. An absorption band occurs when the frequency of an incident photon is resonant with the collective oscillation of the electrons in the conduction band, and this is the localized surface plasmon resonance. The resonance frequency of the LSPR is strongly dependent on the size, shape, interparticle interactions, dielectric properties of the environment and nature of the particles[54].

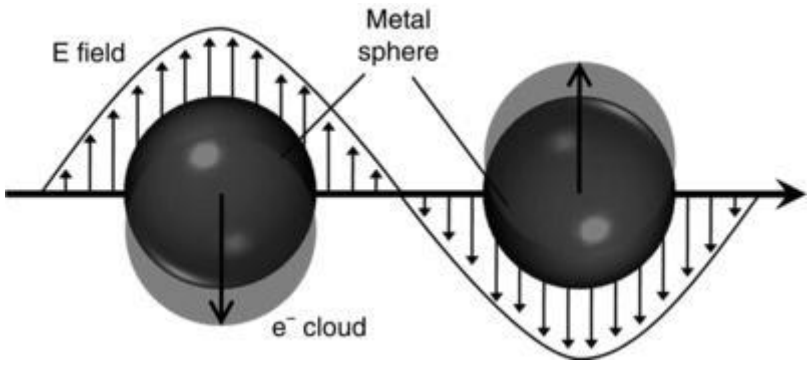

Figure 1.8. Schematic representation of the LSPR in a metal sphere induced by the electric field from an incident electromagnetic wave.

Noble metals such as copper, gold and silver have a remarkable plasmon resonance in the UV-Vis light region, and the nanoparticles prepared with these elements (pure and/or alloys) present an intense LSPR absorption band.

The LSPR provides two important characteristic to the colloidal solution of metal nanoparticles: First, very intense optical properties that are very sensitive to environmental changes and second, a high enhancement of the local electric field near the surface of the nanoparticles.

Metal nanoparticles find potential applications in many different fields, with relevance in physics[55–57] and in chemistry[58,59]. In biomedicine, metal nanoparticles have had an enormous impact and attention[60]. Despite the physical characteristics, gold is a highly stable material against oxidation and corrosion and it reacts with very few compounds. In addition, gold nanoparticles are easy to functionalize via the well known Au-S chemistry[61]. For these reasons, gold nanoparticles have been studied, among others, for the following applications:

Immunogold labelling: Au nanoparticles possess a very high Z contrast in electron microscopy. In addition, the surface of the Au NPs is easy to functionalize. Gold nanoparticles are functionalized with a certain antibody and the specific interaction with cells can be observed by electron microscopy.

Biosensors: Many different nanoconstructs use Au nanoparticles for biosensors. Some works are based on the high environmental dependence of the LSPR absorption band to create optical biosensors[62,63]. Other works use the electric field enhancement that the Au nanoparticles possess in their surface for the well known Surface-Enhanced Raman Spectroscopy (SERS) detection[64,65].

Drug delivery: The strong absorption of photons can be translated into an increment of the local temperature. Some authors have used this concept for energy applications[66,67] but it has been also studied for drug delivery. For example, in a hybrid material consisting in polymers and Au nanoparticles, an external light stimulus would provoke a local increment in the temperature above the melting point of the polymer, which would release the encapsulated drug[68]. Alternatively, Au nanoparticles have been investigated as photothermal therapy[69,70]. In addition, Au nanoparticles have been used as indicators in traceable drug delivery systems[71].

Contrast imaging: Au nanoparticles have been proposed as contrast agents for computed tomography (CT)[72]. Gold has higher absorption than iodine with less bone and tissue interference achieving better contrast with lower X-ray dose. These nanoparticles clear the blood more slowly than iodine agents, permitting longer imaging times[73].

Silver nanoparticles are used to efficiently harvest light and for enhanced optical spectroscopies including metal enhanced fluorescence (MEF)[74] and SERS. Ag nanoparticles have shown an important antibacterial activity, although the mechanism remains uncertain[75]. Silver nanoparticles are incorporated in apparel, footwear, paints, wound dressings, appliances, cosmetics, and plastics for their antibacterial properties.

1.2.3 Fluorescent Nanoparticles

1.2.3.1 Quantum Dots

Quantum dots are nanoparticles composed by semiconductor materials, typically combinations of cadmium and/or lead with sulfur and/or selenide nanocrystals and indium arsenide and/or phosphide. If the size of the quantum dot is small enough (typically less than 10 nm), the quantum confinement effects dominate. Under this scenario, the electronic and optical properties are highly tunable with the size of the nanoparticles.

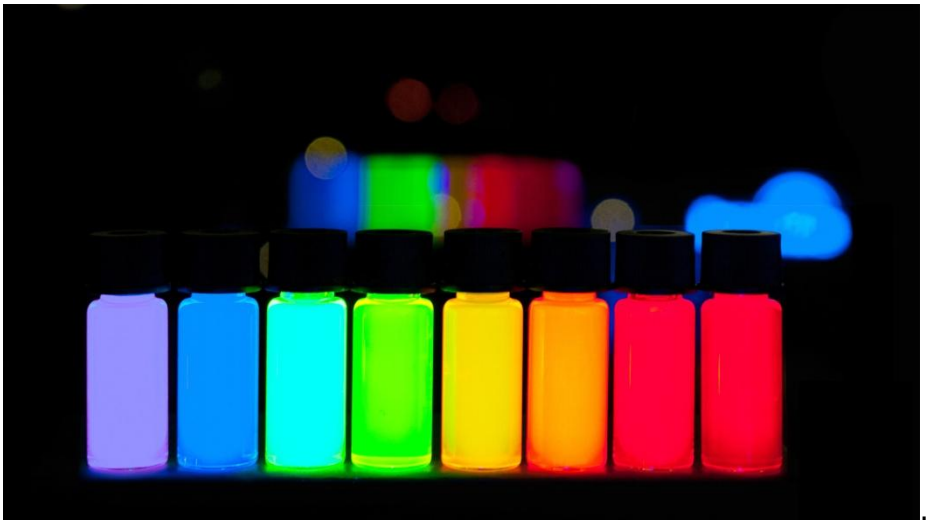

Figure 1.9. Colloidal dispersion of commercially available QDs with different size, under UV illumination.

The fluorescence from the QDs comes from the bandgap between the valence band and the conduction band. The valence band corresponds to the highest occupied molecular orbitals (HOMO) whereas the conduction band corresponds to the lowest unoccupied molecular orbitals (LUMO). The light stimulus promotes electrons from the valence band to the conduction band. These

electrons will recombine and return to the valence band, emitting a photon with the energy associated to the bandgap, and this bandgap depends on the particle size and composition[76].

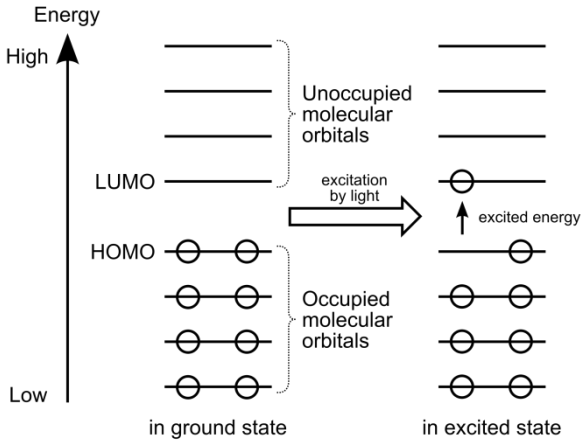

Figure 1.10. Schematic representation of the molecular orbitals with the electrons represented as circles.

The main synthetic method for quantum dots is the colloidal thermal decomposition by hot injection. This method consists in the preparation of a solution at high temperature containing one of the precursors, stabilizing agents and a non-coordinating solvent. At a certain temperature, a solution containing the other precursor is poured to form the quantum dots. By controlling the reaction conditions such as precursor ratios, concentrations and temperature it is possible to control the size of the nanoparticles and therefore their fluorescent properties[77].

Quantum dots present a very high extinction coefficient and a very high fluorescence quantum yield[78]. In addition, QDs do not present photobleaching (degradation of the fluorophore due to the exposition to light).

For these reasons, the QDs have shown a great potential in many different fields from computing to photovoltaic devices[79]. In biomedicine, QDs could be applied as an alternative to the classical organic fluorescent dyes, which typically show lower fluorescence quantum yield and suffer from photobleaching[80]. The quantum dots have far-reaching potential for several biomedical applications, to say: the study of intracellular processes at the single-molecule level, high-resolution cellular imaging and long-term *in vivo*

observation of cell tracking, tumor targeting, and diagnostics in combination with fluorescence spectroscopy and diffuse optical tomography[81].

1.2.3.2 Upconversion nanoparticles

Upconversion nanoparticles are rare-earth doped nanocrystals that present a unique type of fluorescence in which the excitation wavelength is higher than the emission wavelength. In a typical upconversion fluorescence process, NIR photons are absorbed by the fluorophore, emitting UV-Vis photons. This Anti-Stokes emission can be explained as a sequential absorption of photons by the fluorophore, in which two or more low energy photons are converted into one photon of higher energy and as consequence a smaller wavelength. The upconversion photoluminescence process is different from the nonlinear multiphoton absorption, since it's more efficient and it's produced by inexpensive continuous wave (CW) lasers instead of ultrashort pulsed lasers[82].

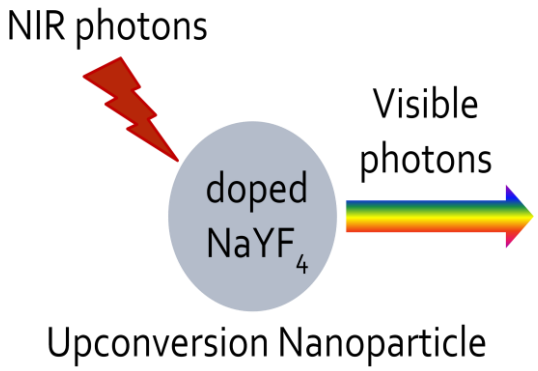

Figure 1.11. Schematic representation of the upconversion fluorescence process in a doped sodium yttrium fluoride nanoparticle

The upconversion fluorescence requires three components to occur: i) the antenna or sensitizer, which is the responsible of harvesting the NIR photons; ii) the activator or emitter, which is the responsible of emitting the upconverted photons; and iii) a low phonon matrix that provides a non vibrational environment that diminishes the non-radiative decays and in which the previous components can exchange energy via resonance energy transfer processes[83]. The most common antenna is the ion ytterbium (Yb^{3+}) that absorb photons at 980 nm. The sensitizers are usually erbium, thulium or holmium ions (Er^{3+}, Tm^{3+}, Ho^{3+}) between others. The emitted photons wavelengths depend on the

sensitizer and therefore this component has to be carefully chosen depending on the application. The most common low phonon matrix consists in β-$NaYF_4$ that is considered to be the most efficient host for upconversion fluorescence[84]. The nanoparticles that present upconversion fluorescence are referred generally as UCNPs (UpConversion NanoParticles), although the chemical composition can differ: e.g.: $NaYF_4$:Yb,Er , $NaYF_4$:Yb,Tm , $NaGdF_4$:Yb,Er … etc. Lanthanide-doped UCNPs are dilute guest−host systems where trivalent lanthanide ions are dispersed as a guest in an appropriate dielectric host lattice with a dimension of less than 100 nm[85]. Generally, the upconversion photoluminescence (UCPL) arises from the 4f−4f orbital electronic transitions with concomitant wave functions localized within a single lanthanide ion[86].

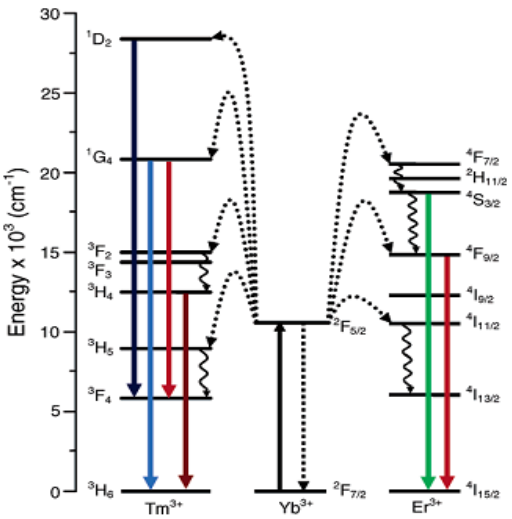

Figure 1.12. Schematic representation of the orbital energy levels involved in the UCPL emission with Yb^{3+} and Tm^{3+} or Er^{3+} doped UCNPs.

The shielding of 4f electrons by the outer complete 5s and 5p shells results in line-like sharp emissions, which exhibit high resistance to photobleaching, and photochemical degradation. The primary forbidden nature of the 4f−4f transition yields very long lifetimes (up to tens of millisecond) for energy levels of lanthanide ions, thus favoring sequential excitations in the excited states of a single lanthanide ion as well as permitting favorable ion−ion interactions in the excited states to allow energy transfers between two or more lanthanide ions. These resulting features of lanthanide dopants determine the basic UC

mechanisms. The UCPL intensity generally has a nonlinear dependence on the excitation light density[87]:

$$I_{UCPL} = KP^n$$

Where I_{UCPL} is the intensity of the upconversion fluorescence, P is the power of the excitation laser, K is a coefficient from the material and n is the number of photons required to produce the UCPL. However, a saturation effect can occur at high P values. Because of the nonlinear nature of the upconversion process, the efficiency of a specific emission is strongly dependent on the excitation density.

Unlike other nanosized materials, UCNPs have similar optical properties to those of the corresponding bulk forms. They both generally produce the same peaks due to the 4f−4f orbital electronic transitions. However, the efficiency and the relative intensity between different UCPL peaks of UCNPs are quite different from their bulk counterpart due to nanosize-induced surface effects. Because of the high surface-to-volume ratio of UCNPs, many of the lanthanide dopants are exposed to surface deactivations due to surface defects, ligands and solvents that possess high phonon energy. As consequence, the UCPL efficiency of UCNPs is much lower than that of their bulk form. The nanoengineering of the surface can diminish this drawback, for example by the synthesis of core@shell UCNPs[88].

UCNPs can be synthesized by different colloidal methods: thermal decomposition, solvothermal synthesis, Ostwald-ripening method, sol−gel processing, coprecipitation method… etc. However, the first three are the most widely used methods because they allow precise control over the size, stoichometric composition, shape and phase of the core and/or the core@shell UCNPs.

Thermal decomposition: The thermolysis strategy generally employs organometallic compounds as precursors, which decompose in a high boiling point organic solvent with the assistance of surfactants at an elevated temperature[89]. The commonly used precursors are lanthanide trifluoroacetate salts whereas the typical solvent and surfactant combination is 1-octadecene

and oleic acid, oleylamine or trioctylphosphine oxide. The stabilization of the nanoparticles is due to the steric hindrance of the long hydrocarbon chains of these surfactants that coordinate to the surface of the nanoparticles.

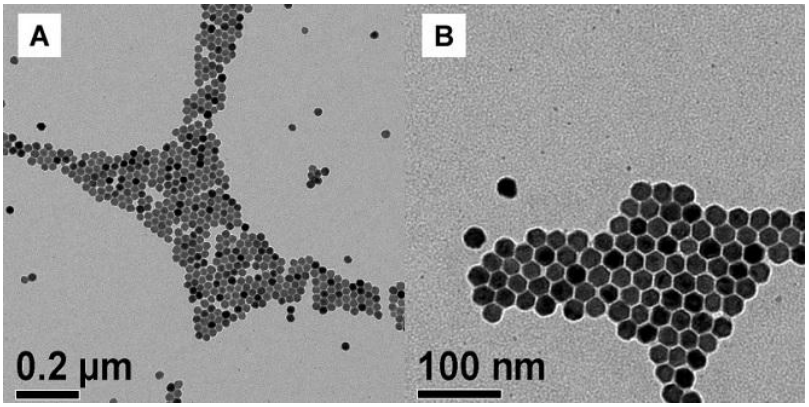

Figure 1.13. TEM images of $NaYF_4$:Yb,Er nanocrystals synthesized by the thermal decomposition method[89].

Solvothermal method: The reaction occurs in a sealed environment under high pressure and temperature, usually above the critical point of the solvent to increase the solubility and reactivity of the inorganic substances[90]. This method yields highly crystalline phases at much lower temperatures and it's easier to scale up. However, it requires specialized stainless steel autoclaves to perform the synthesis. The surfactants that are used in the reaction, to prevent aggregation of the nanoparticles, are generally polyethylenimine (PEI), ethylenediaminetetraacetic acid (EDTA), cetyltrimethylammonium bromide (CTAB) and oleic acid (OA). This method permits to obtain nanoparticles with a size between 300 nm and 10 microns.

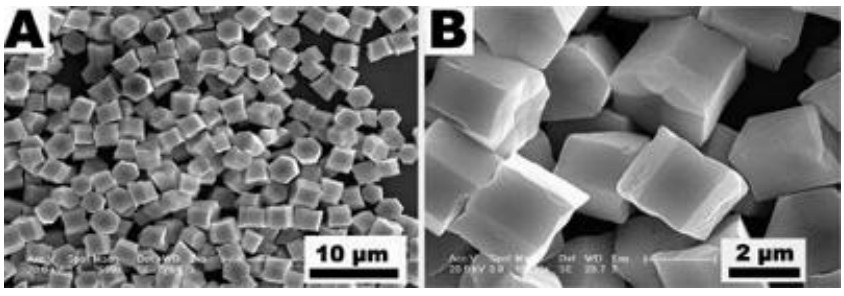

Figure 1.14. SEM images of hexagonal lanthanide doped $NaYF_4$ nanoparticles synthesized by the solvothermal method[90].

Ostwald-Ripening strategy: Ostwald ripening refers to the process in which small particles with high surface-to-volume ratios grow to form larger particles at the expense of smaller ones[91]. Zhang and co-workers synthesized highly uniform hexagonal phase $NaYF_4$:Yb^{3+},Er^{3+}(or Tm^{3+}) UCNPs with controllable shapes and sizes by using OA as the capping ligand and ODE as the high-boiling point solvent[92]. In this process, small sacrificial $NaYF_4$ nanoparticles are formed by coprecipitation at room temperature, which further follow an Ostwald-ripening process at elevated temperature. This strategy is also useful to produce hierarchical core@shell nanoparticles with precise shell thickness control by regulating the concentration of small sacrificial nanoparticles. The Ostwald-ripening strategy yields highly crystalline hexagonal UCNPs with a minimal amount of defects and therefore with an improved upconversion efficiency. In addition, the instrumentation required for this process is relatively assumable and the reaction by-products are not as toxic as the typical ones obtained by thermolysis of organometallic precursors.

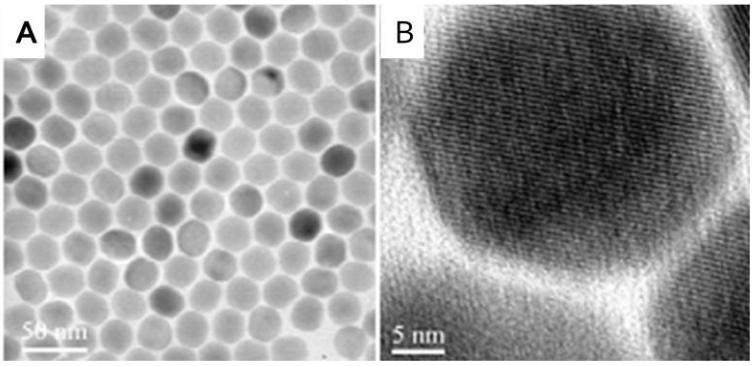

Figure 1.15. TEM micrographs of monodisperse lanthanide doped $NaYF_4$ obtained by the Ostwald ripening method[92].

There are basically five mechanisms for the upconversion process[86], which are named as: a) Excited State Absorption (ESA), b) Energy Transfer Upconversion (ETU), c) Cooperative Sensitization Upconversion (CSU), d) Cross-Relaxation (CR) and e) Photon Avalanche (PE). The mechanisms are depicted in Figure 1.16.

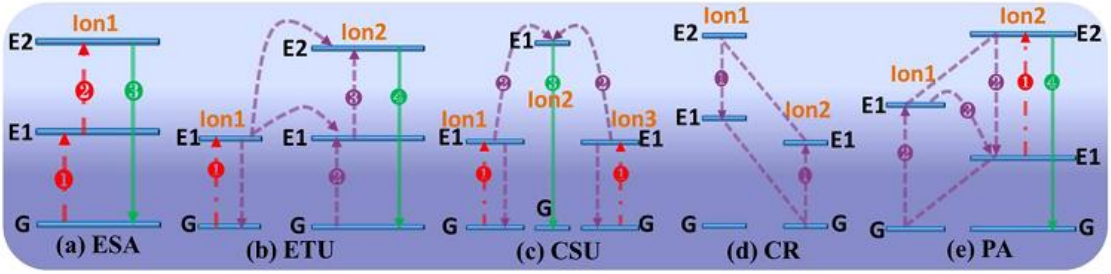

Figure 1.16. Schematic illustration of the different upconversion mechanisms[93].

Excited State Absorption: ESA consists in the successive absorption of pump photons by a single ion due to the ladder-like structure of a simple multilevel system by a three level system with similar energy bandgaps, in which two photons are sequentially absorbed. The equal separation from G to E1 and from E1 to E2 as well as the reservoir capability of the intermediate level E1 permit that when an ion is excited from the ground state to the E1 level, another pump photon has a high possibility of promoting the ion from E1 to the higher-lying state E2 due to the long lifetime of E1 state, before its decay to the ground state. Consequently, upconverted emission will occur from the relaxation from the E2 level to the G level. To achieve highly efficient ESA, a ladder-like arrangement of the energy states of lanthanide is required. Only a few lanthanide ions such as Er^{3+}, Ho^{3+}, Tm^{3+} and Nd^{3+} have such energy level structures[94]. This mechanism is illustrated in Figure 1.16(a).

Energy Transfer Upconversion: ETU involves two neighboring ions: the sensitizer (ion 1) is first excited from the ground state to its metastable level E1 by absorbing a pump photon; it then successively transfers the harvested energy to the excited-state E1 of the activator (ion 2), while sensitizer relaxes to G. The process is repeated, the sensitizer harvests another pump photon and this energy is transferred to the activator from E1 to E2 while the sensitizer relaxes to G state again. The upconverted emission occurs in the activator with the electron transition from E2 to G. The upconversion efficiency of an ETU process is sensitive to the average distance between the neighboring sensitizer-activator couple, which is determined by the concentrations of dopants. The ETU process is of crucial importance for UCNPs, as the most efficient and used systems are composed of Yb^{3+} as sensitizer and Er^{3+}/Tm^{3+} as activators[95]. This mechanism is illustrated in Figure 1.16(b).

Cooperative Sensitization Upconversion: CSU involves the interaction of three ion centers, with ion 1 and ion 3 generally being of the same type. After absorbing pump photons, both ion 1 and ion 3 can be excited to the E1 state, respectively. Both ion 1 and ion 3 then can interact with ion 2 simultaneously, cooperatively transfer the harvested energy, and excite ion 2 to a higher state. The excited ion 2 can relax back to its ground state by emitting an upconveted photon. The efficiency of CSU is generally orders of magnitude lower than the ESA or ETU process, and it has been reported in Yb^{3+} with Tb^{3+}/Eu^{3+}/Pr^{3+} ion pairs[96]. This mechanism is illustrated in Figure 1.16(c).

Cross-Relaxation: CR is an energy transfer process, resulting from ion−ion interactions: ion 1 transfers part of its excited energy to ion 2 through a process of E2 (ion 1) + G (ion 2) → E1 (ion 1) + E1 (ion 2). The CR process depends on ion-ion interactions and therefore it is in close relation with the dopant concentration. CR is the main reason for the so-called “concentration quenching of UCPL”, but it can be intentionally used to tune the color output in UCNPs. This mechanism is illustrated in Figure 1.16(d).

Photon Avalanche: PA is a process that produces UC above a certain threshold of excitation power. Below the threshold, very little UCPL is produced, while the intensity increases by orders of magnitude above the pump threshold. PA is a looping process that involves processes of ESA for excitation light and an efficient CR that produces feedback. The level E1 of ion 2 is initially populated and the looping process starts with the ESA process that elevates ion 2 to the emitting level E2. An efficient CR process of E2 (ion2) + G (ion 1) → E1 (ion 2) + E1 (ion 1) between ion 1 and ion 2 then occurs. Last, ion 1 transfers its energy to ion 2 to populate its level E1, forming a complete loop. The net effect of the looping process is that one ion 2 at metastable E1 state produces two ion 2’s at this state. When the looping process is repeated, two ions 2’s at the E1 state will produce four; four will produce eight, etc. This effect evokes an avalanche effect for populating ion 2 in its E1 state, and thus the PA upconversion from the emitting level of E2. PA generally requires a pump threshold and a long time (in the order of seconds) to show up, and for these reasons it’s easy to identify. This mechanism is illustrated in Figure 1.16(e).

The UCPL emission has many characteristics that are very attractive for biomedical applications[97]. First, the NIR excitation results in no autofluorescence background because there are no naturally occurring upconverting materials in biology. Thus, the signal-to-noise ratio is extremely improved in fluorescence measurements. Second, the excitation wavelength, typically 980 nm, is located in the so-called “biological window” resulting in low photodamage for living cells and high penetration depth. Third, the high chemical stability and photostability as well as the good optical properties compared to other dyes (no photobleaching neither blinking) makes the UCNPs as a very interesting fluorescent dye. In addition, the UCNPs are also known to be non-toxic in vitro as well as in vivo and they are biocompatible when appropriately coated[98].

Due to these attractive characteristics, the UCNPs can be very useful in several biomedical applications:

Phototriggered drug delivery: The NIR light can penetrate deeper in tissues than the UV-Vis light and possesses lower photodamage to living cells. For this reason, UCNPs could be used as a light converter platform, which would localize with high precision the drug release[99,100].

Fluorescence-based biosensors: The extremely low signal-to-noise ratio of fluorescence measurements using upconversion photoluminescence makes the UCNPs as an ideal dye for biosensing applications. In addition, the excellent optical characteristics such as no photobleaching and no blinking together with the high chemical stability provide the basis for creating robust, reproducible and reliable sensors[101,102].

Optical Imaging: The combination of high penetration depth with the low autofluorescence background with NIR excitation permits to use the UCNPs as contrast agents in high contrast bioimaging. Depending on the surface engineering of the UCNPs it is possible to use them in different imaging techniques, such as passive imaging[103], targeted imaging[104] and cellular trafficking[105]. In addition, the NIR excitation and upconverted NIR emission can be used for deep tissue imaging[106]. The Fluorescence Diffuse Optical Tomography (FDOT) is a type of computed tomography that creates a digital 3D

model of a fluorophore-sustained object by reconstructing images made from the light scattered through an object when the tissue medium is illuminated by a narrow collimated beam. The main drawback of FDOT is the autofluorescence of biological molecules within the tissues upon a UV-Vis excitation. For this reason, UCNPs could be used as ideal contrast agents for FDOT[107,108]. In addition, the nanoengineering would permit to create multifunctional systems that could be employed in multimodal imaging, combining FDOT with CT/MRI/PET for accurate disease diagnosis and prediction of treatment response[109–111].

Photodynamic therapy: Photodynamic therapy (PDT) is a clinical treatment that utilizes phototriggered chemical drugs (photosensitizers) to produce reactive oxygen species (typically singlet oxygen $^1O_2$) to kill tumors. Typical PDT treatments involve three components: the photosensitizer, the light source, and the oxygen within the tissue at the disease site[112]. The light source is usually in the visible range, which limits the application of the PDT to superficial diseases. The NIR light can penetrate significantly deeper into tissues than the visible light and therefore the UCNPs could be used as photosensitizers for improved PDT[113].

1.2.4 Silica nanoparticles

The silica nanoparticles are composed of SiO_2 that is usually synthesized by the polymerization of silane monomers such as tetraethylorthosilicate (TEOS) in aqueous or hydro-alcoholic solutions. The silica nanoparticles are often referred as colloidal silica when dispersed in solution.

The most employed method for the synthesis of silica nanoparticles is the Stöber synthesis[114]. The stabilization of these nanoparticles is usually done by electrostatic repulsion, which is enough for maintaining the stability of small nanoparticles (< 100 nm) in solution. The concentrated solutions of silica nanoparticles can flocculate, leading to easily redispersable pellets.

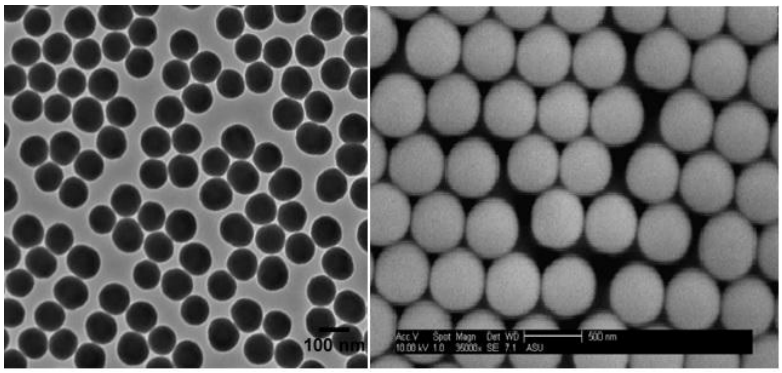

Figure 1.17. Left: TEM image of monodisperse spherical silica nanoparticles with a mean diameter of 100 nm. Right: SEM micrograph of monodisperse spherical silica nanoparticles with a mean diameter of 500 nm.

The SiO_2 nanoparticles do not present any specific properties due to the size reduction: The light absorption in the visible range is almost negligible, which makes the SiO_2 nanoparticles almost transparent to visible light. However, concentrated solutions of silica nanoparticles present a white color due to the light scattering. The SiO_2 nanoparticles can be easily dispersed in aqueous solution. In addition, silica is considered as a biocompatible and innocuous material in vitro and in vivo at relatively high doses[115].

Due to its characteristics, SiO_2 nanoparticles per se do not present any special feature for biomedical applications. However, the fact that SiO_2 is inert is one of the main advantages for its use as coatings for other nanoparticles for in vivo applications[116].

The silica coating offers a reproducible and controllable method to protect other molecules and/or nanoparticles from the environment without altering their inner properties. For example, silica coating has been used for the encapsulation of organic dyes as well as the coating of nanoparticles such as iron oxide, Au and Ag NPs, UCNPs and quantum-dots. In addition, the surface chemistry of the SiO_2 nanoparticles and the SiO_2-coated nanoparticles is well established and permits to functionalize the system with different molecules.

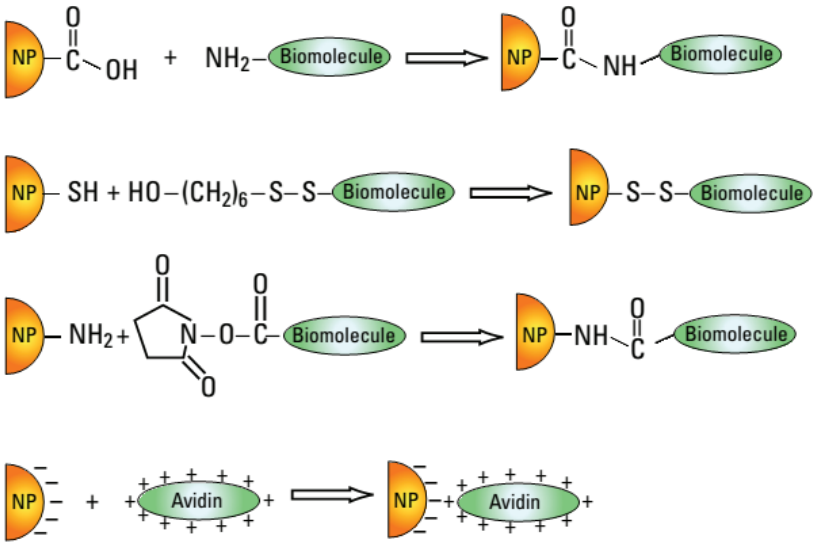

Figure 1.18. Schematic representation of the typical surface functionalization of silica nanoparticles[115], referred as bioconjugation when the functionalization is done with a biomolecule.

The functionalization plays a key role in the application of silica nanoparticles as well as silica-encapsulated or silica-coated nanostructures. In this thesis we study in detail the possibilities of the silica nanoparticles in the biological field.

2. AIMS OF THE WORK

The aims of this work are:

1.- Synthesis of a star shaped amphiphilic block copolymer capable of self-assembling in aqueous solution to serve as drug nanocarrier for water insoluble drugs.

2.- Synthesis of core@shell Fe_3O_4@Au nanoparticles and its combination with star shaped amphiphilic block copolymer to produce multifunctional and aqueous dispersible Fe_3O_4@Au nanoparticles.

3.- Complete and parametric study about the silica coating of inorganic nanoparticles as a tool for the creation of highly homogeneous nanomaterials.

4.- Development of a DNA biosensor platform based on silica coated upconversion nanoparticles and graphene oxide. The sensor should present a very low detection limit.

5.- Development of a NIR-light responsive drug delivery system based on upconversion nanoparticles. The drug should remain active after being released and it should remain inactive in absence of the NIR-light stimulus.

2. OBJETIVOS DEL TRABAJO

Los objetivos de este trabajo son:

1.- Sintetizar un copolímero anfifílico dibloque en estrella capaz de auto-ensamblarse en solución acuosa y que sea capaz de actuar como un nano-transportador de fármacos insolubles en agua.

2.- Realizar la síntesis de nanopartículas tipo núcleo@corteza de Fe_3O_4@Au y su combinación con copolímeros dibloque anfifílicos en estrella para producir nanopartículas de Fe_3O_4@Au multifuncionales y dispersables en medios acuosos.

3.- Estudiar de forma paramétrica el método de recubrimiento con sílice de nanopartículas inorgánicas como herramienta para la creación de nanomateriales altamente homogéneos.

4.- Desarrollar un biosensor de ADN basado en óxido de grafeno y nanopartículas con fluorescencia de conversión ascendente recubiertas con una capa de sílice. Dicho sensor debe presentar un límite de detección muy bajo.

5.- Desarrollar un sistema de liberación de fármacos en respuesta a un estímulo de luz NIR basado en nanopartículas con fluorescencia de conversión ascendente. El fármaco debe mantener su actividad tras ser liberado, pero debe permanecer inactivo en ausencia del estímulo de luz NIR.

3. EXPERIMENTAL PART

3.1 Chemicals

The following products were purchased from Sigma-Aldrich Inc (Saint Louis, MO, USA) and were used as received: ε-caprolactone 99%, D-sorbitol 98%, tin(II) trifluoromethanesulfonate 97%, tetrahydrofuran 99.9% inhibitor free, tetrahydrofuran anhydrous 99.9% inhibitor free over molecular sieve 4Å (H_2O < 0.005%), toluene 99.5%, triethylamine 99.5%, polyoxyethylene (20) sorbitan monooleate (Tween 20®), pyrene 98%, chloroform-d 99.8% atom %D contains 0.03% (v/v) TMS, oleic acid 90%, 1-octadecene 90%, diphenyl ether 99%, oleylamine 70%, n-hexane, acetone 99%, erbium (III) chloride hexahydrate 99.9%, ytterbium (III) chloride hexahydrate 99.9%, yttrium (III) chloride hexahydrate 99.99%, sodium hydroxide 98%, ammonium fluoride 98%, methanol 99.9%, *N,N*-dimethylformamide anhydrous (DMF) 99.8%, tetraethylorthosilicate (TEOS) 99.999%, polyoxyethylene (5) nonylphenylether, branched (IGEPAL CO-520), ammonium hydroxide solution 30%, (3-aminopropyl)triethoxysilane (APTES) 99%, phospahe-buffered saline (PBS) tablets, *N*-(3-(dimethylamino)propyl)-*N'*-ethylcarbodiimide hydrochloride (EDC) 99%, *N*-hydroxysulfosuccinimide sodium salt (Sulfo-NHS) 98%, thulium (III) chloride hexahydrate 99.9%, 5-hydroxy-2-nitrobenzyl alcohol 97%, ethyl 4-bromobutanoate 95%, acryloyl chloride >97%, O-(2-Aminoethyl)-O'-methyl-polyethyleneglycol (Mw 5000 g/mol), Doxorubicin hydrochloride (European Pharmacopeia Reference Standard).

Ethyl-3-(butylamino)-1-(chlorophenyl)-9H-carbazole-4-carboxylate was generously donated by Dr. Damiano Rocchi (Department of Pharmaceutical Chemistry, Faculty of Pharmacy, Complutense University of Madrid).

The following products were purchased from Panreac (Barcelona, Spain) and were used as received: Succinic anhydride 97%, tetrahydrofuran 99.5% stabilized with ~300 ppm BHT.

The following products were purchased from Merck (Whitehouse Station, NJ, USA) and were used as received: Potassium hydroxide 85%, iron (III) chloride hexahydrate 99%.

The following products were purchased from Fluka (Saint Louis, MO, USA) and were used as received: *N,N'*-Dicyclohexylcarbodiimide 99%, 4-(dimethylamino)pyridine 98%, dichloromethane contains ~25 mg/L amylene as stabilizer, Formvar® solution ~1% in 1,2-dichloroethane.

The following products were purchased from Alfa Aesar (Ward Hill, MA, USA) and were used as received: Gold (III) acetate 99%.

Nano Graphene oxide powder with small lateral flake size (diameter 90 nm ± 15 nm and thickness about 1 nm) 99% purity was purchased from Graphene Supermarket (NY, USA).

The DNA sequences were synthesized by the Brown group (School of Chemistry, University of Oxford, UK). The ssDNA probe sequence that was covalently linked to the surface of the nanoparticles was 5′-aminohexyl-TTTTTTTTTTTTTTTTTTTT-3′. The cDNA sequence was 5′-AAAAAAAAAAAAAAAAAAAAAAAAAAAA-3′. The random sequence (noncomplementary ssDNA sequence) was 5′-CTAGATCCGTGTCCTCGT-3′. All the DNA oligomers were purified by reverse-phase HPLC, and the concentration was calculated with UV-Vis spectroscopy.

Ethanol 96º was purchased from Alcoholes Aroca SL (Madrid, Spain).

Deionized water was produced using a Millipore Elix 20 system.

3.2 Instrumentation

3.2.1 Nuclear Magnetic Resonance spectroscopy (NMR)

^{1}H-NMR spectroscopy was used in the characterization of the polymeric moieties in each synthetic step. The ^{1}H-NMR spectra were obtained with a Bruker AVANCE 250 (250 MHz) (Billerica, Massachusetts, USA) using the QNP ^{1}H probe. The samples were prepared by dissolving 2-4 mg of the purified product in a deuterated solvent which contained tetramethylsilane as internal standard. The NMR tubes were Wildman® 3 mm diameter and were purchased from Sigma-Aldrich.

During the data acquisition, the parameters were automatically adjusted by the Top Spin™ software. The spectra processing and analysis were done with the TopSpin™ or the MestreNova software from Mestrelab Research (Santiago de Compostela, Spain).

3.2.2 Diffusion Ordered Spectroscopy (DOSY)

The Diffusion Ordered Spectroscopy (DOSY) is also referred as Pulsed Field Gradient Nuclear Magnetic Resonance (PFG-NMR). With this technique it is possible to measure separately the NMR signals of different species according to their diffusion coefficients. By use of a gradient, molecules can be spatially labeled, i.e. marked depending on their position in the sample tube[117–121]. If they move after this encoding during the following diffusion time (Δ), their new position can be decoded by a second gradient. The intensity change is described by the following equation:

$$\ln\left(\frac{I}{I_0}\right) = -D\gamma^2 G^2 \delta^2 \left(\Delta - \frac{\delta}{3}\right)$$

where I_0 is the initial intensity, I is the observed intensity at a certain gradient strength, D is the diffusion coefficient, γ is the gyromagnetic constant of the observed nucleus, G is the gradient strength, δ is the gradient length, τ is the time between bipolar gradients and Δ is the duration of the stimulated echo (the diffusion time).

The Stejskal-Tanner plot is the representation of the $\ln(I/I_0)$ versus $(\gamma G\delta)^2(\Delta-\delta/3)$ and provides a straight line with a slope –D. The DOSY is a pseudo-2D experiment in which a series of monodimensional spectra are acquired at different gradient strengths. In the acquisition dimension the NMR signal of the ^1H (or other heteronucleus) is represented, whereas in the vertical dimension the intensity of each signal is given by the diffusion coefficient of the molecule to which it belongs. This technique permits to analyze mixtures of compounds without having to physically separate them. In addition, this technique can be also used for monitoring the interactions between small molecules and macromolecules. Figure 3.1 shows a series of monodimensional spectra obtained at different gradient strengths.

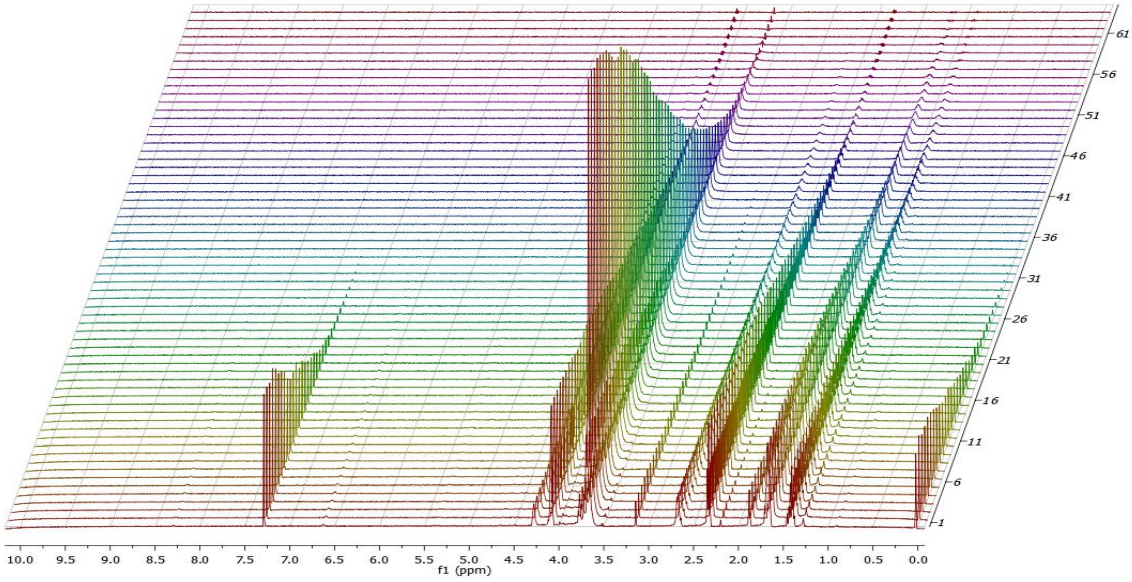

Figure 3.1. Experimental example of a PFG-NMR measurement containing the star-shaped amphiphilic block copolymer based on poly(ε-caprolactone) and poly(ethylene glycol).

These experiments were carried out in a Bruker AVANCE 500 (500 MHz) (Billerica, Massachusetts, USA). The samples were prepared by dissolving 2-4 mg of product in 0.8 mL of chloroform-d. The acquisition parameters were the following: sine shaped gradient pulses time (τ) was set to 1.25 – 2.5 ms, gradient strength (G) ranged from 0.0067 to 0.3203 Tm^{-1} in 16-32 square spaced increments, gradient length (δ) was 0.001 s and diffusion times were acquired with a stimulated echo ranging from 0.06 to 1 s. The gyromagnetic

constant of ^{1}H nucleus is 26751 $radG^{-1}s^{-1}$. The gradient length and diffusion time were adjusted to achieve around 95% signal suppression at maximum gradient strength.

3.2.3 Fourier Transform Infrared Spectroscopy (FTIR)

The FTIR was used for the characterization of the polymeric moieties in each synthetic step. The measurements were performed in a Thermo Scientific Nicolet IR 200 spectrometer (Waltham, MA, USA). Solid samples were measured by preparing a pellet with KBr. Liquid samples were measured using the attenuated total reflection sampling technique (FTIR-ATR) with a ZnSe ATR sampling accessory SpeculATR from Thermo Scientific (Waltham, MA, USA).

3.2.4 Mass spectroscopy

The number average molecular weight (M_n) of the star-shaped polymers was calculated using mass spectroscopy. The measurements were carried out using the Matrix-Assisted Laser Desorption/Ionization (MALDI) technique coupled with a Time Of Flight (TOF) detector. The device was a Bruker MALDI-TOF/TOF Ultraflex spectrometer (Billerica, Massachusetts, USA). A dithranol matrix was used in all the experiments.

3.2.5 Dynamic Light Scattering (DLS)

Light scattering measurements were recorded using a Zetasizer Nano ZS device from Malvern Instruments (Worcestershire, United Kingdom). The accumulation time was determined automatically for each sample. The software provided by Malvern (Zetasizer Software v5.0) calculated the *z*-average (mean intensity) from the correlation function. The hydrodynamic diameter (D_h) was derived using the Einstein-Stokes equation. Weight average molecular weight (M_w) and the second Virial coefficient (A_2) of the polymers were obtained from the Debye plots determined by concentration dependent scattering intensity data. The polymer concentration ranged from 0.5 mg/mL to 10 mg/mL. M_w was obtained from the intercept and A_2 from the slope in the Debye plot, with the following equation:

$$\frac{KC}{R(\theta)} = \frac{1}{M_w} + 2 \cdot A_2 \cdot C$$

where R(θ) is the Rayleigh ratio at a specific measurement angle, C is the concentration and K is the optical contrast obtained from the following equation:

$$K = \frac{4\pi^2 \cdot \left(n \frac{dn}{dC_p} \right)^2}{\lambda_0^4 \cdot N_{av}}$$

where n is the refractive index of the solvent, λ_0 is the incident wavelength, N_{av} is the Avogadro's number and dn/dC_p is the increment of the refractive index in the sample as a function of the polymer concentration. This value was experimentally determined with a double beam differential refractometer J357 from Rudolph Research Analytical (Hackettstown, NJ, USA). The dn/dC_p values for poly(ε-caprolactone) changed from 0.1166 mL/g to 0.1654 mL/g with increasing number of monomer units in the star-shaped polymers.

3.2.6 High-Performance Size-Exclusion Chromatography (HPSEC)

The size exclusion chromatography is commonly known as Gel Permeation Chromatography (GPC) when an organic solvent is used as mobile phase. In this work, GPC was used to calculate the number average molecular weight (M_n) of the polymers. The experiments were carried out with a HPLC-pump, two columns PLgel 5 µm MIXED-C (300 x 7.5 mm) from Agilent Technologies (Santa Clara, CA, USA) coupled with a refractive index detector ETA2020 from Polymer Standards Service (Warwick, RI, USA). Anhydrous tetrahydrofuran served as the mobile phase with a flow rate of 1 mL/min. Sample concentration was 10 mg/mL in anhydrous tetrahydrofuran. The instrument was calibrated using polystyrene standard of known molecular weight and narrow distribution.

3.2.7 Transmission Electron Microscopy (TEM)

The TEM samples were prepared by placing a drop of a diluted solution of sample on a TEM copper grid coated with a Formvar® film and left to dry in air. The size and morphology of the samples were observed with a JEOL JEM 1010 (Tokyo, Japan) electron microscope working at an acceleration voltage of 80 kV

and equipped with a GATAN Megaview II CCD camera (Pleasanton, CA, USA). The nanoparticle size distribution was analyzed with ImageJ software from National Institutes of Health (Bethesda, Maryland, USA) and with Soft Imaging Viewer software from Olympus (Tokyo, Japan), considering over 300 nanoparticles for the statistical analysis.

The High-Resolution TEM (HRTEM) micrographs and the Selected Area Electron Diffraction (SAED) patterns were obtained with a JEOL JEM 2100 electron microscope (Tokyo, Japan) working at an acceleration voltage of 200 kV. A CCD ORIUS SC1000 Model 832 camera (Pleasanton, CA, USA) was used for capturing the HRTEM micrographs. The Energy Dispersive X-ray spectroscopy (EDX) for the elemental analysis of the samples was performed in the electron microscope using the electron beam as excitation source and a X-Max SDD detector from Oxford Instruments (Oxfordshire, United Kingdom).

3.2.8 Fluorescence spectroscopy

The fluorescence spectroscopy was done using a FP 6300 spectrometer from JASCO (Tsukuba, Japan). Excitation and emission band-widths were 10 and 3 nm, respectively. The cuvettes used for fluorescence measurements were 10 x 10 mm square glass cuvettes from Hellma Analytics (Müllheim, Germany).

3.2.9 Upconversion fluorescence measurements

The upconversion fluorescence measurements were performed in a manually aligned setup with a continuous wave 980 nm 500 mW diode laser from Armlaser (San Francisco, CA, USA) as excitation source and a SpectraSuite spectrometer from Ocean Optics (Dunedin, Florida, USA) as detector. The detector was placed at an angle of 90º to the excitation beam, and the emitted fluorescence was collected via fiber optic cable and measured with the software provided by Ocean Optics. A cuvette with the corresponding solvent was measured under illumination with the 980 nm laser beam and set as the blank for each measurement. All measurements were performed with 2.000 msec of integration time and 100 scans to average. All fluorescence experiments were repeated at least three times with independent measurements and the fitted data presented in this work shows the statistically significant mean value ±

error. The represented data (graphs) represent one individual measurement for an easier visualization.

3.2.10 Zeta potential

The Z-potential measurements were performed using a Zetasizer Nano ZS instrument from Malvern Instruments (Worcestershire, United Kingdom), and the accumulation time was determined automatically for each sample. The acquired data was processed using the software provided by Malvern (Zetasizer software v7.03).

3.2.11 Ultraviolet-Visible spectroscopy (UV-Vis)

The UV-Vis measurements were done using a Cary 300 Bio spectrometer from Varian (Palo Alto, CA, USA). The cuvettes used for the UV-Vis measurements were 10 x 10 mm square glass cuvettes from Hellma Analytics (Müllheim, Germany).

3.2.12 Superconducting Quantum Interference Device (SQUID)

The magnetic properties were measured with a MPMS-XL SQUID magnetometer from Quantum Design (San Diego, CA, USA) at 298 K. The specimens were prepared by placing 300 µL of sample (with a known concentration) in a 3 mm diameter glass tube, which was subsequently frozen with liquid nitrogen and sealed by a glazier. After this process, the samples were stored at room temperature prior to the experiment. The magnetic moment was represented as a function of the external magnetic field in the range of −10000 to 10000 Oe. From these measurements it was possible to calculate the magnetization values and the coercitivity of the samples. The magnetometer was calibrated prior to the measurements using metallic Pd as a standard.

3.3 Material synthesis

3.3.1 Synthesis of the amphiphilic star-shaped block copolymer 6bPCL@4bPEG

The synthesis of the star-shaped copolymer was carried out in several stages as summarized in the following scheme:

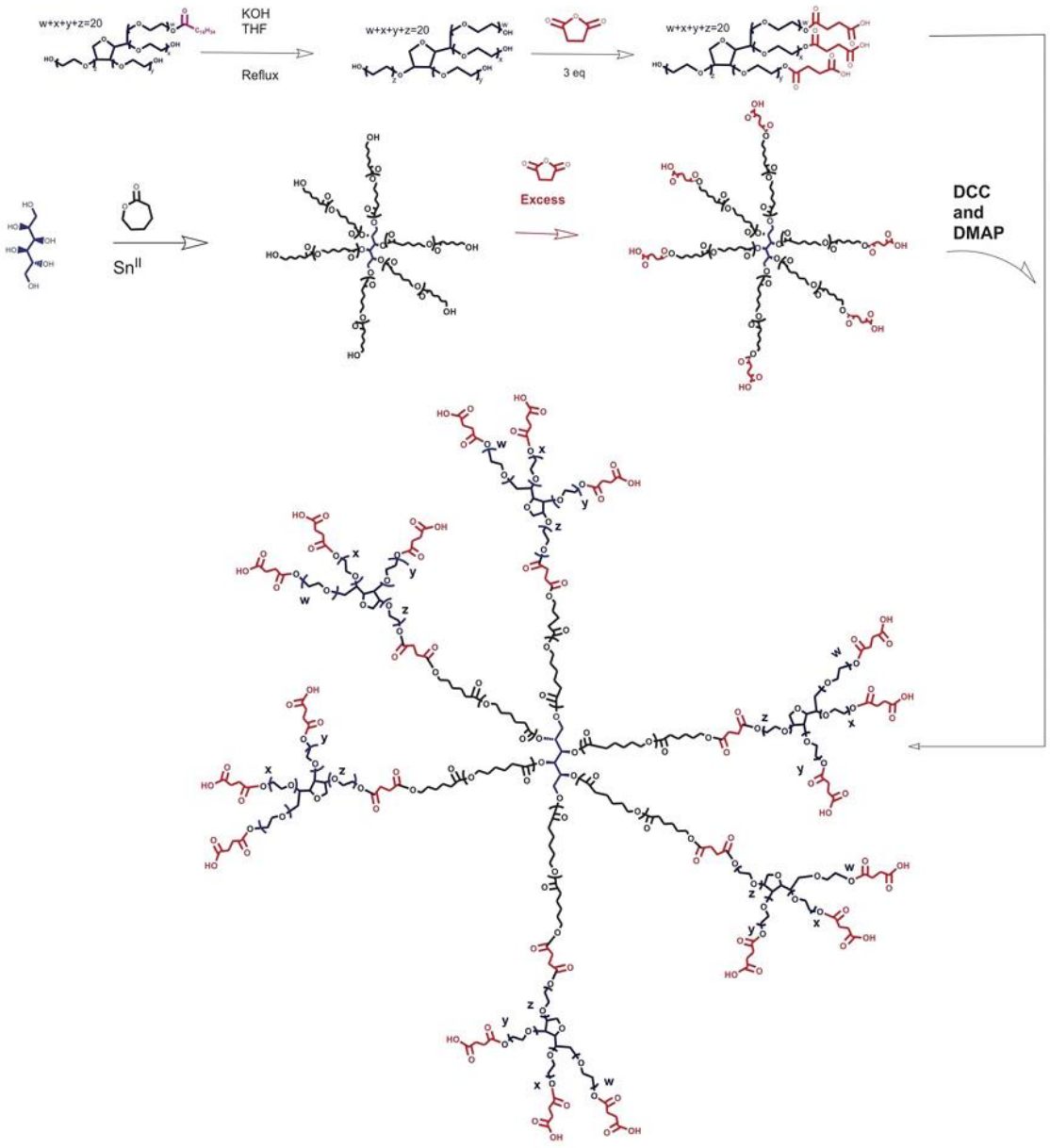

Scheme 3.1. Synthetic pathway to obtain an idealized 4bPEG@6bPCL star-shaped block copolymer

3.3.1.1 Step 1: Preparation of the carboxyl-terminated branched poly(ethylene glycol) moiety: 4bPEG-3-COOH

The star-shaped polyoxyethylene (20) sorbitan (4bPEG-4OH) was obtained after the saponification reaction of polyoxyethylene (20) sorbitan monooleate. Briefly, 10 mL (7.4 mmol) of polyoxyethylene (20) sorbitan monooleate were poured into a round bottom flask with 1 g (17.8 mmol) of KOH and 20 mL of THF. This mixture was heated to reflux (70 ºC) during 24 h, and then the product was concentrated and added to a mixture of hexane/acidic water (1/1 v/v). The aqueous phase, in which the 4bPEG-4OH was dissolved, was separated from the organic phase, which contained the oleic acid, using a separation funnel. This process was repeated three times to ensure the purification of the 4bPEG-4OH. The organic phase was discarded and the aqueous phase was neutralized and evaporated. The yield of this reaction was approximately 71 %. Next, a solution containing 0.45 g (4.5 mmol) of succinic anhydride and 1 g (4.5 mmol) of tryethylamine in 10 mL of anhydrous THF was added dropwise and under vigorous magnetic stirring onto a solution of 1.5 g (1.5 mmol) of 4bPEG-4OH in 10 mL of anhydrous THF. The mixture was stirred for 12 h at 75 ºC. This reaction permitted to introduce three carboxyl groups per 4bPEG molecule, leaving one hydroxyl group as anchoring point for the PCL moiety (4bPEG-3COOH-1OH). The product of this reaction was dried by evaporating the THF in a rotary evaporator and dissolved in water at pH 3. Subsequently the 4bPEG-3COOH-1OH was extracted with CH_2Cl_2 in a separation funnel. This procedure was repeated at least three times. Next, the organic phase was evaporated under reduced pressure and the product was collected as a pale yellow colored viscous liquid. The yield of this reaction was approximately 72%.

3.3.1.2 Step 2: Synthesis of the carboxyl-terminated star-shaped poly(ε-caprolactone) moiety

The star-shaped poly(ε-caprolactone) with six branches was synthesized by the ring opening polymerization (ROP) of the monomer (ε-caprolactone) at 80 ºC using D-sorbitol as symmetric initiator and stannous trifluoromethanesulphonate as catalyst. In a typical experiment, 5 mL of ε-CL, 50 mg of D-sorbitol and 5 mg

of stannous trifluoromethanesulphonate were poured into a round bottom flask with 5 mL of anhydrous toluene. The reaction was left for 12 hours under magnetic stirring. The product of the reaction (6bPCL) was extracted by precipitation with cold methanol and filtration and dried under reduced pressure. The yield of this reaction was approximately 85%. Next, the 6bPCL end groups were modified by the reaction with an excess of succinic anhydride and triethylamine. Briefly, 1 g (0.33 mmol) of 6bPCL, 0.24 g (2.4 mmol) of succinic anhydride and 0.7 g (2.4 mmol) of triethylamine were dissolved in 20 mL of anhydrous THF and heated to reflux overnight under magnetic stirring. The product was dried in a rotary evaporator, dissolved in 20 mL of $CHCl_3$ and purified in a separation funnel against 60 mL of acidic water three times. The aqueous phase was discarded and the 6bPCL-COOH was obtained as a white solid after the solvent evaporation. The yield of the reaction was approximately 95%. The number of monomer units in each branch of the star-shaped PCL moiety could be effectively controlled by modifying the monomer to initiator ratio, which yielded star-shaped polymers with different molecular weight.

3.3.1.3 Coupling between the 4bPEG and the 6bPCL subunits

The synthesis of the amphiphilic star-shaped 6bPCL@4bPEG copolymer was carried out by the coupling reaction between the carboxylic groups of the 6bPCL moieties and the free hydroxyl group of the 4bPEG-3COOH-1OH moieties. For this, 7 equivalents of dicyclohexylcarbodiimide (DCC), 7 equivalents of 4-(dimethylamino)pyridine (4-DMAP) and 1 equivalent of 6bPCL-COOH were dissolved in anhydrous THF at 0 ºC. This mixture was stirred for 2 h for the carboxyl activation. Subsequently, 7 equivalents of 4bPEG-3COOH-1OH dissolved in anhydrous THF were poured into the previous solution and stirred at 0 ºC for 1 h. Then, the temperature was raised to 25 ºC and the mixture was left to react for 4 days at room temperature. After this, the mixture was cooled to 0 ºC, which caused the precipitation of dicyclohexylurea crystals, which are the typical reaction by-products from this coupling reaction. These crystals were filtered out with a 200 nm PTF filter. The THF was then evaporated under reduced pressure and the product of the reaction was purified in a dyalisis membrane (molecular cutdown 2000) against 1000 mL of water for 1 week (the water was renewed every day). The product was a pale yellow

colored viscous solid when the solvent was removed by freeze-drying. The yield of the reaction was approximately 82%.

3.3.2 Synthesis of hydrophobic iron oxide nanoparticles

The monodisperse hydrophobic Fe_3O_4 nanoparticles were synthesized by thermal decomposition of the iron (III) oleate complex[122]. The iron (III) oleate complex was prepared as follows: 480 mg of NaOH (12 mmol) were dissolved in 50 mL of water and 80 mL of EtOH. Next, 4 mL of oleic acid (12 mmol) were added under vigorous stirring to the mixture, and the pH was adjusted to 7. Afterwards, 1.08 g of iron (III) chloride hexahydrate (4 mmol) were dissolved in 10 mL of water and added under stirring. Then, 140 mL of hexane were poured and the mixture was stirred and refluxed at 70 ºC for 4 hours. After this time, the upper layer of hexane showed a red brownish color due to the presence of the iron (III) oleate complex. The organic phase was washed three times against 30 mL of water in a separation funnel. Finally, the iron (III) oleate complex was collected after the evaporation of the organic phase in a rotary evaporator under reduced pressure. To produce monodisperse hydrophobic Fe_3O_4 nanoparticles, 900 mg of the as-prepared iron oleate complex (1 mmol) and 1156.56 mg of oleic acid (4 mmol) were dissolved in 8 mL of 1-octadecene in a three necked round bottom flask equipped with a thermometer, nitrogen gas flow and a reflux condenser. The flask was placed in a heating mantle and heated at 120 ºC for 1 hour without the reflux condenser to remove all trace solvents. After this time, the reflux condenser was placed and set at 40 ºC and the reaction temperature was raised to 320 ºC and kept at this temperature for 45 minutes. Afterwards, the reaction was cooled down to room temperature and the nanoparticles were precipitated from the reaction mixture by centrifugation with acetone and re-dispersed in hexane. The cleaning procedure was repeated at least three times and nanoparticles were re-dispersed and stored in hexane.

3.3.3 Synthesis of hydrophobic core@shell Fe_3O_4@Au nanoparticles

Monodisperse and individual hydrophobic core@shell Fe_3O_4@Au nanoparticles were synthesized by a modification of the method reported by Zhong and coworkers[123]. In a typical synthesis, 500 µL of hexane solution of Fe_3O_4 nanoparticles (0.05 mmol of Fe content), 282 mg of oleic acid (1 mmol), 1600

mg of oleylamine (6 mmol) and different amount of gold (III) acetate ranging from 0.38 mmol to 3.8 mmol were dissolved in 10 mL of diphenyl ether and poured into a three necked round bottom flask, equipped with a thermometer, nitrogen gas flow and a reflux condenser. The flask was placed in an oil bath and the temperature was set to 160 ºC and let to react for 90 minutes. The reaction was then cooled down to room temperature and the Fe_3O_4@Au nanoparticles were extracted by centrifugation with ethanol and re-dispersed in hexane. The cleaning procedure was repeated at least three times and the Fe_3O_4@Au nanoparticles were re-dispersed and stored in hexane.

3.3.4 Synthesis of monodisperse Upconversion nanoparticles (UCNPs)

The synthesis of $NaYF_4$:Yb,Er nanoparticles was performed by following a previously reported procedure[92] slightly modified: yttrium(III) chloride hexahydrate (236.62 mg, 0.78 mmol), ytterbium(III) chloride hexahydrate (77.5 mg, 0.20 mmol), and erbium(III) chloride hexahydrate (7.63 mg, 0.02 mmol) were dissolved in a three-necked round-bottomflask with oleic acid (6 mL, 19 mmol) and 1-octadecene (15 mL, 46.9 mmol) and heated at 160°C for 1 h and 30 min under nitrogen atmosphere. After this time, a solution of sodium hydroxide (100 mg, 2.5 mmol) and ammoniumfluoride (148.16 mg, 4 mmol) dissolved in 10 mL of methanol was added dropwise in the reaction under vigorous stirring. This mixture was slowly heated to 100°C for 2 h under nitrogen atmosphere and then 30 more minutes under vacuum. Next, the flask containing the mixture was set up with a thermometer, a reflux condenser, and nitrogen atmosphere and was placed in a heating mantle. The temperature was raised to 300°C and left to react for 1 h and 30 min. Subsequently, the mixture was left to cool to room temperature, and the $NaYF_4$:Yb,Er nanoparticles were collected by centrifugation (8500 rpm, 10 min) with a mixture of hexane, ethanol, and water (2:1:1 v/v). The pellet was redispersed with 5 mL of ethanol and centrifuged in a mixture of ethanol and water (1:1 v/v). This process was repeated three times. Finally, the purified $NaYF_4$:Yb,Er nanoparticles were redispersed and stored in hexane.

The $NaYF_4$:Yb,Tm nanoparticles were synthesized by the same procedure but using different quantities: 226.3 mg (0.75 mmol) of $YCl_3 \cdot 6H_2O$, 96.87 mg (0.25 mmol) of $YbCl_3 \cdot 6H_2O$ and 1.15 mg (0.003 mmol) of $TmCl_3 \cdot 6H_2O$.

The upconversion nanoparticles can be dispersed in hexane and other organic solvents, showing the upconversion fluorescence when excited with a 980 nm laser, see Figure 3.2

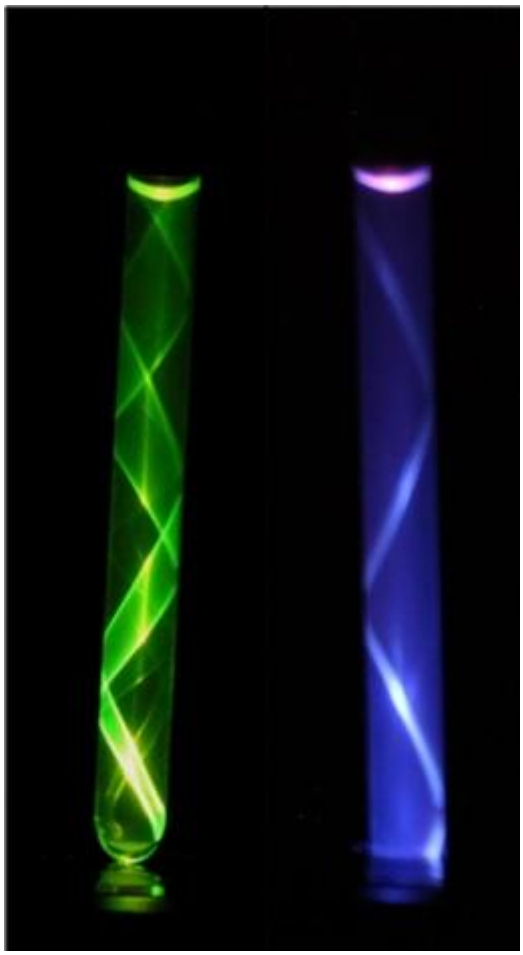

Figure 3.2. Picture taken from two NMR tubes containing the hexane dispersion of $NaYF_4$:Yb,Er (left) and $NaYF_4$:Yb,Tm (right). The samples were excited with a 980 nm laser from the bottom. The room light was turned off to take the pictures.

In Figure 3.2 it is possible to observe the upconverted fluorescence emission of the Erbium-doped UCNPs (visible green fluorescence) and the Thulium-doped UCNPs (visible blue fluorescence) under the excitation with a 980 nm laser.

3.3.5 Synthesis of UCNPs@SiO_2 nanoparticles

The silica coating of the synthesized UCNPs was achieved by the base-catalyzed polymerization of TEOS in a reverse microemulsion. Briefly, 240 mg of IGEPAL CO-520 and 5 mL of a hexane solution with the UCNPs (2 mg/mL) were mixed with an ultrasound bath. Then, ammonium hydroxide solution (40μL, 30%) was added and gently mixed. The solution turned totally transparent, which indicated the formation of the microemulsion. The reaction started when TEOS (30 μL, 0.14 mmol) was added under stirring, and it was left to react overnight at room temperature. The reaction finished when the microemulsion was destabilized with 5 mL of methanol. The core@shell UCNPs@SiO_2 nanoparticles were purified by centrifugation (3 × 8500 rpm, 10 min) with ethanol.

3.3.6 Surface Modification of the $NaYF_4$:Yb,Er@SiO_2 nanoparticles

The carboxylic acid-functionalized NaYF4:Yb,Er@SiO_2 nanoparticles (UCNPs@SiO_2−COOH) were prepared by sequential functionalization steps. First, the surface was functionalized with amino groups by the addition of APTES (150μL, 0.68 mmol) to the synthesized UCNPs@SiO_2 dissolved in 5 mL of ethanol. This mixture was stirred at room temperature overnight. The UCNPs@SiO_2−NH_2 nanoparticles were centrifuged (3×) and dispersed in 5 mL of anhydrous DMF. Then, succinic anhydride (150 mg, 1.49 mmol) was dissolved in 3 mL of anhydrous DMF, added dropwise to the solution containing the UCNPs@SiO_2−NH_2, and stirred at room temperature overnight. The ring-opening reaction led to the carboxylic acid-functionalized upconversion@silica nanoparticles, which were collected by centrifugation. The DMF solvent traces were removed after several centrifugation steps with ethanol. Finally, the UCNPs@SiO_2−COOH nanoparticles were dispersed in water.

The DNA was covalently attached to the surface of the nanoparticles by the carbodiimide coupling reaction. This reaction produced a covalent bond between the carboxylic acid group on the surface of the UCNPs@SiO_2 nanoparticles and the amino group in the 5′ end of the probe ssDNA sequence. The EDC coupling reaction was performed as follows: The UCNPs@SiO_2−COOH nanoparticles were dispersed in a borate-buffered

solution (0.001 M) at a concentration of 1.82 mg/mL. This solution (200μL, 0.364 mg of nanoparticles) was added to an eppendorf tube prior to the addition of an EDC solution in borate buffer (20μL, 0.3 M) and a Sulfo-NHS solution in borate buffer (40 μL, 0.3 M). The mixture was shaken for 5 min, and then the aqueous solution of probe ssDNA (30μL, 220.65μM) was added. The reaction was stirred overnight, and the probe ssDNA-functionalized nanoparticles (UCNPs@SiO_2-ssDNA) were purified by centrifugation (16400 rpm, 20 min) twice. The purified UCNPs@SiO_2-ssDNA nanoparticles were collected with PBS solution (0.01 M, pH 7.4) and stored at −20°C.

3.3.7 Surface modification of the $NaYF_4$:Yb,Tm@SiO_2 nanoparticles

The amino functionalized $NaYF_4$:Yb,Tm@SiO_2 nanoparticles were prepared as previously described and dispersed in 5 mL of anhydrous THF.

With the aim of providing colloidal stability to the amine functionalized $NaYF_4$:Yb,Tm@SiO_2 nanoparticles, methoxypolyethylene glycol (Mw 5000) chains were attached to the surface of the nanoparticles. This was achieved through several steps as follows:

3.3.7.1 *Synthesis of Methoxypolyethylene glycol carboxylic acid*: O-(2-aminoethyl)-O'-methyl-polyethylenglycol (500 mg, 0.1 mmol), triethylamine (100 μl, 1 mmol) and succinic anhydride (100 mg, 1 mmol) were dissolved in THF and heated to reflux overnight. After that, the product of this reaction was dried using a rotary evaporator and then it was dissolved in water. Subsequently the methoxypolyethylene glycol carboxylic acid was extracted with CH_2Cl_2 using a separation funnel.

3.3.7.2 *Attachment of the methoxypolyethylene glycol carboxylic acid on the surface of the $NaYF_4$:Yb,Tm@SiO_2 nanoparticles*: Methoxypolyethylene glycol carboxylic acid (25 mg, $5 \cdot 10^{-3}$ mmol) was dissolved in 5 mL of a PBS solution (0.1 M sodium phosphate, NaCl, 0.15 M, pH 7.3) prior to the addition of an EDC solution in PBS (100 μL, 0.2 M) and Sulfo-NHS (200 μL, 0.2M). This mixture was stirred for 10 min. After that, 5 mL of a PBS solution containing 25 mg of amine functionalized $NaYF_4$:Yb,Tm@SiO_2 nanoparticles were added. The reaction mixture was stirred overnight at room temperature. The

$NaYF_4$:Yb,Tm@SiO_2-PEG nanoparticles were purified by centrifugation (10.000 rpm, 20 minutes) three times and stored in the refrigerator.

The PEG-functionalized UCNPs@SiO_2 nanoparticles were then functionalized with a photodegradable linker. This molecule was 4-(3-(acryloyloxymethyl)-4-nitrophenoxy)butanoic acid (*o*-NBA) that was synthesized in several steps as represented in the scheme 3.2

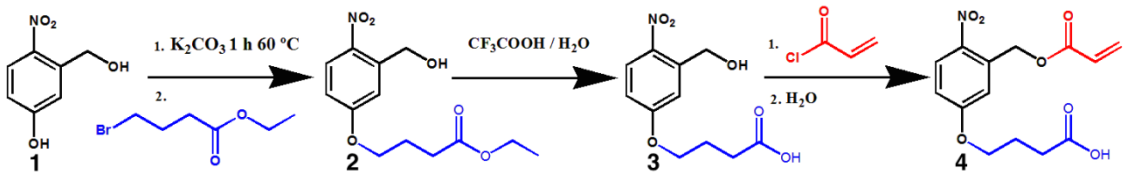

Scheme 3.2. Synthetic pathway to obtain the desired photodegradable molecule.

3.3.7.3 Attachment of the photodegradable anchoring molecule on the surface of the $NaYF_4$:Yb,Tm@SiO_2–PEG nanoparticles: EDC (25 mg, 0.15 mmol) and sulfo-NHS (50 mg, 0.28 mmol) were mixed with 4-(3-(acryloyloxymethyl)-4-nitrophenoxy)butanoic acid (25 mg, 0.08 mmol) in 5 mL of DMF. This mixture was stirred for 10 min and after this time, 25 mg of $NaYF_4$:Yb,Tm@SiO_2-PEG nanoparticles dispersed in 5 mL of DMF were poured. The reaction mixture was stirred overnight at room temperature and purified by centrifugation (10000 rpm, 20 minutes) twice. The nanoparticles were dissolved in 5 mL of Milli-Q water and stored in the refrigerator.

Finally, the anticancer drug doxorubicin (Dox) was covalently linked to the photodegradable molecule in the surface of the nanoparticles. The process was performed as follows:

3.3.7.4 Attachment of doxorubicin on the photodegradable 5-hydroxyl-2-nitrobenzyl alcohol derivate anchored on the surface of $NaYF_4$:Yb,Tm@SiO_2-PEG nanoparticles. The attachment of doxorubicin on the surface of the particles was performed by using the thiol-acrylate Michael addition reaction[124]. Prior to this coupling reaction, doxorubicin was modified with a thiol group according to a previously reported method (ref): 2-iminothiolane hydrochloride (2-IT, 1 mM, 250 µL) and Dox (0.5 mM, 300 µL) were mixed at room

temperature for 20 min. Then 5 mL of the previously obtained $NaYF_4$:Yb,Tm@SiO_2-PEG nanoparticles (25 mg) were incubated with the thiolated Dox solution overnight. The thiol-acrylate Michael addition is considered a “click-chemistry”-like reaction that is very specific between these functional groups, can be carried out under mild reaction conditions. The product was centrifuged at 14000 rpm for 20 min, and the precipitates were washed three times with Milli-Q water, combining centrifugation and redispersion in an ultrasound bath in order to remove the not anchored Dox. This cleaning process was repeated until a transparent supernatant was obtained and the red precipitate was collected and stored in the dark for further experiments. As result, the surface of the $NaYF_4$:Yb,Tm@SiO_2 nanoparticles was co-functionalized with PEG chains and with a photodegradable molecule directly linked with doxorubicin. The whole process is summarized in scheme 3.3.

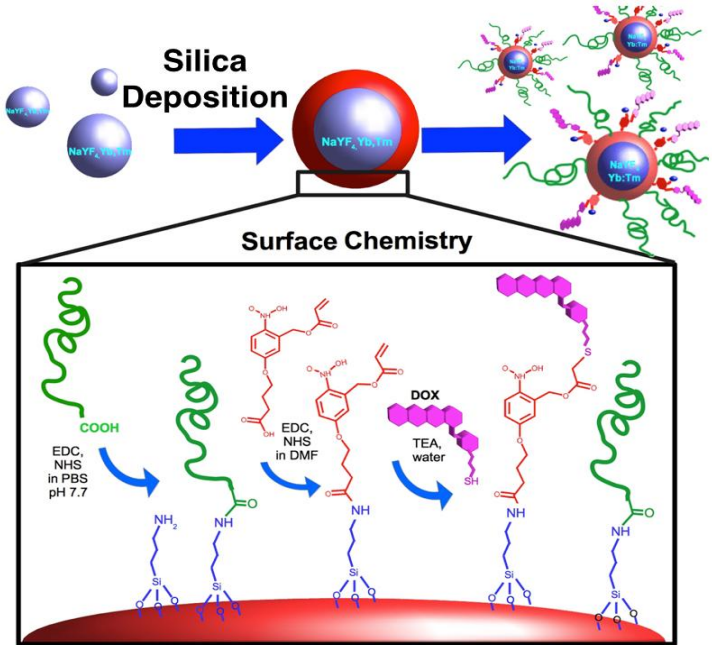

Scheme 3.3. Schematic representation of the surface modification of the silica-coated UCNPs, which yields PEG- and Dox-functionalized UCNPs@SiO_2 nanoparticles.

3.4 Proceedings

3.4.1 Preparation of polymeric nanoparticles

Polymeric nanoparticles were prepared by the nanoprecipitation method. This method consists of two steps: First, the amphiphilic molecule is dissolved in a good solvent for both moieties. Second, an excess of a co-solvent with specific solubility for one of the parts is added. Under this scenario, the amphiphilic molecules self-assemble yielding core-shell structure, in which the insoluble moiety is located in the core and the soluble moiety occupy the shell, minimizing the surface energy and stabilizing the colloidal system. The final structure and stability of the polymeric nanoparticles obtained by this method will depend on several parameters: there are solvent-related parameters such as the nature, addition rate and ratio between solvent and co-solvent (including the possible evaporation or dialysis to remove the first one); and molecule-related parameters such as nature and relative hydrophobic/hydrophilic character. In this work we have addressed the influence of the polymer concentration on the final structure of the polymeric nanoparticles. For this, different concentrations of the amphiphilic star-shaped block copolymer were first dissolved in 1 mL of THF, which is a good solvent for both the PCL and PEG moieties. Then, the previous solution was poured on 9 mL of deionized water under vigorous stirring. Samples were left to stabilize for at least 48 h, leaving the THF free to evaporate[125]. At this water/THF ratio the morphology of the polymeric nanoparticles is quenched because the structure became kinetically locked in the experimental time scale[126].

3.4.2 Determination of the Critical Aggregation Concentration (CAC)

The CAC of the amphiphilic star-shaped block copolymer was determined by the pyrene fluorescence method reported by Okano and coworkers[127]. Pyrene is a hydrophobic fluorescent dye with several fluorescence peaks, whose intensity strongly depends on the environment of the molecule. The relative intensity between two of them (Intensity at 384 nm and Intensity at 374 nm) could reveal the CAC of an amphiphilic molecule when represented as a function of the molecule concentration. In this work, pyrene was dissolved in

THF at a concentration of 100 µmol/L. Then, 5 µL of the pyrene solution were added into 2 mL of aqueous solution containing the amphiphilic star-shaped block copolymer with various concentrations ranging from 1.0 x 10^{-4} to 2.0 mg/mL. Sample solutions were stirred for 2 days at 20 ºC to completely remove the THF. Ratios of fluorescence emission intensity at 384 and 374 nm (I_3/I_1) were analyzed for determining critical aggregation concentration.

3.4.3 Drug entrapping within polymeric micelles

The drug entrapping within the amphiphilic star-shaped block copolymer was performed by the nanoprecipitation method. A fluorescent and highly water insoluble molecule was used as model drug in these experiments. This molecule was ethyl-3-(butylamino)-1-(4-chlorophenyl)-9H-carbazole-4-carboxylate (PCPC), which is a chloro-phenylcarbazol derivate.

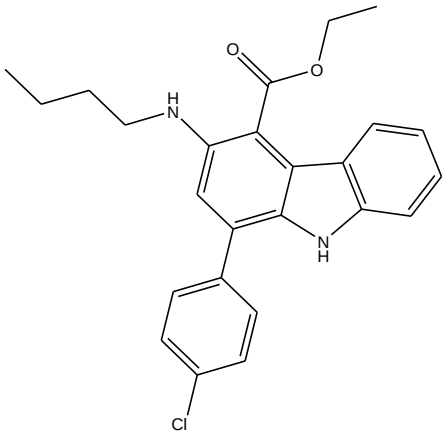

ethyl-3-(butylamino)-1-(4-chlorophenyl)-9H-carbazole-4-carboxylate (PCPC)

PCPC and the amphiphilic star shaped block copolymer were dissolved in 1 mL of THF and poured on 9 mL of deionized water. The final concentrations were 0.5 mg/mL of PCPC and 2 mg/mL of the polymer. The samples were left to stabilize for at least 48 h leaving the THF free to evaporate.

A similar procedure was used for the physical entrapment of the hydrophobic Fe_3O_4@Au nanoparticles within the amphiphilic star-shaped block copolymer. The polymer and the nanoparticles were dissolved in 1 mL of THF and added to 9 mL of deionized water under vigorous stirring. The final concentration of the polymer was 0.1 mg/mL whereas the concentration of the nanoparticles was

varied from 0.1 to 1.4 mg/mL. All the samples were left to stabilize for at least 48 h leaving the THF free to evaporate.

3.4.4 NIR laser irradiation experiments

A CW 980 nm laser pointer (Armlaser, USA) was used to irradiate the nanoparticle dispersions as well as the 96 well plates. The power of the NIR laser beam hitting the sample was constant during the experimental time scale at 6.3 W/cm^2.

3.4.4.1 Phototriggered release of Dox: The phototriggered release of Dox in solution was done by mixing 7 mg of Dox-loaded UCNPs@SiO_2 with 7 mL PBS buffer solution. This mixture was divided in seven aliquots. Each of these aliquots was irradiated with a 980 nm NIR laser for different periods of time at a fixed power density of 6.3 W/cm^2 and an exposition area of 0.5 cm^2. After the irradiation, the samples were centrifuged and the supernatant was collected for analyzing the Dox content. A control experiment was done following the same methodology but without any NIR irradiation. The release profile of Dox molecules was quantified by monitoring the increasing fluorescence signals at 590 nm.

3.4.4.2 in vitro cell viability measurements of Dox-loaded UCNP@SiO_2 nanoparticles: *in vitro* cytotoxicity of Dox-loaded UCNP@SiO_2 nanoparticles was assayed against human HeLa cells. HeLa cells were seeded in a 96-well plate at a density of $9.6 \cdot 10^3$ cells per well and cultured in 5% CO_2 at 37 ºC for 24 h. Then, the Dox-loaded UCNP@SiO_2 nanoparticles were plated at different concentrations and exposed to the CW 980 nm laser for 5 minutes at a power density of 6.3 W/cm^2. Several control experiments were performed with the aim of differentiating the influence of the different nanoparticles in the cell viability: i) Dox-loaded UCNP@SiO_2 nanoparticles were plated at the same concentrations but not exposed to the stimulus, ii) UCNP@SiO_2 nanoparticles without Dox were plated at the same concentrations and treated with and without the CW 980 nm laser raditation for 5 minutes and iii) 5 minute radiation to untreated cells to test the influence of the laser beam on the cell viability.

After the addition of the nanoparticles and the exposure to the stimulus, the cells were incubated in 5% CO_2 at 37 ºC for 48 h. Cell viability was determined using the MTT assay. The results obtained from the cell viability were represented as the media and the standard deviation, calculated from three independent experiments.

4. RESULTS 1

Polymeric nanoparticles with tunable architecture formed by biocompatible star shaped block copolymer

4.1 Introduction

During the last years the development of copolymers that self-assemble in aqueous solutions has attracted tremendous attention due to their important applications in bio and nanotechnology[128–132]. These molecules present two well differentiated regions, one hydrophobic and other hydrophilic, which form amphiphilic compounds that create micelles or nanostructures like polymersomes when they are dispersed in the appropriate media[133]. These mesoscopic systems can be loaded with molecules that are poorly soluble in water (like many anticancer drugs) are accommodated in the hydrophobic part while the hydrophilic shell stabilizes the whole system, allowing the drug dispersion in aqueous media of water insoluble drugs[134]. The copolymeric systems can form nanostructures at lower concentrations than other surfactants such as Solutol HS15, Cremophor EL or Polysorbate 80, which have been extensively used in pharmaceutical technology during the last decades[135]. This advantage reduces the disaggregation effect that appears after diluting the solution containing the micelles. In addition, these systems permit to load bigger amounts of drug, reducing the surfactant concentration in the pharmaceutical formulations[16]. However, problems related with possible kidney toxicity of the currently available copolymers like Pluronic derivates[136] have prompted scientists to explore other systems like ramified copolymers, which are being also studied for drug release. Star shaped block copolymers are globular nanostructures containing multiple arms connected to a central core[137]. These macromolecules exhibit enhanced properties in comparison with their linear analogs such as smaller hydrodynamic diameter, lower solution viscosity, and major micelle stability[138–140]. The synthesis of star shaped block copolymers is simpler than that of the dendrimer based systems and can be carried out according to the “core-first and arm-first” strategy. In this method, the shell and the core of the star shaped block copolymer are synthesized separately. In both syntheses a symmetric initiator with multiple functional groups is employed to begin the polymerization. Each functional group is the starting point of each polymer chain, which is typically synthesized via ATRP[141–143], nitroxide living polymerization[144–146], or ring opening polymerization (ROP)[147,148]. Among

others, ROP is by far the most used method to produced polyesters like poly(ε-caprolactone) (PCL), poly(lactide) or poly(glycolide), which are considered to be biocompatible and the FDA has approved materials with these polymers for their use in humans. In this chapter, we have synthesized the PCL core via ROP using D-sorbitol as symmetric initiator. By controlling the reaction conditions it was possible to modify the molecular weight of the core, which tunes up the hydrophobic character of the amphiphilic copolymer. Subsequently, the core was functionalized and covalently bound to ramified poly(ethylene glycol) (PEG) subunits that constituted the shell of the star shaped block copolymer. The use of branched PEG subunits provides higher stealth capacity which avoids the recognition of the colloidal particles by the reticuloendothelial system (RES) and confers them longer circulation time in the bloodstream and larger distribution volume[149–151]. The well differentiated aqueous solubility of each part provides the amphiphilic nature that allows these molecules to self-assemble in water with fascinating architectures that depend on the polymer concentration. In addition, the solubilizing capacity of the system has been tested using a chloro-phenylcarbazole derivate as model drug. This molecule belongs to a family of drugs with a remarkably potent KSP inhibitory activity (KSP stands for kinesin spindle protein). The inhibition of this enzyme results in mitotic arrest in prometaphase by forming an irregular monopolar spindle. The antimitotic activity of this compound makes it very interesting for use in anticancer therapy[152]. However, as many other anticancer drugs, the scarce water solubility of this molecule (0.35 mg/mL) makes necessary its combination with solubilizing agents for pharmaceutical applications[153].

4.2 Results and discussion

4.2.1 Synthesis of the amphiphilic star shaped block copolymer

4.2.1.1 Preparation of the carboxyl-terminated branched poly(ethylene glycol) moiety: 4bPEG-3-COOH

The saponification reaction of the polyoxyethylene 20 sorbitan monooleate yielded a viscous liquid that was characterized by FTIR and ^{1}H-NMR. The

spectra confirmed the hydrolysis of the reactant that led to a ramified PEG with four branches terminated in hydroxyl groups. Subsequently, 3 of these end groups were transformed into carboxylic groups by reacting 1 equivalent of 4bPEG with 3 equivalents of succinic anhydride. The ^{1}H-NMR spectrum of the 4bPEG-3COOH-1OH is shown in Figure 4.1. The major resonance peaks appear at 2.87 ppm (7), 3.70-3.95 ppm (6) and 4.2 ppm (8). They were assigned to protons from the succinic group "-OOC-C**H$_2$**-C**H$_2$**-COO-", the ethylene glycol monomer units "-O-C**H$_2$**-C**H$_2$**-O-", and the protons forming the ester bond "C**H$_2$**-O-CO-", respectively. The integration ratio between the peaks assigned to the 4bPEG subunits (6) and the terminal succinic groups (7) indicated that an average of three succinic acid groups were introduced per molecule of 4bPEG, thus leaving one hydroxyl end group available for further reactions. The FTIR measurements support these results, as it is shown in Figure 4.2. The relative intensity of the band at 3500 cm^{-1}, which was assigned to the stretching vibration of the hydroxyl groups (O-H), increased after the saponification reaction and diminished after the reaction with succinic anhydride. In addition, the band at 1740 cm^{-1}, which was assigned to the stretching vibration of the carbonyl groups (C=O), disappeared after the saponification reaction and was very intense after the reaction with succinic anhydride.

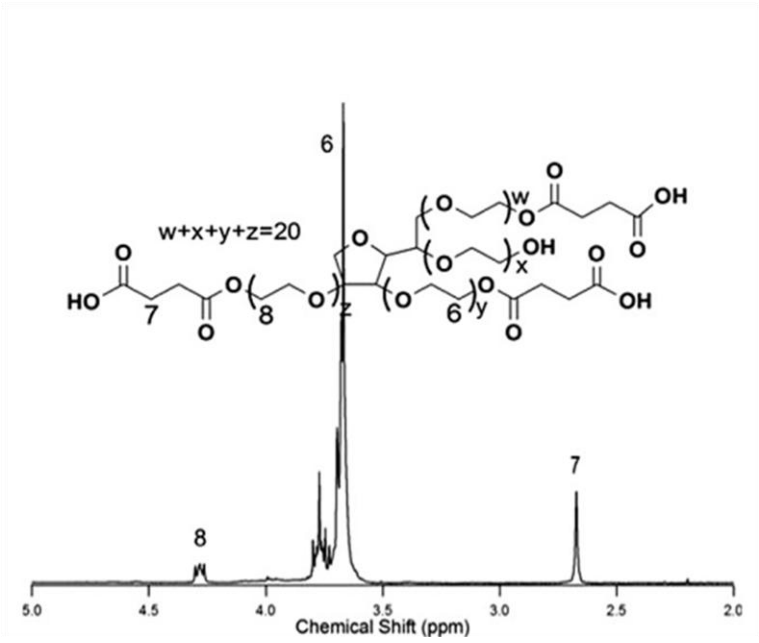

Figure 4.1. ^{1}H-NMR spectrum of the 4bPEG-3COOH-1OH moiety.

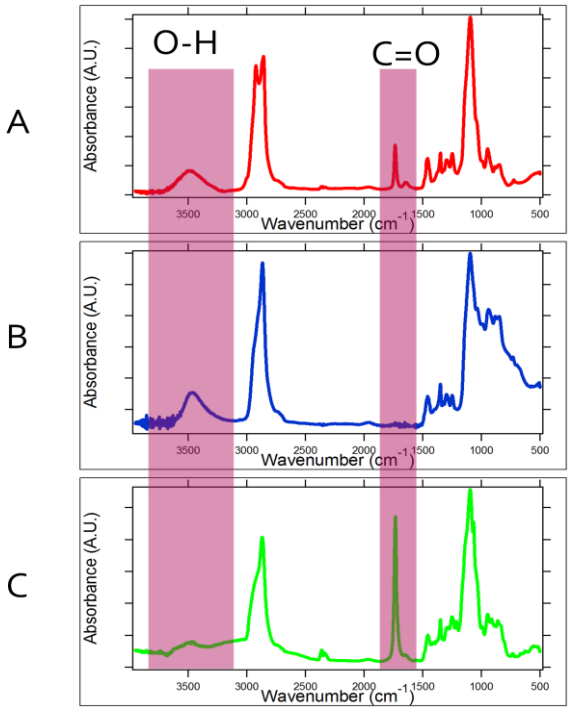

Figure 4.2. FTIR spectra of A) the starting polyoxyethylene (20) sorbitan monooleate, B) 4bPEG-4OH obtained from the saponification reaction and C) 4bPEG-3COOH-1OH obtained from the reaction with 3 eq. of succinic anhydride.

4.2.1.2 Synthesis of the carboxyl-terminated star-shaped poly(ε-caprolactone) moiety

It was possible to obtain star shaped PCL with different molecular weights by varying the monomer to initiator ratio. The M_w and the M_n were calculated with DLS, ^{1}H-NMR, GPC and MALDI-TOF for each synthesis, and the results are presented in Table 1. The results demonstrated that the molecular weight of the star shaped PCL macromolecule was proportional to the ratio of monomer vs initiator.

Table 4.1. The M_w was calculated from DLS and the M_n was calculated by a) ^{1}H-NMR, b) GPC and c) MALDI-TOF.

Sample	Ratio monomer:initiator	M_w (g/mol)	(a) M_n (g/mol)	(b) M_n (g/mol)	(c) M_n (g/mol)
6bPCL-1	45:1	7.8×10^3	6.0×10^3	5.6×10^3	5.5×10^3
6bPCL-2	80:1	1.2×10^4	1.2×10^4	9.7×10^3	8.7×10^3
6bPCL-3	145:1	1.8×10^4	1.5×10^4	1.3×10^4	Na
4bPEG	-	1.3×10^3	1.0×10^3	1.2×10^3	1.0×10^3

The star shaped PCL with 6 branches obtained with a monomer:initiator ratio of 45 (named as 6bPCL-1) had a M_n of 5500 g/mol as determined by MALDI-TOF. This molecular weight was considered as ideal for creating an amphiphilic compound with maximum solubilizing capacity, because after binding the 4bPEG subunits the resulting macromolecule would have a weight ratio of 1:1 between the hydrophobic and the hydrophilic groups. The ^{1}H-NMR spectrum of 6bPCL-1 is shown in Figure 4.3. The major resonance peaks are attributed to the monomer units of the PCL. The peak of the methylene protons from the ester groups (5) "-C**H$_2$**-CO-O-" were detected at 2.3 ppm while the peaks of the methylene protons of the end groups (5') "-C**H$_2$**-OH" were detected at 3.62 ppm. The degree of polymerization was inferred by the integration of these two signals.

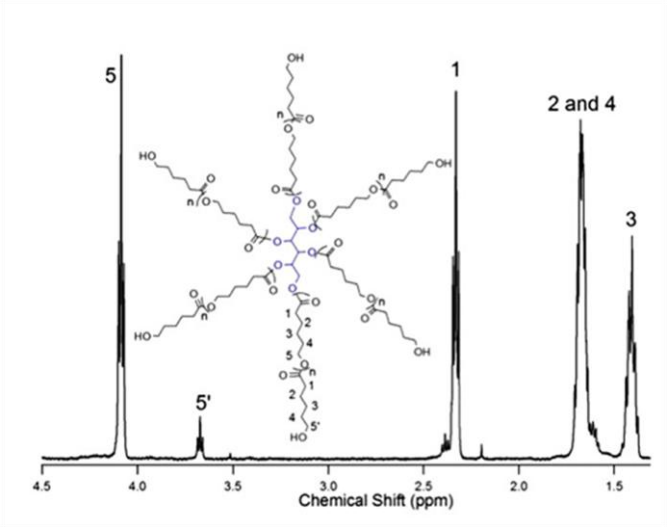

Figure 4.3. ^{1}H-NMR spectrum of the 6bPCL moiety.

The GPC traces and MALDI-TOF spectra are shown in Figure 4.4.

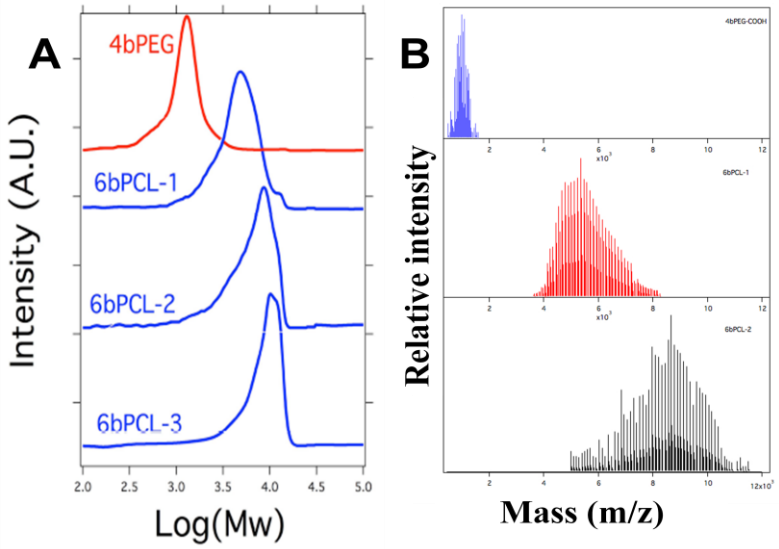

Figure 4.4. A) GPC traces of the 4bPEG moiety and the 6bPCL cores and B) MALDI-TOF spectra of the 4bPEG moiety and the 6bPCL cores. The molecular weight of the sample 6bPCL-3 was out of range for this technique.

The hydroxyl end groups of the selected sample, 6bPCL-1, were subsequently modified into carboxyl end groups by the reaction with an excess of succinic anhydride. This modification was confirmed by FTIR measurements that are shown in Figure 4.5. The band corresponding to the hydroxyl groups, located at 3540 and 3439 cm^{-1} disappeared after the reaction, whilst the relative intensity of the band at 1725 cm^{-1}, which correspond to the ester groups, increased in comparison with the reference bands at 2925 and 2810 cm^{-1} that correspond to the stretching vibration of the aliphatic C-H units of the ε-caprolactone.

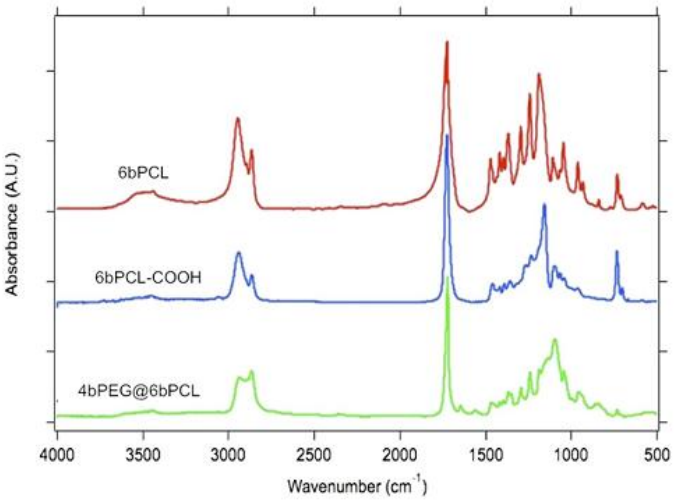

Figure 4.5. FTIR spectra of the 6bPCL (red), the carboxyl terminated 6bPCL (blue) and the amphiphilic star shaped block copolymer (green).

4.2.1.3 Coupling between the 4bPEG and the 6bPCL subunits

The 4bPEG and the 6bPCL subunits were covalently linked by the EDC coupling. Figure 4.6 shows the ^{1}H-NMR spectrum of the 4bPEG@6bPCL star shaped block copolymer. The integration ratio between the peak at 3.7 ppm (6) of the 4bPEG subunits and the peak at 2.33 ppm (1) of the 6bPCL subunits indicates that each 6bPCL core was bound to an average of 5.2 4bPEG moieties. The M_n calculated from the ^{1}H-NMR spectrum was 12.700 g/mol whereas the one measured by GPC was 10.200 g/mol. The GPC curve is shown in Figure 4.7.

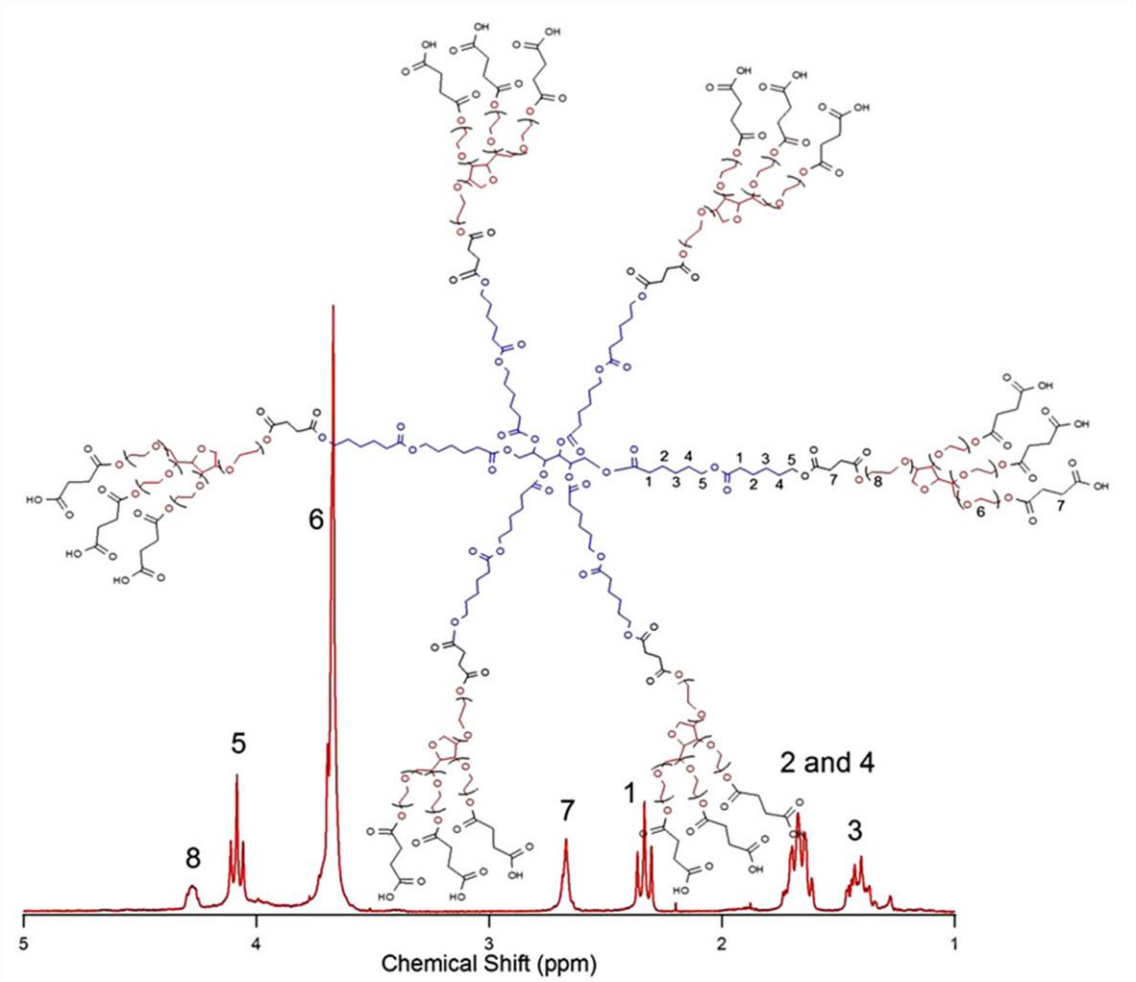

Figure 4.6. Idealized chemical structure and ^{1}H-NMR spectrum of the amphiphilic star shaped block copolymer composed by 4bPEG and 6bPCL.

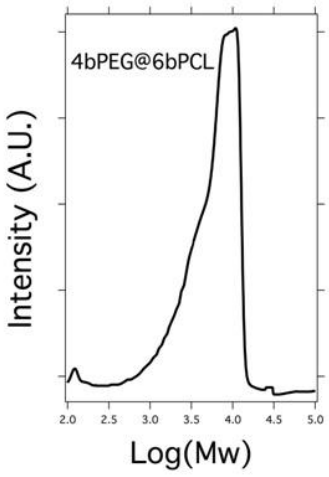

Figure 4.7. GPC curve of the 4bPEG@6bPCL polymer.

The effective coupling of the subunits was demonstrated by PFG-NMR analysis. The plot of $Ln(I/I_0)$ versus $(\gamma\delta G)^2(\Delta-\delta/3)$ would give a straight line with slope –D if the diffusion of the probe molecules has a single component. The diffusion coefficients of the 4bPEG and the 6bPCL moieties in chloroform were individually calculated. The results of these experiments are shown in Figure 4.8. Here one can observe that there was a big difference between the diffusion coefficient of both subunits that were 2.2 x 10^{-5} cm^2/s for the 4bPEG and 6.4 x 10^{-6} cm^2/s for the 6bPCL. By contrast, after covalently binding both subunits, the PFG-NMR measurement revealed that all the peaks assigned to each subunit (6bPCL, 4bPEG and the succinic anhydride) presented the same diffusion coefficient, which was approximately 5.3 x 10^{-6} cm^2/s. The processed 2D spectrum is shown in Figure 4.9. The diffusion coefficient of the 4bPEG@6bPCL macromolecule was slightly smaller than that of the 6bPCL, indicating that the new molecule was bigger than the precursors. This result demonstrated that all the subunits moved together and therefore they were all forming one molecule, and was considered as a proof of the covalent binding of all the subunits.

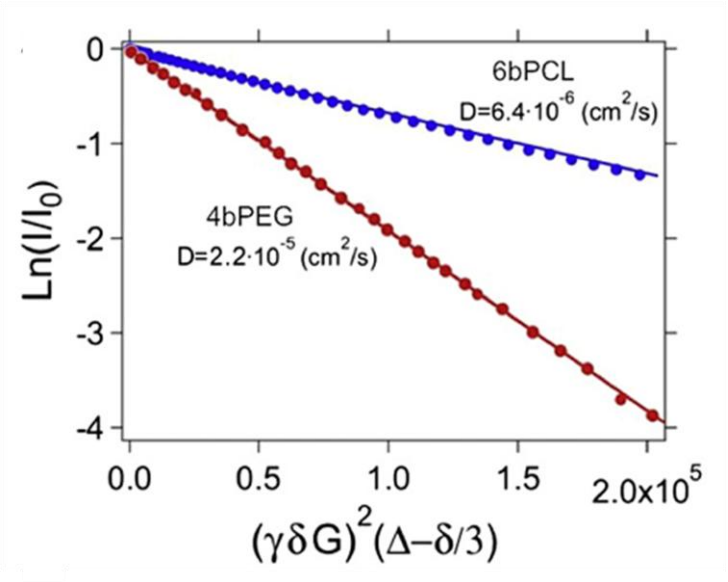

Figure 4.8. Stejskal-Tanner plot of the PFG-NMR data obtained for the 4bPEG and the 6bPCL samples at 25 ºC. The solid lines represent linear least-squares fitted to data.

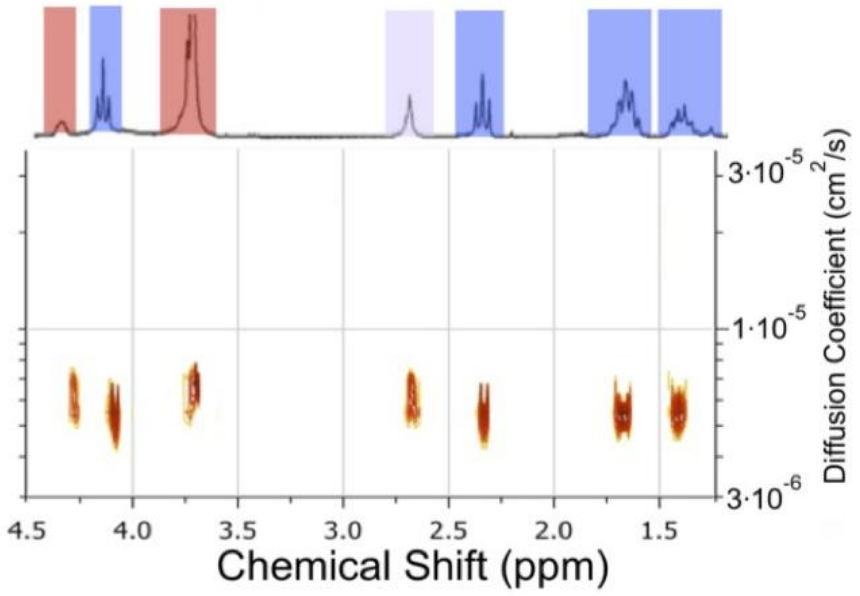

Figure 4.9. ^{1}H-DOSY 2D representation of the spectra obtained for the star shaped 4bPEG@6bPCL block copolymer. The assignments of the ^{1}H peaks corresponding to i) the 4bPEG subunit are marked in red, ii) the 6bPCL subunit are marked in blue and iii) the succinic anhydride are marked in grey.

Additionally the absence of signal above 5.3 x 10^{-6} cm^2/s demonstrated that there were not unbound subunits of 4bPEG or 6bPCL after the purification process. The hydrodynamic diameter of the 4bPEG@6bPCL macromolecule in $CDCl_3$ was calculated with the diffusion coefficient obtained by DOSY using the Einstein-Stokes equation:

$$D = \frac{kT}{3\pi\eta D_h}$$

where D_h is the hydrodynamic diameter, *k* is the Boltzmann constant, T is the temperature, η is the medium viscosity and D is the diffusion coefficient.

The calculated hydrodynamic diameter of the 4bPEG@6bPCL macromolecule was 1.5 nm.

4.2.2 Self-Assembly in aqueous media

The self-assembly and aggregation structure of the amphiphilic star shaped block copolymer were studied by DLS and TEM. The polymeric nanoparticles were assembled by a nanoprecipitation method with THF and water. Using this

methodology we investigated the influence of the polymer concentration. Figure 4.10 (A-E) shows the TEM micrographs from the polymeric nanoparticles obtained at concentrations of 1, 2, 5, 7 and 10 mg/mL. The insets in each TEM micrograph depict the particle size distribution analysis measured by DLS.

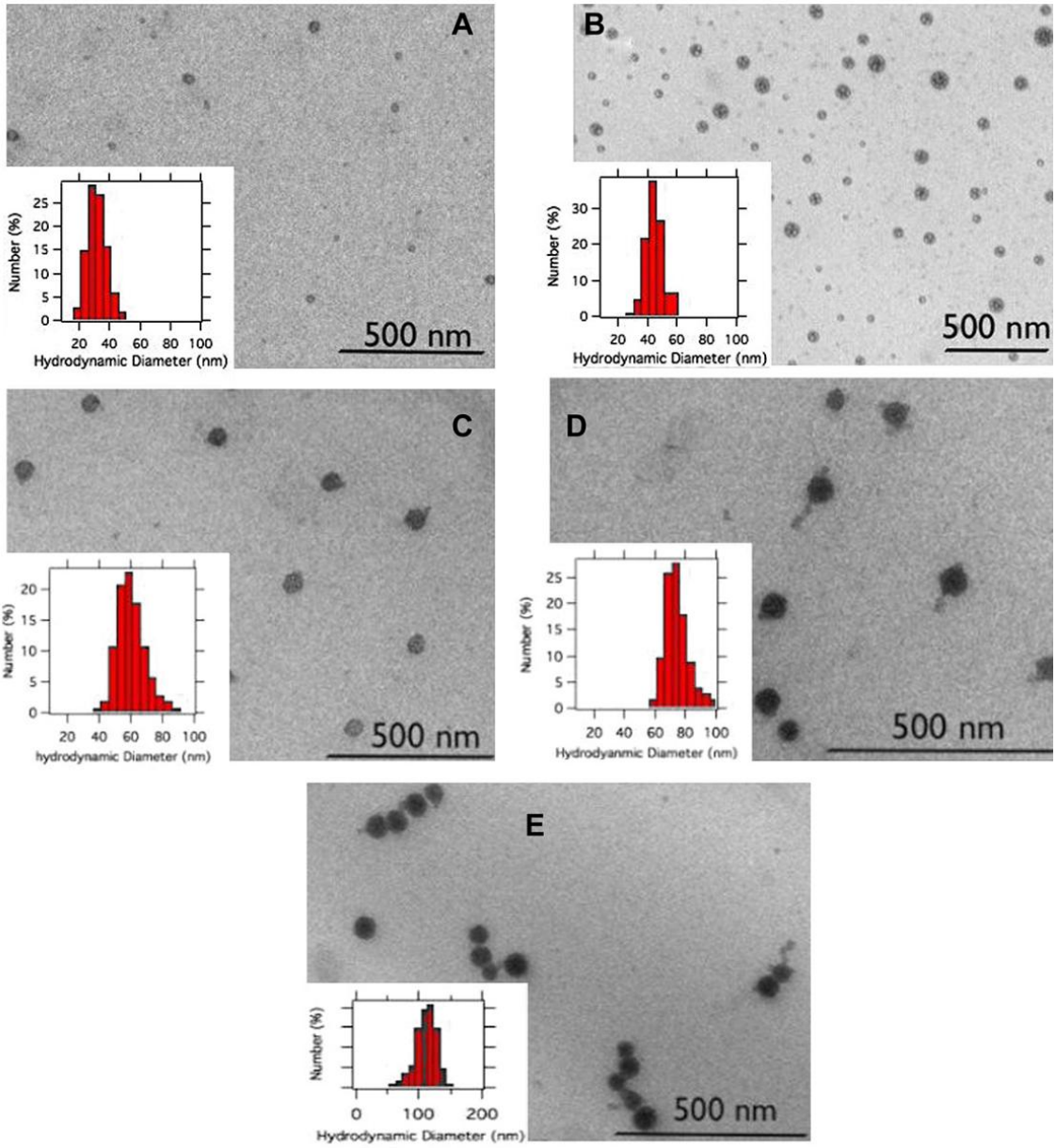

Figure 4.10. TEM micrographs of the structures formed by the amphiphilic star shaped block copolymer in aqueous solution. A) 1 mg/mL, B) 2 mg/mL, C) 5 mg/mL, D) 7 mg/mL, E) 10 mg/mL

In all cases we observed the formation of polymeric nanoparticles with a mean hydrodynamic diameter ranging from 37 ± 6 nm to 120 ± 10 nm as determined

by DLS. The TEM micrographs revealed that the aggregation structure strongly depended on the polymer concentration. When the polymer concentration was 1 mg/mL or less, the 4bPEG@6bPCL self-assembled into nanovesicles (Figure 4.10A). Taking into account that the calculated hydrodynamic diameter of the star shaped block copolymer was 1.5 nm and that the wall thickness of the polymeric nanovesicles was around 3 nm, we hypothesize that the nanovesicle wall was formed by a bilayer structure with two hydrophilic shell layers of PEG and one hydrophobic core of PCL[154], as depicted in Scheme 4.1A. The formation of these nanovesicles could be attributed to the presence of the PCL subunit within the block copolymer. Dennis Discher and coworkers showed that the rigidity of the hydrophobic part of a diblock copolymer based on PEO-PCL was intrinsically related with the formation of nanovesicles[128,129,155]. They observed that an increment of the polymer rigidity provokes the formation of these arrangements because they present minor curvature in comparison with the micelles. The 4bPEG@6bPCL polymer could self assemble into nanovesicles due to the crystallinity of the core as well as the high number of arms, which could lead to an increment in the stretching of the core-forming block[156,157]. Both effects provoked a penalty against high curvature and the system minimized the interfacial tension through the formation of vesicles instead of micelles[158–162]. However, an increment of the polymer concentration facilitated the aggregation of the nanovesicles creating fused structures (Figure 4.10B), which would evolve towards raspberry like structures. These events could be explained by means of the proximity model, which postulates the possibility that neighboring membranes fuse each other[163]. For this to happen, the vesicles should have defects in their surfaces to act as linking points[164]. In rigid structures, the increase of defects leads to an increase in the curvature, which is concomitant with the size reduction[165]. This effect was observed at high polymer concentration[166]. The empty spaces within the different structures diminished from 10 nm to 3 nm as measured by TEM, which support the size reduction of the precursor vesicles with the increase of the polymer concentration.

At higher polymer concentration, the self-assembled structures were denser and no empty spaces were observed inside them. However, under these

conditions a small tail was observed, which was more noticeable at higher polymer concentrations (Figure 4.10C-D). This small tail seems to act as a seeding point to form necklace structure (Figure 4.10E) at the highest experimental concentration. A possible explanation for the tail formation could be given by the scaling model of Vilgis and Halperin (VH)[167,168], which provides theoretical knowledge for understanding these structures[169]. The VH model considers a crystalline-coil A-B diblock copolymer that aggregates in a highly B-selective solvent, which at high concentrations will aggregate forming micelles with a chain-folded crystalline core. According to VH, the increment of the polymer concentration would lead to the formation of a more stretched corona due to the repulsion of the PEG subunits. As result, the densely packed corona would promote the formation of structures with major curvature making the system to evolve towards necklace entanglements, which were observed in the TEM micrographs.

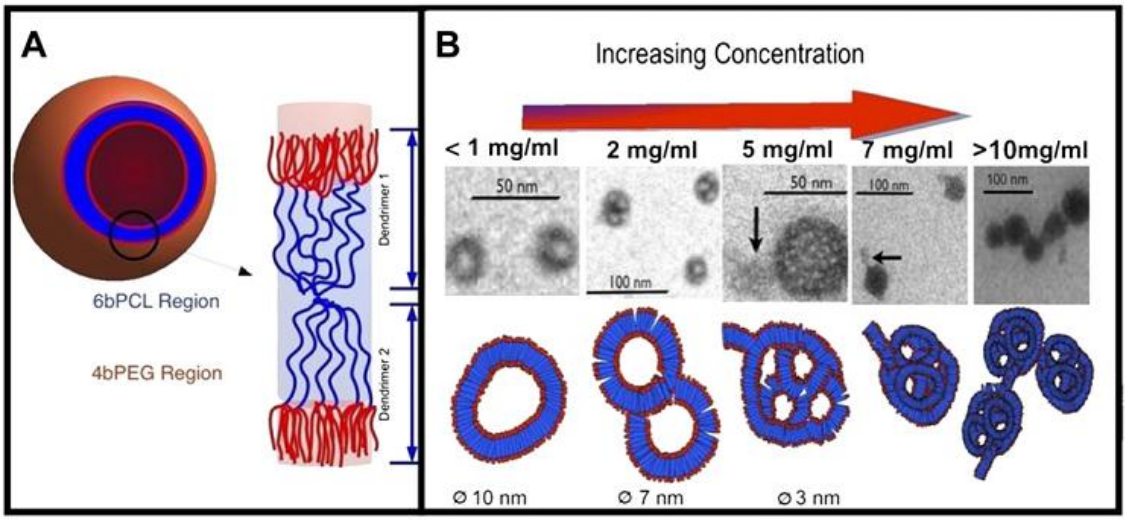

Scheme 4.1. A) Possible structure of a nanovesicle and B) magnification of polymeric nanoparticles obtained by the self-assembly of the amphiphilic star shaped block copolymer at different concentrations.

4.2.3 Drug entrapping

The ability to self-assemble in aqueous media can be used to entrap hydrophobic drugs and opens the possibility to use this system as a nanocarrier. The critical aggregation concentration (CAC) of the amphiphilic star shaped block copolymer was calculated by the pyrene fluorescence method.

The results are shown in Figure 4.11, and the CAC value of the 4bPEG@6bPCL was 0.08 mg/mL. This value is much lower than that of the critical micelle concentration (CMC) of low molecular weight surfactants (e.g. sodium dodecylsulfate has a CMC value of 2.47 mg/mL) and therefore the 4bPEG@6bPCL assemblies are more stable in diluted conditions.

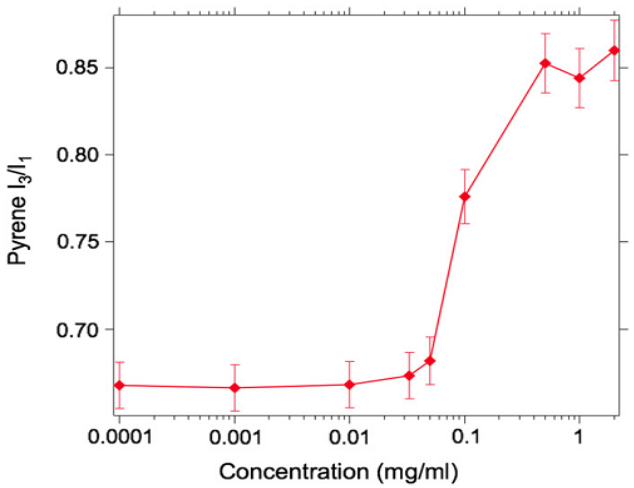

Figure 4.11. Variation of the fluorescence intensity ratio (I_3/I_1) of pyrene (0.25 µM) as a function of the amphiphilic star shaped block copolymer concentration.

The capability of the amphiphilic star shaped block copolymer to solubilize in water highly insoluble molecules was studied with the molecule PCPC. This chlorophenylcarbazole derivate belongs to a group of anticancer drugs[152]. However, one major drawback is the low solubility in aqueous media (0.35 µg/mL) of this molecule, which require a solubilizing agent for its use in biological systems. On the other hand, the photoluminescence of this drug makes it easily traceable and therefore a good model-drug.

When 300 µL of a solution of PCPC in THF (5 mg/mL) were poured into 3 mL of water a green turbid dispersion was obtained, which was associated with the formation of clusters of PCPC whose size was between 200 nm and 2 µm (Figure 4.12C). The PCPC precipitated in less than one hour rendering an opaque dispersion as observed in the cuvette (Figure 4.12D). The big size of the clusters of PCPC would hinder the extravasation and would reduce the distribution volume of the drug[150,151]. However, the PCPC could be effectively entrapped within the amphiphilic star shaped block copolymer structures, thus

permitting the dispersion of the drug in aqueous media. The polymeric nanoparticles loaded with drug had a mean hydrodynamic diameter of 65 nm (Figure 4.12A), which is an ideal size for in vivo applications[170]. The dispersion of 0.5 mg/mL of PCPC and 2 mg/mL of 4bPEG@6bPCL in water was homogeneous and transparent as observable in the cuvette (Figure 4.12B), and the colloidal dispersion was stable for several weeks without any visual evidence of precipitation. These results demonstrated the suitability of the amphiphilic star shaped block copolymer 4bPEG@6bPCL to act as a drug nanocarrier in pharmaceutical applications.

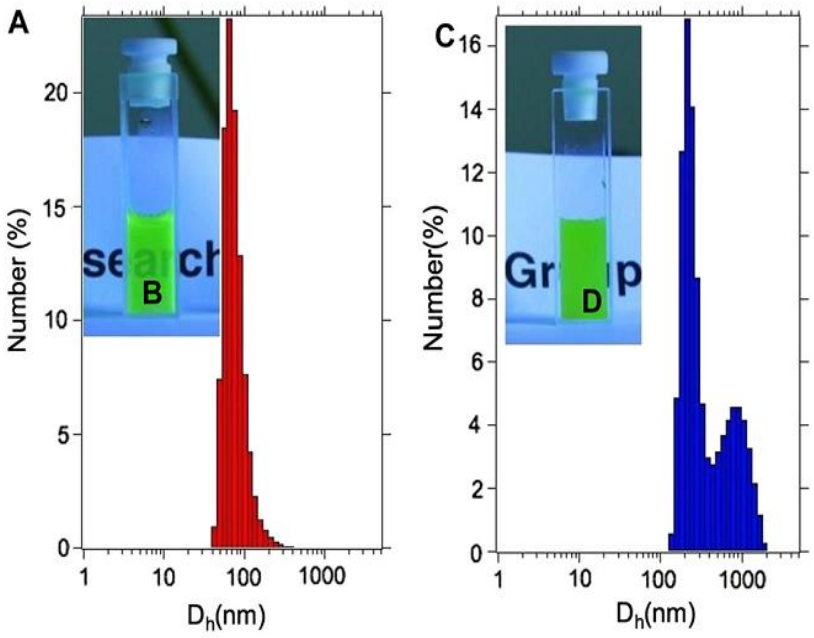

Figure 4.12. A) Size distribution of an aqueous dispersion of PCPC (0.5 mg/mL) in the presence of 4bPEG@6bPCL (2 mg/mL) measured by DLS. C) Size distribution of an aqueous dispersion of PCPC (0.5 mg/mL) measured by DLS. The insets B and D are the pictures taken, under UV illumination, from the cuvettes corresponding to the transparent dispersion of PCPC and 4bPEG@6bPCL in water and the opaque dispersion of PCPC in water, respectively.

4.3 Conclusions

In this chapter we have synthesized an amphiphilic star shaped block copolymer, composed by ramified PCL as the core forming block and ramified PEG as the shell block. All the components are recognized as biocompatible and the PCL is also biodegradable. The parametric study with different techniques permitted to characterize each synthetic step and the final macromolecule. The presence of a hydrophobic part and a hydrophilic part was the driving force for its self-assembly in water, creating polymeric nanostructures whose architecture was strongly affected by the polymer concentration. The capacity of this molecule to self-assemble was employed to encapsulate and disperse in aqueous solution a highly water insoluble molecule. These results demonstrated that the amphiphilic star shaped block copolymer can be used as a drug nanocarrier.

5. RESULTS 2

Efficient synthesis of core@shell Fe_3O_4@Au nanoparticles

5.1 Introduction

Iron oxide nanoparticles have attracted much interest due to their potential applications in biomedicine, and have been used in imaging cancer cells[171], specific targeting[172], hyperthermia treatment of solid tumors[173], and contrast enhancement agents in magnetic resonance imaging (MRI)[174]. Nevertheless, one of the major limitations of the use of these nanoparticles in biomedical applications is related with their poor colloidal stability in physiological conditions[175]. For this reason, scientists have developed different techniques for coating the surface of the magnetic nanoparticles with organic layers like surfactants or polymers[176], inorganic shells made of silica[177], or by combining both organic and inorganic coatings[178]. These methods enhance the stability of the nanoparticles and provide functional groups that can serve as a platform for immobilizing biomolecules of interest.

An interesting approach to provide colloidal stability and functionality is by covering the magnetic nanoparticles with a noble metal shell of Au, which is chemically stable under physiological conditions and can be easily functionalized throughout the well-known Au-SH chemistry[179]. The incorporation of Au can be used to enhance the hyperthermia capacity of the nanoparticles[180], and to provide additional physical properties like X-ray attenuation coefficient that can be used in computed tomography as contrast agents in Dual-Mode MR/CT Imaging systems[181]. Furthermore, the plasmonic properties can be exploited for localizing hyperthermic effects, which would be tremendously important for its application toward tumor cell thermolysis and tissue ablation[182]. Thus, many research efforts have been made to develop hierarchical nanostructures that combine in one both Au and Fe_3O_4 in a core@shell structure[183,184]. Sun and coworkers[185] used hydrophobic Fe_3O_4 nanoparticles as seeds. The Fe_3O_4 nanoparticles were first transferred to an aqueous solution with CTAB and subsequently were covered with a gold shell by gently reducing hydrogen tetrachloroaurate hydrate ($HAuCl_4 \cdot 3H_2O$). Another strategy was developed by Zhong and coworkers[183,186] and involved the formation of the Fe_3O_4 core and the subsequent reduction of Au on the surface of the iron oxide nanoparticles to create the Au shell, giving as result highly-monodisperse

Fe_2O_3@Au and Fe_3O_4@Au nanoparticles. The strategy starts with the synthesis of Fe_3O_4 seeds. After that, gold is deposited onto the surface of Fe_3O_4 nanoparticles by reduction of $Au(CH_3COO)_3$ using 1,2-hexadecanediol in the presence of capping agents at elevated temperature (180–190 ºC). A key element of this process involves careful manipulation of the reaction temperature to control the thermally activated partial desorption of the capping layer from the core, the deposition of Au on the exposed Fe_3O_4 surface, and the subsequent re-encapsulation of the Au shell surface by the capping agent.

An alternative strategy developed also by Zhong and coworkers[187] consists in thermally activated processing of Fe_3O_4 nanoparticles and Au nanoparticles as precursors in a mixed solution. This strategy is based on the thermally induced homo-interparticle coalescence of metal nanoparticles[188]. The basis stems from the decrease of melting point, especially the surface melting, for many nanosized metal particles. Compared with the dramatically decreased melting temperature of gold nanoparticles, iron oxide nanoparticles did not exhibit coalescence in the range of 140-190 ºC.

In this work we have used the synthesis of Fe_3O_4@Au nanoparticles using the methodology described by Zhong due to its high reproducibility and nanoparticle monodispersity[183]. The main drawback of this method is the production of a large amount of pure Au nanoparticles, which require very tedious purification processes to obtain the desired Fe_3O_4@Au nanoparticles. In this chapter we present a systematic study for the optimization of this synthesis, demonstrating the influence of two key parameters, which are the Au:Fe_3O_4 molar ratio and the reaction temperature. The results obtained varying the Au:Fe_3O_4 ratio permitted to optimize this parameter and limit the formation of undesired pure Au nanoparticles. The TEM micrographs revealed that the Au shell thickness was independent on the Au:Fe_3O_4 ratio and we discuss this unexpected result as a consequence from the reaction mechanism. On contrary, the Au shell thickness was dependent on the reaction temperature. This study would permit a better understanding of this methodology for the synthesis of core@shell nanoparticles in which the shell is formed by Au. The production in high yield of hybrid Fe_3O_4@Au nanoparticles could be potentially used for a wide range of applications, with a special highlight in biomedicine.

However, these nanoparticles are hydrophobic and cannot be used for biological applications without further steps of functionalization that would provide them aqueous solubility. There are several strategies to provide aqueous solubility via chemical modification of the surface of the nanoparticles[189,190] and via physical entrapment into liposomes[191–193] or micellar structures[194–197]. However, the physical entrapment of hydrophobic nanoparticles within polymeric nanostructures formed with amphiphilic block copolymers has not been deeply studied yet. Taton *et al.*[198–200] and Eisenberg *et al.*[201,202] published pioneering works in this field that demonstrated the great potential of the resulting hybrid nanomaterials. In this chapter we studied the phase transfer of the hydrophobic Fe_3O_4@Au nanoparticles to aqueous solution by using the star-shaped amphiphilic block copolymer based on a branched PCL core and a branched PEG shell described in the previous chapter. The hybrid nanomaterial obtained by this method presented multifunctional properties due to the structure at the nanoscale.

5.2 Results and discussion

5.2.1 Characterization of hydrophobic iron oxide nanoparticles

Iron oxide nanoparticles were prepared by thermal decomposition of the iron (III) oleate complex in the presence of oleic acid and 1-octadecene at high temperature[122]. The solution turned from brownish to dark brown color, which corresponded with the formation of the iron oxide nanoparticles. The presence of monodisperse and individual iron oxide nanoparticles with a narrow size distribution was confirmed by TEM micrographs, as shown in Figure 5.1a. Figure 5.1b shows the HR-TEM image of Fe_3O_4 nanoparticles, and the Figure 5.1c depicts the SAED pattern of the nanoparticles.

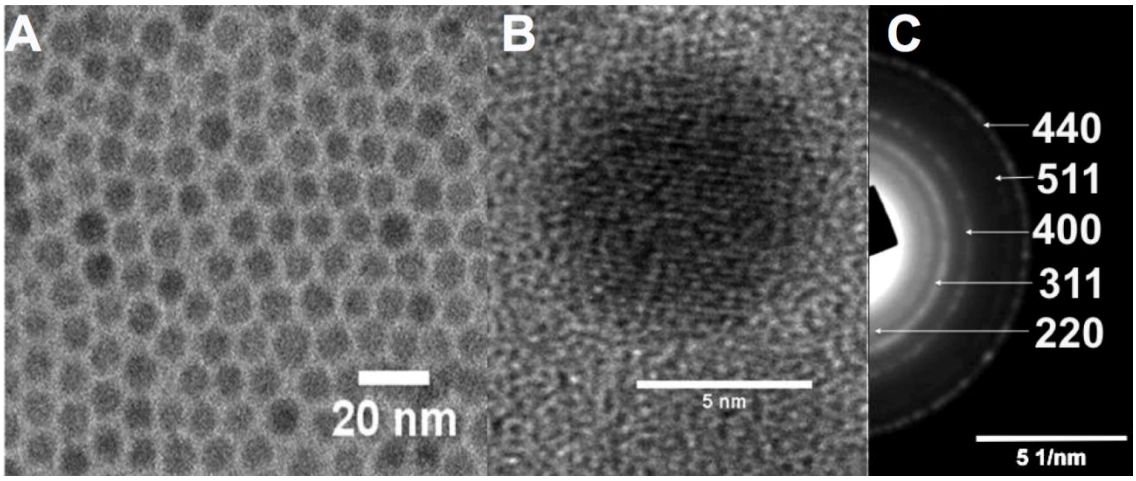

Figure 5.1. a) Representative TEM micrograph showing the monodisperse iron oxide nanoparticles obtained by thermal decomposition b) HR-TEM of a single iron oxide nanoparticle c) SAED pattern of the nanoparticles.

The size distribution analysis obtained from the TEM pictures gave as result a mean diameter of 7.5 ± 0.6 nm. Furthermore, the hexane dispersion of the hydrophobic iron oxide nanoparticles was stable for over a year without any evidence of precipitation. The HR-TEM micrograph shows the lattice fringe of the <220> lattice plane (3,01 Å) and the SAED analysis showed the typical reflections attributed to the FCC spinel Fe_3O_4 structure[203].

5.2.2 Characterization of hydrophobic core@shell Fe_3O_4@Au nanoparticles

The hydrophobic core@shell Fe_3O_4@Au nanoparticles were synthesized using the iron oxide nanoparticles as seeding points for the deposition of Au by a briefly modified procedure which was previously published[183]. In our experimental conditions we did not use 1,2-hexadecanediol because we found that it was unnecessary for the synthesis. We observed that Au and Fe_3O_4@Au nanoparticles could be obtained by using oleylamine both as reducing and capping agent and Gold (III) acetate as Au precursor. The mixture of oleic acid and oleylamine and the high temperature in diphenyl ether favored the Au deposition on the surface of Fe_3O_4 nanoparticles[204]. The Fe_3O_4@Au nanoparticles were characterized by TEM, EDS, UV-Vis, DLS and magnetization measurements.

Figure 5.2a shows a representative TEM micrograph of the as obtained Fe_3O_4@Au nanoparticles, Figure 5.2b shows the HR-TEM image of Fe_3O_4@Au nanoparticles, and Figure 5.2c depicts the SAED pattern of the nanoparticles.

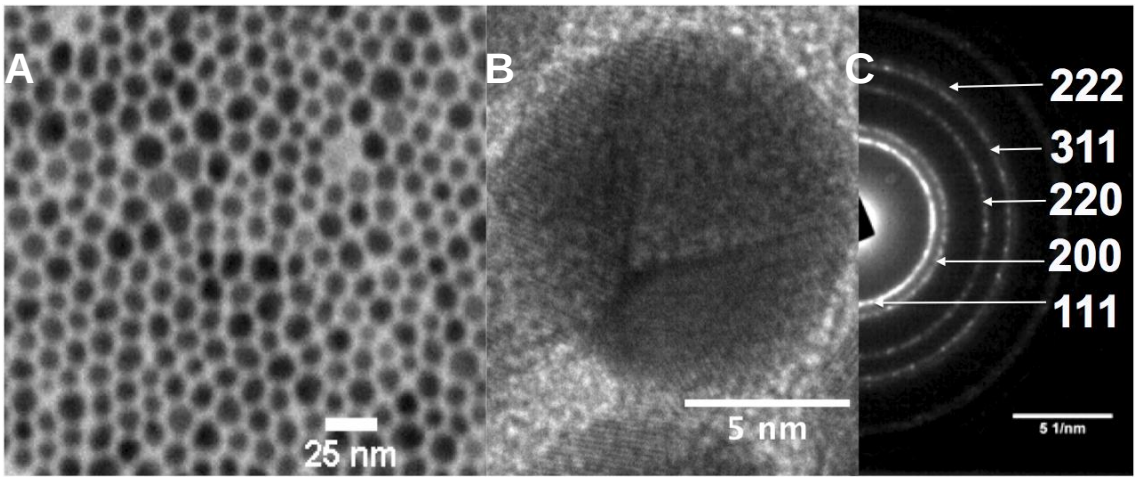

Figure 5.2. a) Monodisperse Fe_3O_4@Au nanoparticles b) HR-TEM of a single Fe_3O_4@Au nanoparticle c) SAED pattern of the nanoparticles.

The size distribution obtained from the TEM picture gave as result a mean diameter of 11 ± 2.2 nm. In the HR-TEM micrograph it is observed the crystalline structure of a single Fe_3O_4@Au nanoparticle in which the Au <111> lattice plane is predominant (2.4 Å) and the SAED analysis showed the typical reflections attributed to the Au crystalline structure[205]. Moreover, in Figure 5.1b it is noticeable the presence of twinned planes in the Au shell, which were frequently observed. The reflections of the Fe_3O_4 core could not be observed by this technique due to the well-known heavy atom effect[206].

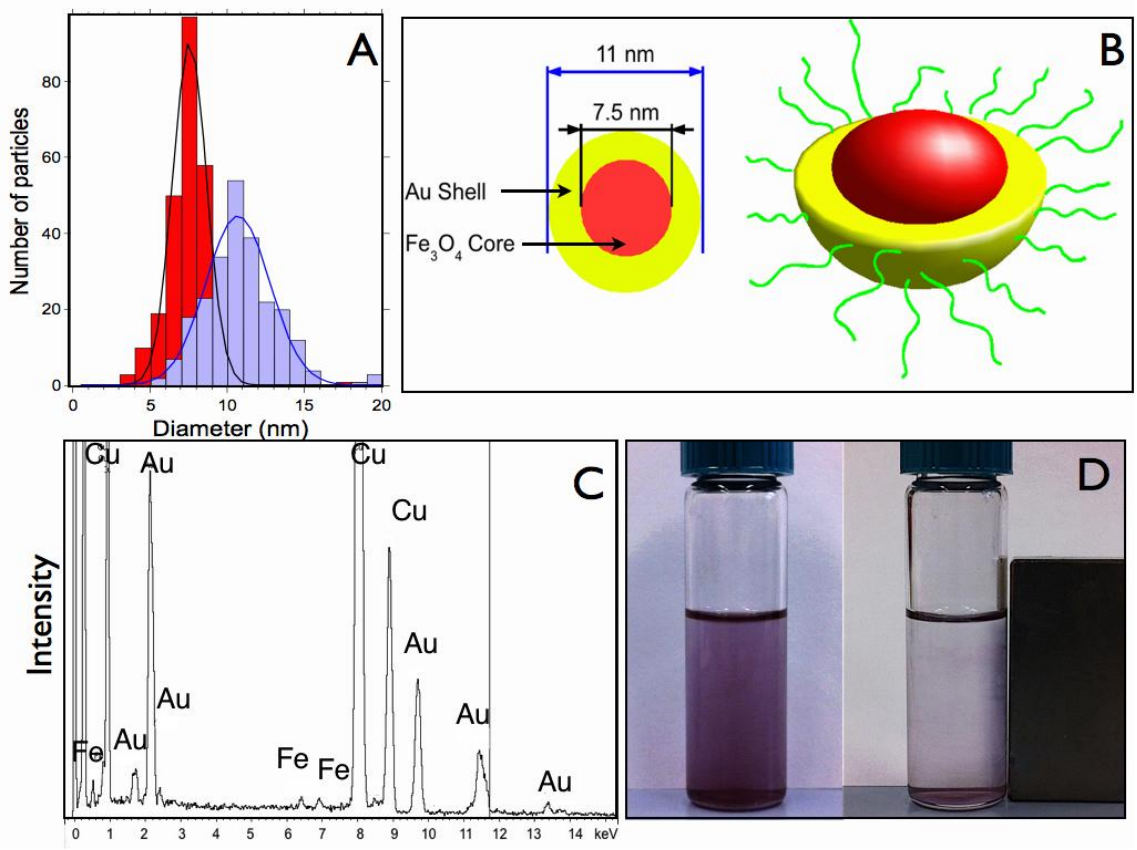

Figure 5.3. A) Size distribution analysis of Fe_3O_4 nanoparticles (in red) and Fe_3O_4@Au (blue) nanoparticles measured by TEM. B) Idealized scheme of the Fe_3O_4@Au nanoparticles. C) Energy Dispersive Spectroscopy spectrum of the Fe_3O_4@Au nanoparticles. D) Fe_3O_4@Au nanoparticle dispersion in hexane/ethanol in the absence and presence of a magnetic field (B=0.4 T).

Figure 5.3a shows the size distribution analysis of the initial Fe_3O_4 nanoparticles (7.5 ± 0.6 nm) and that of the Fe_3O_4@Au nanoparticles (11 ± 2.2 nm). The diameter of the nanoparticles increased an average of 3.5 nm, as depicted in Figure 5.3b. This result was attributed to the presence of the Au shell. In addition, the absence of uncoated Fe_3O_4 nanoparticles in the TEM micrographs would indicate that the structure of the Fe_3O_4@Au nanoparticles is a core@shell structure. The composition of the Fe_3O_4@Au nanoparticles was studied by EDS microanalysis that provided qualitative determinations of their elemental composition (Figure 5.3c). The EDS spectrum revealed the presence of iron, with a Kα peak at 6.400 keV and a Kβ peak at 7.059 keV and gold with a Mα peak at 2.1 keV, Lα at 9.7 keV and Lβ at 11.4 keV. The presence of the copper peaks is due to the copper TEM grid. The analysis of the peak

intensities provided the atomic percentage between gold and iron, which were 90 % and 10 % respectively. These results are in agreement with those calculated theoretically for spherical core@shell particles with a core of 7 nm and a shell of 3 nm[207].

The inner response to an external magnetic field of the Fe_3O_4 cores remained in the Fe_3O_4@Au nanoparticles and could be directly observed. Figure 5.3D shows that in the presence of a magnetic field the nanoparticles migrate towards the magnet. The magnetic properties of the Fe_3O_4@Au nanoparticles were studied using a superconducting quantum interference device (SQUID). The comparison of the magnetization curves between Fe_3O_4 and Fe_3O_4@Au displayed a significant difference shown in Figure 5.4.

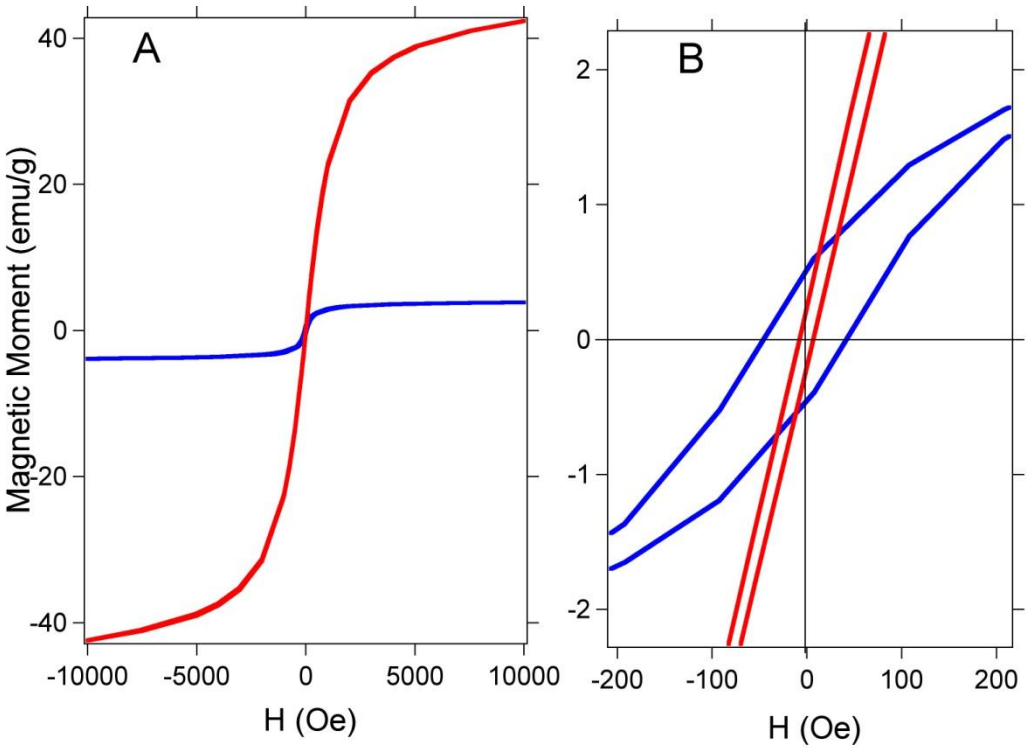

Figure 5.4. a) Magnetization curve as a function of the applied field for Fe_3O_4 nanoparticles (red curve) and Fe_3O_4@Au nanoparticles (blue curve) at room temperature. b) Magnification of the curves.

The saturation magnetization and coercivity were determined from SQUID measurements. The magnetic data displayed two major differences between Fe_3O_4 and Fe_3O_4@Au nanoparticles. First, the maximum magnetization values were 45 emu/g and 4 emu/g for Fe_3O_4 and Fe_3O_4@Au, respectively. Second, the coercivities of Fe_3O_4 and Fe_3O_4@Au nanoparticles were 19 and 80 Oe, respectively. The reduction of the maximum magnetization in the Fe_3O_4@Au indicates that there was less magnetic material per gram of sample[208]. Furthermore, the coercivity showed a clear increase for the Fe_3O_4@Au nanoparticles, which could be attributed to the larger size of Fe_3O_4@Au that leads to a less-effective coupling of the magnetic dipole moments. In contrast, the magnetic dipole moments in the case of uncoated Fe_3O_4 nanoparticles are coupled more effectively, and hence the particles tend to have a lower coercivity[209,210].

5.2.3 Study of the key parameters of the synthesis: Optimizing the yield of Fe_3O_4@Au nanoparticles via the Au:Fe_3O_4 molar ratio

The technological applications of core@shell nanoparticles will often require a precise control of the shell thickness. For this, it is necessary to carefully set the reaction parameters that might influence the production of the desired nanoparticles. In this work we studied the influence of a key parameter of this synthesis that is the Au:Fe_3O_4 ratio. A set of syntheses varying the Au:Fe_3O_4 molar ratio from 0.3 to 8 were performed. The results of these experiments were analyzed by TEM, see Figure 5.5.

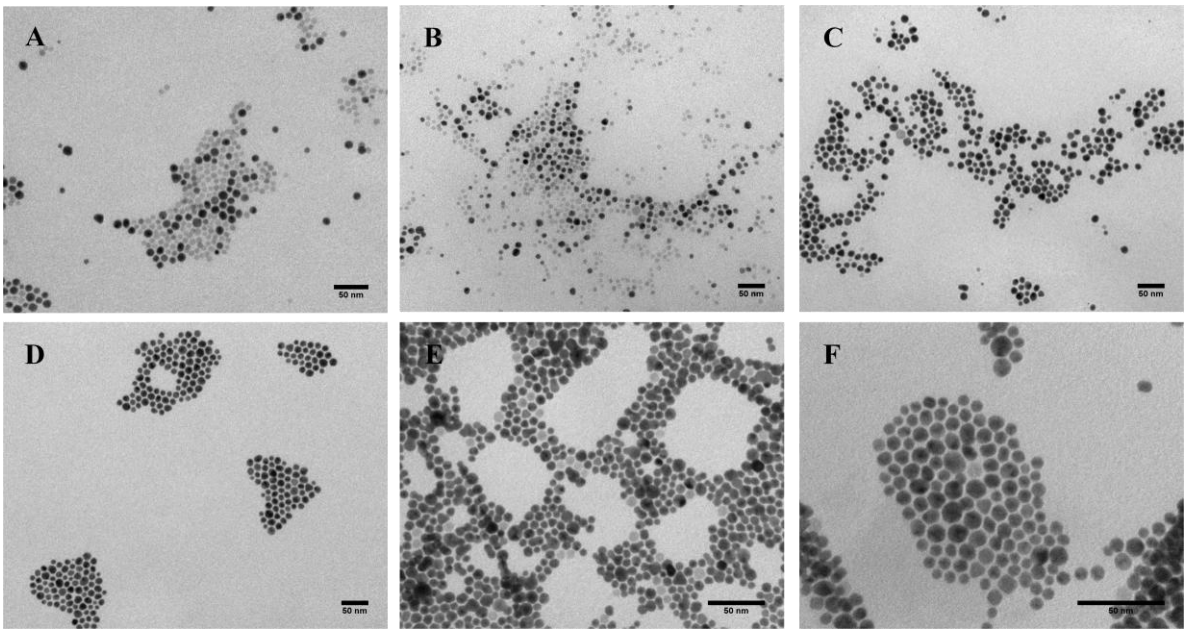

Figure 5.5. Representative TEM micrographs of the as obtained nanoparticles synthesized with different Au:Fe_3O_4 ratios a) 0.3 b) 1 c) 2.5 d) 3.7 e) 5.5. f) 8. All scale bars are 50 nm.

In Figure 5.5a and 5.5b it is noticeable the presence of two different types of nanoparticles, which differ mainly in their contrast in TEM operated in bright field imaging mode. Iron oxide nanoparticles have less contrast in TEM than Au nanoparticles and therefore the bright nanoparticles were considered as Fe_3O_4. However the darker nanoparticles could not be only attributed to Fe_3O_4@Au nanoparticles because there could be pure Au nanoparticles without magnetic core, which would not be differentiated by their contrast. For this reason, the population of darker nanoparticles was considered as 'Au-containing nanoparticles'. As it can be seen in Figure 5.5, as the Au:Fe_3O_4 ratio increased, the number of uncoated Fe_3O_4 nanoparticles was reduced. This reduction was concomitant with an increment in the number of Au-containing nanoparticles. However, these Au-containing nanoparticles appeared even at low ratios of Au:Fe_3O_4 and showed a similar size and shape. The proportion of Au-containing and was defined as χ (number of Au containing nanoparticles/total number of nanoparticles) was represented as a function of the Au:Fe_3O_4 ratio, as shown in Figure 5.6A.

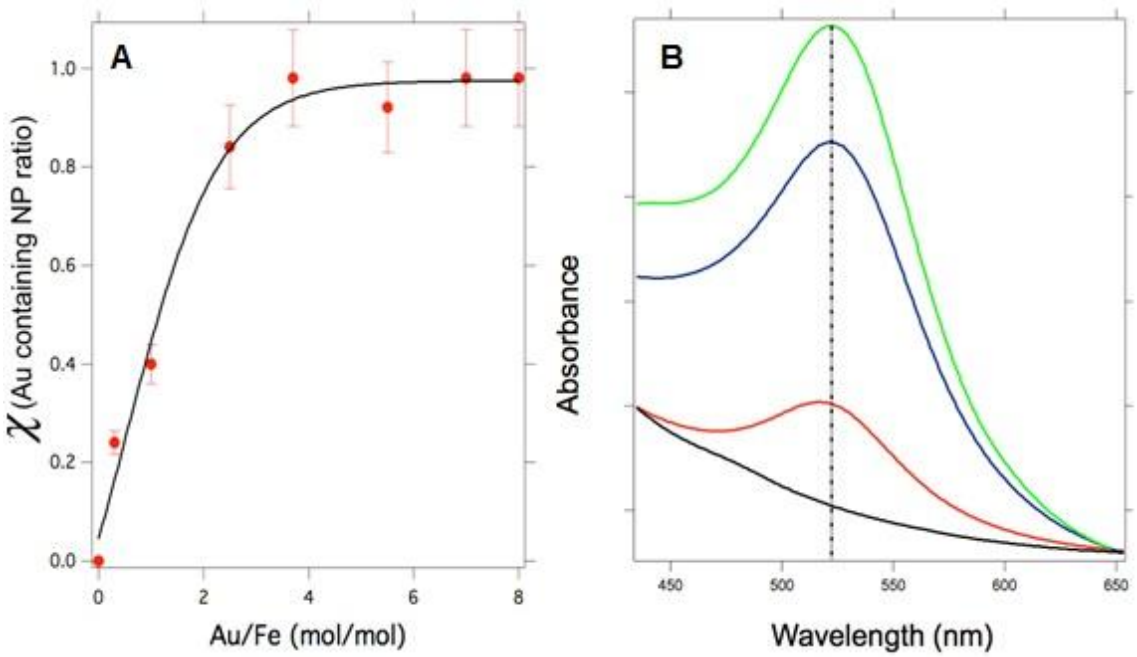

Figure 5.6. A) Proportion of Au containing nanoparticles versus the Au:Fe_3O_4 ratio. B) UV-Vis spectra of the nanoparticles obtained with different Au:Fe_3O_4 ratio; 0 (black), 0.3 (red), 3.7 (blue) and 7 (green).

Figure 5.6a depicts that χ increased with the Au:Fe_3O_4 ratio until it reached a plateau close to 1, which is the maximum possible value, for ratios of 3.7 and above. The Figure 6b shows the UV-Vis spectra of representative nanoparticles obtained at different Au:Fe_3O_4 ratios. The absorption band with a maximum at 521 nm corresponded to the surface plasmon resonance (SPR) of Au nanospheres in hexane[211] except for the sample of uncoated Fe_3O_4 nanoparticles that did not show that band. The SPR band showed a similar profile and maximum wavelength independently from the Au:Fe_3O_4 ratio, which only influenced the maximum intensity. Both the TEM micrographs and the UV-Vis measurements demonstrated that the Au shell thickness was not influenced by the Au:Fe_3O_4 ratio. However, we found that this parameter had a strong influence on the yield of Fe_3O_4@Au nanoparticles. This result is of key relevance for the optimization of the synthesis of Fe_3O_4@Au nanoparticles, because if the synthesis is performed using a high Au:Fe_3O_4 ratio, the Au shell thickness would remain constant and therefore the excess of Au reagent would provoke a homogeneous nucleation, leading to pure Au nanoparticles without a Fe_3O_4 core. We performed a control experiment using the same experimental

conditions without Fe_3O_4 seeds and we could observe the formation of polydisperse Au nanoparticles (Figure 5.7a). This result demonstrates the relevance of using the optimized Au:Fe_3O_4 ratio, because otherwise it would be tedious to purify the desired Fe_3O_4@Au nanoparticles from the pure and less homogeneous Au nanoparticles. In addition, another control experiment was carried out by pouring together the iron (III) oleate complex and the gold (III) acetate in 1-octadecene and heating up to 300 ºC. This control experiment resulted in dumbbell-like nanoparticles formed by Au-Fe_3O_4, which can be easily distinguished by the different TEM contrast (Figure 5.7b). This control experiment demonstrated that under these experimental conditions it is possible to circumvent the lattice mismatch between gold and iron oxide and also that there is no tendency to form alloys between them.

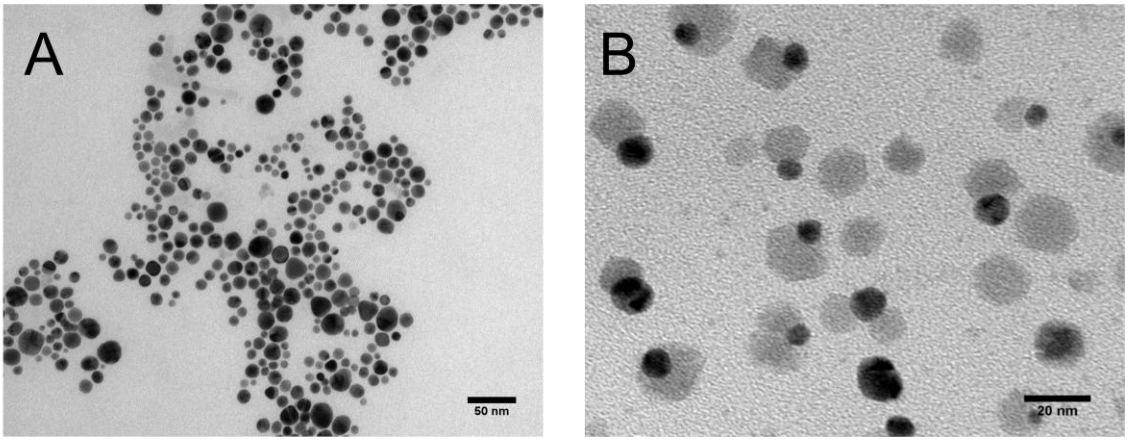

Figure 5.7. a) Control experiment without iron oxide seeds that led to the formation of polydisperse pure Au nanoparticles. b) Control experiment with iron (III) oleate complex that led to the formation of dumbbell-like Au-Fe_3O_4 nanoparticles.

Our experiments revealed that the optimum Au:Fe_3O_4 ratio for obtaining in high yield the Fe_3O_4@Au nanoparticles was 3.7 for our synthetic conditions. However, the uncoated Fe_3O_4 nanoparticles that we used had a mean diameter of 7.5 nm, and therefore the optimized Au:Fe_3O_4 ratio would probably be different for nanoparticles of different size.

A possible explanation for these results could be given in terms of the reaction mechanism proposed by Zhong and coworkers[183,184]. In these two works, the Au nanoshell was formed either by the deposition of the Au reagent directly onto the Fe_3O_4 seeds or by the heterogeneous coalescence of melted Au nanocolloids at high temperature. In our experimental conditions it would be possible that the Au nanocolloids were formed *in situ* by the reaction between gold (III) acetate and oleylamine. These nanocolloids could be melted at high temperature thus allowing the heterogeneous coalescence. In this way, the Au shell formation mechanism would require the following steps: i) formation of Au nanocolloids, ii) capping shell desorption, iii) the deposition of melted Au nanocolloids on the exposed Fe_3O_4 surface and iv) heterogeneous coalescence to form the final Au shell.

Our experimental results could be explained by this mechanism if the deposition of the melted Au nanocolloids onto the Fe_3O_4 seeds was the slowest step whereas the following processes were faster and irreversible. Under these conditions, once an initial amount of Au nanocolloids were deposited on the surface of Fe_3O_4 nanoparticle, the system would evolve rapidly toward a core@shell structure. This would explain that at low Au:Fe_3O_4 ratios, we observed fully coated and non-coated nanoparticles and we could not observe patchy or hetero-nanoparticles. By contrast, when the Au:Fe_3O_4 ratios were in the plateau region, the quantity of Au precursor was enough for the deposition on the majority of the Fe_3O_4 seeds and therefore we could observe a higher degree of coating. However, a large excess of Au:Fe_3O_4 ratio would also lead to homogeneous coalescence of Au nanocolloids, as we could not observe an increment of the Au shell thickness. In addition, we observed in the HR-TEM images a large quantity of nanoparticles with twinned planes (Figure 5.2b). This could be due to the deposition of various melted Au nanocolloids on the exposed surface of a single iron oxide nanoparticle that after the subsequent heterogeneous coalescence would lead to these structures, which support our proposed mechanism.

5.2.4 Study of the key parameters of the synthesis: Influence of the reaction temperature

Although the Au shell thickness could not be controlled with the Au:Fe_3O_4 ratio, there are other parameters that could play an important role in the control of the Au shell thickness. For instance, some authors have extensively studied the influence of the chain length of the capping agents[212], which demonstrated that the shorter the chain length, the bigger the nanoparticles. In this work we have studied the influence of the reaction temperature because preliminary works seemed to indicate that the melting temperature of the nanoparticles is intrinsically related with their size[213,214].

The influence of the temperature in the evolution of gold nanoparticles has been studied by Zhong and coworkers[188]. In their study, they observed a size and shape evolution of thiolate-encapsulated gold nanoparticles upon increasing the reaction temperature from 100 to 138ºC. In this work we have studied the influence of the reaction temperature, in the range between 190 to 270 ºC, on the formation of Fe_3O_4@Au nanoparticles. The TEM micrographs are shown in Figure 5.8.

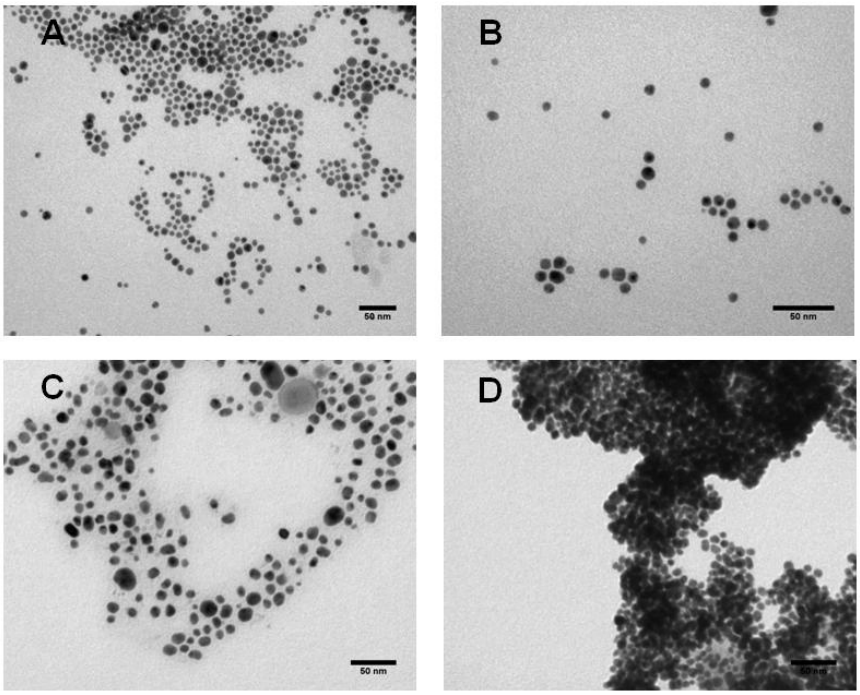

Figure 5.8. TEM micrographs from the Fe_3O_4@Au nanoparticles synthesized at different reaction temperatures: a) 210 ºC b) 230 ºC c) 250 ºC and d) 270 ºC. Scale bars are 50 nm.

Figure 5.9a depicts the size distribution analysis obtained by DLS measurements of the Fe_3O_4@Au nanoparticles synthesized at different reaction temperatures, using a Au:Fe_3O_4 molar ratio of 7.

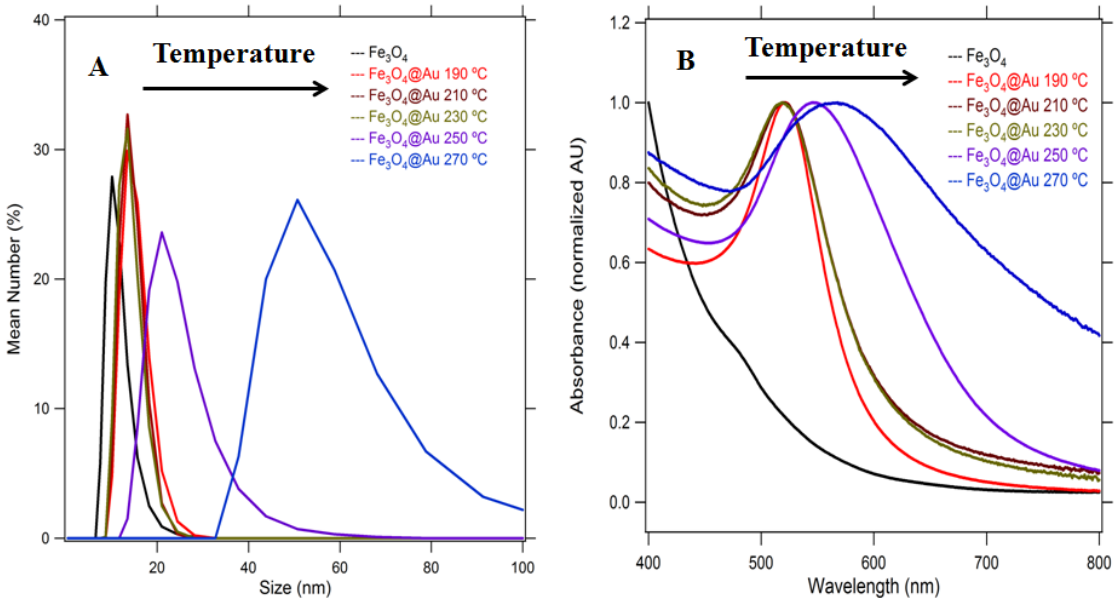

Figure 5.9. a) Size distribution obtained by DLS of the Fe_3O_4@Au nanoparticles synthesized at different reaction temperatures. b) UV-Vis spectra of the Fe_3O_4@Au nanoparticles synthesized at different reaction temperatures.

These results showed that the reaction temperature does not influence the Au shell thickness between 190 and 210 ºC. However, we found a size evolution of the Au shell thickness when the reaction temperature was above 230 ºC: Between 230 and 250 ºC, we observed a significant increase of the Au nanoshell from 3 to 10 nm, as demonstrated by DLS. In addition, the SPR band of the nanoparticles was studied by UV-Vis spectroscopy, see Figure 5.9b. Here we can observe that the maximum of the SPR band was at 521 nm when the nanoparticles were synthesized at a reaction temperature between 190 and 210 ºC, and that the SPR maximum was red-shifted when the nanoparticles were synthesized above 230 ºC. These results are in agreement with the DLS data, because the increment in size of spherical Au nanoparticles provokes red-shifts of their SPR bands. A picture taken from the cuvettes containing the as-synthesized nanoparticles is shown in Figure 5.10.

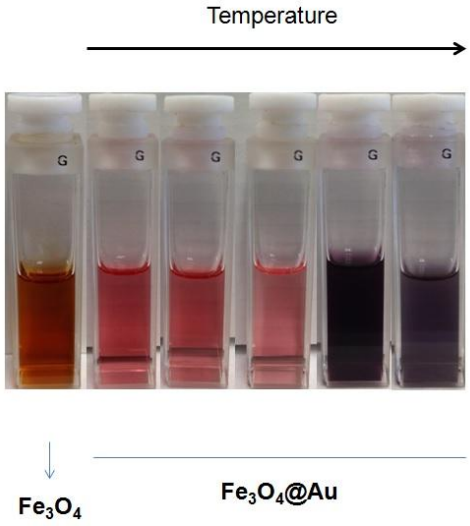

Figure 5.10. Picture taken from the cuvettes containing the Fe_3O_4 and the Fe_3O_4@Au nanoparticles synthesized at different reaction temperatures. The different colors observed are in concordance with the data obtained by both DLS and UV-Vis spectroscopy measurements.

5.2.5 Solubilizing the Fe_3O_4@Au nanoparticles: A multifunctional hybrid nanomaterial

The optimized Fe_3O_4@Au nanoparticles could be successfully solubilized in aqueous media with the star-shaped amphiphilic block copolymer based on PCL and PEG by the nanoprecipitation method. The resulting hybrid nanomaterial was highly stable in aqueous solution, observable by naked eye (see Figure 5.11). The hydrophobic Fe_3O_4@Au nanoparticles were completely unstable in aqueous solution in less than one hour and formed a black precipitate. On contrary, the samples containing the nanoparticles and a small quantity of the amphiphilic star-shaped block copolymer were stable and showed the typical pink color of diluted solutions of well-dispersed 11 nm Fe_3O_4@Au nanoparticles. These samples were stable for over a year without any visible evidence of aggregation or precipitation.

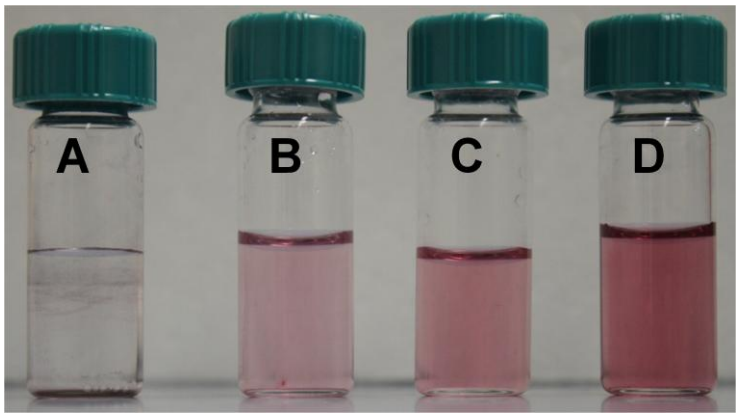

Figure 5.11. Picture taken from the vials containing the aqueous solutions containing a) Fe_3O_4@Au nanoparticles without the star-shaped amphiphilic block copolymer, b), c) and d) 0.1 mg/mL of the star-shaped amphiphilic block copolymer with 0.1, 0.3 and 0.5 mg/mL of Fe_3O_4@Au nanoparticles, respectively.

The capability of the amphiphilic star-shaped block copolymer for solubilizing the Fe_3O_4@Au nanoparticles was studied as a function of the nanoparticles-to-polymer ratio. The concentration of the polymer was set at 0.1 mg/mL and the nanoparticles-to-polymer ratio was varied from 1 to 14. The samples were analyzed by DLS and UV-Vis spectroscopy. The DLS measurements were

performed assuming a bimodal distribution, since a population of nanoparticles could be stabilized whereas another population could be forming aggregates. Figure 5.12 shows the plot of the results from the DLS experiments.

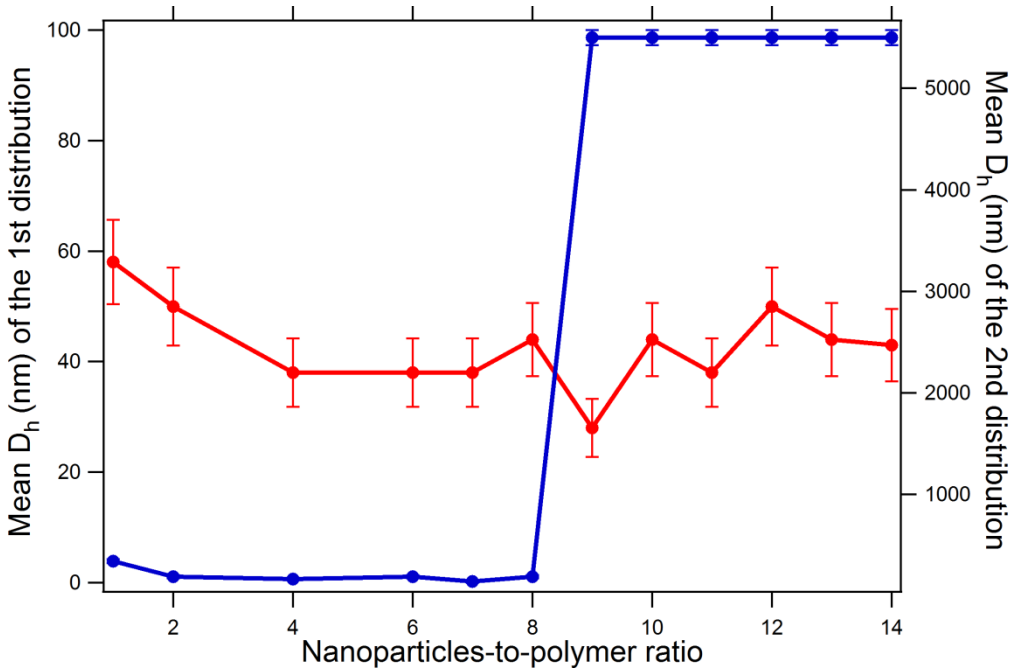

Figure 5.12. DLS results plot: The red curve represents the mean hydrodynamic diameter of the first distribution, with the values in the left axis. The blue curve corresponds to the mean hydrodynamic diameter of the second distribution, with the values in the right axis.

The DLS results showed that independently from the nanoparticles-to-polymer ratio, there was always a first size distribution attributed to small and stable nanoparticles, with a hydrodynamic diameter ranging from 30 to 60 nm approximately. On contrary, the bimodal analysis showed a significant difference between the samples with a nanoparticles-to-polymer ratio of 8 and below when compared to the samples with ratios of 9 and above. This second size distribution was attributed to major nanostructures formed by polymer and nanoparticles for the samples with ratios of 8 or below. The hydrodynamic diameter of these structures ranged from 140 nm to 250 nm. However, the second size distribution of the samples with a nanoparticles-to-polymer ratio of 9 and above showed a mean hydrodynamic diameter around 5500 nm, which was attributed to the sample aggregation. A control experiment performed with an aqueous solution of Fe_3O_4@Au nanoparticles without the amphiphilic star-

shaped block copolymer confirmed that the aggregates presented a hydrodynamic diameter around 5500 nm. Therefore, the DLS experiments demonstrated that the amphiphilic star-shaped block copolymer could completely stabilize in water the hydrophobic Fe_3O_4@Au nanoparticles with a nanoparticles-to-polymer ratio up to 8. The samples with a nanoparticles-to-polymer ratio of 9 and higher contained a stable population but also presented a non-stabilized distribution attributed to aggregated nanoparticles.

These results are in agreement with those obtained from the UV-Vis spectroscopy measurements, which are shown in Figure 5.13.

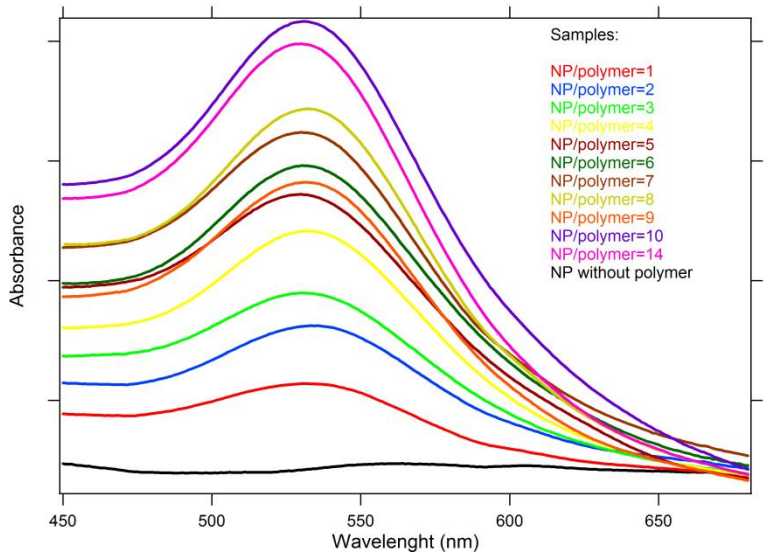

Figure 5.13. UV-Vis measurements of the samples containing the Fe_3O_4@Au nanoparticles and the amphiphilic star-shaped block copolymer with different nanoparticles-to-polymer ratios.

The SPR band of the Fe_3O_4@Au nanoparticles remained constant with the maximum absorption at 532 nm, independently from the nanoparticles-to-polymer ratio. This result suggests that the hydrophobic nanoparticles were stabilized without forming aggregates, which would provoke a red-shift in the SPR band due to particle intercoupling. The big aggregates did not show any SPR band, as it can be observed in the black curve that corresponds to the aqueous solution of hydrophobic nanoparticles without polymer.

5.3 Conclusions

In this chapter we have done a systematic study of the synthesis of core@shell Fe_3O_4@Au nanoparticles by a high temperature reaction using the Fe_3O_4 nanoparticles as seeds and gold (III) acetate as Au precursor. We have demonstrated that the Au:Fe_3O_4 ratio is a key parameter that should be optimized in order to obtain the maximum yield of Fe_3O_4@Au nanoparticles and to avoid tedious and time-consuming purification processes. In our study, for the Fe_3O_4 nanoparticles with a mean diameter of 7.5 nm, the optimized Au:Fe_3O_4 ratio was 3.7; when the reaction was performed with lower ratios we obtained both coated and uncoated Fe_3O_4 nanoparticles whereas when the reaction was performed with higher ratios we obtained a mixture of pure Au nanoparticles and Fe_3O_4@Au nanoparticles. With these results, we suggested an addition to the reaction mechanism proposed by Zhong and coworkers, in which the deposition of Au nanocolloids onto the surface of the Fe_3O_4 nanoparticles would be the slowest and limiting step, whereas the heterogeneous coalescence to form the final Au shell would be fast and irreversible. We demonstrated that the reaction temperature affects the Au shell thickness. When the reaction temperature increased above 230 ºC, we could observe a significant increase in the Au shell.

A hybrid nanomaterial was formed by the self-assembly of the hydrophobic Fe_3O_4@Au nanoparticles and the 4sPEG@6sPCL amphiphilic star-shaped block copolymer by the nanoprecipitation method. The encapsulation process was studied with DLS and UV-Vis spectroscopy and both techniques showed the superb solubilizing properties of the amphiphilic star-shaped block copolymer, which was able to stabilize the hydrophobic nanoparticles in aqueous solution in a nanoparticles-to-polymer ratio up to 8:1.

The structuring at the nanoscale permitted to stabilize in aqueous solution the Fe_3O_4@Au nanoparticles with the amphiphilic star-shaped block copolymer led to a multifunctional hybrid material, with magnetic attraction to an external magnetic field and a plasmonic band. The hybrid nanomaterial presented an enormous stability, without any visible signs of aggregation for more than a year.

6. RESULTS 3

Exploring the possibilities of the Silica coating

6.1 Introduction

Creating systems with multiple components that can be arranged in a certain manner is of great scientific interest[215]. The materials engineering at the nanoscale has advantages in diverse fields, from catalysis to fundamental physics. Regarding to biomedicine, the organized multicomponent systems are showing great potential for detection and diagnosis techniques[216] as well as for the improvement of the treatments with highly toxic drugs[217], reducing their side effects while enhancing their efficacy. The nanostructured materials had opened a field that for many authors represents the medicine of the future: theranostics[218], which consists in combining in one material a therapeutic compound and a diagnostic probe. Besides all the technical requirements that such materials would have to fulfill, the drug should remain encapsulated or inactive through all the diagnostic process, and be released or activated on demand through external stimuli. In addition, it would be desirable that the systems could be targeted to a specific organ or tissue[219].

For achieving all these properties in just one material, it is necessary to effectively control the organization of many components at the nanoscale. The surface functionalization is a critical step because it may largely determine the suitability of the system[220–222], as the surface components could target the nanoparticles to a specific organ[223], provide a special self-assembly[224], increase the lifetime in the bloodstream[225], etc. Nature provides the best demonstration about how important the surface functionalization is. For instance, the activity of each cell in the organism is highly dependent on the cell surface molecules. The rational design of advanced functional materials is frequently bioinspired in this way.

Systems based on liposomes and polymersomes have demonstrated to be very effective as nanocarriers for drug administration and release[226], but the possibilities of further surface functionalization are limited to few examples[227–229]. The inorganic coatings emerged as an alternative to the classic systems organic coatings[230] and in this field, silica coating has shown to be special[116,231]: Stöber contributed with the polymerization of silane monomers to produce uniform silica nanoparticles with a controllable diameter from around 100 nm to

several micrometers that could be easily functionalized in further steps[114]. The Stöber conditions involved a hydro-alcoholic media with ammonia and tetraethyl orthosilicate (TEOS) as silane monomer. This method can be used with nanoparticles to form a uniform silica coating with controllable thickness[232]. However, the formation of insoluble silica aggregates is a common drawback, and the tendency of silica to aggregate often leads to multicore nanoparticles within a silica shell. In addition, the polar reaction media can't be used to encapsulate hydrophobic nanoparticles. These problems could be overcome by the controlled polymerization of the silane monomers in a confined space like the water droplets of a reverse microemulsion[233]. With this alternative method it is possible to obtain silica nanoparticles that are colloidally stable in polar solvents (water, alcohols, DMF…) and that can be further functionalized by the well-established silica chemistry[234]. It has been demonstrated that this method also permits to encapsulate hydrophobic nanoparticles with a remarkable homogeneity and reproducibility within a single silica nanoparticle through a simple ligand exchange[235,236].

During the past decade, the silica coating of single hydrophobic nanoparticles via the reverse microemulsion method has been extensively investigated[237–240]. However, most of the previous work was focused on silica coating of nanoparticles of different sizes, with the aim of achieving a one-to-one coating of magnetic[241] and fluorescent nanoparticles[242]. More recently, the silica coating regulations were studied by Li and coworkers[243]. In this work, they studied the synthetic parameters that influenced the silica shell thickness for coating Fe_3O_4 nanoparticles with different core sizes. It was reported that the thickness of silica shells could be tuned by changing the amount of nanoparticles and TEOS, but the tuning was very limited and free-core silica or multi-core silica appeared frequently. The ratio between Igepal CO-520 and ammonia (w-coefficient) was a key parameter, since it determines the number and size of aqueous domain, which is crucial to a one-to-one matching of the number of core nanoparticles with that of aqueous domains. Li and coworkers reported that the match of the number of Fe_3O_4 nanoparticles and amount of surfactant is essential in realizing the one-to-one coating for nanoparticles with different sizes. According to these regulations, for a given w-coefficient and a given nanoparticle size, the

thickness of the silica shell increases as the amount of TEOS increases. In addition, they proposed a mechanism for the silica coating of hydrophobic nanoparticles based on a ligand exchange. On this basis, we deepen into the method with the aim of exploring its possibilities and its limitations.

In this chapter we explore this methodology to control the silica shell thickness, encapsulate organic compounds and/or nanoparticles, create core@shell nanostructures with different core nature, and to modify the surface of silica coated nanoparticles with different functionalities.

Herewith, we demonstrate that what makes this strategy really interesting is that is an open-source-like method that offers a high versatility: It makes possible to combine almost any nanoparticle, compound and surface functionalization. It is basically one method that permits to design materials engineered at the nanoscale for many different applications.

6.2 Results and discussion

6.2.1 Silica coating of inorganic nanoparticles: Control over the shell thickness

Following a previously published procedure[234], we started the silica coating of inorganic Fe_3O_4 nanoparticles. The highly monodisperse hydrophobic iron oxide nanoparticles were obtained by the thermal decomposition method[122]. The silica coating was performed by the basic hydrolysis of the silane precursor (TEOS) in a reverse microemulsion formed by hexane as continuous phase, aqueous ammonia as dispersed phase and IGEPAL CO520 as surfactant. It is important to note that there are several parameters that influence the silica shell thickness in this synthetic procedure[244,245], which are: i) the w-coefficient which is the water/IGEPAL ratio that must be matched with the number of nanoparticles; ii) the TEOS/nanoparticles ratio and iii) the reaction time. The nanoparticle size can also affect the silica shell thickness, but this parameter could be included in the TEOS/NPs ratio via the specific surface: smaller nanoparticles present higher specific surface available for ligand exchange, which would consume

more silica reagent and consequently reduce the TEOS/NPs ratio. Table 6.1 summarizes the influence of these parameters over the silica shell thickness obtained from the literature[234,240,246].

Table 6.1. Relation between the key parameters and the silica shell thickness

Parameter	If increased	If decreased	Cause
TEOS/NPs ratio	>Thickness	<Thickness	Quantity of reagent
Water/surfactant ratio (w)	>Thickness	<Thickness	Size of water droplets
Reaction time	>Thickness	<Thickness	Kinetic control of the reaction

As it was reported by Li and coworkers, it is necessary to match the quantity of nanoparticles with the w-coefficient to ensure a one-to-one coating. For a given w-coefficient and nanoparticle size, the thickness of the silica shell increases as the amount of TEOS increases. However, this strategy permits to tune the thickness in a very narrow range, from 5 to 8 nm. In our study, all attempts to tune the silica shell thickness by varying only one parameter failed. For example, the silica shell thickness could not be drastically reduced by only diminishing the w-coefficient. On the other hand, a vast increase in the w-coefficient could lead to the destabilization of the microemulsion rendering polydisperse samples (Figure 6.1A) instead of increasing the silica shell thickness. In addition, the thickness could not be increased by increasing too much the TEOS/Nanoparticles ratio. This resulted in the formation of many empty silica spheres of similar size as the core@shell ones (Figure 6.1B). On the other hand, the reduction of this parameter resulted in the formation of multi-core@shell nanoparticles, which compromised the homogeneity of the sample (Figure 6.1C).

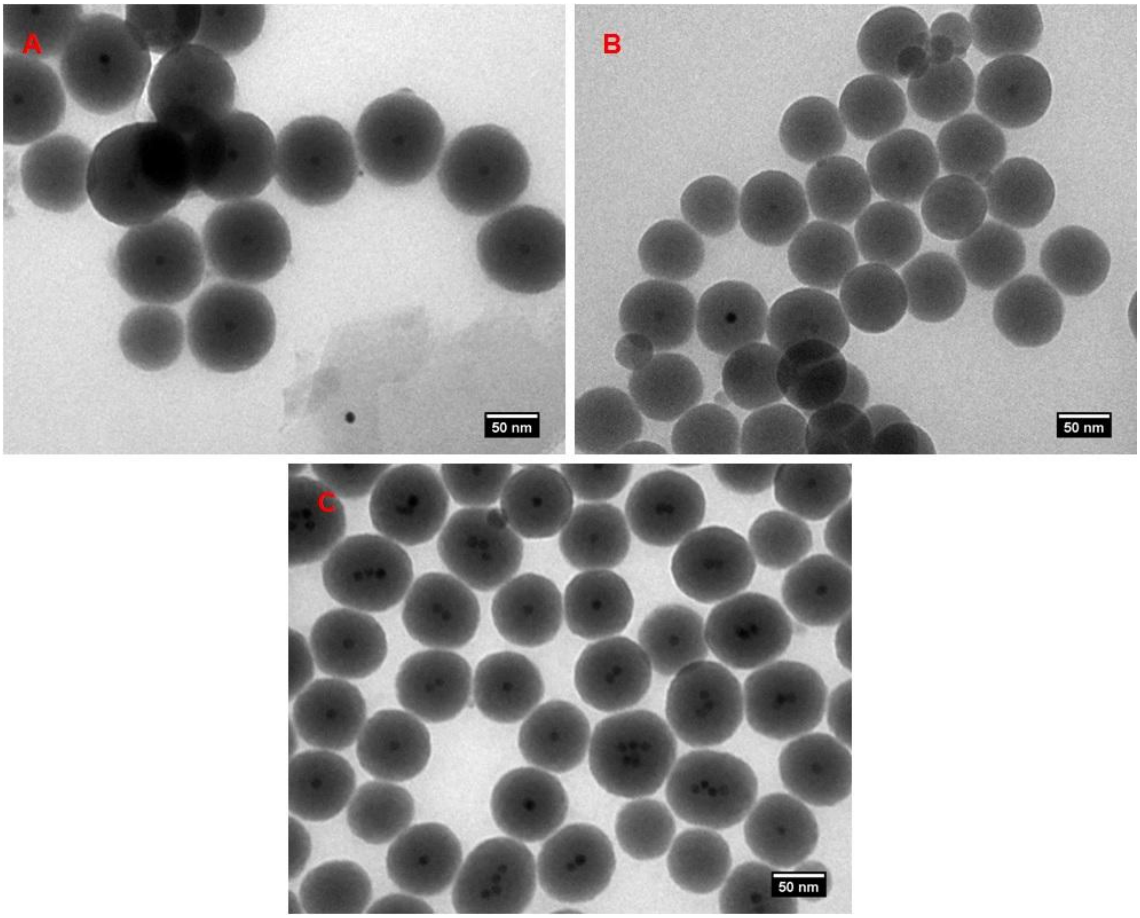

Figure 6.1. TEM micrographs of our attempts to control the silica shell thickness when coating Fe_3O_4 nanoparticles by changing only one parameter: a) increased w-coefficient, b) increased TEOS/NPs ratio and c) reduced TEOS/NPs ratio.

In contrast, we observed that by combining these parameters we can finely control the silica shell thickness over a wide range, from approximately 30 nm to <1 nm.

Table 6.2 shows the synthetic conditions for each synthesis of the silica shell control experiments, the obtained mean diameter of the core@shell nanoparticles and the silica shell thickness. The nanoparticles were analyzed by TEM micrographs: The mean total diameter was measured over 200 nanoparticles. The mean silica shell thickness was measured from the ending of the silica shell to the beginning of the magnetite core of the same particles. The diameter of the Fe_3O_4 nanoparticles was 7.5 nm.

Table 6.2. Synthetic conditions used in each experiment to obtain different silica shell thickness. (*) The silica shell thickness was too small to be accurately measured (< 0.5 nm).

Exp num	SPIONs 20 mg/mL (same size)	TEOS	IGEPAL CO520	Ammonia solution	Time	Result mean total diameter	Result mean silica shell thickness
1	10 µL	5 µL	240 mg	40 µL	3 h	16 nm	4 nm
2	10 µL	10 µL	240 mg	40 µL	3 h	20 nm	6.5 nm
3	10 µL	15 µL	240 mg	40 µL	3 h	20 nm	6 nm
4	10 µL	20 µL	240 mg	40 µL	3 h	22 nm	7 nm
5	10 µL	25 µL	240 mg	40 µL	3 h	23 nm	7.5 nm
6	10 µL	30 µL	240 mg	40 µL	3 h	25,5 nm	9 nm
7	10 µL	5 µL	240 mg	40 µL	1 h	8,5 nm	<0.5 nm*
8	10 µL	10 µL	240 mg	40 µL	1 h	16 nm	4.5 nm
9	10 µL	15 µL	240 mg	40 µL	1 h	14,5 nm	3.5 nm
10	10 µL	20 µL	240 mg	40 µL	1 h	16 nm	4 nm
11	10 µL	25 µL	240 mg	40 µL	1 h	18 nm	5 nm
12	10 µL	30 µL	240 mg	40 µL	1 h	20 nm	6 nm
13	10 µL	20 µL	240 mg	40 µL	24 h	55 nm	21 nm
14	10 µL	30 µL	340 mg	40 µL	24 h	82 nm	35 nm

Our experimental results demonstrated that the silica shell thickness could be tuned in a wide range, from 0.5 to 35 nm. In experiments 1 to 6 we maintain constant the w-coefficient, and the results are in concordance with the observations reported by Li and coworkers: for a constant w-coefficient and particle size, the shell thickness increased when the amount of TEOS increased. The experiments 7-12 demonstrated that, in addition to the w-coefficient, the reaction time also plays a role that would permit to finely tune the silica shell thickness with nanometric precision. These results have been plotted in Figure 6.2 and the volume of the silica shell thickness increases linearly with the amount of TEOS.

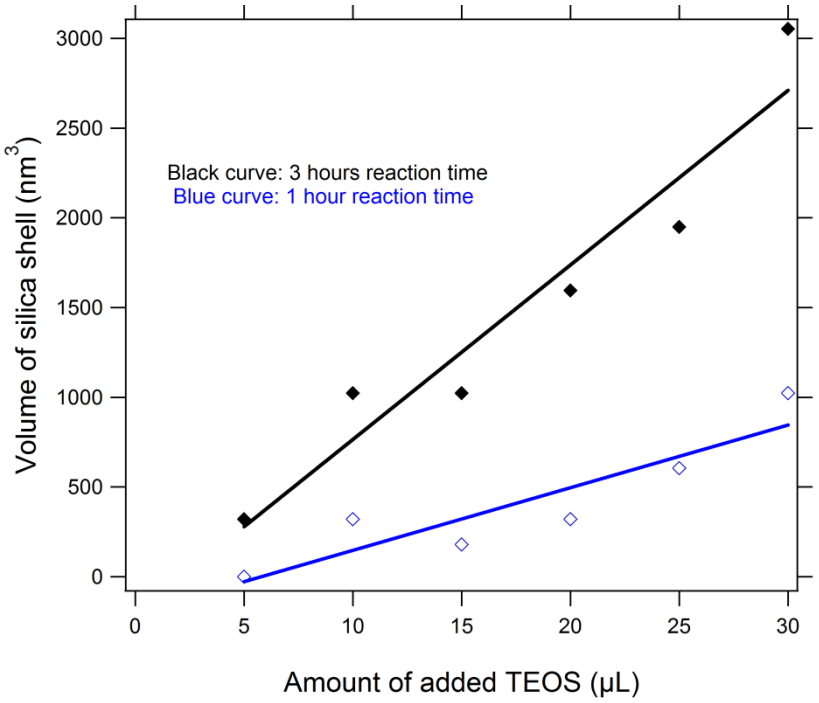

Figure 6.2. Representation of the silica shell volume increase as a function of the amount of added TEOS.

However, the reaction time showed a great importance for obtaining thicker silica shell thicknesses, as demonstrated with experiments 4, 10 and 13: with the same w-coefficient and TEOS/nanoparticles ratio, the variation of the reaction time permitted to tune the silica shell thickness from 4 to 21 nm. Reaction times above 24 hours did not produce any significant difference in the silica shell thickness, which would indicate that all silica precursors reacted. In addition, the increase of the TEOS above 30 µL produced the formation of silica aggregates. Therefore, the maximum silica shell thickness that we could obtain was 35 nm when TEOS was increased to 30 µL.

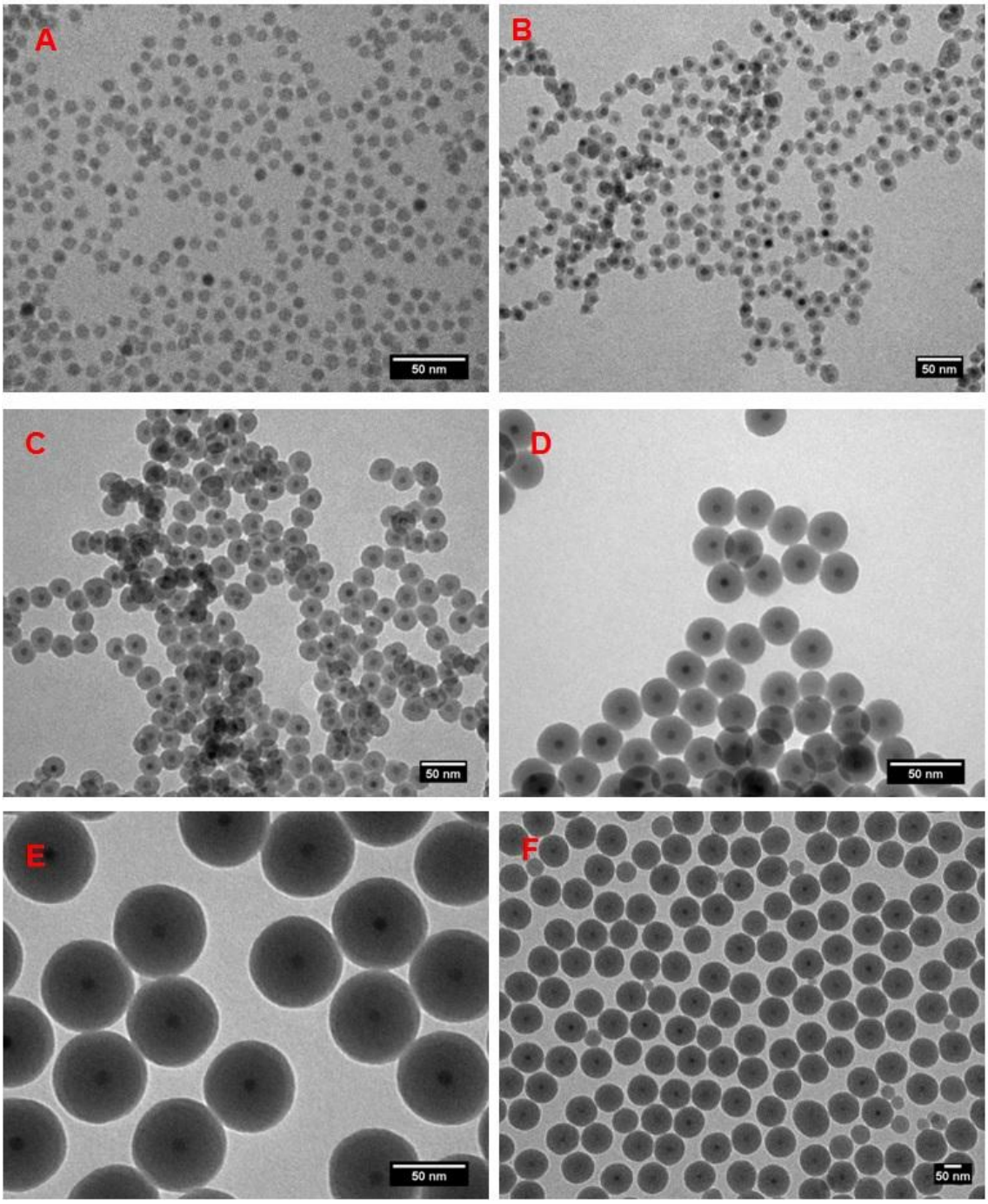

Figure 6.3. Representative TEM micrographs of the Fe_3O_4@SiO_2 nanoparticles with different shell thickness: a) less than 1 nm, b) 3.5 nm, c) 6 nm, d) 9 nm, e) 21 nm and f) 35 nm.

Figure 6.3 shows some representative TEM micrographs to summarize the silica shell control obtained by the combination of the key parameters as detailed in the previous table. These experiments demonstrated that it is possible to tune the silica shell thickness over a wide range, without

compromising neither the stability nor the homogeneity of the final nanoparticles. In addition, these parameters have been studied with highly monodisperse and individual Fe_3O_4 nanoparticles with approximately 7.5 nm of diameter and therefore the parameters may vary for other samples with different sizes and/or compositions. The method can be extended to different nanoparticles. For instance, hydrophobic upconversion nanoparticles were coated with silica to achieve a tunable shell thickness ranging from 3 to 19 nm, as shown in Figure 6.4.

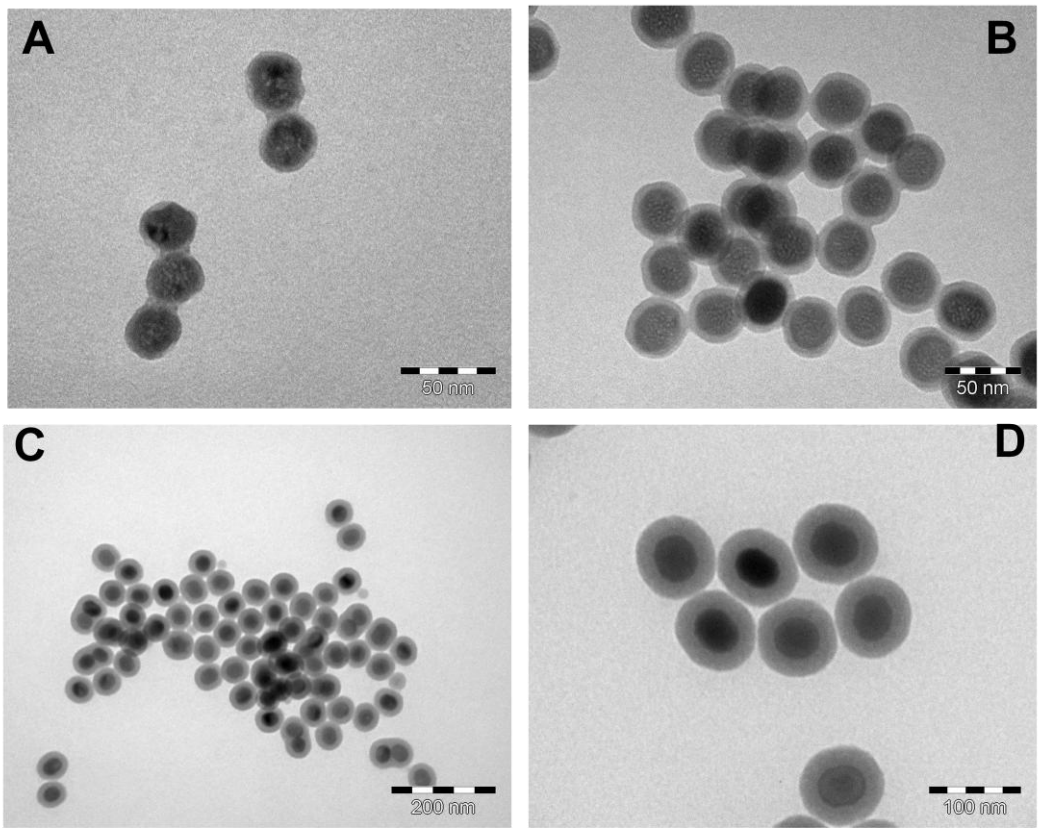

Figure 6.4. UCNPs@SiO_2 nanoparticles with different silica shell thickness: A) 3 nm B) 5 nm C) 11 nm and D) 19 nm.

To obtain the one-to-one coating, it was necessary to fix the quantity of upconversion nanoparticles to the w-coefficient and therefore in these reactions the volume of nanoparticles was increased to 500 µL of a 20 mg/mL solution in hexane.

6.2.2 Co-encapsulation of nanoparticles and molecules within the silica shell

The encapsulation of molecules within silica nanoparticles has received an important scientific attention[116,247,248].The silanization in a reverse microemulsion can be also used to co-encapsulate water soluble molecules within the silica shell. This fact opens a new possibility for the fabrication of hybrid materials combining into one an inorganic and an organic part, leading to an improved system with more properties than those constituted by only one component. The main restrictions are that the desired molecule must be totally soluble in the basic media of the aqueous phase and must not have surfactant activity, so that the microemulsion remains stable during the process.

The co-encapsulation process begins with the preparation of a concentrated solution of the aqueous soluble molecule in ammonia. Then, the process is similar to a typical synthesis and the microemulsion is formed with the molecule of interest in the aqueous phase. It is worth to mention that the process can be performed without previous inorganic nanoparticles, which would yield silica spheres encapsulating the molecules.

In this chapter we have studied the encapsulation of two different water soluble molecules within the silica shell. In both cases, the purification steps were realized carefully: After the synthesis, the dispersions of the nanoparticles were centrifuged and the supernatant was discarded. The pellet was redispersed in ethanol and cleaned in an ultrasound bath for 15 minutes to remove any physisorbed molecule in the surface of the nanoparticles. This process was repeated until the supernatant was completely transparent, to ensure that all the molecules in the final purified solution were encapsulated in the silica shell.

SiO_2@PTEBS:

PTEBS is a fluorescent water soluble π-π conjugated polymer based on poly(3-ethoxy-butyl-sulfonate-thiopehene-2,5-diyl). The fluorescent properties of this polymer and derivates has been extensively studied in our group[249,250] for sensing applications. In this chapter we have encapsulated PTEBS within silica nanoparticles as a proof of concept, in which we demonstrated that the

nanoparticles are fluorescent after the encapsulation process of the PTEBS, see Figure 6.5.

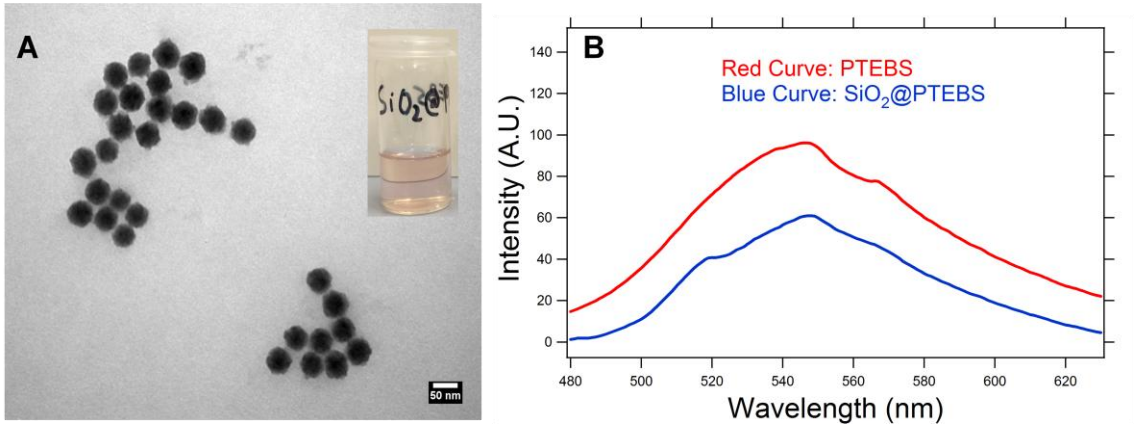

Figure 6.5. A) TEM micrograph of the SiO_2@PTEBS nanoparticles. Scale bar is 50 nm. The inset is a picture taken from the vial containing the nanoparticles. B) Photoluminescence of the original PTEBS polymer (red curve) and the PTEBS encapsulated in the silica nanoparticles (blue curve). The excitation wavelength was 420 nm.

In the TEM micrographs, the SiO_2@PTEBS nanoparticles showed a higher contrast and appeared darker than the normal SiO_2 nanoparticles synthesized in the same conditions, indicating that the PTEBS is effectively encapsulated in the nanoparticles. In addition, the TEM micrographs confirmed that the encapsulation of molecules within the silica did not significantly affect the size and shape of the final nanoparticles.

Fe_3O_4@SiO_2@Methylene Blue:

Methylene blue (MB) is a commonly used molecule in biomedicine for stain, cyanide poisoning and as a drug in the treatment of methemoglobinemia. Recent studies have also demonstrated that MB could be used as a photoactive compound in photodynamic therapy[251,252]. However, photodynamic therapy requires the accumulation of the photosensitizer in a specific location, and the high aqueous solubility of this molecule would lead to an enormous distribution of the drug. The encapsulation of MB in a confined space with magnetic properties would be an interesting approach to improve the photodynamic therapy. In this chapter we have prepared such nanosystem based on

Fe_3O_4@SiO_2@MB nanoparticles. The MB shows a characteristic blue color in aqueous solution, which is retained in the Fe_3O_4@SiO_2@MB nanoparticles, see Figure 6.6A. When the sample was exposed to an external magnetic field, after a short time the solution was transparent, and a blue precipitate was formed in the wall of the vessel near the magnet (Figure 6.6B).

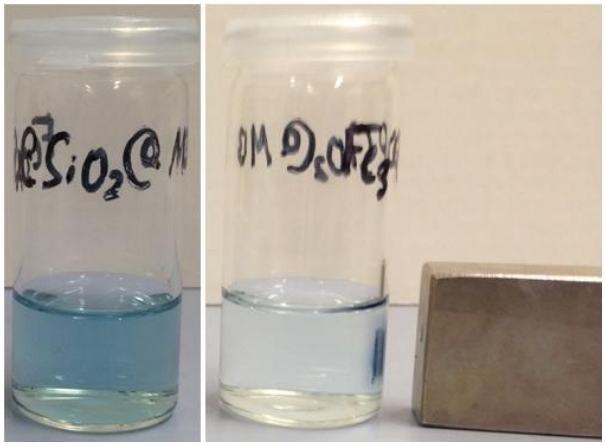

Figure 6.6. Left: Picture taken from the solution of Fe_3O_4@SiO_2@MB nanoparticles. Right: The same solution after being exposed to an external magnetic field of 0.4 T.

This experiment could also confirm that the methylene blue was effectively encapsulated within the Fe_3O_4@SiO_2 nanoparticles, and therefore the non-encapsulated MB was removed during the purification process.

In addition, we studied the drug loading capacity of MB in this process using UV-Vis spectroscopy. The drug loading capacity is defined as follows:

$$E_{eff} = \frac{mg(MB)}{mg(sample)} \times 100$$

Where mg(MB) is the weight of Methylene Blue in milligrams in the sample and the mg(sample) is the total weight of the sample. The mg(MB) value was obtained from UV-Vis measurements (Figure 6.7).

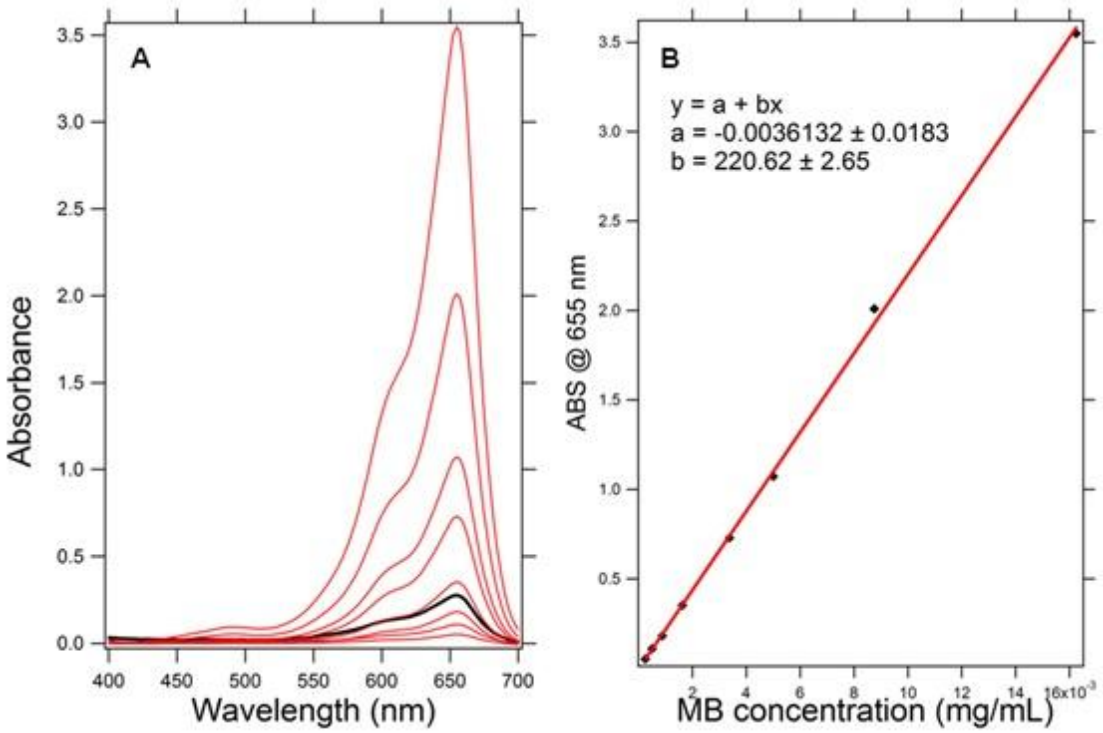

Figure 6.7. A) UV-Vis spectra of the known concentrations of methylene blue (red curves) and the UV-Vis spectrum of the Fe_3O_4@SiO_2@MB nanoparticles (black curve). B) Linear fit of the absorbance of MB at 655 nm versus MB concentration.

Figure 6.7A shows the UV-Vis spectra of MB solutions. In the experimental range of concentrations, the absorbance was directly proportional to the MB concentration as stated by the Beer-Lambert law. Figure 6.7B shows the calibration plot and the linear regression obtained experimentally for MB. Using this calibration we found that the concentration of encapsulated MB was $1.267 \cdot 10^{-3}$ mg/mL.

The total weight of the sample was calculated by weighing the solid residue after drying 1 mL of the Fe_3O_4@SiO_2@MB solution. The mean mg(sample) obtained from these experiments was 0.47 $\pm$ 0.04 mg. Subsequently, the drug loading capacity for MB within the Fe_3O_4@SiO_2 nanoparticles was calculated to be 0.269%.

6.2.3 Extension of the method: Tunable core in the silica shell

Monodisperse SiO_2 nanoparticles can be synthesized without using any previously synthesized nanoparticles or seeds[253]. Furthermore, this methodology can be also applied to different inorganic cores. In this chapter we have developed several syntheses of core@shell nanoparticles with different core nature. In all cases, hydrophobic inorganic nanoparticles with a homogeneous size distribution were prepared according to previously published procedures: Gold nanoparticles (AuNPs) and silver nanoparticles (AgNPs) were prepared in toluene with oleylamine as both reducing and capping agent[254]. Rare-earth doped β-$NaYF_4$ nanoparticles (UCNPs) were synthesized by thermal decomposition of the salt precursors in the presence of oleic acid, which acts as capping agent[92]. CdSe/ZnS alloys were used as Quantum dots (QDs) and were prepared following a previously published procedure[255] with oleic acid as capping agent. The Fe_3O_4 nanoparticles (SPIONs) were synthesized by thermal decomposition of the iron (III) oleate complex in the presence of oleic acid that acts as capping agent.

Koole and coworkers[236] proposed a possible reaction mechanism for the silanization reaction in a reverse microemulsion. In this work, the authors proposed a ligand exchange between the organic capping agent of the QDs and the activated -or hydrolyzed- silane precursor (TEOS), as depicted in Figure 6.8.

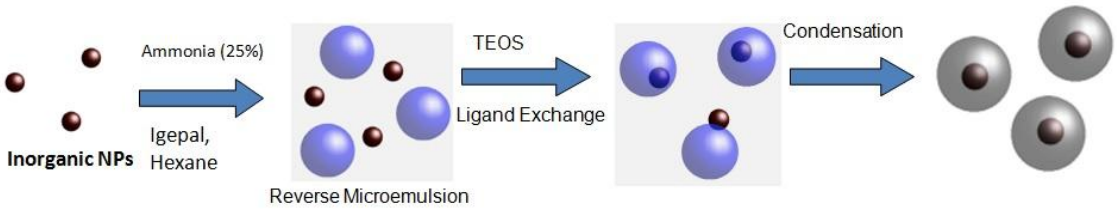

Figure 6.8 Schematic representation of the mechanism involved in the silica coating of inorganic nanoparticles. 1) Ligand exchange between the capping agents of the nanoparticles with Igepal and/or TEOS. 2) Phase transfer of the nanoparticle into the aqueous domain. 3) Condensation of the silica to form the final core@shell nanoparticles.

This ligand exchange rate and yield would be determined by the affinity between the nanoparticle surface with the leaving ligand and the hydrolyzed TEOS. Therefore, strongly bound capping agents would be harder to exchange than the weakly bound ones. This parameter depends on the nature of the capping agent and the nature of the inorganic nanoparticle. Oleic acid (as model of the carboxylic acids with a long hydrocarbon chain) is generally considered as a weakly bound capping agent, whereas oleylamine (model of the primary amines with a long hydrocarbon chain) is known to bind strongly to the surface of the nanoparticles. The thiolated capping agents are usually considered as the strongest for bonding with the nanoparticles, especially with metal nanoparticles[197,256]. In this chapter we have used oleic acid-coated and oleylamine-coated nanoparticles for the silica coating in a reverse microemulsion. The synthetic conditions were similar for all the syntheses, and the conditions for obtaining the Fe_3O_4@SiO_2 nanoparticles were considered as reference. The concentration of nanoparticles was calculated for each sample considering the different size and density of the nanoparticles, so that the TEOS/NPs ratio was constant between the different samples.

Figure 6.9 shows the TEM micrographs of the different inorganic nanoparticles that were coated with a silica shell by the reverse microemulsion method.

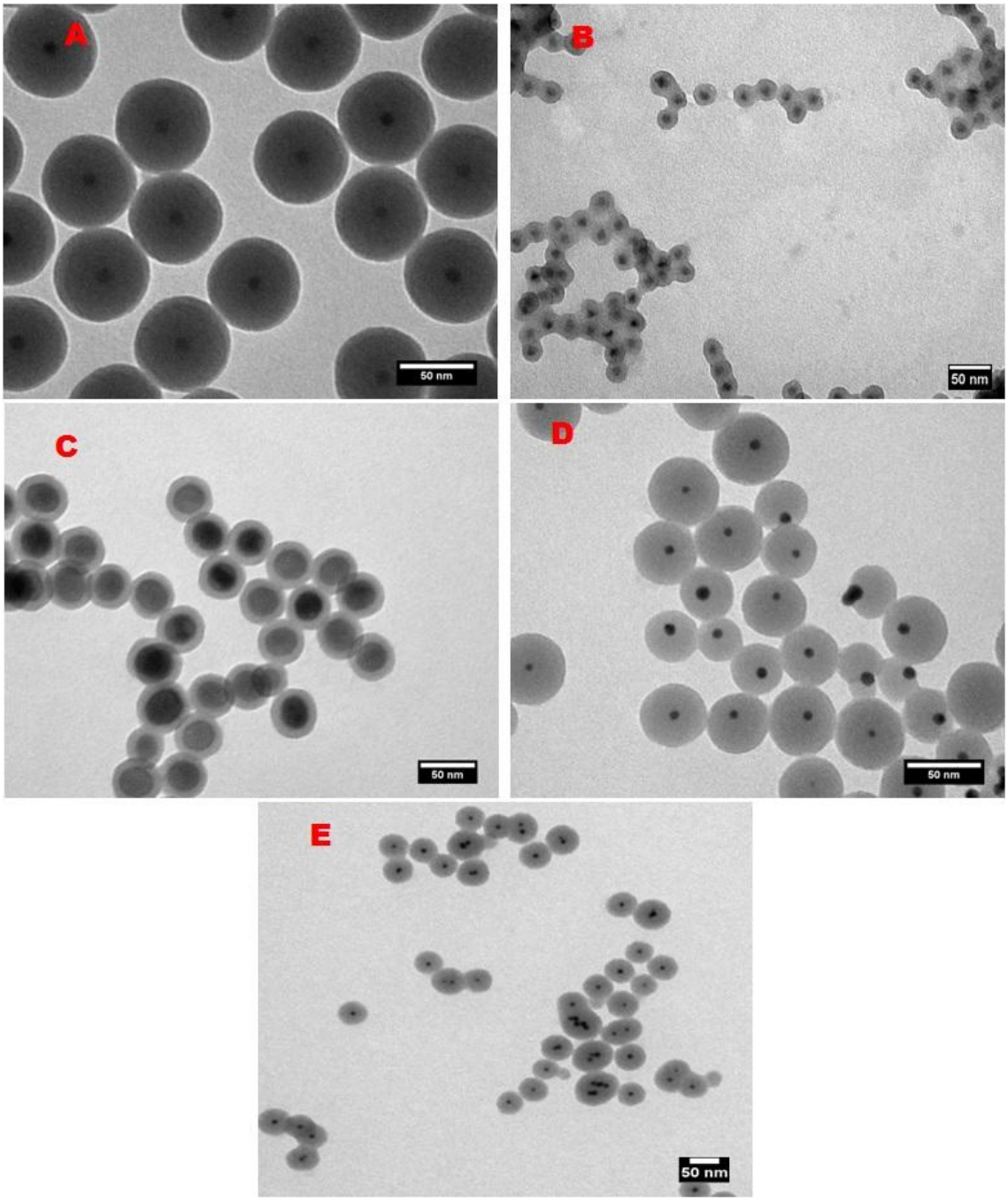

Figure 6.9. TEM micrographs of A) Fe_3O_4@SiO_2 B) CdSe/ZnS@SiO_2, C) $NaYF_4$:Yb,Er@SiO_2, D) Ag@SiO_2 and E) Au@SiO_2 nanoparticles. Scale bars are 50 nm.

These results demonstrated that the methodology could be applied for different kind of materials like iron oxide, quantum dots, upconversion, gold and silver nanoparticles. Despite some modifications in the synthetic parameters, such as matching the number of nanoparticles to the w-coefficient, our experiments revealed that this methodology was independent from the nature of the

nanoparticles, which confirmed that the mechanism would be related with the ligand exchange between the reagents and the capping agents of the nanoparticles. We observed that the yield was higher when the nanoparticles were coated with oleic acid (SPIONs, UCNPs and QDs). The TEM micrographs (Figure 6.9A-C) showed that the nanoparticles were homogeneously coated (the nanoparticle was in the middle of the silica shell) and also the quantity of multi-core nanoparticles was negligible. On the contrary, when the nanoparticles were coated with oleylamine (AuNPs and AgNPs) the TEM micrographs (Figure 6.9D-E) showed that the nanoparticles were less homogeneously coated by silica and also there are more multi-core nanoparticles. Theoretically, the yield of $Au@SiO_2$ and $Ag@SiO_2$ nanoparticles could be increased by changing the capping agent. However, all our attempts to produce oleic acid-capped AuNPs and AgNPs failed.

The silica coating of the inorganic nanoparticles provided aqueous solubility to the system without altering the properties of the inner material. In the previous section it was demonstrated that the silica coated iron oxide nanoparticles were still magnetically attracted by an external magnetic field. The optical properties of the fluorescent QDs and UCNPs nanoparticles as well as of the plasmonic Au and Ag nanoparticles were not affected by the silica shell, see Figures 6.10 and 6.11, respectively.

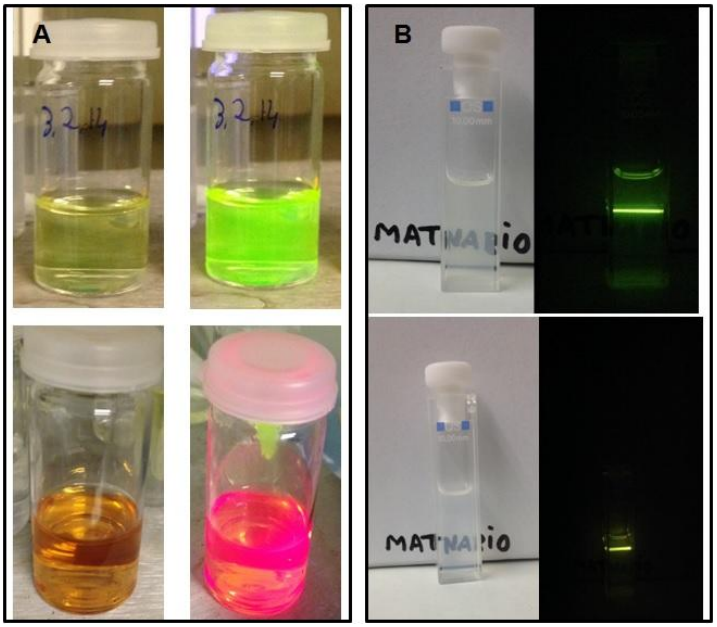

Figure 6.10. A) Pictures taken from green and red QDs@SiO_2 solutions in the absence (left) and under UV illumination (right). B) Pictures taken under room illumination (left) and under a CW 980 nm laser radiation without room light (right) from UCNPs in hexane (upper row) UCNPs@SiO_2 in ethanol (lower row).

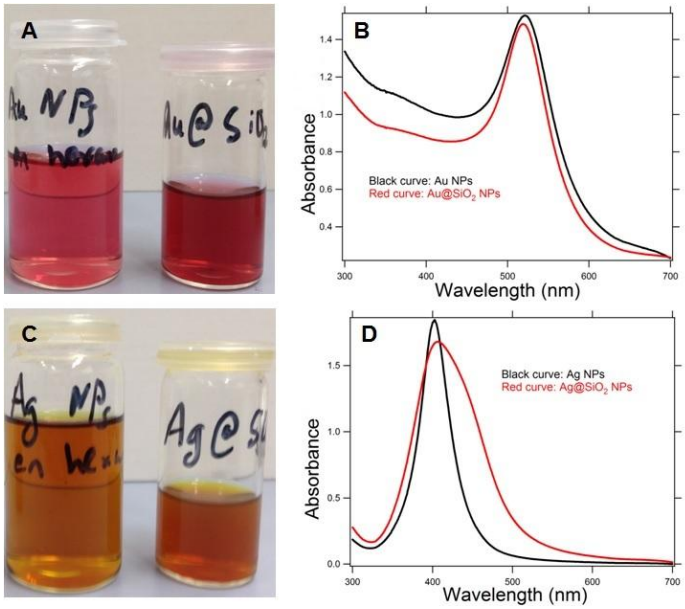

Figure 6.11. A) Dispersion of Au NPs in hexane (left) and Au@SiO_2 in ethanol (right). B) UV-Vis spectra of the Au NPs (black curve) and Au@SiO_2 nanoparticles (red curve). C) Dispersion of Ag NPs in hexane (left) and Ag@SiO_2 in ethanol (right). D) UV-Vis spectra of the Ag NPs (black curve) and Ag@SiO_2 nanoparticles (red curve).

In Figure 6.10A one can observe that the CdSe/ZnS@SiO_2 nanoparticles remained fluorescent under excitation with a UV lamp. Therefore, the Quantum Dots (both green and red QDs) were successfully transferred to aqueous solution without altering the fluorescence properties. In Figure 6.10B it is shown that the $NaYF_4$:Yb,Er@SiO_2 nanoparticles presented the upconversion fluorescence under excitation with a CW 980 nm laser, in the same way that the original nanoparticles dispersed in hexane did. In Figure 6.11 one can observe that the Au@SiO_2 and Ag@SiO_2 nanoparticles presented a similar UV-Vis spectrum profile as the original nanoparticles.

6.2.4 Surface functionalization on the silica shell

An important advantage of having inorganic nanoparticles coated with silica is that this cover can be easily functionalized[257,258]. In this chapter we have already demonstrated that the silica shell can be used to encapsulate different molecules. Another possibility is that the silica shell can be easily functionalized, which permits to attach molecules that can bind drugs, enzymes, biopolymers, etc. Thus, the polymerization of the silane precursor in basic media leads to nanoparticles with a negatively charged surface (Si-O^-). The functionalization pathway often starts with the reaction of a functionalized silane monomer which acts as an end group in the polymerization[259,260]. This well established protocol for the addition of a monolayer can be carried out in “one-pot”, together with the reverse microemulsion. However, the results are not always reproducible.

For the above reason we proceeded with the surface functionalization always after the purification of the core@shell nanoparticles. Figure 6.12 shows the chemical structure of several silane precursors. The tetraethyl orthosilicate (TEOS) has four good leaving groups and therefore can be further polymerized. On the contrary, (3-aminopropyl)triethoxysilane (APTES) and the other functionalized silane precursors, GPS and MPS, possesses a functionalization in a bad leaving group that remain within the structure and avoids further polymerization of silane monomers. Therefore, these molecules can be incorporated in the surface of the silica nanoparticles as monolayers.

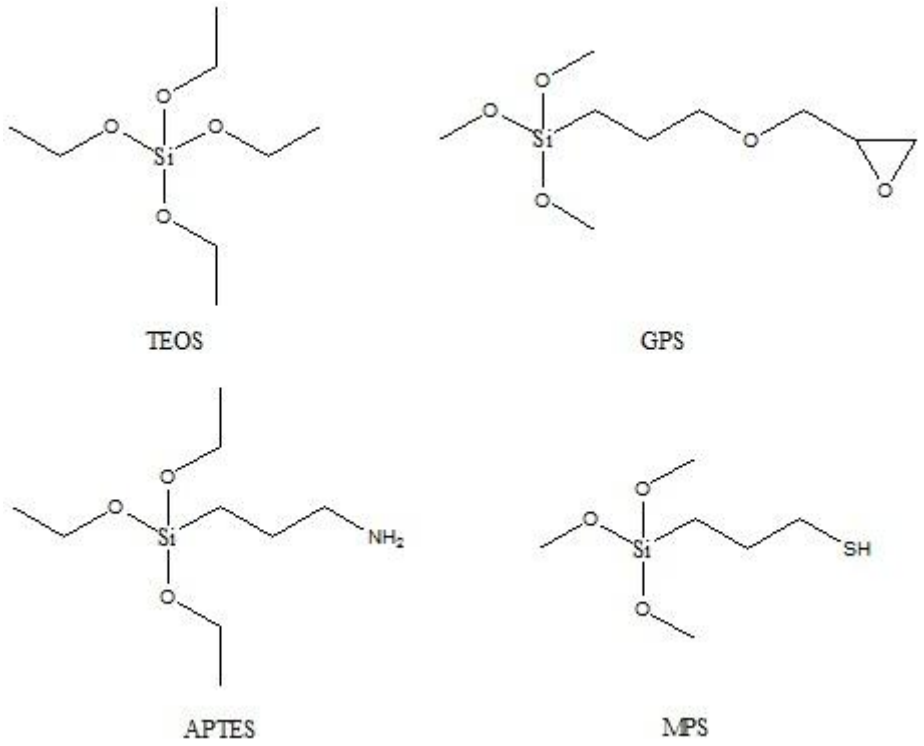

Figure 6.12. Chemical structures of commercially available silane reagents: tetraethyl orthosilicate (TEOS), (3-glycidyloxypropyl)trimethoxysilane (GPS), (3-aminopropyl)triethoxysilane (APTES) and (3-mercaptopropyl)trimethoxysilane (MPS).

Figure 6.12 shows the most used silane reagents in nanoparticle synthesis, but it is important to note that there are hundreds of commercially available monomers with different functional groups that can be used in a similar way. The surface functionalization with these silane reagents can be directly performed in a suitable solvent for the nanoparticles, for the reagent and if possible for the functionalized nanoparticles. The selected solvent for this first step was ethanol, in which the nanoparticles and an excess of functional silane reagent were mixed and stirred overnight at room temperature. The functionalized particles were purified by centrifugation (8500 rpm 10 minutes) and the supernatant containing the unreacted silane reagent was discarded. The functionalization could be determined by Z-potential measurements and FTIR spectroscopy, as shown in Figure 6.13.

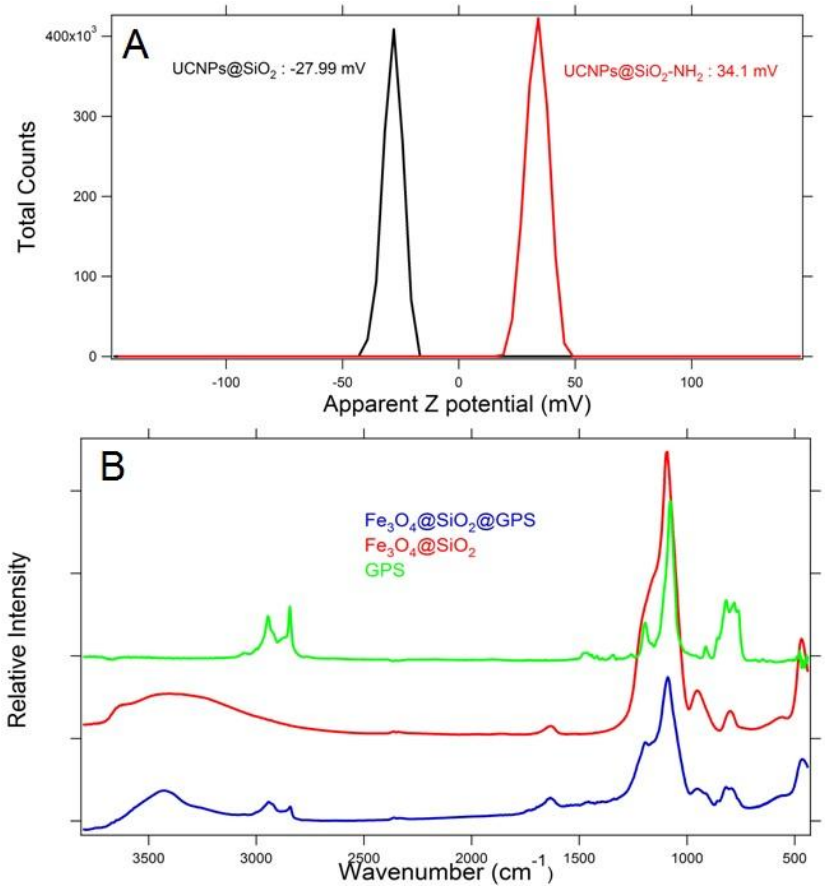

Figure 6.13. A) Z-potential measurements of UCNPs@SiO_2 nanoparticles (black curve) and amino-functionalized UCNPs@SiO_2 nanoparticles (red curve). B) FTIR spectra of Fe_3O_4@SiO_2 nanoparticles (red curve) and epoxy-functionalized Fe_3O_4@SiO_2 nanoparticles (blue curve). The green curve is the FTIR spectrum of the GPS silane reagent, measured as control.

This first functionalization step provides functional groups (amino, mercapto, epoxy, vinyl…) in the surface of the silanized nanoparticles. However, the engineering of advance functional materials often require the attachment of complex molecules such as vitamins, polymers, enzymes, antibodies, DNA, drugs… etc. This can be realized by exploiting highly selective reactions between the functional groups in the surface of the nanoparticles and the functional groups in the molecule to be attached. It is important to note that there is not just one reaction to anchor any molecule to the surface of the nanoparticles, and therefore the synthetic pathway must be carefully designed taking into consideration many parameters: stability of the molecule in different reaction conditions, functional groups available and specificity of the reaction,

expected yield, etc. In addition, the chemical reactions that can be performed at room temperature are preferable for the stability of the silanized nanoparticles. Among others, EDC coupling and “click” chemistry have been demonstrated as very useful pathways to attach biomolecules to different surfaces. Both reactions are very specific and can be carried out in aqueous solution at room temperature, which avoids the denaturation of proteins and the destabilization of the nanoparticles. In this section we have used these reactions to attach different molecules such as DNA, folic acid, polyethylene glycol (PEG) and doxorubicin.

6.2.5 Covalent binding of biomolecules to the functionalized silica surface

Below we will show several examples of covalent attachment of biomolecules to silica coated nanoparticles.

DNA:

Deoxyribonucleic acid is a biopolymer that self-assembles in a unique manner according to the base pairing rules. This characteristic makes the DNA as an ideal candidate for many biomedical applications. In this chapter we have studied the DNA attachment to silanized upconversion nanoparticles for sensing applications. Monodisperse $NaYF_4$:Yb(20%),Er(2%) (UCNPs) were coated with a SiO_2 shell by the reverse microemulsion method[261]. The surface of the nanoparticles was functionalized first with amino groups by the reaction with APTES (30 µL) in 5 mL of ethanol. After the purification steps, succinic anhydride (200 mg) and the amino-functionalized UCNPs@SiO_2 nanoparticles were mixed in 8 mL of DMF, which yielded carboxylic acid-functionalized UCNPs@SiO_2 nanoparticles. The functionalization steps were confirmed by Z-potential measurements (see Figure 6.14).

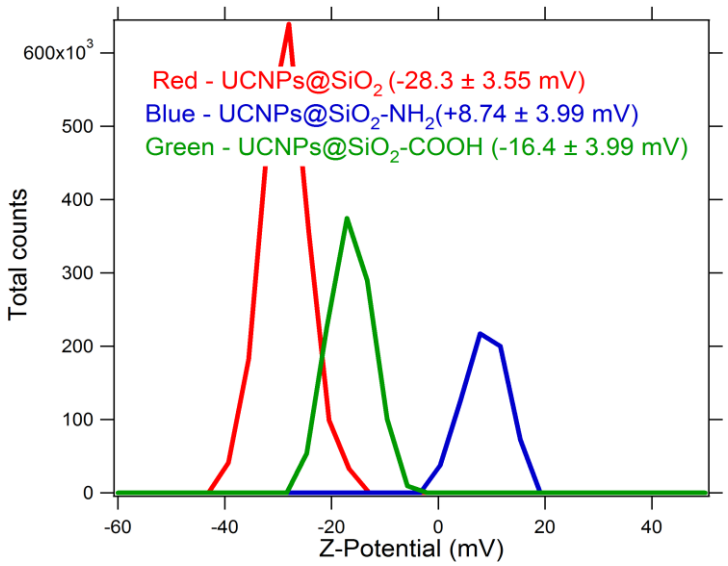

Figure 6.14. Z-potential measurements of the surface-functionalized upconversion nanoparticles: UCNPs@SiO2 nanoparticles (red curve); UCNPs@SiO2-NH2 nanoparticles (blue curve); and UCNPs@SiO2-COOH nanoparticles (green curve).

The single strand DNA oligomers were synthesized with a hexylamine residue in 5' and a fluorescent dye (Cy3) in 3'. The attachment of this DNA chains to the surface of the nanoparticles was performed by the coupling reaction catalyzed by 1-ethyl-3-(3-dimethylaminopropyl)carbodiimide (EDC) between the carboxylic acid groups in the nanoparticles and the amine groups of the DNA oligomers. The reaction was performed in a borate buffer solution (BBS) to prevent the denaturation of the DNA. The coupling reaction was performed by mixing 2 mL of the carboxylic acid-functionalized UCNPs@SiO_2 nanoparticles (1.82 mg/mL), 20 µL of EDC (0.3 M in BBS) and 40 µL of Sulfo-NHS (0.3 M in BBS). This mixture was shaken for 5 minutes, and then the aqueous solution of DNA oligomers (30 µL, 220.65 µM) was added. The reaction was stirred overnight and the DNA-functionalized nanoparticles were purified by centrifugation at 16400 rpm for 20 minutes and redispersed in PBS solution. The purification was repeated twice. The presence of the DNA within the nanoparticles was determined by the fluorescence of the Cy3 dye in the 3' end of the DNA branches (Figure 6.15).

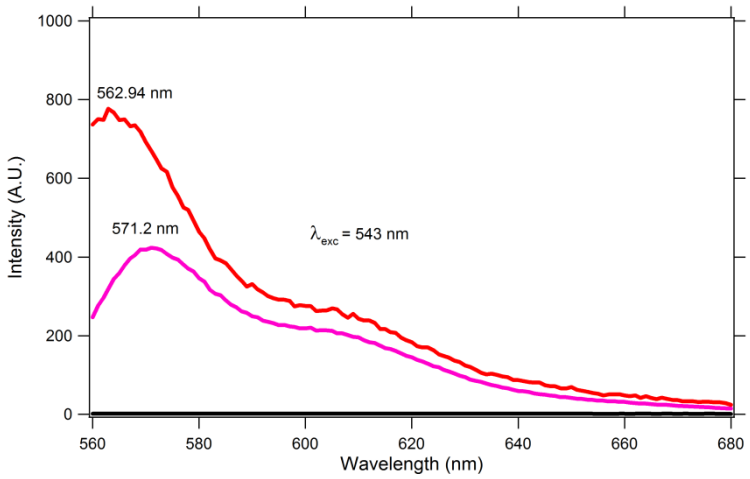

Figure 6.15: Fluorescence spectra obtained from the solutions containing: the DNA-Cy3-functionalized UCNPs@SiO_2 nanoparticles (red curve), the supernatant of the reaction containing the non-anchored DNA-Cy3 (pink curve), and UCNPs@SiO_2 nanoparticles without DNA-Cy3 functionalization (black curve). The excitation wavelength was 543 nm.

This measurement stated the presence of the Cy3 within the nanoparticles after all the centrifugation and redispersion steps, including the exposition to an ultrasound bath. This result indicated that the EDC coupling reaction was effective and therefore the DNA oligomers were covalently attached to the surface of the nanoparticles.

FOLIC ACID:

Folic acid is a very important biomolecule, also referred as vitamin B_9 or vitamin M. This molecule is crucial for the cell growth and it is believed that cancer cells and tissues over-express folate receptors[262]. In this section we performed the covalent attachment of folic acid molecules onto the surface of silanized upconversion nanoparticles with a very high yield, which could serve as a targeting ligand towards tumoral tissues. Monodisperse $NaYF_4$:Yb(20%),Er(2%) (UCNPs) were coated with a SiO_2 shell by the reverse microemulsion method. The surface of the nanoparticles was functionalized first with amino groups by the reaction with APTES (30 µL) in 5 mL of ethanol. The folic acid was anchored to the surface by the EDC coupling reaction in DMF: 0.3 mg of EDC and 0.6 mg of Sulfo-NHS were dissolved with an excess of folic acid (200 mg) in 10 mL of DMF. Next, 5 mL of a DMF solution containing 2 mg of amino-

functionalized UCNPs@SiO_2 nanoparticles were added dropwise. The EDC coupling reaction would yield amide groups formed between the amino groups of the nanoparticles and the carboxylic groups of the folic acid. The mixture was stirred at room temperature overnight, and the folic acid-functionalized nanoparticles were purified by centrifugation at 10.500 rpm 20 minutes. The supernatant containing the excess of folic acid, reagents and reaction by-products was discarded. The yellow pellet was redispersed with ethanol and the sample was exposed to an ultrasound bath for 5 minutes to release any physically absorbed molecules in the surface of the nanoparticles. This process was repeated three times, until a clean and transparent supernatant was obtained. The yellow-colored pellet suggested the presence of folic acid with the nanoparticles, which was quantified using UV-Vis spectroscopy (see Figure 6.16)

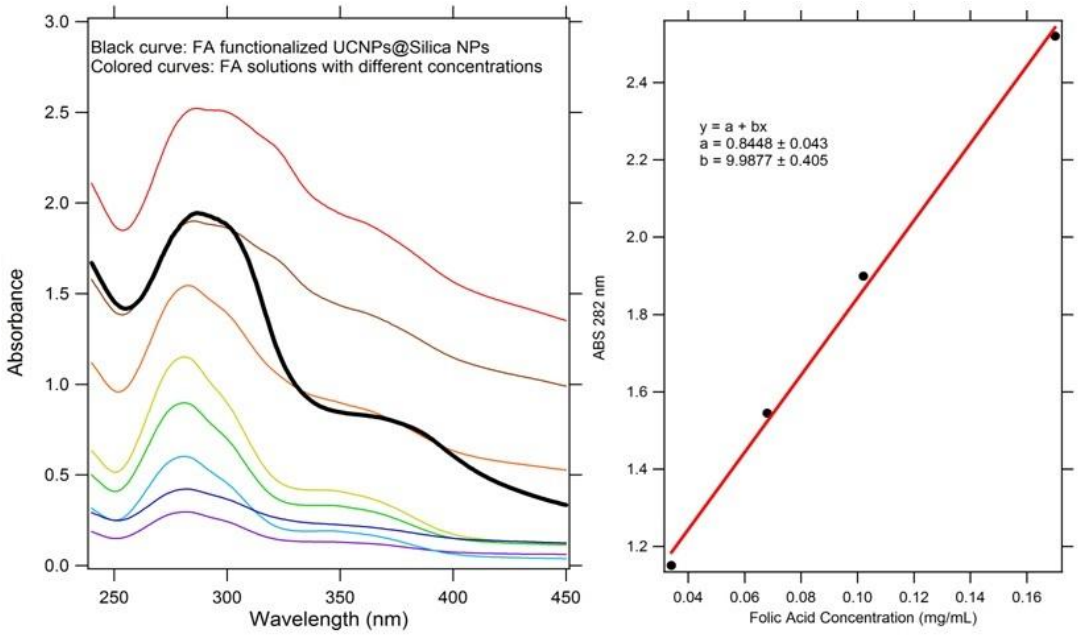

Figure 6.16: Left: UV-Vis measurements of the folic acid solutions at different known concentrations (from 0.006 to 0.17 mg/mL) and the curve obtained with the folic acid-functionalized UCNPs@SiO_2 nanoparticles (black curve). Right: Representation of the absorption value at 282 nm versus the folic acid concentration ranging from 0.04 to 0.17 mg/mL.

The representation of the absorption at 282 nm against the concentration of folic acid rendered a linear calibration curve between 0.04 and 0.17 mg/mL of

folic acid. The folic acid concentration in the sample with nanoparticles was calculated to be 0.11 mg/mL. The percentage of folic acid within the nanoparticles was 5.5%, which is a very high value for this kind of nanosystem[263].

PEG:

Polyethylene glycol is a commercially available aqueous soluble polymer that is present in several applications[264]. Regarding to biomedicine, PEG is the most used polymer due to its characteristics: it is generally recognized as biocompatible and non toxic; it is known for providing stealth properties to nanomaterials against the reticulo-endothelial system (RES) that increases their lifetime in bloodstream; and it is used for exploiting the enhanced permeability and retention effect (EPR) in tumors. In this section we have successfully attached PEG chains to silanized $NaYF_4$:Yb,Tm nanoparticles by EDC coupling: Methoxypolyethylene glycol carboxylic acid (25 mg, $5 \cdot 10^{-3}$ mmol) was dissolved in 5 mL of a PBS solution (0.1 M sodium phosphate, NaCl, 0.15 M, pH 7.3) prior to the addition of an EDC solution in PBS (100 µL, 0.2 M) and Sulfo-NHS (200 µL, 0.2M). This mixture was stirred for 10 min. After that, 5 mL of a PBS solution containing 25 mg of amino-functionalized $NaYF_4$:Yb,Tm@SiO_2 nanoparticles were added. The reaction mixture was stirred overnight at room temperature. The PEG-functionalized $NaYF_4$:Yb,Tm@SiO_2 nanoparticles were purified by centrifugation (10.000 rpm, 20 minutes) three times. The Figure 6.17 depicts the FTIR spectra of $NaYF_4$:Yb,Tm (dotted line) $NaYF_4$:Yb,Tm@SiO_2 (blue line) and $NaYF_4$:Yb,Tm@SiO_2-PEG (red line) nanoparticles.

The FTIR spectrum of the pristine $NaYF_4$:Yb,Tm nanoparticles presented the characteristic bands between 2900 and 2700 cm^{-1} due to existence of CH_2 and CH_3 groups and two bands at 1558 and 1403 cm_{-1}, which corresponded to the asymmetric and symmetric stretching vibration of the COO^- groups, respectively. These bands were attributed to the presence of oleic acid as capping agent on the surface of the nanoparticles. After coating the $NaYF_4$:Yb,Tm nanoparticles. After coating the nanoparticles with SiO_2 the spectrum showed the characteristic absorption peaks of silica located at 1100, 935, and 750 cm^{-1}, which were attributed to the stretching of Si-OH

groups and the symmetric stretching of the Si-O-Si groups, respectively. After grafting the PEG chains, the FTIR spectrum of these nanoparticles depicted new bands located at 1452, 1344, 1259, 960, and 840 cm^{-1} as well as an increment of the intensity of those bands localized between 3000 and 2800 cm^{-1}, which were attributed to the presence of the PEG chains.

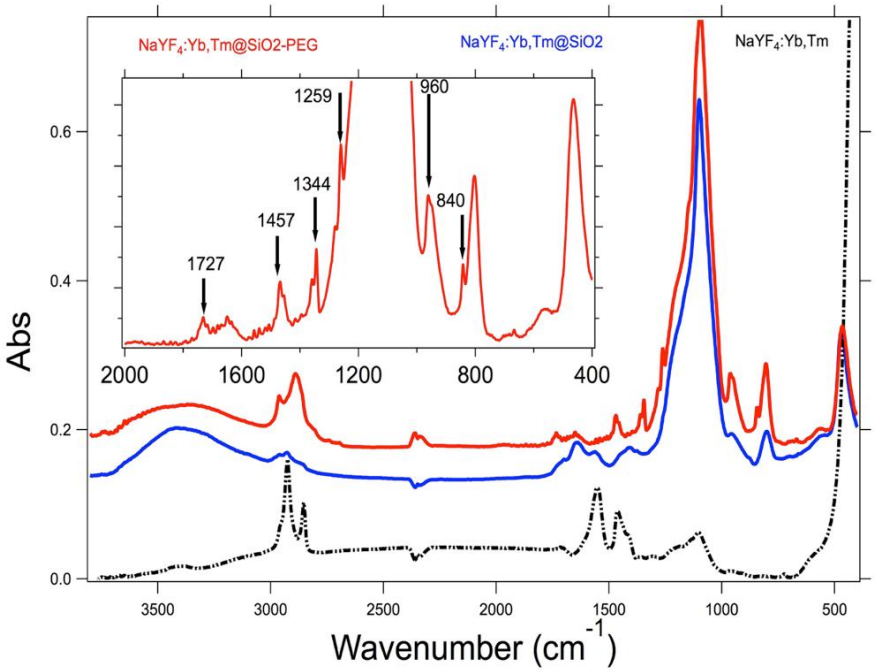

Figure 6.17. FTIR spectra of $NaYF_4$:Yb,Tm (dotted black line), $NaYF_4$:Yb,Tm@SiO_2 (blue line) and $NaYF_4$:Yb,Tm@SiO_2-PEG (red line). The inset depicts a magnification of $NaYF_4$:Yb,Tm@SiO_2-PEG spectra in the region comprised between 2000 and 400 cm^{-1}.

These results indicated that the PEG chains were present with the nanoparticles after all the purification steps. In addition, the colloidal dispersion in water of the PEG-functionalized $NaYF_4$:Yb,Tm@SiO_2 nanoparticles showed more stability when compared to the colloidal dispersion in water of amino-modified $NaYF_4$:Yb,Tm@SiO_2 nanoparticles.

DOXORUBICIN:

Doxorubicin (Dox) is a drug used in anticancer chemotherapy. The chemical structure is an anthracycline (see Figure 6.18) that works by intercalating DNA.

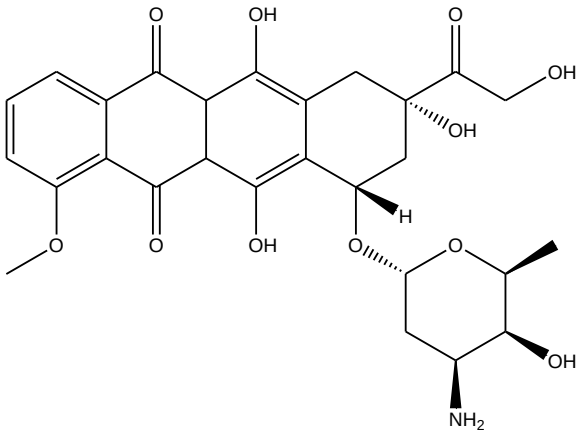

Figure 6.18: Chemical structure of doxorubicin.

The therapy with Dox is usually related with severe side effects and therefore it would be desirable to localize the drug specifically in tumoral tissues, which is commonly known as drug targeting. The majority of the scientific efforts to achieve this targeting have been focused into the EPR effect[265], tumoral pH[266] or oxygen differences[267] for the activation or deactivation of a prodrug, and specific targeting through the use of cell markers or antibodies[268–270]. Alternatively, externally stimuli responsive systems are emerging as another option for localizing the effect of a drug[271–273]. We have developed a photoresponsive material that was loaded with Dox. When the system was exposed to the light stimulus, the drug was released. For this, $NaYF_4$:Yb,Tm@SiO_2 nanoparticles were synthesized and the surface was functionalized with PEG and a photoresponsive molecule (*o*-NBA) that was conveniently modified, see Figure 6.19. The *o*-NBA derivative was attached to the surface of the nanoparticles by the EDC coupling reaction between the amino groups in the surface of the nanoparticles and the carboxylic acid of the photoresponsive molecules in DMF.

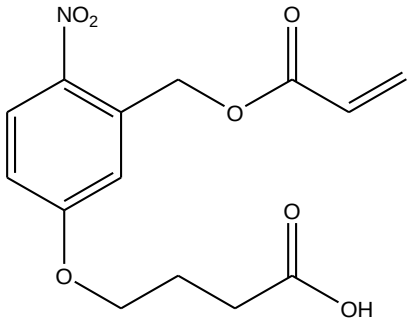

Figure 6.19. 4-(3-(acryloyloxymethyl)-4-nitrophenoxy)butanoic acid. Structure of the modified *ortho*-nitrobencylalcohol photoresponsive molecule.

The presence of the *o*-NBA derivate in the nanoparticles was demonstrated with UV-Vis spectroscopy. As shown in Figure 6.20, the maximum at about 320 nm corresponds to the *o*-NBA derivate.

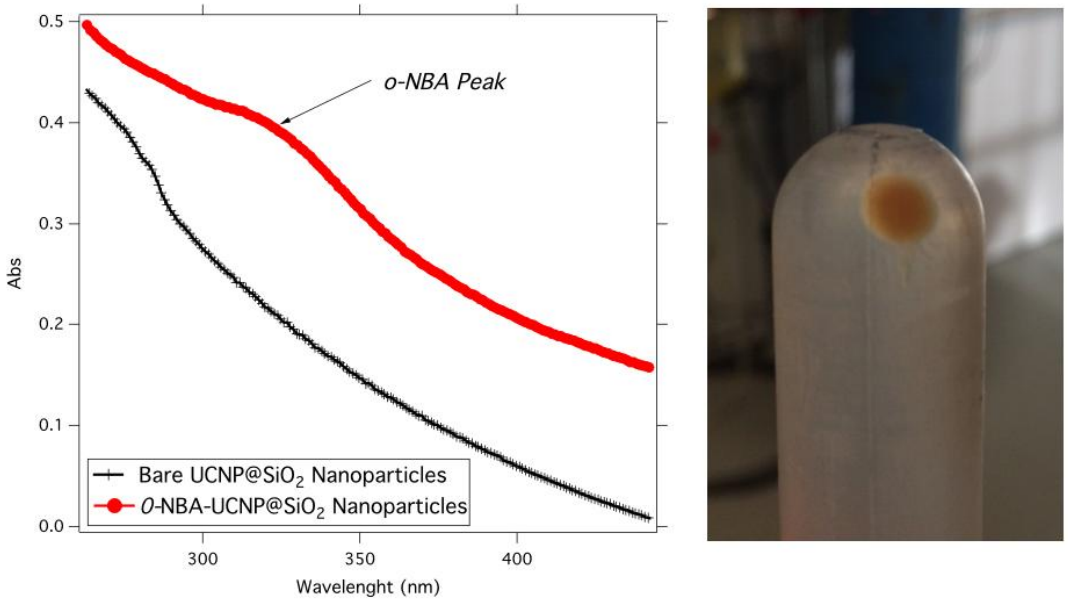

Figure 6.20. Left: UV-Vis spectra of bare UCNP@SiO_2 nanoparticles (black) and the photoresponsive *o*-NBA-functionalized UCNP@SiO_2 nanoparticles. Right: Picture taken from the last centrifugation step of the *o*-NBA-functionalized $NaYF_4$:Yb,Tm nanoparticles.

The Dox was attached directly to the photoresponsive molecules in the surface of the $NaYF_4$:Yb,Tm@SiO_2 nanoparticles by a thiol-acrylate Michael addition reaction[124]. Prior to this reaction, Dox was thiolated according to a previously published procedure[274]. The thiol-acrylate reaction was considered as ideal in our synthetic pathway because it is very specific and can be performed at room

temperature: 25 mg of PEG and *o*-NBA functionalized $NaYF_4$:Yb,Tm@SiO_2 nanoparticles were dissolved in 5 mL of Milli-Q water. An excess of thiolated Dox (300 mg) in 2 mL of Milli-Q water was added to the previous solution and the mixture was stirred at room temperature overnight. The purification of the Dox-functionalized $NaYF_4$:Yb,Tm@SiO_2 nanoparticles was performed by centrifugation at 13500 rpm for 20 minutes, and the precipitates were washed three times with Milli-Q water, combining centrifugation and redispersion in an ultrasound bath in order to remove the not anchored Dox. This cleaning process was repeated until a transparent supernatant was obtained (see Figure 6.21B). The presence of Dox was determined by UV-Vis spectroscopy (Figure 6.21A).

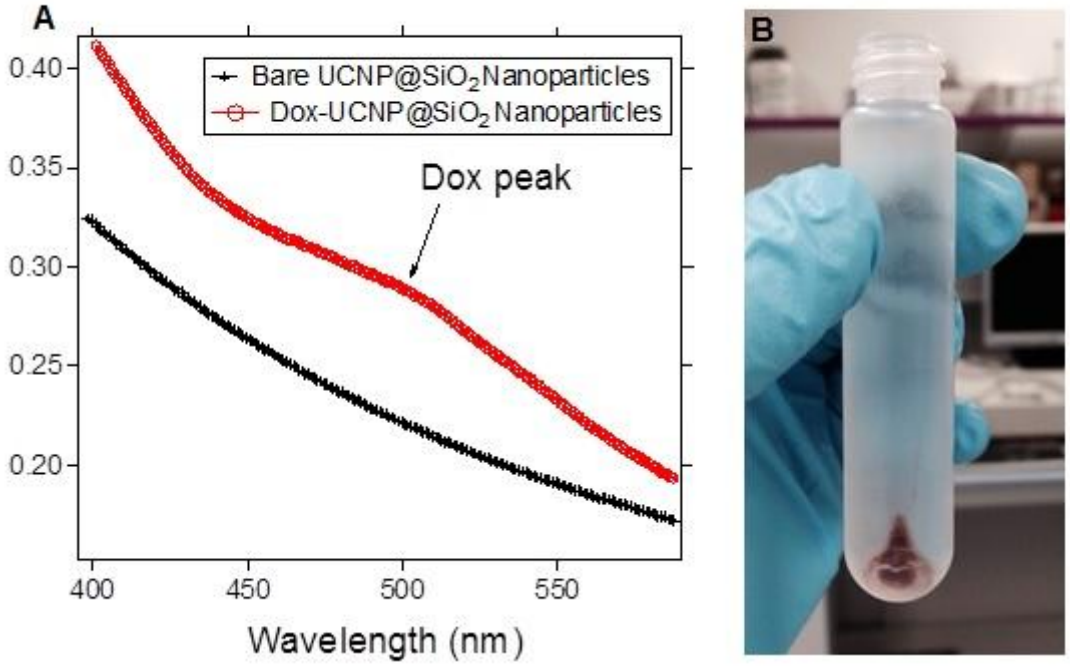

Figure 6.21. A) UV-Vis spectroscopy measurements of the $NaYF_4$:Yb,Tm@SiO_2 nanoparticles and Dox-loaded $NaYF_4$:Yb,Tm@SiO_2 nanoparticles. B) Picture taken from the last centrifugation step of the Dox-loaded $NaYF_4$:Yb,Tm@SiO_2 nanoparticles.

This result indicated that the thiol-acrylate Michael addition reaction was appropriate for attaching the Dox directly to the photocleavable molecule in the surface of silanized nanoparticles. It is important to note that the Dox should be covalently bound to the photocleavable molecule in the hydroxyl group with a

nitro group in *ortho*. Otherwise, the photodegradation of the *o*-NBA molecule would not release the Dox.

With these examples, such as DNA, Folic acid, PEG and Dox, we demonstrated that this method is very versatile and it is possible to anchor any molecule for a certain application in the surface of the silica.

6.3 Conclusions

The controlled polymerization of TEOS in a reverse microemulsion has been studied as a building block for nanoengineered materials. By controlling the reaction conditions the silica shell thickness can be controlled. Furthermore, we demonstrated that this methodology permits to encapsulate hydrophilic molecules within the silica shell and that this method can be used to provide a homogeneous silica coating to a great variety of inorganic nanocrystals: iron oxide, gold, silver, quantum dots and upconversion nanoparticles. Such versatility opens the possibility for combining many different properties from inorganic nanomaterials such as plasmonics, superparamagnetism or fluorescence with many different organic molecules. Moreover, the silica coating of the inorganic nanoparticles provided colloidal stability in aqueous media to the system, without altering the original properties of the inorganic cores. In addition, it has been demonstrated that the silica surface can be further modified with different functional groups and molecules. Putting all these possibilities together, the silica coating has demonstrated a special potential in the design of multifunctional nanostructured materials that could be applied in a wide range of fields.

We have used these silica based building blocks for the synthesis of functional materials for different applications: sensors, nanocarriers, catalysts, and stimuli-responsive drug delivery systems. The next two chapters are applications of silica coated upconversion fluorescence nanoparticles for DNA sensing and for phototriggered drug delivery.

7. RESULTS 4

Application of Silica coated UCNPs (I):

Highly selective DNA sensor based on Upconversion Nanoparticles and Graphene Oxide

7.1 Introduction

DNA is a biopolymer that can self-assemble in a unique manner according to the Watson-Crick base pairing rules. This self-assembly between two complementary polymer chains, known as hybridization, is very specific and is based on the cooperative hydrogen bonds produced between the base pairs, rendering a double helix structure. The DNA base-pair complementarities have shown great potential in nanotechnology as structural material in DNA origami[275], polyhedral structures[276], nano-mechanical devices[277], and as templates for the self-assembly of other materials such as gold nanoparticles[278–280]. This hybridization process has also been of great interest in biomedicine for application in sensors[281]. The specificity of the self-assembly between complementary DNA strands can be employed for the detection of certain sequences of interest, which are related to viral[282] or bacterial[283] infections as well as in the detection of specific human DNA or mRNA sequences for the diagnosis of diseases[284] or mutations[285].

Biosensors based on controlled quenching of fluorescence labels have shown significant advantages when employed as molecular beacons for amplified detection of metal ions and organic molecules[286–288]. Such sensors are typically designed with an energy transfer pair in which the fluorescence of the donor is effectively quenched by the acceptor. The addition of complementary target DNA or RNA induces a separation between the donor and the acceptor, and consequently the fluorescence of the donor is turned on proportionally to the concentration of the target. The sensing of DNA using these assays is often based on a self-complementary sequence within a hairpin loop that creates an intimate contact between the quencher and the fluorescent dye. Upon the addition of the complementary DNA, the hybridization results in the separation of the fluorophore from the quencher and the fluorescence can be detected[289–291]. Other assays can detect the activity of DNAase enzymes, which can selectively cleave a specific nucleotide sequence, thus separating the fluorophore from the quencher and restoring the fluorescence[292]. Although there are many strategies for the design of DNA-based sensors, the detection sensitivity is determined by the fluorophores. The commonly used organic dyes

suffer from photobleaching, while inorganic quantum dots exhibit blinking effects. However, the main drawback is the excitation wavelength of these fluorophores, which is normally located in the UV-Vis region. As consequence, the fluorescence background originating from biomolecules[293] and the inner filter effect caused by the absorption of other species[294] limit the detection sensitivity. These drawbacks could be overcome using upconversion nanoparticles (UCNPs) as fluorescence donors[295]. The UCNPs are lanthanide-doped inorganic materials, which are able to absorb two or more low-energy photons and emit fluorescence at a shorter wavelength than the excitation wavelength[296]. It is important to note that the upconversion fluorescence is produced by the inner 4f-4f orbital electronic transitions that are shielded by the complete 5s and 5p orbitals and as consequence the emission lines are very sharp and stable. The UNCPs have shown several advantages as fluorescence probes due to their high chemical and photochemical stability, low toxicity, large Stokes shifts, lack of photobleaching and absence of blinking. Due to these advantages, the UCNPs have been used in different applications[297–302]. However, the most important feature that makes the UCNPs an alternative to classical organic dyes is the excitation wavelength, which is located in the near-infrared (NIR) region (typically 980 nm). At this excitation wavelength biomolecular autofluorescence is avoided, while obtaining a lower light scattering when compared with UV-Vis radiation[303]. For these reasons, the signal-to-noise ratio can be greatly enhanced by using UCNPs as biological labels[304]. However, the quenching of this fluorescence is only possible on the surface of the particles[305]. For this reason, the upconversion fluorescence should be emitted by small nanoparticles, in which the surface-related effects are dominant. Thus, an effective quencher for upconversion fluorescence is difficult to find[306]. Up to date, only gold nanoparticles and graphene derivates have been successfully used as quenchers for upconversion fluorescence[307,308]. Graphene oxide (GO) has been used as an ultra-highly efficient quencher for UCNPs, when the nanoparticles are in intimate contact with the GO surface[102]. For this to happen, it would be necessary to functionalize the UCNPs with molecules capable of physisorbing onto the GO surface. It has been demonstrated that single-strand DNA (ssDNA) biopolymers have a strong affinity for the surface of GO due to strongly attractive π-π interactions between

the aromatic nucleobases and the highly unsaturated structure of GO[309]. In contrast, in the case of double-strand DNA (dsDNA) the π electrons are involved in forming the duplex via base-stacking interactions and therefore they are not available for interactions with the GO surface. On this basis, it would be possible to design a fluorescence sensor for DNA using UCNPs and GO as fluorescence resonance energy transfer (FRET) pair. Such upconversion fluorescence probes would be functionalized with ssDNA and should be highly monodisperse and small enough to permit the FRET with GO. In the presence of the complementary DNA strand (cDNA) the hybridization process would lead to dsDNA, and the upconversion fluorescence would be detectable.

In this work a fluorescence DNA sensor platform is demonstrated using the FRET pair formed by UCNPs as fluorophores and GO as quencher. Erbium- and ytterbium-doped β-$NaYF_4$ nanoparticles were used as fluorescent donors, which are known as one of the most efficient upconverting nanomaterials[310]. The ratio between the ssDNA-functionalized UCNPs and GO was optimized to obtain the maximum sensitivity, and the biosensor was evaluated using the cDNA sequence at different concentrations. In addition, the hybridization conditions of the DNA sequences were studied as a function of the temperature. A strong relationship was found between these conditions and the sensitivity of the sensor. By using relative emission/upconversion measurements compared to a reference, it was possible to determine the presence of cDNA with a great sensitivity and specificity with a fast and reproducible methodology.

7.2 Results and discussion

7.2.1 Synthesis and surface functionalization of upconversion nanoparticles

The synthesis of $NaYF_4$:Yb,Er nanoparticles produced highly monodisperse spherical UCNPs with a mean diameter of 29.1 ± 2.2 nm as measured by TEM micrographs (Figure 7.1A). These nanoparticles could be easily dispersed in organic solvents such as hexane due to the presence of oleic acid as capping and stabilizing agent. The UCNPs were subsequently coated with a silica shell

by the reverse microemulsion method. With this procedure it was possible to obtain monodisperse spherical core@shell $NaYF_4$:Yb,Er@SiO_2 nanoparticles in which each upconversion nanoparticle was covered with silica, and no large aggregates with multiple-core were found. The overall mean diameter of the UCNPs@SiO_2 nanoparticles was 47.34 ± 3.8 nm with a silica shell thickness of ~11 nm as analyzed with TEM micrographs (Figure 7.1B). The UCNPs@SiO_2 nanoparticles could be dispersed in polar solvents such as ethanol or water. The obtained nanoparticles showed the characteristic upconversion fluorescence spectrum for ytterbium- and erbium doped $NaYF_4$ nanoparticles when excited with a CW 980 nm 500 mW laser diode (Figure 7.1C). The upconversion fluorescence with these erbium-doped nanoparticles showed the emissions at 534 and 549 nm (green emission corresponding to the transition $^4S_{3/2} \rightarrow {}^4I_{15/2}$) and at 654 nm (red emission corresponding to the transition $^4F_{9/2} \rightarrow {}^4I_{15/2}$)[311]. The quantum efficiency of particles having the same size, composition, and structure is ~0.1%[312]. The nanoparticles dispersed in water formed a transparent solution in which the upconversion fluorescence could be observed by the naked eye when the sample was excited with the 980 nm laser (Figure 7.1D).

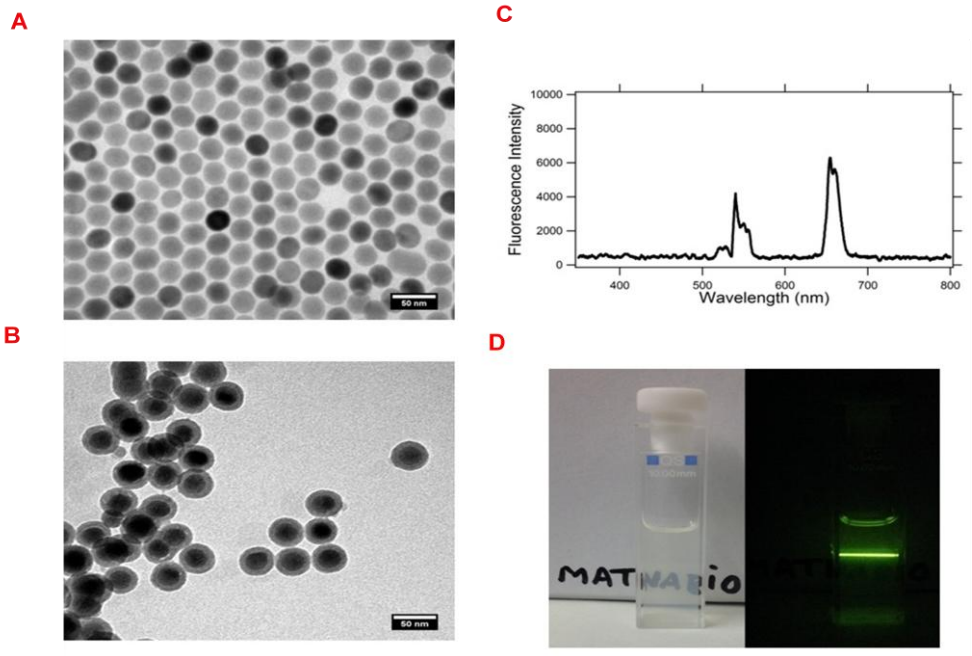

Figure 7.1. A) TEM micrograph of monodisperse $NaYF_4$:Yb,Er nanoparticles. B) TEM micrograph of monodisperse $NaYF_4$:Yb,Er@SiO_2 nanoparticles. Scale

bars are 50 nm. C) Fluorescence spectrum of a diluted solution in ethanol of the silanized upconversion nanoparticles when excited with a CW 980 nm laser. D) Pictures taken of a diluted solution of upconversion nanoparticles in hexane without laser excitation (left) and the same solution under the excitation with the NIR laser. The room light was turned off to take this picture.

The surface of the $NaYF_4$:Yb,Er@SiO_2 nanoparticles was modified in several steps prior to the covalent attachment of the ssDNA sequence (Figure 7.2).

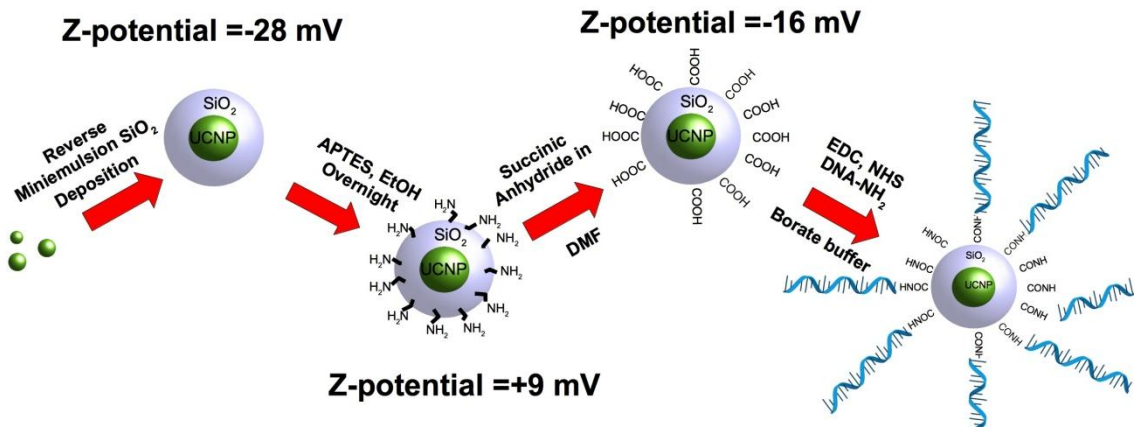

Figure 7.2. Schematic illustration of the chemical route for the surface functionalization of UCNPs@SiO_2 nanoparticles with ssDNA.

The first experimental step was the silanization of the upconversion nanoparticles. Then, the surface was modified with amino groups using APTES. These amino groups acted as nucleophiles for the reaction with succinic anhydride, which led to carboxylic acid functionalized UCNPs@SiO_2 nanoparticles. The final experimental step was the EDC coupling reaction between the amino-modified probe ssDNA sequence and the obtained carboxylic acid in the surface of the nanoparticles, as detailed in the previous chapter.

7.2.2 Optimization and evaluation of the ssDNA sensor based on UCNPs and Graphene Oxide

The FRET pair between UCNPs@SiO_2-ssDNA and Graphene Oxide (GO) was studied for the optimization of the sensor. First, the concentration of

UCNPs@SiO2-ssDNA nanoparticles was set to 0.4 mg/mL. Different concentrations of GO (ranging from 0 to 1 mg/mL) were prepared and incubated with the nanoparticles at 40 ºC for one hour. Then, the samples were left to cool down to room temperature prior to the fluorescence measurements. Figure 7.3 depicts the fluorescence intensity of the UCNPs@SiO_2-ssDNA as a function of the GO concentration.

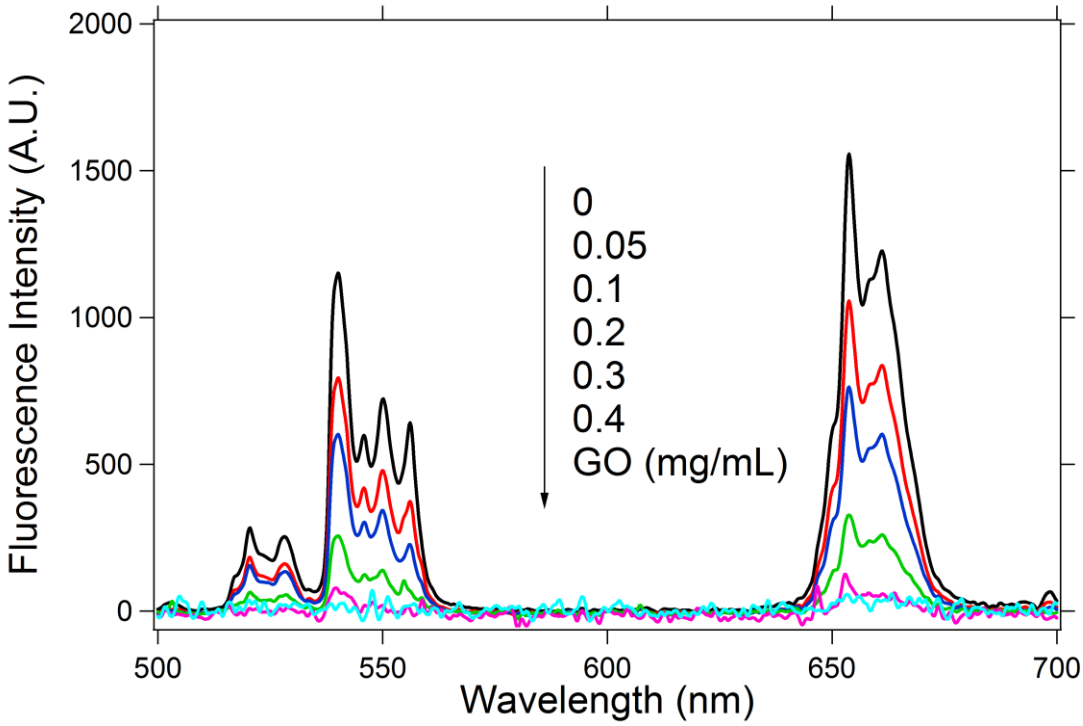

Figure 7.3. Upconversion fluorescence spectra of the UCNPs@SiO_2-ssDNA nanoparticles (0.4 mg/mL) in the presence of different concentrations of graphene oxide (excitation wavelength 980 nm). Higher concentrations of GO result in reduced upconversion intensity.

Figure 7.3 depicts the reduction of fluorescence intensity of UCNPs@SiO_2-ssDNA (0.4 mg/mL) when the concentration of graphene oxide increased. The analysis of the fluorescence quenching of UCNPs@SiO_2-ssDNA at 549 nm and 654 nm as a function of the GO concentration is shown in figure 7.4. Figure 7.4a shows the absolute intensity; while Figure 7.4b shows the same data normalized to the value without GO.

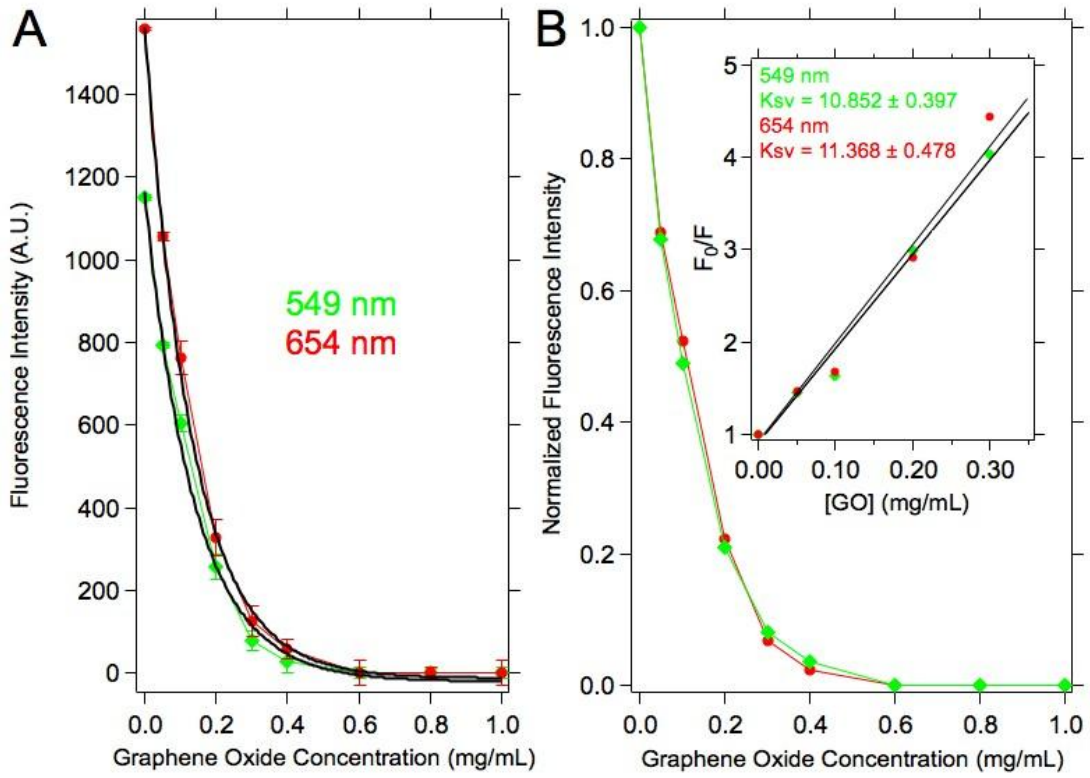

Figure 7.4. Representation of A) the maximum fluorescence intensity and B) normalized fluorescence intensity of the UCNPs@SiO_2-ssDNA (0.4 mg/mL) measured at 549 and 654 nm as a function of the GO concentration. The inset in figure 4B) represents the Stern−Volmer plot for the fluorescence quenching with GO of the emission bands located at 549 nm (green line) and 654 nm (red line) respectively.

Clearly, the fluorescence intensity was quenched for more than 95% when the concentration of GO reached around 0.3 mg/mL. A further addition of GO resulted only in a very small increase in quenching. As shown in figure 7.4b, this behavior was similar for both nanoparticle emission wavelengths located at 549 nm and 654 nm, respectively. These observations led us to hypothesize 0.3 mg/mL of GO as the optimum concentration for quenching the fluorescence emission of 0.4 mg/ml of the UCNPs@SiO_2-ssDNA.

A quantitative measure of the fluorescence quenching is given by the Stern−Volmer constant KSV, defined by:

$$F_0/F = 1+Ksv \cdot [GO]$$

where F_0 and F are the intensities of fluorescence in the absence and in the presence of the quencher, respectively, and [GO] is the concentration of quencher. For the UCNPs@SiO_2-ssDNA quenched by GO the obtained Ksv was around 11 mL/mg for both wavelengths, indicating that the quenching mechanism was due to FRET between the UCNPs and the GO and not by a simple absorption process in which the GO would absorb the photons emitted by the UCNPs. If this was the case, the fluorescence quenching of the photons at 549 nm would have been higher than that of the photons at 654 nm, due to the absorption spectrum of GO (Figure 7.5).

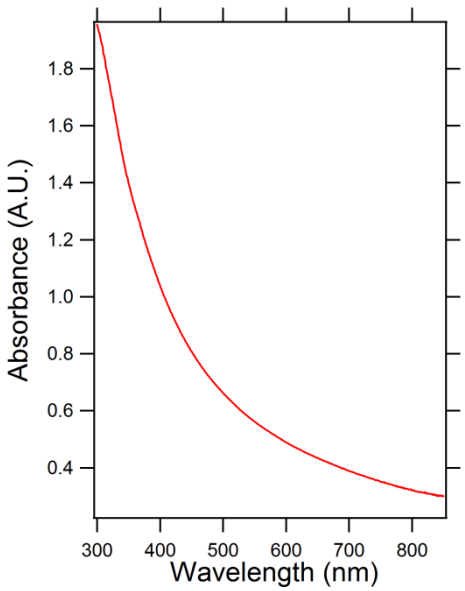

Figure 7.5. UV-Vis absorption spectrum of 0.3 mg/mL graphene oxide in PBS buffered aqueous solution.

With the aim of assessing the importance of the interaction between the ssDNA and GO on the fluorescence quenching of the UCNPs@SiO_2-ssDNA, we compared the fluorescence of UCNPs@SiO_2 with and without ssDNA at a concentration of 0.4 mg/mL (Figure 7.6).

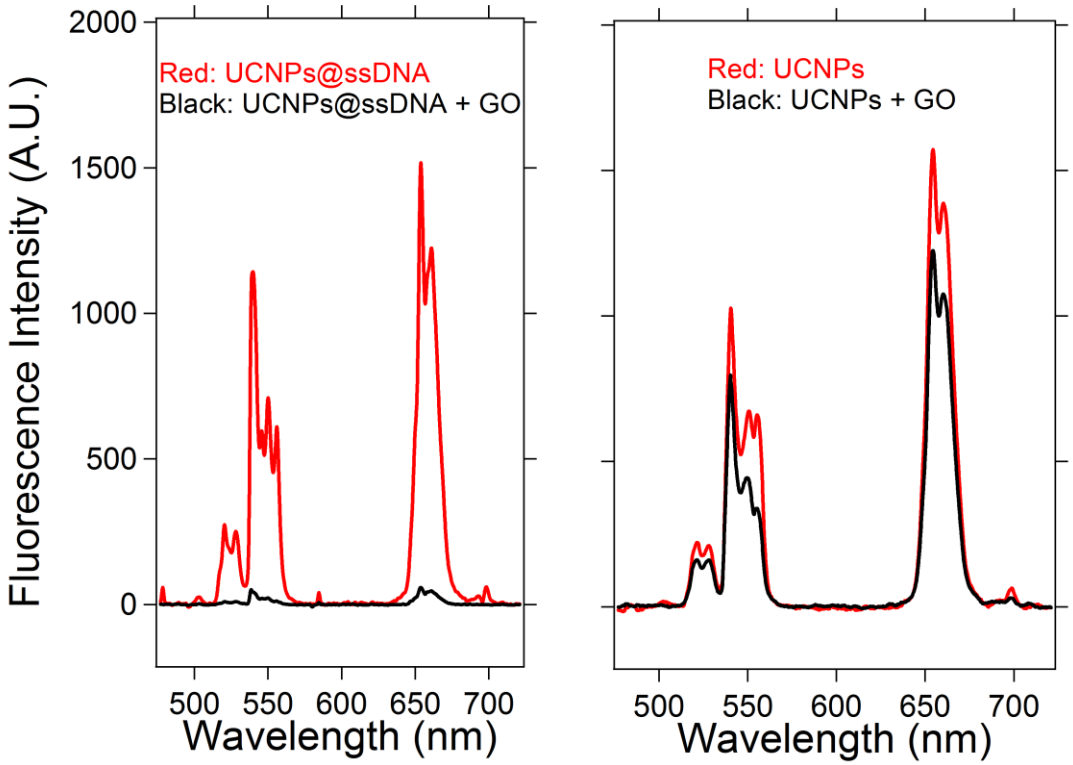

Figure 7.6. Left: Fluorescence intensity of 0.4 mg/mL of UCNPs@SiO_2-ssDNA nanoparticles in the presence (black curve) and in the absence (red curve) of 0.3 mg/mL of GO. Right: Fluorescence intensity of 0.4 mg/mL of UCNPs@SiO_2 nanoparticles in the presence (black curve) and in the absence (red curve) of 0.3 mg/mL of GO. Both samples were incubated for 1 hour at 40 ºC.

0.3 mg/mL of GO was able to quench the 97% of the fluorescence emission of the UCNPs@SiO2-ssDNA. By contrast, under the same experimental conditions, the fluorescence quenching observed on UCNPs@SiO_2 nanoparticles without DNA was around 16% as shown in Figure 7.6. These results demonstrated that the FRET based fluorescence quenching was specific for UCNPs@SiO_2-ssDNA nanoparticles and was due to the attractive π-π interactions between the ssDNA and the GO surface.

A means to disrupt the attractive π-π interactions between the ssDNA and the GO surface could be hybridization of the ssDNA strand with its complementary ssDNA sequence. This would induce a conformational change of the DNA strands that would prevent the adsorption of the UCNPs@SiO_2-ssDNA nanoparticles on the GO surface. As a result, the UCNPs@SiO_2-ssDNA nanoparticles would retain their fluorescence. In order to prove this, 0.4 mg/mL

of UCNPs@SiO_2-ssDNA nanoparticles were incubated in PBS with different concentrations of the complementary ssDNA (from 0.1 nM to 400 nM) for 2 minutes at 90 ºC and then slowly cooled down to 40 ºC. After this time, a solution of GO in PBS was added up to a final concentration of 0.3 mg/mL. The mixture was incubated for 1 hour at 40 ºC and then cooled down to room temperature prior to performing the fluorescence measurements. Figure 7.7 represents the fluorescence intensity of UCNPs@SiO2-ssDNA nanoparticles in the presence of GO and different concentrations of the complementary ssDNA.

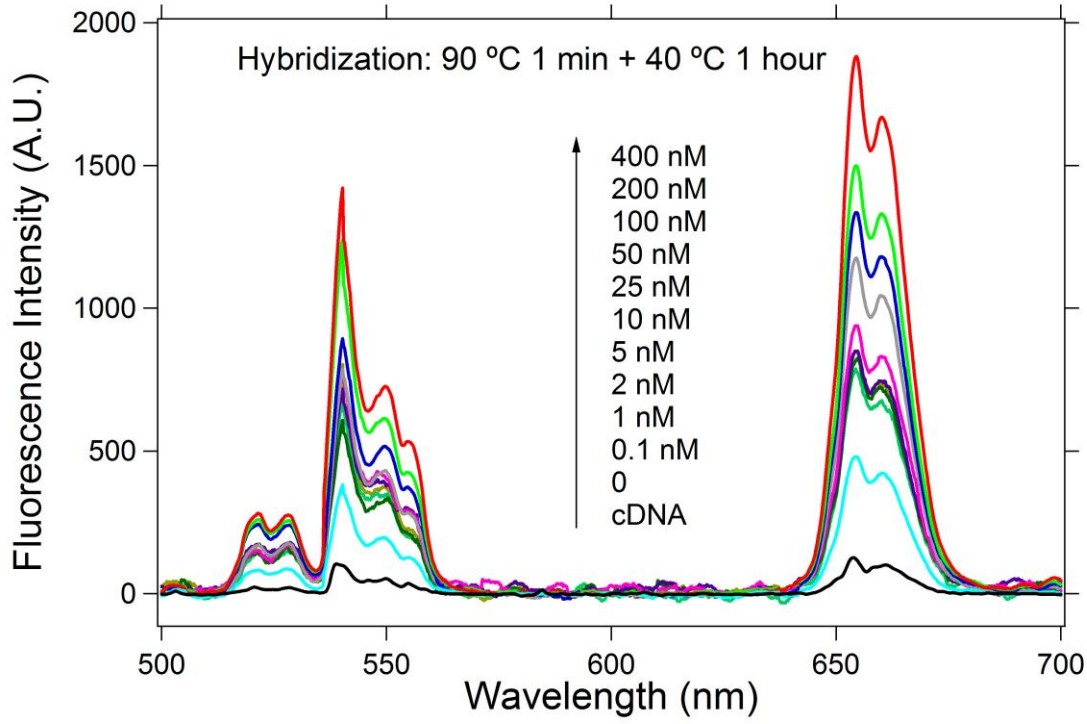

Figure 7.7. Representation of the fluorescence spectra of the UCNPs@SiO_2-ssDNA nanoparticles (0.4 mg/mL) in the presence of different concentrations of complementary ssDNA and 0.3 mg/mL of GO (colored curves). The black curve is the fluorescence spectrum without the addition of complementary ssDNA (excitation wavelength 980 nm).

The fluorescence intensity of the UCNPs@SiO_2-ssDNA nanoparticles shows a gradual recovery with increasing concentrations of the complementary ssDNA. The analysis of the maximum intensity as a function of the concentration of the complementary ssDNA is presented in Figure 7.8 for the two upconversion wavelengths at 549 nm and 654 nm.

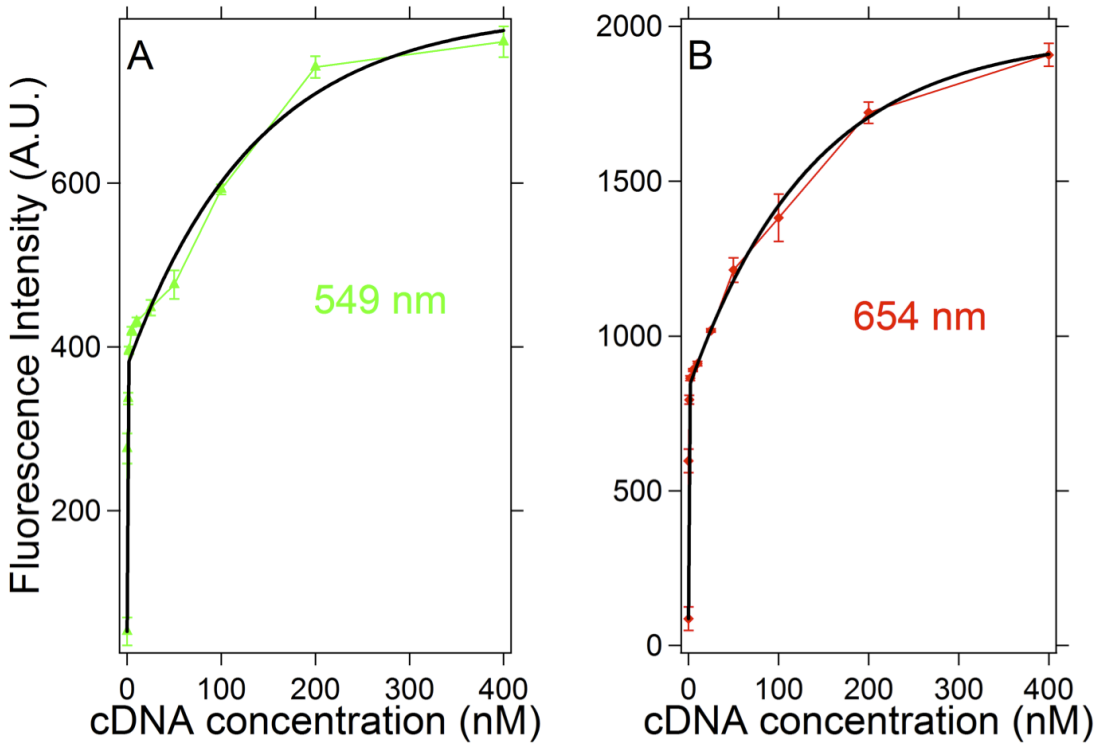

Figure 7.8. Representation of the maximum fluorescence intensity bands measured at 549 nm (left) and 654 nm (right) of the UCNPs@SiO_2-ssDNA nanoparticles as a function of the complementary ssDNA concentration.

Figure 7.8 shows a trend in the fluorescence intensity upon the addition of the cDNA consisting of two parts. At low concentrations of cDNA (below 2 nM) the fluorescent intensity increases steeply, while in larger concentrations of cDNA there is an additional significant fluorescent increase with a much smaller, saturating slope. This increase is probably due to the gradually larger number of hybridization events near the nanoparticle surface as the concentration of the cDNA is increased.

The fluorescence intensity measured with the highest concentration of cDNA (400 nM) was close to that of the solution of UCNPs@SiO_2-ssDNA (0.4 mg/mL) without GO. Thus, we hypothesize that the saturation of the fluorescent intensity at high cDNA concentrations corresponds to a saturation of hybridization events near the nanoparticle surface.

The upconversion fluorescence intensity was represented as a function of the complementary DNA concentration, and we observed a double exponential increase in which at lower concentrations of cDNA the upconversion

fluorescence intensity increased more than that at higher concentrations of cDNA. The double exponential equations obtained from the curve fitting for 549 nm and 654 nm, respectively, were the following:

$$y = (816.8 \pm 54) + (-428.09 \pm 50.8) \cdot e^{(-0.0067113 \pm 0.00214) \cdot cDNA} + (-182.74 \pm 32.7) \cdot e^{(-1.7031 \pm 1.11) \cdot cDNA}$$

$$y = (1984.5 \pm 40) + (-1136 \pm 37.7) \cdot e^{(-0.0069295 \pm 0.00062) \cdot cDNA} + (-298.59 \pm 36.8) \cdot e^{(-1.6515 \pm 0.567) \cdot cDNA}$$

The detection limit of the target sequence for this DNA biosensor was experimentally demonstrated to be at the level of 100 pM. However, the theoretical detection limit inferred from the double exponential fitting function was 5 pM, limited by the error of the baseline measurement in absence of cDNA. This error was established to be caused by the systematic variation between subsequent recorded spectra. In the excitation arrangement as depicted in Fig. 7.1d, a pencil of light of around 20x20x250 µm3 was collected by the spectrometer. Thus, the total detection volume was around 100 pL, giving a total amount of cDNA detected in our experiments of around 10 zeptomoles. This detection limit is lower than other GO−DNA sensors recently published. Thus, for instance, Liu *et al*.[313] published a GO−DNA sensor based on DNA-functionalized GO and DNA-Au nanoparticles, which showed a detection limit of 200 nM. Luo *et al*.[314] designed a GO−DNA sensor based on the capacity of GO to inhibit the catalytic activity of the horseradish peroxidase when it was in close contact with the surface of the GO. Thus, by attaching this enzyme to the GO surface by means of a DNA strand, they were able to develop a DNA sensor with a detection limit of 34 pM. Another interesting GO−DNA sensor was designed by Zhao *et al*.[315] This DNA sensor was based on the use of fluorescent dye-labeled ssDNA strands, which can interact with GO by π-π stacking interactions. This fact quenched the fluorescence and inhibited the degradation by the exonuclease III, since the physisorbed DNA is not accessible to the enzyme. The hybridization with the complementary DNA not only hampers the dsDNA physisorbtion but also permits their enzymatic degradation and the release of the fluorescent dye, allowing the quantification of target DNA with a detection limit of 20 pM.

The specificity of the sensor was evaluated with a control experiment, in which the UCNPs@SiO_2-ssDNA nanoparticles (0.4 mg/mL) were incubated in PBS in the presence of non-complementary DNA sequences at concentrations from 100 nM to 1 μM. The incubation was performed at 90 ºC for 2 minutes and then a solution of GO in PBS was added obtaining a final concentration of 0.3 mg/mL. The solution was left for 1 hour at 40 ºC. After cooling down to room temperature, the upconversion fluorescence was measured (see Figure 7.9).

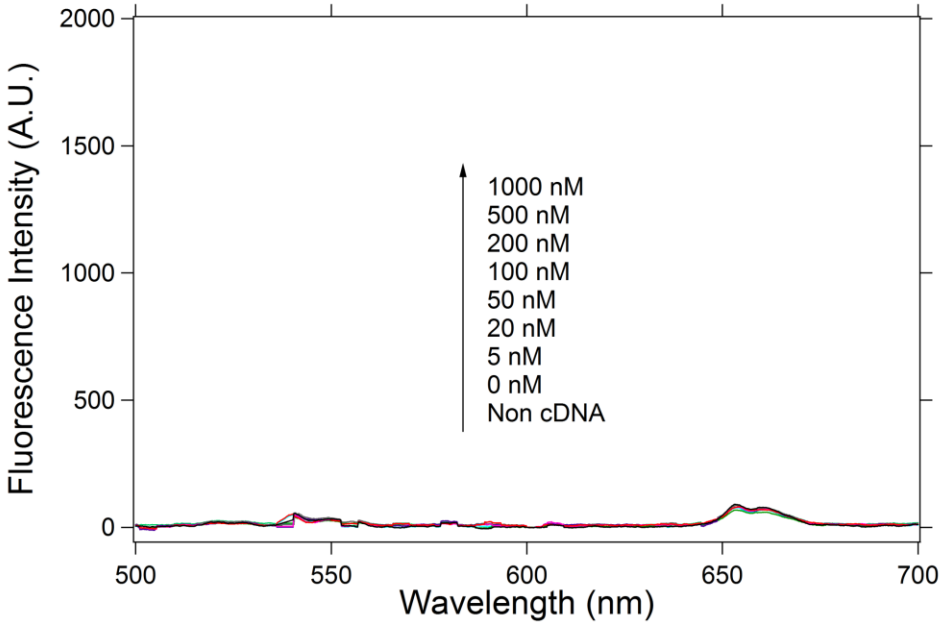

Figure 7.9. Representation of the upconversion fluorescence spectra of the UCNPs@SiO_2-ssDNA nanoparticles (0.4 mg/mL), hybridized at 90 ºC for 2 minutes and at 40 ºC for 1 hour, with different concentrations of a non-complementary ssDNA and 0.3 mg/mL of GO (colored curves).

Figure 7.9 shows that independently of the concentration of non-complementary DNA strands, the UCNPs@SiO_2-ssDNA were quenched by GO. These observations demonstrate the DNA selectivity of the biosensor platform. The curve fittings are represented in Figure 7.10.

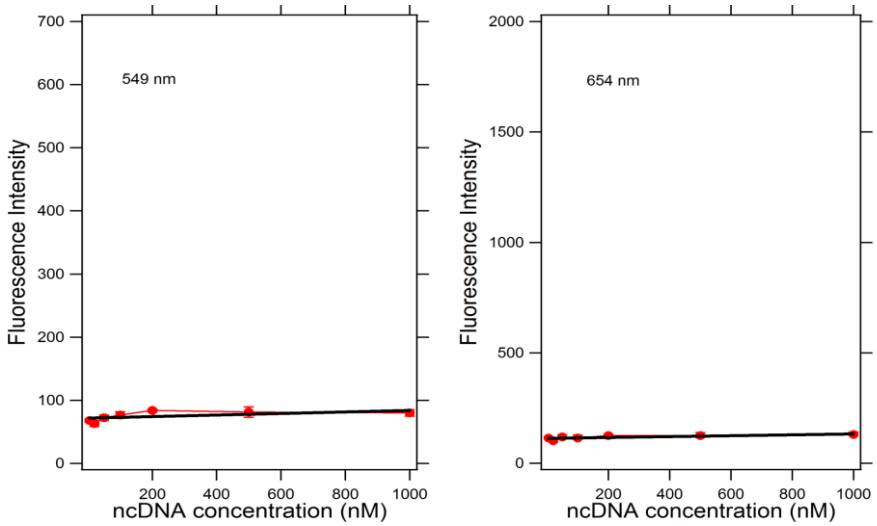

Figure 7.10. Curve fitting of the upconversion fluorescence intensity against the non-complementary DNA concentration for the emission at 549 nm (left) and 654 nm (right).

In this work we also demonstrated that the hybridization conditions strongly influenced the sensitivity of the DNA sensor. In the Figure 7.11 we represented the upconversion fluorescence intensity as a function of the cDNA concentration at different hybridization conditions (90 ºC for 2 minutes and 1 hour at 40 ºC and 40 ºC for 2 hours). This figure shows graphically that the experimental detection limit was three orders of magnitude lower when the samples were hybridized at 90 ºC. We observed this result in both of the emission wavelength maximums of Erbium, 549 nm and 654 nm.

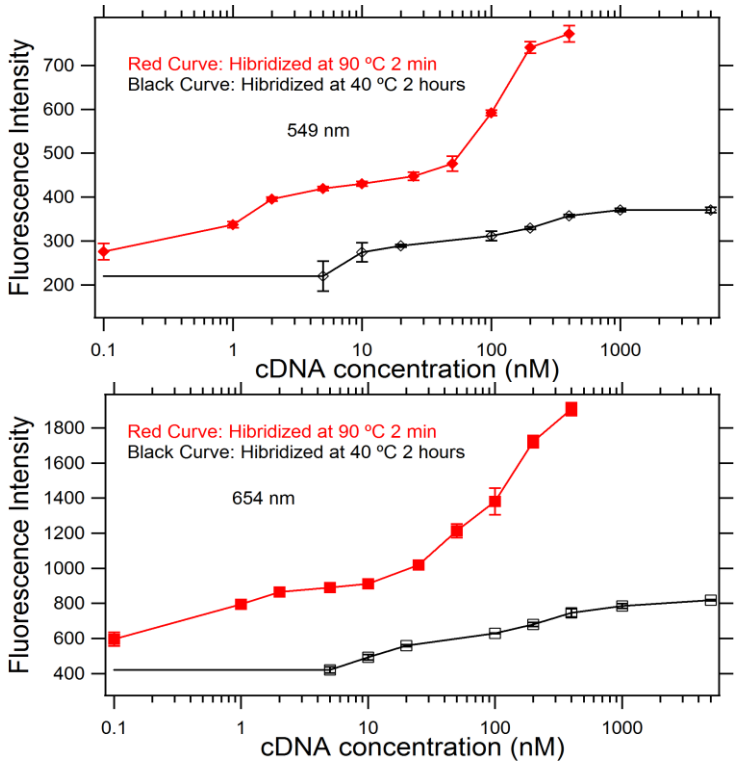

Figure 7.11. Upconversion fluorescence intensity as a function of the cDNA concentration at 549 nm (upper figure) and at 654 nm (lower figure). The red curves represent the results obtained when the hybridization was performed at 90 ºC for two minutes and 1 hour at 40 ºC. The black curves represent the results obtained when the hybridization was performed at 40 ºC for two hours.

As summary, the upconversion fluorescence intensities obtained with the DNA concentration (cDNA and non cDNA) constant at 400 nM were significantly different. Figure 7.12 depicts the upconversion fluorescence intensity obtained at this concentration with cDNA with the different hybridization conditions and the upconversion fluorescence intensity obtained at the same concentration of non-complementary DNA. Figure 7.13 shows a schematic representation of the DNA sensor platform.

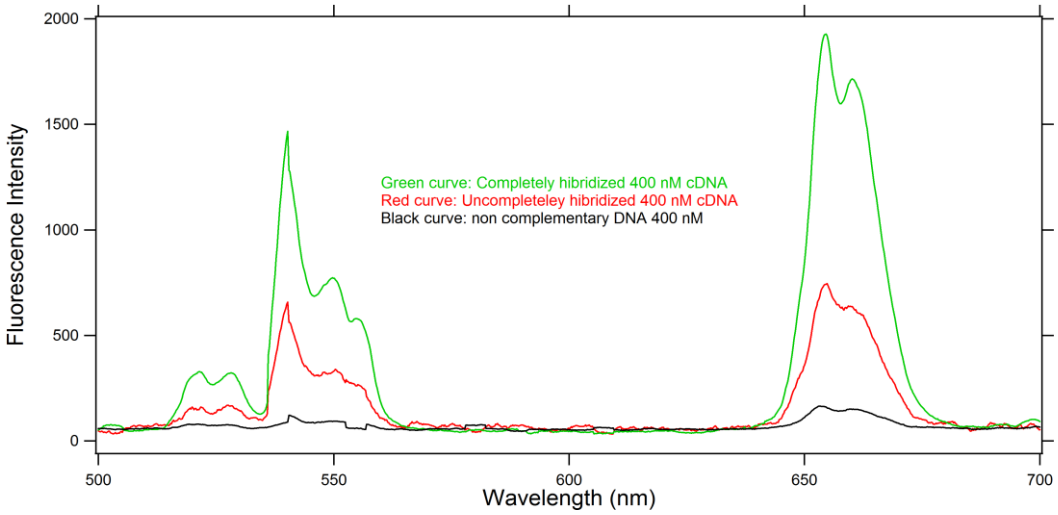

Figure 7.12. Upconversion fluorescence curves when the UCNPs@SiO_2-ssDNA were hybridized with: 400 nM of cDNA at 90 ºC for 2 minutes and 1 hour at 40 ºC (green); 400 nM of cDNA at 40 ºC for 2 hours (red); and 400 nM of non cDNA at 90 ºC for 2 minutes and 1 hour at 40 ºC (black).

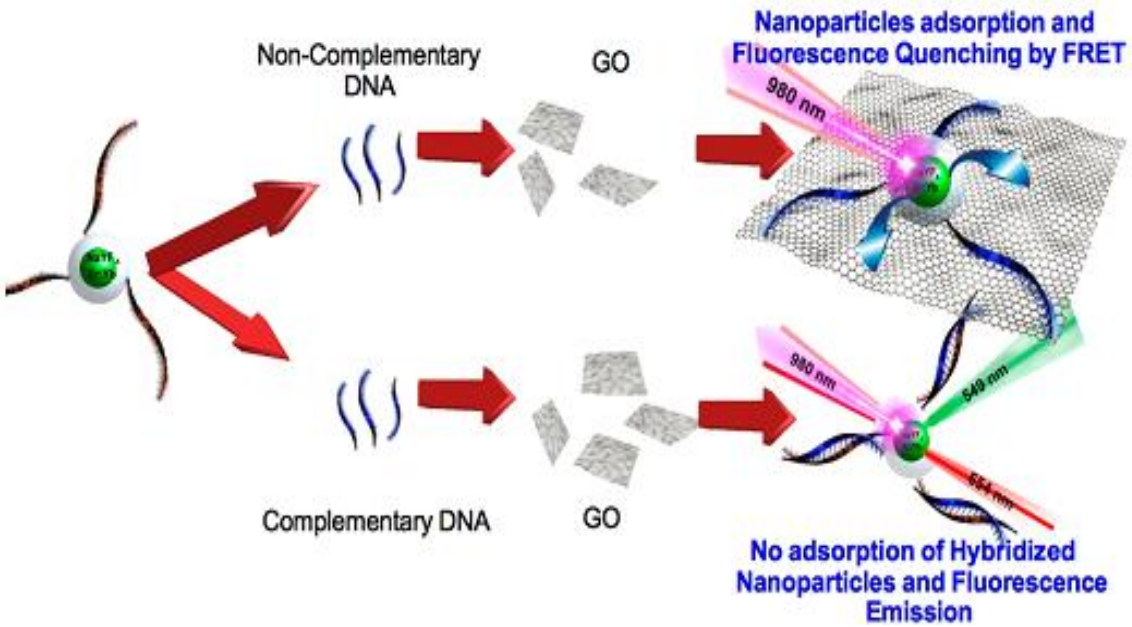

Figure 7.13. Schematic representation of the proposed sensor platform in the presence or absence of complementary DNA.

7.3 Conclusions

In this work a DNA biosensor platform was prepared by exploiting the FRET pair formed between upconversion nanoparticles and graphene oxide. The UCNPs were synthesized and functionalized with ssDNA. In the absence of cDNA, the ssDNA coated UPCNs were physisorbed on the surface of the GO and their fluorescence was quenched. When the cDNA was present, the UPCNs were not able to physisorb onto the GO template and thus the fluorescence remained. The fluorescence intensity was correlated to the concentration of cDNA. The detection limit was experimentally showed to be in the pM range, which corresponded in our experimental conditions to zeptomoles of cDNA. To the best of our knowledge, this is the first FRET pair that reports such a high sensitivity and specificity for DNA sensing.

8. RESULTS 5

Application of Silica coated UCNPs (II): Phototriggered Doxorubicin release with NIR light using Upconversion Nanoparticles

8.1 Introduction

Stimuli responsive materials that undergo structural changes in response to external stimuli like pH[316], temperature[317], light[318], etc., are of major interest due their potential applications in electronics, photonics and biomedicine. In the biomedical field, the use of materials capable to respond against external stimuli have emerged as ideal candidates to control the drug release and to minimize the side effects associated with the use of certain drugs[319]. This is of special interest in the cancer treatment, where the imbalance between risk and benefits leads to reject the use of toxic molecules that could serve as therapeutic tools if they were conveniently administered. This has prompted scientists to develop silenced drug delivery systems that can be activated on demand once they have reached the target tissue. For instance, the activation by means of alternating magnetic fields has been exploited as an interesting and versatile route to control the drug release[320,321]. Another interesting approach relays on the use of electric current to switch "on-off" the drug release[322]. However the scarce capacity to localize with precision these stimuli into the target tissue has prompted scientists to use light as external stimulus to locally control the drug release. Initially, UV-Vis light was used to trigger the release of drugs after inducing conformational changes[323], solubility variations[324] or the photodegradation of a specific protective group[325]. However, in-vitro studies demonstrated that the UV-Vis light can be toxic for living cells and it is widely absorbed in tissue, which restricts the light penetration to few microns[326,327]. To solve these problems, NIR light has been used as external stimuli to control the drug release with plasmonic coupled systems, in which the temperature increase upon irradiation provoked the drug release[328].

An alternative to this approach would be the use of upconversion fluorescence nanoparticles that can "transform" the NIR light into UV-Vis[329]. These nano-particles present upconversion photoluminescence, which is a unique type of Anti-Stokes fluorescence in which the excitation wavelength is higher than the emission wavelength[330]. In a typical upconversion process, two or more low-energy photons are converted into a high-energy photon[331]. This process can occur in Ytterbium and Thulium doped $NaYF_4$ nanoparticles ($NaYF_4$:Yb,Tm as

UCNPs), which can absorb NIR light at a wavelength of 980 nm and emit UV-Vis photons[332,333]. The UV-Vis emission can be combined with photodegradable ortho-nitrobenzylalcohol molecules[334] to create light responsive anchoring points that could release the drug upon the irradiation with NIR light[335].

In this chapter we have developed a phototriggered drug delivery system based on UCNPs, which have been functionalized with ortho-nitrobenzylalcohol derivate molecules (o-NBA). The photodegradable molecules anchored on the surface of the nanoparticles were used to link Doxorubicin (Dox), a potent cytotoxic drug. The NIR-light-triggered drug release rendered an “on-off” delivery system that could be used in biomedical applications. The silica coating was used to render aqueous solubility to the UCNPs and also as template for anchoring in the surface the protodegradable molecule and the Dox, as well as PEG to enhance the aqueous solubility.

8.2 Results and discussion

8.2.1 Synthesis and surface functionalization of upconversion nanoparticles

The general strategy used to functionalize the UCNPs is depicted in Scheme 8.1.

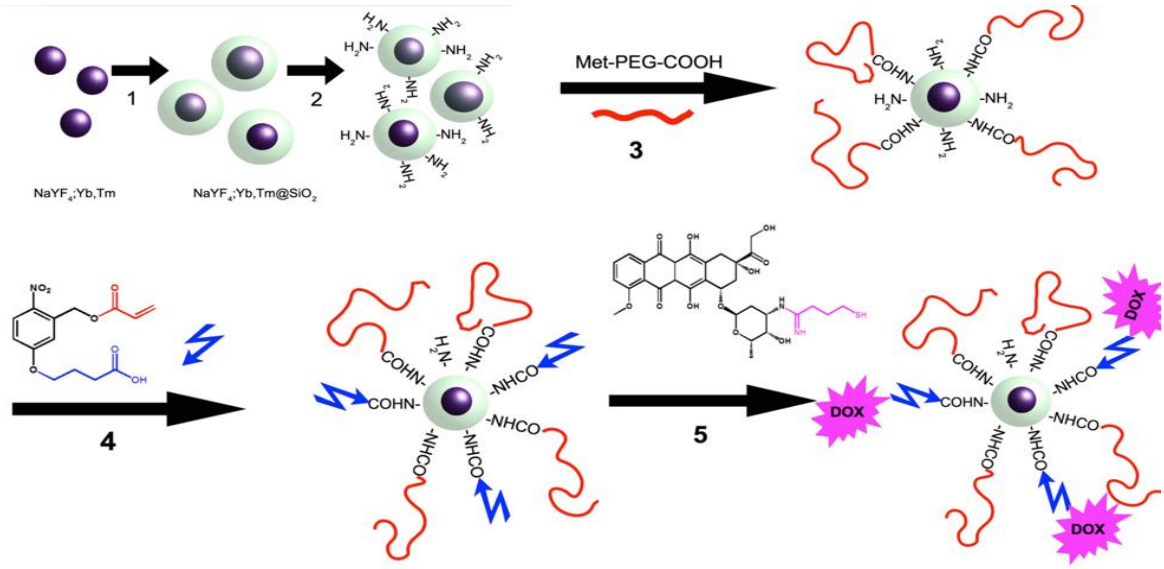

Scheme 8.1. Synthetic pathway for the synthesis of the NIR light responsive drug delivery system.

The synthesis of the $NaYF_4$:Yb,Tm nanoparticles rendered hexagonal crystals with an average length of 43 ± 1.5 nm and a mean width of 38 ± 1.2 nm, as shown in Figure 8.1A. X-ray diffraction and EDX analysis confirmed that the synthesized nanoparticles were crystalline with a structure that corresponded to β-$NaYF_4$, see Figure 8.1C. The atomic structure was studied by energy dispersive X-ray spectroscopy (EDX) in the TEM, which revealed that the chemical structure of the nanoparticles was $NaYF_4$ doped with Yb and Tm (Figure 8.1D). Next, a thin layer of SiO_2 with a thickness of 8.5 ± 0.1 nm was grown on the UCNPs using the reverse microemulsion method[21]. This step increased the size of the UCNPs@SiO_2 nanoparticles to a mean diameter of 52 ± 2.5 nm as one can observe in Figure 8.1B. The silanized nanoparticles showed the upconversion emission when excited with a CW 980 nm laser, which is depicted in Figure 8.1B as inset. The plot profile of the UCNPs@SiO_2 nanoparticles is depicted in Figure 8.2.

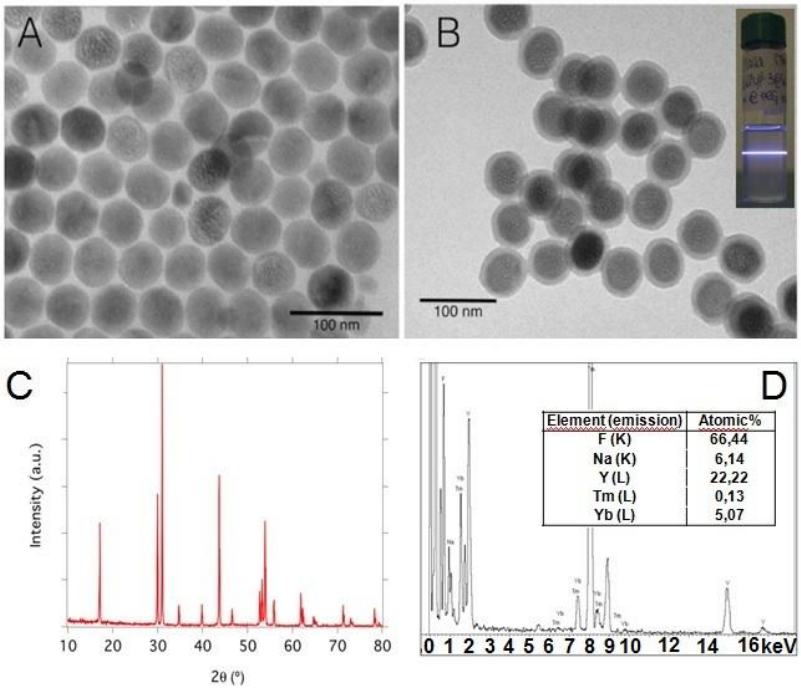

Figure 8.1. A) TEM image of the UCNPs before the silica coating. B) TEM image of UCNPs@SiO_2 nanoparticles. The inset shows the upconverted emission of the UCNPs@SiO_2 under a 980 nm CW laser excitation. C) XRD pattern of the UCNPs. D) EDX spectrum of the UCNPs. The table inside shows the atomic percentage of each atom obtained from the spectrum (automatic, standardless).

The deposition of the SiO_2 shell permitted introducing functional groups that allowed further chemical functionalization. After this step the UCNP@SiO_2 nanoparticles were treated with APTES. The introduction of APTES yielded a variation of the Z-potential of the UCNPs@SiO_2, which varied from -26.5 ± 2.85 mV to +9.14 ± 2.49 mV. Such a variation of the Z-potential reduced their colloidal stability. This problem was solved by grafting the surface with PEG chains[336]. The immobilization of PEG chains was monitored by FTIR as showed in the chapter 3.

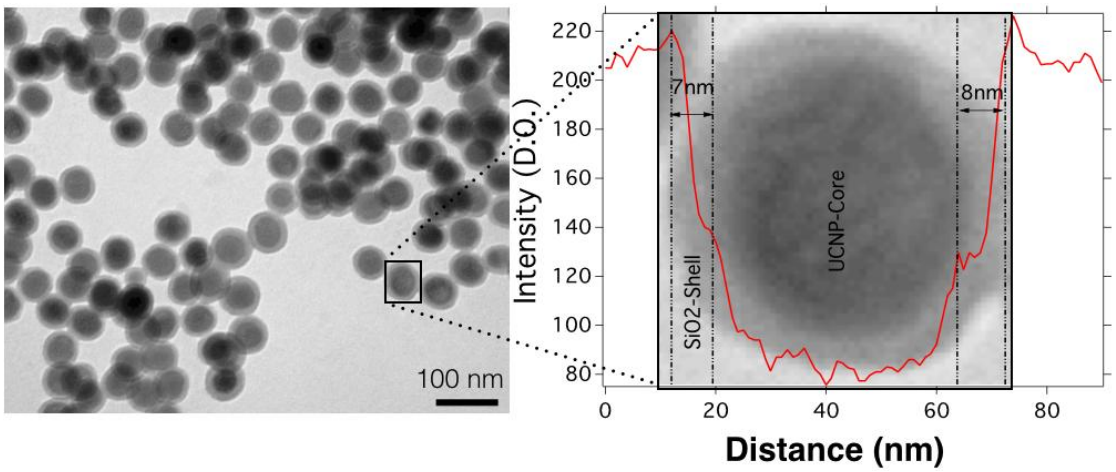

Figure 8.2. Representative TEM micrograph of UCNPs@SiO_2 nanoparticles and a magnified UCNP@SiO_2 nanoparticle with the profile analysis.

After that, the surface was functionalized with the photodegradable o-NBA, which was synthesized as a bifunctional molecule capable to react with the surface of the UCNPs@SiO_2 nanoparticles in one side and serve as anchoring point for the Dox in the other side. The immobilization of the o-NBA produced a variation in the UV-Vis spectra of the UCNPs, which showed a new absorption band around 345 nm. Once the o-NBA was immobilized on the surface of the UCNPs, the Dox was linked to the acrylate moiety of the o-NBA by using the thiol-Michael addition[337]. As result, the UV-Vis spectra of the Dox-loaded UCNPs@SiO_2 showed a new absorption band at 550 nm, which corresponded to the anchored Dox (Figure 8.3A).

The UCNPs@SiO_2 emitted multicolor NIR to UV-Vis upconversion fluorescence when they were excited with a 980 nm CW laser, as shown in Figure 8.3B. The emission bands at 345 nm and 365 nm overlapped with the absorption bands of the o-NBA, which could trigger their photodegradation, giving as result the release of the Dox. This could be used to control the drug release and to focus the pharmacological effect on a specific zone, where the light stimuli can be located.

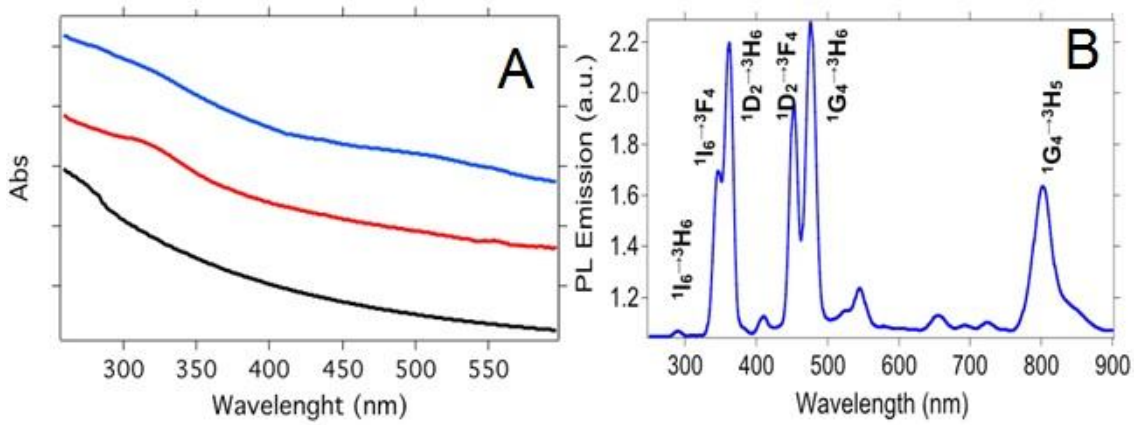

Figure 8.3. A) UV-Vis spectra of the bare UCNPs@SiO_2 nanoparticles (black curve), the *o*-NBA functionalized nanoparticles (red curve) and the doxorubicin functionalized nanoparticles (blue curve). B) Photoluminescence emission spectrum of the UCNPs@SiO_2 nanoparticles using a CW 980 nm laser as excitation source.

8.2.2 Determination of the amount of Doxorubicin attached on the surface of the nanoparticles

The Dox content could not be directly determined in the nanosystem by UV-Vis spectroscopy due to the light scattering of the colloids. To determine the amount of doxorubicin loaded on the surface of the nanoparticles, 4 mg of Dox-loaded UCNP@SiO_2 were poured in 2 mL of MilliQ water, which contained 0.1 mL of HF (35% w/w). This solution was stirred for 24 hours at room temperature to ensure the etching of the silica and therefore the subsequent Dox release. The sample was then centrifuged to remove any precipitates and the red colored supernatant containing only the released Dox was analyzed by UV-Vis spectroscopy. The absorbance was measured at 480 nm and compared against a calibration curve of Dox.

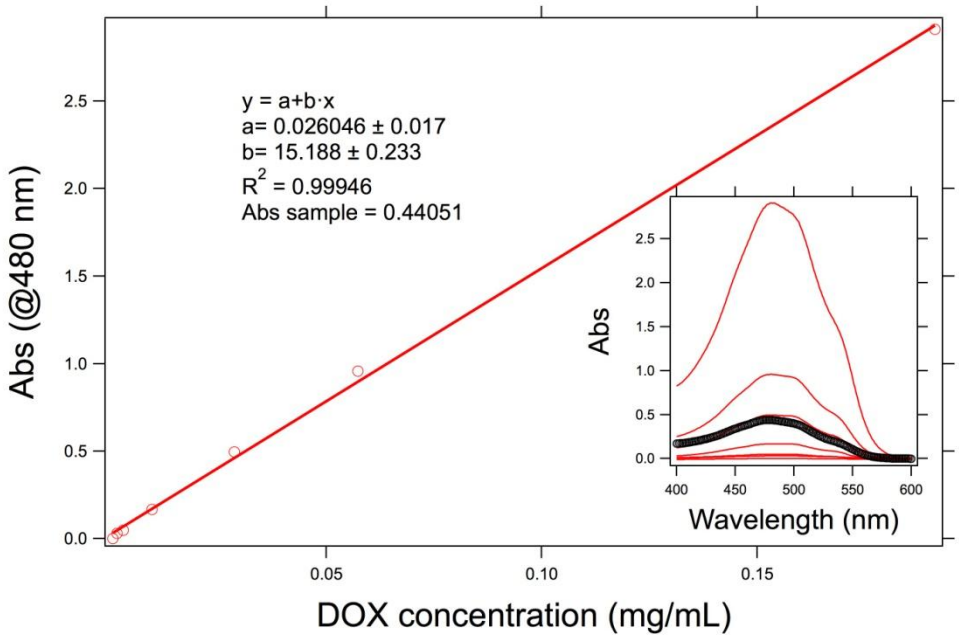

Figure 8.4. UV-Vis calibration curve of doxorubicin in water at 480 nm. The inset shows the absorption spectra of different concentration of doxorubicin (red curves) and the sample (black curve)

From this experiment, we inferred that the drug loading capacity (100 x quantity of drug / quantity of drug + quantity of colloids) was 1.4% w/w, which represents the amount of doxorubicin loaded in the nanosystem. This amount of loaded drug within a nanosystem is low when compared to the drug loading capacity of other methods like physical entrapment within micelles (54% w/w[338]) but it is similar to the amount of drug loaded by other covalent attachment methods (1-5% w/w[339,340]). The drug encapsulation capacity (100 x quantity of loaded drug/ total quantity of used drug) could not be calculated because the Dox was used in excess in the reaction.

8.2.3 Study of the Doxorubicin release upon the NIR light stimulus

The Dox release upon NIR radiation was studied as follows: different samples of Dox-loaded UCNP@SiO_2 were irradiated with a 980 nm CW laser beam with an intensity of 6.2 W/cm^2 for different periods of time. After the exposure, the colloidal dispersions were centrifuged and the supernatant was analyzed to study the amount of Dox released. Figure 8.5A shows the Fluorescence spectra obtained from the supernatants after different irradiation times.

The percentage of Dox released upon NIR radiation was determined with a calibration curve, see Figure 8.5B. As control experiment, the amount of Dox released in the absence of NIR light was also determined (blue points in Figure 8.5B).

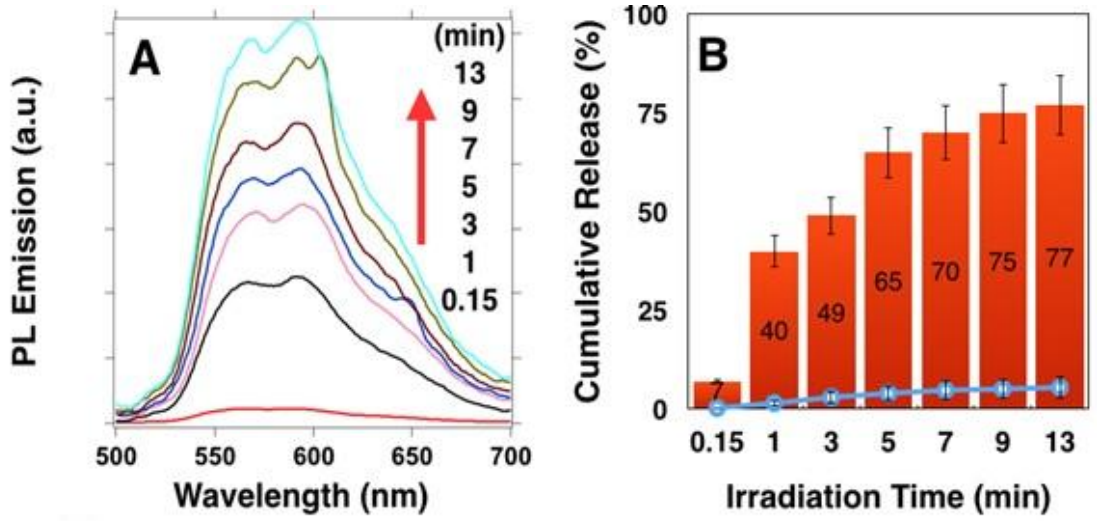

Figure 8.5. A) PL emission of the supernatants (λ_{exc}= 475 nm) obtained after exposing the samples to a 980 nm CW laser with an intensity of 6.3 W/cm^2 from 0.15 to 13 min. B) Cumulative release in percentage of Dox as a function of the irradiation time (bars) and cumulative release of Dox from particle dispersion without NIR stimulus (blue points).

These experiments indicated that effectively, upon exposure with a 980 nm CW laser, the Dox-loaded UCNP@SiO_2 nanoparticles were able to release the drug. The amount of Dox released increased significantly when the system was exposed to the NIR laser for longer periods of time. On the contrary, a negligible amount of drug was observed in the supernatant of non-stimulated samples. These results clearly demonstrated that the NIR light triggered the release of the Dox as a result of the *o*-NBA degradation.

The mechanism involved in the *o*-NBA degradation was described by Wirz *et al*[335]. According with this mechanism, the emission of UV light from the UCNP@SiO_2 at 345 nm and 365 nm could be absorbed by the *o*-NBA linkers, creating an intermediate that after cyclization would evolve towards the molecule cleavage and the subsequent release of the Dox. The Scheme 8.2

summarizes the action mechanism that could occur on the surface of the Dox loaded UCNP@SiO_2 upon irradiation with the 980 nm CW laser light.

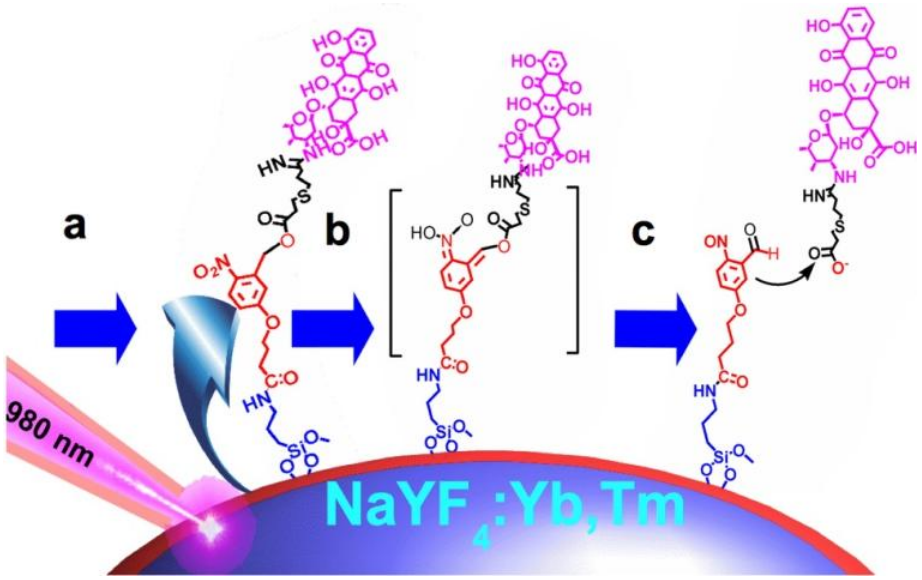

Scheme 8.2. Phototriggered drug release mechanism proposed for the Dox-loaded UCNP@SiO_2 nanoparticles upon exposition to a 980 nm CW laser light.

8.2.4 In-vitro evaluation of the activity of the phototriggered Doxorubicin release system

To study whether the proposed system could be effectively used as a functional NIR-light triggered drug delivery system, we performed in vitro studies with HeLa cells.

We first tested the influence of the NIR radiation on the cell viability. For that, HeLa cells were exposed to the NIR laser beam for 5 min with a 980 nm CW laser with an intensity of 6.3 W/cm^2. The cell viability after 48 h of the irradiation was 100%, as shown in figure 8.6.

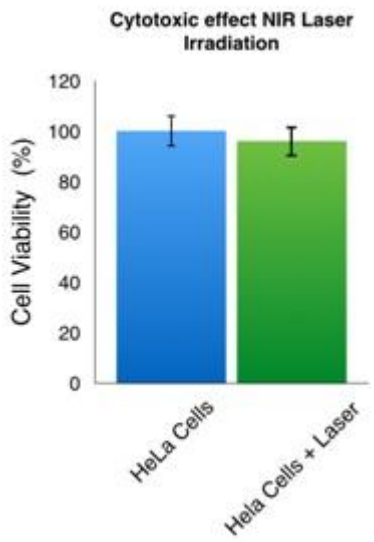

Figure 8.6. Cell viability of HeLa cultures after being irradiated with a CW 980 nm NIR laser light for 5 min (green bar) and the control experiment without laser radiation (blue bar).

In addition, we studied the inner cytotoxicity of the UCNP@SiO_2 nanoparticles as well as the influence of the emitted UV light from UCNP@SiO_2 upon the NIR excitation. In these control experiments, different amounts of UCNP@SiO_2 nanoparticles were poured in a HeLa cell culture in the presence and in the absence of the NIR light. After that, the cell viability was assessed via MTT assay.

As shown in Figure 8.7, the cell viability of samples treated with UCNP@SiO_2+NIR laser and those treated with bare UCNP@SiO_2 without NIR laser showed low cytotoxicity, even after 48 h of incubation at concentrations as high as 100 µg/mL. These results were consistent with previous reports, which have proved that the UCNPs have low toxicity and can be used for *in vivo* studies[341]. Additionally, these experiments showed that under our experimental conditions, not only the NIR light but also the upconverted emission of UV did not show a significant decrease in the cell viability. The low cytotoxicity of the upconverted UV light might be attributed to the short exposition time of the experiments, which was of 5 minutes just after pouring the UCNP@SiO_2 in the cell culture[342]. The cytotoxic effect of the Dox-loaded UCNP@SiO_2 nanoparticles without being exposed to NIR light also presented a very low cytotoxic effect. However, the cell viability was slightly lower than the previous

samples at higher concentrations of sample. However, at higher nanoparticle concentration, the cell viability was slightly lower than in the previous case. This result would confirm the reduction of the Dox accessibility, when the drug is covalently attached on the surface of the nanoparticles.

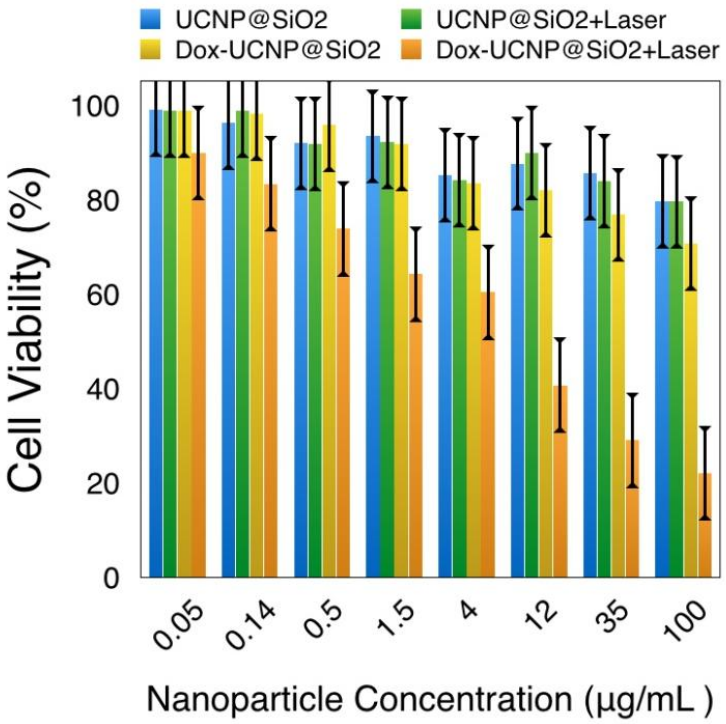

Figure 8.7. Inhibition of HeLa cell growth in the presence of varying concentrations of blue bars: $NaYF_4$:Yb,Tm@SiO_2 nanoparticles; green bars: $NaYF_4$:Yb,Tm@SiO_2 nanoparticles exposed to the laser stimulus; yellow bars: Dox-loaded $NaYF_4$:Yb,Tm@SiO_2 nanoparticles; and orange bars: Dox-loaded $NaYF_4$:Yb,Tm@SiO_2 nanoparticles exposed to the laser stimulus. The laser radiation was constant (5 minutes with an exposure intensity of 6.3 W/cm^{-2}). The cell viability was calculated with the MTT assay after 48 hours of incubation.

By contrast, when the cells were incubated with Dox-loaded UCNP@SiO_2 nanoparticles and were exposed to the 5 minute stimulus of NIR light, the cell viability was reduced progressively as the sample concentration increased, showing a cell viability of 21% at a concentration of 100 µg/mL of nanoparticles. From this result we could infer that the IC_{50} for the Dox-loaded UCNP@SiO_2

nanoparticles was 12 µg/mL. According to the calculated amount of attached drug, this concentration could release around 0.168 µg/mL of Dox. This value is in concordance with the IC_{50} obtained for free Dox, which was 0.16 µg/mL, see Figure 8.8.

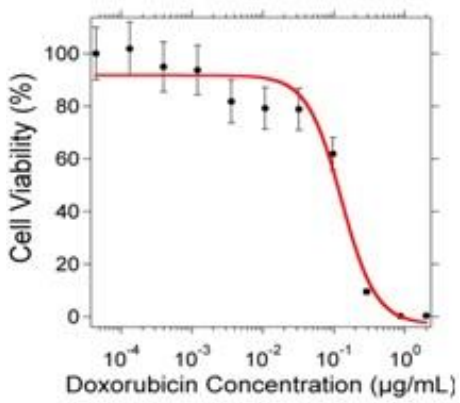

Figure 8.8.Cell viability of HeLa cultures as a function of different concentrations of doxorubicin.

The results of these *in vitro* experiments demonstrated that the cell viability decreased when the Dox was released from the nanoparticles and it was concentration dependent. The drug delivery system consisted in three parts: i) covalently linked drug in the nanoparticles, ii) photocleavable molecule and iii) UV photons upconverted from the 980 nm laser light. The control experiments showed that the cell viability was not significantly affected when any of the parts was missing: The $NaYF_4$:Yb,Tm@SiO_2 nanoparticles without Dox were not toxic for the HeLa cells with or without the laser stimulus and the Dox-loaded $NaYF_4$:Yb,Tm@SiO_2 nanoparticles were not toxic without the laser stimulus. The influence of the 980 nm laser radiation to the cells was also studied and it was found that under our experimental conditions it was negligible.

8.3 Conclusions

In this work a new kind of Dox-loaded $NaYF_4$:Yb,Tm@SiO_2 nanosystem has been successfully prepared. The obtained material showed upconversion fluorescence when it was exposed to a CW 980 nm laser, emitting UV photons at 346 nm and 369 nm. This emission was able to cleave a photodegradable molecule anchored on the surface of the nanoparticles, which acted as linker for covalently immobilizing Doxorubicin. As result, Doxorubicin was released from the nanoparticles when they were exposed to the CW 980 nm laser. This phototriggered drug delivery system was tested *in vitro* on HeLa cells and the cytotoxicity was calculated via MTT assay. The results of this study showed that effectively the Dox-loaded UCNP@SiO_2 nanoparticles reduced the cell viability of the HeLa cancer cells when exposed to the NIR light stimulus. This cytotoxic effect was dependent on the sample concentration and it was not observed in the absence of NIR light, absence of Dox, or absence of nanoparticles, which demonstrated the capacity of the proposed system to minimize the side effects of highly toxic drugs with potential application on cancer therapy.

9. REFERENCES

1. Drexler, Eric - citation to Feynmans talk in 1959. at <http://metamodern.com/2009/12/29/theres-plenty-of-room-at-the-bottom"-feynman-1959/>

2. Drexler, K. E. Molecular engineering: An approach to the development of general capabilities for molecular manipulation. *Proc. Nat. Acad. Sci.* **78,** 5275–5258 (1981).

3. Drexler, E. *Engines of Creation: The Coming Era of Nanotechnology*. (Anchor Books, 1986).

4. Cahay, M. *Quantum Confinement VI: Nanostructured Materials and Devices*. (The Electrochemical Society, 2001).

5. Wagner, V., Dullaart, A., Bock, A. & Zweck, A. The emerging nanomedicine landscape. *Nat. Biotechnol.* **24,** 1211–1217 (2006).

6. Freitas, R. A. What is nanomedicine? *Nanomedicine Nanotechnology, Biol. Med.* **1,** 2–9 (2005).

7. Quansah, J. K. Synthetic polymer for biocompatible biomaterials. in *Materials Literature seminar* (2004).

8. Labet, M. & Thielemans, W. Synthesis of polycaprolactone: a review. *Chem. Soc. Rev.* **38,** 3848–3504 (2009).

9. Anna, C. & Charles, A. Biodegradability of Plastics. *Int. J. Mol. Sci.* **9,** 3722–3742 (1992).

10. Ghoroghchian, P. P. *et al.* Bioresorbable vesicles formed through spontaneous self-assembly of amphiphilic poly(ethylene oxide)-block-polycaprolactone. *Macromolecules* **39,** 1673–1675 (2006).

11. Veronese, F. & Harris, J. Introduction and overview of peptide and protein pegylation. *Adv. Drug Deliv. Rev.* **54,** 453–456 (2002).

12. Letchford, K. & Burt, H. A review of the formation and classification of amphiphilic block copolymer nanoparticulate structures: micelles, nanospheres, nanocapsules and polymersomes. *Eur. J. Pharm. Biopharm.* **65,** 259–269 (2007).

13. Cho, H. K., Cheong, I. W., Lee, J. M. & Kim, J. H. Polymeric nanoparticles, micelles and polymersomes from amphiphilic block copolymer. *Korean J. Chem. Eng.* **27,** 731–740 (2010).

14. Raspaud, E., Lairez, D., Adam, M. & Carton, J. Triblock Copolymers in a Selective Solvent. Aggregation Process in Dilute Solution. *Macromolecules* **27,** 2956–2964 (1994).

15. Moorefield, C. N. & Newkome, G. R. Unimolecular micelles: Supramolecular use of dendritic constructs to create versatile molecular containers. *Comptes Rendus Chim.* **6,** 715–724 (2003).

16. Li, G. *et al.* Polymeric micelles with water-insoluble drug as hydrophobic moiety for drug delivery. *Biomacromolecules* **12,** 2016–2026 (2011).

17. Alvarez-Lorenzo, C., Sosnik, A. & Concheiro, A. PEO-PPO block copolymers for passive micellar targeting and overcoming multidrug resistance in cancer therapy. *Curr. Drug Targets* **12,** 1112–1130 (2011).

18. Xu, W., Ling, P. & Zhang, T. Polymeric micelles, a promising drug delivery system to enhance bioavailability of poorly water-soluble drugs. *J. Drug Deliv.* **2013,** 340315 (2013).

19. Hiemenz, P. C. & Rajagopalan, R. *Principles of Colloids and Surface Chemistry*. (Marcel Dekker Inc, 1997).

20. Pugh, R. J. & Bergström, L. *Surface and Colloid Chemistry in Advanced Ceramics Processing*. (Marcel Dekker Inc, 1994).

21. Serrano-Ruiz, D. *et al.* Nanosegregated polymeric domains on the surface of Fe3O4@SiO2 nanoparticles. *J. Polym. Sci. Part A Polym. Chem.* **52,** 2966–2975 (2014).

22. Laurent, S. *et al.* Magnetic Iron Oxide Nanoparticles: Synthesis, Stabilization, Vectorization, Physicochemical Characterizations, and Biological Applications. *Chem. Rev.* **108,** 2064–2110 (2008).

23. Obare, S. O., Jana, N. R. & Murphy, C. J. Preparation of Polystyrene- and Silica-Coated Gold Nanorods and Their Use as Templates for the Synthesis of Hollow Nanotubes. *Nano Lett.* **1,** 601–603 (2001).

24. Thanh, N. T. K., Maclean, N. & Mahiddine, S. Mechanisms of nucleation and growth of nanoparticles in solution. *Chem. Rev.* **114,** 7610–30 (2014).

25. Park, J., Joo, J., Soon, G. K., Jang, Y. & Hyeon, T. Synthesis of monodisperse spherical nanocrystals. *Angew. Chemie - Int. Ed.* **46,** 4630–4660 (2007).

26. Serrano-Ruiz, D. *et al.* Synthesis and Chemical Modification of Magnetic Nanoparticles Covalently Bound to Polystyrene-SiCl2-Poly(2-vinylpyridine). *J Polym Sci Part B Polym Phys* **48,** 1668–1675 (2010).

27. Senpan, A. *et al.* Conquering the dark side: Colloidal iron oxide nanoparticles. *ACS Nano* **3,** 3917–3926 (2009).

28. Massart, R. Preparation of Aqueous Magnetic Liquids in Alkaline and Acidic Media. *IEEE Trans. Magn.* **17,** 1981–1982 (1981).

29. Sugimoto, T. & Matijevic, E. Formation of Uniform Spherical Magnetite Particles by Cristallization from Ferrous Hydroxide Gels. *J. Colloid Interface Sci.* **74,** 227–243 (1980).

30. Xuan, S., Wang, Y.-X. J., Yu, J. C. & Leung, K. C.-F. Tuning the Grain Size and Particle Size of Superparamagnetic Fe3O4 Microparticles. *Chem. Mater.* **21,** 5079–5087 (2009).

31. Soon, G. K. *et al.* Kinetics of monodisperse iron oxide nanocrystal formation by 'heating-up' process. *J. Am. Chem. Soc.* **129,** 12571–12584 (2007).

32. Ho, C. H. *et al.* Shape-controlled growth and shape-dependent cation site occupancy of monodisperse Fe3O4 nanoparticles. *Chem. Mater.* **23,** 1753–1760 (2011).

33. Gupta, A. K. & Gupta, M. Synthesis and surface engineering of iron oxide nanoparticles for biomedical applications. *Biomaterials* **26,** 3995–4021 (2005).

34. Tartaj, P., del Puerto Morales, M., Veintemillas-Vergaguer, S., Gonzalez-Carreño, T. & Serna, C. J. Progress in the preparation of magnetic nanoparticles for applications in biomedicine. *J. Phys. D. Appl. Phys.* **42,** 182–197 (2009).

35. Colombo, M. *et al.* Biological applications of magnetic nanoparticles. *Chem. Soc. Rev.* **41,** 4306 (2012).

36. Laurenti, M. *et al.* Synthesis of Thermosensitive Microgels with a Tunable Magnetic Core. *Langmuir* **27,** 10484–10491 (2011).

37. Edelman, R. R. & Warach, S. Magnetic Resonance Imaging. *N. Engl. J. Med.* **328,** 708–716 (1993).

38. Shokrollahi, H. Contrast agents for MRI. *Mater. Sci. Eng. C* **33,** 4485–4497 (2013).

39. Dobson, J. Magnetic Nanoparticles for Drug Delivery. *Drug Deliv. Res.* **67,** 55–60 (2006).

40. Peng, X.-H. *et al.* Targeted magnetic iron oxide nanoparticles for tumor imaging and therapy. *Int. J. Nanomedicine* **3,** 311–321 (2008).

41. Sensenig, R., Sapir, Y., MacDonald, C., Cohen, S. & Polyak, B. Magnetic nanoparticle-based approaches to locally target therapy and enhance tissue regeneration in vivo. *Nanomedicine* **7,** 1425–1442 (2012).

42. Chomoucka, J. *et al.* Magnetic nanoparticles and targeted drug delivering. *Pharmacol. Res.* **62,** 144–149 (2010).

43. Serrano-Ruiz, D., Laurenti, M., Ruiz-Cabello, J., Lopez-Cabarcos, E. & Rubio-Retama, J. Hybrid microparticles for drug delivery and magnetic resonance imaging. *J. Biomed. Mater. Res. Part B Appl. Biomater.* **101B,** 498–505 (2013).

44. Sonvico, F. *et al.* Folate-Conjugated Iron Oxide Nanoparticles for Solid Tumor Targeting as Potential Specific Magnetic Hyperthermia Mediators: Synthesis , Physicochemical Characterization , and in Vitro Experiments Folate-Conjugated Iron Oxide Nanoparticles for Solid Tumor. *Bioconjugate Chem.* **16,** 1181–1188 (2005).

45. Jones, M. R., Osberg, K. D., MacFarlane, R. J., Langille, M. R. & Mirkin, C. a. Templated techniques for the synthesis and assembly of plasmonic nanostructures. *Chem. Rev.* **111,** 3736–3827 (2011).

46. Brust, M., Walker, M., Bethell, D., Schiffrin, D. J. & Whyman, R. Synthesis of thiol Derivatised Gold Nanoparticles in a Two Phase Liquid/Liquid System. *J. Chem. Soc., Chem. Commun.* 801 (1994).

47. Turkevich, J., Stevenson, P. C. & Hillier, J. A study of the nucleation and growth processes in the synthesis of colloidal gold. *Discuss. Faraday Soc.* **11,** 55–75 (1951).

48. Niu, W., Zhang, L. & Gu, X. Seed mediated growth of noble metal nanocrystals: crystal growth and shape control. *Nanoscale* **5,** 3172–3181 (2013).

49. Liz-Marzan, L. M. Nanometals: formation and color. *Mater. Today* **7,** 26–31 (2004).

50. Mie, G. Contributions to the optics of diffuse media, specially colloid metal solutions. *Ann. Phys.* **25,** 377–445 (1908).

51. Collin, R. *Field Theory of Guided Waves*. (Wiley, 1990).

52. Raether, H. *Surface Plasmons*. (Springer, 1998).

53. Moskovits, M. Surface-enhanced spectroscopy. *Rev. Mod. Phys.* **57,** 783–826 (1985).

54. Mirkin, C. A. & Ratner, M. A. Controlled synthesis and quantum-size effect in gold-coated nanoparticles. *Annu. Rev. Phys. Chem.* **101,** 1593 (1997).

55. Lukyanchuk, B. *et al.* The Fano resonance in plasmonic nanostructures and metamaterials. *Nat. Mater.* **9,** 707–715 (2010).

56. Maier, S. *Plasmonics: Fundamentals and applications*. (Springer, 2007).

57. Camden, J. P., Dieringer, J. a, Zhao, J., Duyne, R. P. Van & Duyne, R. P. V. a N. Controlled Plasmonic Nanostructures for Surface-Enhanced Spectroscopy and Sensing. *Acc. Chem. Res.* **41,** 1653–1661 (2008).

58. Corma, A. & Garcia, H. Supported gold nanoparticles as catalysts for organic reactions. *Chem. Soc. Rev.* **37,** 2096–2126 (2008).

59. Linic, S., Christopher, P. & Ingram, D. B. Plasmonic-metal nanostructures for efficient conversion of solar to chemical energy. *Nat. Mater.* **10,** 911–921 (2011).

60. Liao, H., Nejl, C. L. & Hafner, J. H. Biomedical applications of plasmon resonant metal nanoparticles. *Nanomedicine* **1,** 201–208 (2006).

61. Gao, J., Huang, X., Liu, H., Zan, F. & Ren, J. Colloidal stability of gold nanoparticles modified with thiol compounds: bioconjugation and application in cancer cell imaging. *Langmuir* **28,** 4464–71 (2012).

62. McFarland, A. D. & Van Duyne, R. P. Single Silver Nanoparticles As Real Time Optical Sensors With Zeptomole Sensitivity. *Nano Lett.* **3,** 1057–1062. (2003).

63. Haes, A. J. *et al.* Nanoscale Optical Biosensor: Short Range Distance Dependence of the Localized Surface Plasmon Resonance of Noble Metal Nanoparticles. *J. Phys. Chem. B* **108,** 6961–6968 (2004).

64. Dasary, S. S. R., Singh, A. K., Senapati, D., Yu, H. & Ray, P. C. Gold nanoparticle based label-free SERS probe for ultrasensitive and selective detection of trinitrotoluene. *J. Am. Chem. Soc.* **131,** 13806–13812 (2009).

65. Shafer-Peltier, K. E., Haynes, C. L., Glucksberg, M. R. & Duyne, R. P. Van. Toward a Glucose Biosensor Based on Surface-Enhanced Raman Scattering. *J. Am. Chem. Soc.* **125,** 588–593 (2003).

66. Fang, Z. *et al.* Evolution of light-induced vapor generation at a liquid-immersed metallic nanoparticle. *Nano Lett.* **13,** 1736–1742 (2013).

67. Neumann, O. *et al.* Solar vapor generation enabled by nanoparticles. *ACS Nano* **7,** 42–49 (2013).

68. Wu, G. *et al.* Remotely triggered liposome release by near-infrared light absorption via hollow gold nanoshells. *J. Am. Chem. Soc.* **130,** 8175–8177 (2008).

69. O'Neal, D. P., Hirsch, L. R., Halas, N. J., Payne, J. D. & West, J. L. Photo-thermal tumor ablation in mice using near infrared-absorbing nanoparticles. *Cancer Lett.* **209,** 171–176 (2004).

70. Kang, B., Mackey, M. a. & El-Sayed, M. a. Nuclear targeting of gold nanoparticles in cancer cells induces DNA damage, causing cytokinesis arrest and apoptosis. *J. Am. Chem. Soc.* **132,** 1517–1519 (2010).

71. Huang, X. H., El-Sayed, I. H., Qian, W. & El-Sayed, M. a. Cancer cell imaging and photothermal therapy in the near-infrared region by using gold nanorods. *J. Am. Chem. Soc.* **128,** 2115–2120 (2006).

72. Xi, D. *et al.* Gold nanoparticles as computerized tomography (CT) contrast agents. *RSC Adv.* **2,** 12515–12524 (2012).

73. Hainfeld, J. F., Slatkin, D. N., Focella, T. M. & Smilowitz, H. M. Gold nanoparticles: a new X-ray contrast agent. *Br. J. Radiol.* **79,** 248–253 (2006).

74. Contreras-Caceres, R. *et al.* Temperature Controlled Fluorescence on Au@Ag@PNIPAM-PTEBS Microgels: Effect of the Metal Core Size on the MEF Extension. *Langmuir* **30,** 15560–15567 (2014).

75. Kim, J. S. *et al.* Antimicrobial effects of silver nanoparticles. *Nanomedicine Nanotechnology, Biol. Med.* **3,** 95–101 (2007).

76. El-Sayed, M. A. Small Is Different: Shape-,Size-, and Composition-Dependent Properties of Some Colloidal Semiconductor Nanocrystals. *Acc. Chem. Res* **37,** 326 (2004).

77. Dabbousi, B. O. *et al.* (CdSe)ZnS core-shell quantum dots: Synthesis and characterization of a series of highly luminescent nanocrystallites. *J. Phys. Chem. B* **101,** 9463–9475 (1997).

78. Yu, W. W., Qu, L., Guo, W. & Peng, X. Experimental Determination of the Extinction Coefficient of CdTe , CdSe , and CdS Nanocrystals. *Chem. Mater.* **125,** 2854–2860 (2003).

79. Gonzalez-Pedro, V., Xu, X., Mora-Sero, I. & Bisquert, J. Modeling High-Efficiency Quantum Dot Solar Cells. *ACS Nano* **4,** 5783–5790 (2010).

80. Medintz, I. L., Uyeda, H. T., Goldman, E. R. & Mattoussi, H. Quatum dot bioconjugates for imaging, labelling and sensing. *Nat. Mater.* **4,** 435–446 (2005).

81. Klostranec, J. M. & Chan, W. C. W. Quantum Dots in Biological and Biomedical Research: Recent Progress and Present Challenges. *Adv. Mater.* **18,** 1953–1964 (2006).

82. Wang, F. *et al.* Simultaneous phase and size control of upconversion nanocrystals through lanthanide doping. *Nature* **463,** 1061–1065 (2010).

83. Wright, J. C. Up-conversion and excited state energy transfer in rare-earth doped materials. *Top. Appl. Phys.* **15,** 239–295 (2007).

84. Wang, F. & Liu, X. Recent advances in the chemistry of lanthanide-doped upconversion nanocrystals. *Chem. Soc. Rev.* **38,** 976–989 (2009).

85. Chen, G., Yang, C. & Prasad, P. N. Nanophotonics and Nanochemistry: Controlling the Excitation Dynamics for Frequency Up- and Down-Conversion in Lanthanide-Doped Nanoparticles. *Acc. Chem. Res.* **46,** 1474–1486 (2013).

86. Chen, G., Ågren, H., Ohulchanskyy, T. Y. & Prasad, P. N. Light upconverting core–shell nanostructures: nanophotonic control for emerging applications. *Chem. Soc. Rev.* **44,** 1680–1713 (2015).

87. Liu, H., Liang, H., Somesfalean, G., Chen, G. & Zhang, Z. Upconversion Emission Enhancement in Yb^{3+}/Er^{3+}-Codoped Y_2O_3 Nanocrystals by Tridoping with Li^+ Ions. *J. Phys. Chem. C* **112,** 12030–12036 (2008).

88. Wang, Y., Tu, L., Zhao, J. & Sun, Y. Upconversion luminescence of β-$NaYF_4$: Yb^{3+}, Er^{3+}@β-$NaYF_4$ core/shell nanoparticles: Excitation power density and surface dependence. *J. Phys. Chem. C* **113,** 7164–7169 (2009).

89. Boyer, J. C., Cuccia, L. a & Capobianco, J. a. Synthesis of Colloidal Upconverting $NaYF_4$:Er^{3+}/Yb^{3+} and Tm^{3+}/Yb^{3+} Monodisperse Nanocrystals. *Nano Lett.* **7,** 847–852 (2007).

90. Li, C., Quan, Z., Yang, J., Yang, P. & Lin, J. Highly Uniform and Monodisperse $NaYF_4:Ln^{3+}$ (Ln = Eu, Tb, Yb/Er, and Yb/Tm) Hexagonal Microprism Crystals: Hydrothermal Synthesis and Luminescent Properties. *Inorg. Chem.* **46,** 6329–6337 (2007).

91. Voorhees, P. W. The theory of Ostwald ripening. *J. Stat. Phys.* **38,** 231–252 (1985).

92. Li, Z. & Zhang, Y. An efficient and user-friendly method for the synthesis of hexagonal-phase $NaYF_4$:Yb, Er/Tm nanocrystals with controllable shape and upconversion fluorescence. *Nanotechnology* **19,** 345606–345611 (2008).

93. Chen, G., Qiu, H., Prasad, P. N. & Chen, X. Upconversion nanoparticles: Design, nanochemistry, and applications in Theranostics. *Chem. Rev.* **114,** 5161–5214 (2014).

94. Auzel, F. Upconversion and Anti-Stokes Processes with f and d Ions in Solids. *Chem. Rev.* **104,** 139–173 (2004).

95. Chen, G., Ohulchanskyy, T. Y., Kumar, R., Ågren, H. & Prasad, P. N. Ultrasmall monodisperse $NaYF_4:Yb^{3+}/Tm^{3+}$ nanocrystals with enhanced near-infrared to near-infrared upconversion photoluminescence. *ACS Nano* **4,** 3163–3168 (2010).

96. Pushkar, A. A., Uvarova, T. V. & Kiiko, V. V. Up-conversion multiwave (White) luminescence in the visible spectral range under excitation by IR laser diodes in the active $BaY_2F_8:Yb^{3+},Pr^{3+}$ medium. *Opt. Spectrosc.* **111,** 273–276 (2011).

97. Bouzigues, C., Gacoin, T. & Alexandrou, A. Biological applications of rare-earth based nanoparticles. *ACS Nano* **5,** 8488–8505 (2011).

98. Abdul Jalil, R. & Zhang, Y. Biocompatibility of silica coated $NaYF_4$ upconversion fluorescent nanocrystals. *Biomaterials* **29,** 4122–4128 (2008).

99. Yan, B., Boyer, J. C., Habault, D., Branda, N. R. & Zhao, Y. Near infrared light triggered release of biomacromolecules from hydrogels loaded with upconversion nanoparticles. *J. Am. Chem. Soc.* **134,** 16558–16561 (2012).

100. Liu, J., Bu, W., Pan, L. & Shi, J. NIR-triggered anticancer drug delivery by upconverting nanoparticles with integrated azobenzene-modified mesoporous silica. *Angew. Chemie - Int. Ed.* **52,** 4375–4379 (2013).

101. Wu, S. *et al.* Multiplexed fluorescence resonance energy transfer aptasensor between upconversion nanoparticles and graphene oxide for the simultaneous determination of mycotoxins. *Anal. Chem.* **84,** 6263–6270 (2012).

102. Liu, C., Wang, Z., Jia, H. & Li, Z. Efficient fluorescence resonance energy transfer between upconversion nanophosphors and graphene oxide: a highly sensitive biosensing platform. *Chem. Commun.* **47,** 4661–4663 (2011).

103. Chatterjee, D. K., Rufaihah, A. J. & Zhang, Y. Upconversion fluorescence imaging of cells and small animals using lanthanide doped nanocrystals. *Biomaterials* **29,** 937–943 (2008).

104. Xiong, L. *et al.* High Contrast Upconversion Luminescence Targeted Imaging in Vivo Using Peptide-Labeled Nanophosphors. *Anal. Chem.* **81,** 8687–8694 (2009).

105. Wang, M. *et al.* Immunolabeling and NIR-Excited Fluorescent Imaging of HeLa Cells by Using NAYF4:Yb,Er Upconversion Nanoparticles. *ACS Nano* **3,** 1580–1586 (2009).

106. Chen, G. *et al.* ($NaYbF_4:Tm^{3+}$)/CaF2 Core/Shell Nanoparticles with Efficient Near-Infrared to Near-Infrared Upconversion for High-Contrast Deep Tissue Bioimaging. *ACS Nano* **6,** 8280–8287 (2012).

107. Xu, C. T., Axelsson, J. & Andersson-Engels, S. Fluorescence diffuse optical tomography using upconverting nanoparticles. *Appl. Phys. Lett.* **94,** 11–14 (2009).

108. Xu, C. T. *et al.* High-resolution fluorescence diffuse optical tomography developed with nonlinear upconverting nanoparticles. *ACS Nano* **6,** 4788–4795 (2012).

109. He, M. *et al.* Dual Phase-Controlled Synthesis of Uniform Lanthanide-Doped NaGdF4 Upconversion Nanocrystals via an OA/Ionic Liquid Two-Phase System for In Vivo Dual-Modality imaging. *Adv. Mater.* **21,** 4470–4477 (2011).

110. Sun, Y. *et al.* Fluorine-18 labeled rare-earth nanoparticles for positron emission tomography (PET) imaging of sentinel lymph node. *Biomaterials* **32,** 2999–3007 (2011).

111. Cheng, L. *et al.* Multifunctional nanoparticles for upconversion luminescence/MR multimodal imaging and magnetically targeted photothermal therapy. *Biomaterials* **33,** 2215–2222 (2012).

112. Hopper, C. Photodynamic therapy: a clinical reality in the treatment of cancer. *Lancet Oncol.* **1,** 212–219 (2000).

113. Idris, N. M. *et al.* In vivo photodynamic therapy using upconversion nanoparticles as remote-controlled nanotransducers. *Nat. Med.* **18,** 1580–1585 (2012).

114. Stöber, W., Fink, A. & Bohn, E. Controlled Growth of Monodisperse Silica Spheres in the Micron Size Range. *J. Colloid Interface Sci.* **26,** 62–69 (1968).

115. NanoComposix. *UV/Vis/IR Spectroscopy Analysis of Nanoparticles*. (2012). at <https://cdn.shopify.com/s/files/1/0257/8237/files/nanoComposix_Guidelines_for_UV-vis_Analysis.pdf>

116. Wang, L. *et al.* Watching Silica Nanoparticles Glow in the Biological World. *Anal. Chem.* **1,** 647–654 (2006).

117. Matsukawa, S. & Ando, I. A Study of Self-Diffusion of Molecules in Polymer Gel by Pulsed-Gradient Spin - Echo ^{1}H NMR. *Macromolecules* **29,** 7136–7140 (1996).

118. Masaro, L., Zhu, X. X. & Macdonald, P. M. Self-diffusion of oligo- and poly(ethylene glycol)s in poly(vinyl alcohol) aqueous solutions as studied by pulsed-gradient NMR spectroscopy. *Macromolecules* **31,** 3880–3885 (1998).

119. Yamane, Y., Matsui, M., Kimura, H., Kuroki, S. & Ando, I. Diffusional inhomogeneity of probe molecules in chemically cross-linked polymer gels as studied by time-dependent diffusion NMR. *Macromolecules* **36,** 5655–5660 (2003).

120. Kamiguchi, K., Kuroki, S., Satoh, M. & Ando, I. Diffusion of probe polystyrenes with different molecular weights in poly(methyl methacrylate) gels and inhomogeneity of the network structure as studied by time-dependent diffusion NMR spectroscopy. *Polymer* **46,** 11470–11475 (2005).

121. Johnson Jr., C. S. Diffusion ordered nuclear magnetic resonance spectroscopy: principles and applications. *Prog. Nucl. Magn. Reson. Spectrosc.* **34,** 203–256 (1999).

122. Park, J. *et al.* Ultra-large-scale syntheses of monodisperse nanocrystals. *Nat. Mater.* **3,** 891–895 (2004).

123. Wang, L. *et al.* Monodispersed Core-Shell Fe3O4@Au Nanoparticles. *J. Phys. Chem. B* **109,** 21593–21601 (2005).

124. Li, G. Z. *et al.* Investigation into Thiol-(meth)acrylate Michael Addition Reactions Using Amine and Phosphine Catalysts. *Polym. Chem.* **1,** 1196–1203 (2010).

125. Mya, K. Y., Lin, E. M. J., Gudipati, C. S., Gose, H. B. A. S. & He, C. Self-assembly of block copolymer micelles: synthesis via reversible addition-fragmentation chain transfer polymerization and aqueous solution properties. *J. Phys. Chem. B* **114,** 9128–9134 (2010).

126. Du, H., Zhu, J. & Jiang, W. Study of controllable aggregation morphology of ABA amphiphilic triblock copolymer in dilute solution by changing the solvent property. *J. Phys. Chem. B* **111,** 1938–1945 (2007).

127. Wei, L., Nakayama, M., Akimoto, J. & Okano, T. Effect of block compositions of amphiphilic block copolymers on the physicochemical properties of polymeric micelles. *Polymer* **52,** 3783–3790 (2011).

128. Discher, D. E. & Eisenberg, A. Polymer vesicles. *Science* **297,** 967–973 (2002).

129. Geng, Y. *et al.* Shape effects of filaments versus spherical particles in flow and drug delivery. *Nat. Nanotechnol.* **70,** 249–255 (2007).

130. Mintzer, M. a & Simanek, E. E. Nonviral Vectors for Gene Delivery. *Chem. Rev.* **109,** 259–302 (2008).

131. Duncan, R. The dawning era of polymer therapeutics. *Nat Rev Drug Discov* **2,** 347–360 (2003).

132. Börner, H. G. Strategies exploiting functions and self-assembly properties of bioconjugates for polymer and materials sciences. *Prog. Polym. Sci.* **34,** 811–851 (2009).

133. Ding, J. & Lui, G. Polyisoprene-block-poly(2-cinnamoylethylmethacrylate) Vesicles and their Aggregates. *Macromolecules* **30,** 655–657 (1997).

134. Larson, N. & Ghandehari, H. Polymeric conjugates for drug delivery. *Chem. Mater.* **24,** 840–853 (2012).

135. Suksiriworapong, J., Sripha, K., Kreuter, J. & Junyaprasert, V. B. Investigation of polymer and nanoparticle properties with nicotinic acid and p -aminobenzoic acid grafted on poly(ε-caprolactone)-poly(ethylene glycol)-poly(ε-caprolactone) via click chemistry. *Bioconjug. Chem.* **22,** 582–594 (2011).

136. Kabanov, A. V., Batrakova, E. V. & Miller, D. W. Pluronic block copolymers as modulators of drug efflux transporter activity in the blood–brain barrier. *Adv. Drug Deliv. Rev.* **55,** 151–164 (2003).

137. Hadjichristidis, N. Synthesis of Miktoarm Star Polymers. *J. Polym. Sci. Part A Polym. Chem.* **37,** 857–871 (1999).

138. Hadjichristidis, N., Iatrou, H., Pitsikalis, M. & Mays, J. Macromolecular architectures by living and controlled/living polymerizations. *Prog. Polym. Sci.* **31,** 1068–1132 (2006).

139. Gao, H. & Matyjaszewski, K. Low-polydispersity star polymers with core functionality by cross-linking macromonomers using functional ATRP initiators. *Macromolecules* **40,** 399–401 (2007).

140. Nabid, M. R. *et al.* Self-assembled micelles of well-defined pentaerythritol-centered amphiphilic A_4B_8 star-block copolymers based on PCL and PEG for hydrophobic drug delivery. *Polymer* **52,** 2799–2809 (2011).

141. Zhang, X., Xia, J. & Matyjaszewski, K. End-Functional Poly(tert -butyl acrylate) Star Polymers by Controlled Radical Polymerization. *Macromolecules* **33,** 2340–2345 (2000).

142. Abraham, S., Ha, C.-S. & Kim, I. Synthesis of poly(styrene-block-tert-butyl acrylate) star polymers by atom transfer radical polymerization and micellization of their hydrolyzed polymers. *J Polym Sci Part A* **31,** 6367–6378 (2006).

143. Matyjaszewski, K. & Xia, J. Atom transfer radical polymerization. *Chem. Rev.* **101,** 2921–2990 (2001).

144. Tsoukatos, T., Pispas, S. & Hadjichristidis, N. Star-branched polystyrenes by nitroxide living free-radical polymerization. *J. Polym. Sci. Part A Polym. Chem.* **39,** 320–325 (2001).

145. Pasquale, A. J. & Long, T. E. Synthesis of star-shaped polystyrenes via nitroxide-mediated stable free-radical polymerization. *J. Polym. Sci. Part A Polym. Chem.* **39,** 216–223 (2001).

146. Hawker, C. J. Architectural Control in 'Living' Free Radical Polymerizations: Preparation of Star and Graft Polymers. *Angew. Chemie - Int. Ed.* **34,** 1456–1459 (2003).

147. Trollsås, M. *et al.* Highly Functional Branched and Dendri-Graft Aliphatic Polyesters through Ring Opening Polymerization. *Macromolecules* **31,** 2756–2763 (1998).

148. Kricheldorf, H. R. Polypeptides and 100 years of chemistry of amino acid N-carboxyanhydrides. *Angew. Chemie - Int. Ed.* **45,** 5752–5784 (2006).

149. Mosqueira, V. C. F. *et al.* Relationship between complement activation, cellular uptake and surface physicochemical aspects of novel PEG-modified nanocapsules. *Biomaterials* **22,** 2967–2979 (2001).

150. Photos, P. J., Bacakova, L., Discher, B., Bates, F. S. & Discher, D. E. Polymer vesicles in vivo: Correlations with PEG molecular weight. *J. Control. Release* **90,** 323–334 (2003).

151. Woodle, M. C. Sterically stabilized liposome therapeutics. *Adv. Drug Deliv. Rev.* **16,** 249–265 (1995).

152. Takeuchi, T. *et al.* Structure-activity relationships of carboline and carbazole derivatives as a novel class of ATP-competitive kinesin spindle protein inhibitors. *J. Med. Chem.* **54,** 4839–4846 (2011).

153. Vila-Jato, J.-L. & Calvo, P. in *Nanotecnología Farmacéutica, Realidades y Posibilidades Farmacoterapéuticas* 251–312 (Real Academia Nacional de Farmacia, 2009).

154. Rajagopal, K. *et al.* Curvature-coupled hydration of semicrystalline polymer amphiphiles yields flexible worm micelles but favors rigid vesicles: Polycaprolactone-based block copolymers. *Macromolecules* **43,** 9736–9746 (2010).

155. Srinivas, G., Discher, D. E. & Klein, M. L. Key roles for chain flexibility in block copolymer membranes that contain pores or make tubes. *Nano Lett.* **5,** 2343–2349 (2005).

156. Strandman, S. *et al.* Effect of the number of arms on the association of amphiphilic star block copolymers. *Macromolecules* **41,** 8855–8864 (2008).

157. Le Dévédec, F., Strandman, S., Baille, W. E. & Zhu, X. X. Functional star block copolymers with a cholane core: Thermo-responsiveness and aggregation behavior. *Polymer* **54,** 3898–3903 (2013).

158. Tao, W. *et al.* A linear-hyperbranched supramolecular amphiphile and its self-assembly into vesicles with great ductility. *J. Am. Chem. Soc.* **134,** 762–764 (2012).

159. Hermel-Davidock, T. J., Tang, S. H., Murray, D. J. & Hahn, S. F. Control of the Block Copolymer Morphology in Templated Epoxy Thermosets. *J. Polym. Sci. Part B Polym. Phys.* **34,** 3338–3348 (2007).

160. Dean, J. M., Grubbs, R. B., Saad, W., Cook, R. F. & Bates, F. S. Mechanical properties of block copolymer vesicle and micelle modified epoxies. *J. Polym. Sci. Part B Polym. Phys.* **41,** 2444–2456 (2003).

161. Zhang, J., Wang, L. Q., Wang, H. & Tu, K. Micellization phenomena of amphiphilic block copolymers based on methoxy poly(ethylene glycol) and either crystalline or amorphous poly(caprolactone-b-lactide). *Biomacromolecules* **7,** 2492–2500 (2006).

162. Dong, W. F., Kishimura, A., Anraku, Y., Chuanoi, S. & Kataoka, K. Monodispersed polymeric nanocapsules: spontaneous evolution and morphology transition from reducible hetero-PEG PICmicelles by controlled degradation. *J. Am. Chem. Soc.* **131,** 3804–3805 (2009).

163. Koide, A. *et al.* Semipermeable polymer vesicle (PICsome) self-assembled in aqueous medium from a pair of oppositely charged block copolymers: Physiologically stable micro-/nanocontainers of water-soluble macromolecules. *J. Am. Chem. Soc.* **128,** 5988–5989 (2006).

164. Zhou, Y. & Yan, D. Real-time membrane fusion of giant polymer vesicles. *J. Am. Chem. Soc.* **127,** 10468–10469 (2005).

165. Rubio-Retama, J. *et al.* Polymer chain dynamics of core-shell thermosensitive microgels. *Macromolecules* **41,** 4739–4745 (2008).

166. Marrink, S. J. & Mark, A. E. The mechanism of vesicle fusion as revealed by molecular dynamics simulations. *J. Am. Chem. Soc.* **125,** 11144–11145 (2003).

167. Vilgis, T. & Halperin, A. Aggregation of coil-crystalline block copolymers: equilibrium crystallization. *Macromolecules* **24,** 2090–2095 (1991).

168. Lin, C. M., Li, C. S., Sheng, Y. J., Wu, D. T. & Tsao, H. K. Size-dependent properties of small unilamellar vesicles formed by model lipids. *Langmuir* **28,** 689–700 (2012).

169. Semenov, A. M., Nyrkova, I. A. & Khokhlov, A. R. Polymers with Strongly Interacting Groups: Theory for Nonspherical Multiplets. *Macromolecules* **28,** 7491–7500 (1995).

170. Gaucher, G., Marchessault, R. H. & Leroux, J. C. Polyester-based micelles and nanoparticles for the parenteral delivery of taxanes. *J. Control. Release* **143,** 2–12 (2010).

171. Selvan, S. T., Patra, P. K., Ang, C. Y. & Ying, J. Y. Synthesis of silica-coated semiconductor and magnetic quantum dots and their use in the imaging of live cells. *Angew. Chemie - Int. Ed.* **46,** 2448–2452 (2007).

172. Xie, H. *et al.* Fe3O4/Au Core/Shell Nanoparticles Modified with Ni^{2+} - Nitrilotriacetic Acid Specific to Histidine-Tagged Proteins. *J. Phys. Chem. C* **114,** 4825–4830 (2010).

173. Wang, S. H. *et al.* Dendrimer-Functionalized Iron Oxide Nanoparticles for Specific Tageting and Imaging of Cancer Cells. *Adv. Mater.* **17,** 3043–3050 (2007).

174. Li, J. *et al.* Facile one-pot synthesis of Fe3O4@Au composite nanoparticles for dual-mode MR/CT imaging applications. *ACS Appl. Mater. Interfaces* **5,** 10357–10366 (2013).

175. Chin, S. F., Makha, M., Raston, C. L. & Saunders, M. Magnetite ferrofluids stabilized by sulfonato-calixarenes. *Chem. Commun.* 1948–1950 (2007).

176. Shamim, N., Hong, L., Hidajat, K. & Uddin, M. S. Thermosensitive polymer (N-isopropylacrylamide) coated nanomagnetic particles: Preparation and characterization. *Colloids Surfaces B Biointerfaces* **55,** 51–58 (2007).

177. Choi, J. *et al.* Fabrication of silica-coated magnetic nanoparticles with highly photoluminescent lanthanide probes. *Chem. Commun.* 1644–1646 (2007).

178. Serrano-Ruiz, D. *et al.* Nanosegregated Polymeric Domains on the Surface of Fe_3O_4@SiO_2 Particles. *J. Polym. Sci. Part A Polym. Chem.* **52,** 2966–2975 (2014).

179. Daniel, M. C. & Astruc, D. Gold Nanoparticles: Assembly, Supramolecular Chemistry, Quantum-Size-Related Properties, and Applications Toward Biology, Catalysis, and Nanotechnology. *Chem. Rev.* **104,** 293–346 (2004).

180. Mohammad, F., Balaji, G., Weber, A., Uppu, R. M. & Kumar, C. S. S. R. Influence of Gold Nanoshell on Hyperthermia of SuperParamagnetic Iron Oxide Nanoparticles. *J. Phys. Chem. C* **114,** 19194–19201 (2010).

181. Gao, J., Gu, H. & Xu, B. Multifunctional magnetic nanoparticles: design, synthesis, and biomedical applications. *Acc. Chem. Res.* **42,** 1097–1107 (2009).

182. Song, H. M., Wei, Q., Ong, Q. K. & Wei, A. Plasmon-resonant nanoparticles and nanostars with magnetic cores: Synthesis and magnetomotive imaging. *ACS Nano* **4,** 5163–5173 (2010).

183. Wang, L. *et al.* Monodispersed Core-Shell Fe_3O_4@Au Nanoparticles. *J. Phys. Chem. B* **109,** 21593–21601 (2005).

184. Wang, L., Luo, J., Schadt, M. J. & Zhong, C.-J. Thin film assemblies of molecularly-linked metal nanoparticles and multifunctional properties. *Langmuir* **26,** 618–632 (2010).

185. Xu, Z., Hou, Y. & Sun, S. Magnetic Core/Shell Fe_3O_4/Au and Fe_3O_4/Au/Ag Nanoparticles with Tunable Plasmonic Properties. *J. Am. Chem. Soc.* 8698–8699 (2007).

186. Wang, L. *et al.* Iron-oxide-gold core-shell nanoparticles and thin film assembly. *J. Mater. Chem.* **15,** 1821–1832 (2005).

187. Park, H.-Y. *et al.* Fabrication of magnetic core@shell Fe oxide@Au nanoparticles for interfacial bioactivity and bio-separation. *Langmuir* **23,** 9050–9056 (2007).

188. Maye, M. M., Zheng, W., Leibowitz, F. L., Ly, N. K. & Zhong, C.-J. Heating-induced evolution of thiolate-encapsulated gold nanoparticles: A strategy for size and shape manipulations. *Langmuir* **16,** 490–497 (2000).

189. Wang, Y., Wong, J. F., Teng, X. & Lin, X. Z. 'Pulling' Nanoparticles into Water: Phase Transfer of Oleic Acid Stabilized Monodisperse Nanoparticles into Aqueous Solutions of Cyclodextrin. *Nano Lett.* **3,** 1555–1559 (2003).

190. Chen, Z. *et al.* Versatile Synthesis Strategy for Carboxylic Acid - functionalized Upconverting Nanophosphors as Biological Labels. *J. Am. Chem. Soc.* **130,** 3023–3029 (2008).

191. Al-Jamal, W. T. & Kostarelos, K. Liposome-nanoparticle hybrids for multimodal diagnostic and therapeutic applications. *Nanomedicine* **2,** 85–98 (2007).

192. Malam, Y., Loizidou, M. & Seifalian, A. M. Liposomes and nanoparticles: nanosized vehicles for drug delivery in cancer. *Trends Pharmacol. Sci.* **30,** 592–599 (2009).

193. Paasonen, L., Laaksonen, T., Johans, C. & Yliperttula, M. Gold nanoparticles enable selective light-induced contents release from liposomes. *J. Control. Release* **122,** 86–93 (2007).

194. Lin, C.-A. J. *et al.* Design of an Amphiphilic Polymer for Nanoparticle Coating and Functionalization. *Small* **4,** 334–341 (2008).

195. Cushing, B. L., Kolesnichenko, V. L. & Connor, C. J. O. Recent Advances in the Liquid-Phase Syntheses of Inorganic Nanoparticles. *Chem. Rev.* **104,** 3893–3946 (2004).

196. Pellegrino, T. *et al.* Hydrophobic Nanocrystals Coated with an Amphiphilic Polymer Shell: A General Route to Water Soluble Nanocrystals. *Nano Lett.* **4,** 703–707 (2004).

197. Sperling, R. A. & Parak, W. J. Surface modification, functionalization and bioconjugation of colloidal inorganic nanoparticles. *Phil. Trans. R. Soc. A* **368,** 1333–1383 (2010).

198. Kang, Y. & Taton, A. T. Core/Shell Gold Nanoparticles by Self-Assembly and Crosslinking of Micellar, Block-Copolymer Shells. *Angew. Chemie - Int. Ed.* **44,** 409–412 (2005).

199. Kim, B.-S., Qiu, J.-M., Wang, J.-P. & Taton, A. T. Magnetomicelles: Composite Nanostructures from Magnetic Nanoparticles and Cross-Linked Amphiphilic Block Copolymers. *Nano Lett.* **5,** 1987–1991 (2005).

200. Kim, B.-S. & Taton, A. T. Multicomponent Nanoparticles via Self-Assembly with Cross-Linked Block Copolymer Surfactants. *Langmuir* **23,** 2198–2202 (2007).

201. Azzam, T. & Eisenberg, A. Monolayer-Protected Gold Nanoparticles by the Self-Assembly of Micellar Poly(ethylene oxide)-b-Poly(e-caprolactone) Block Copolymer. *Langmuir* **23,** 2126–2132 (2007).

202. Mai, Y. & Eisenberg, A. Selective Localization of Preformed Nanoparticles in Morphologically Controllable Block Copolymer Aggregates in Solution. *Acc. Chem. Res.* **45,** 1657–1666 (2012).

203. Sun, S. *et al.* Monodisperse MFe_2O_4 (M = Fe, Co, Mn) Nanoparticles. *J. Am. Chem. Soc.* **126,** 273–279 (2004).

204. Wang, L. *et al.* Core@Shell nanomaterials: gold-coated magnetic oxide nanoparticles. *J. Mater. Chem.* **18,** 2629–2635 (2008).

205. Jadzinsky, P. D., Calero, G., Ackerson, C. J., Bushnell, D. A. & Kornberg, R. D. Structure of a Thiol Monolayer-Protected Gold Nanoparticle at 1.1 Å Resolution. *Science* **318,** 430–433 (2007).

206. Nakamoto, M., Yamamoto, M. & Fukusumi, M. Thermolysis of gold(I) thiolate complexes producing novel gold nanoparticles passivated by alkyl groups. *Chem. Commun.* 1622–1623 (2002).

207. Gallo-Páramo, J. Design and synthesis of biofunctional magnetic/fluorescent glyco-nanoparticles and quantum dots and their application as specific molecular imaging probes. (CIC biomaGUNE, 2011).

208. Yang, H. H. *et al.* Magnetite-Containing Spherical Silica Nanoparticles for Biocatalysis and Bioseparations. *Anal. Chem.* **76,** 1316–1321 (2004).

209. Boal, A. K., Frankamp, B. L., Uzun, O., Tuominen, M. T. & Rotello, V. M. Modulation of Spacing and Magnetic Properties of Iron Oxide Nanoparticles through Polymer-Mediated 'Bricks and Mortar' Self-assembly. *Chem. Mater.* **16,** 3252–3256 (2004).

210. Kolhatkar, A. G., Jamison, A. C., Litvinov, D., Willson, R. C. & Lee, R. T. Tuning the magnetic properties of nanoparticles. *Int. J. Mol. Sci.* **14,** 15977–16009 (2013).

211. Link, S. & El-Sayed, M. A. Size and Temperature Dependence of the Plasmon Absorption of Colloidal Gold Nanoparticles. *J. Phys. Chem. B* **103,** 4212–4217 (1999).

212. Prasad, B. L. V., Stoeva, S. I., Sorensen, C. M. & Klabunde, K. J. Digestive ripening of thiolated gold nanoparticles: The effect of alkyl chain length. *Langmuir* **18,** 7515–7520 (2002).

213. Qi, W. H. & Wang, M. P. Size and shape dependent melting temperature of metallic nanoparticles. *Mater. Chem. Phys.* **88,** 280–284 (2004).

214. Shimizu, T., Teranishi, T., Hasegawa, S. & Miyake, M. Size evolution of alkanethiol-protected gold nanoparticles by heat treatment in the solid state. *J. Phys. Chem. B* **107,** 2719–2724 (2003).

215. Roco, M. C. & Bainbridge, W. S. Societal implications of nanoscience and nanotechnology: Maximizing human benefit. *J. Nanoparticle Res.* **7,** 1–13 (2005).

216. Cheon, J. & Lee, J.-H. Synergistically integrated nanoparticles as multimodal probes for nanobiotechnology. *Acc. Chem. Res.* **41,** 1630–1640 (2008).

217. Kawasaki, E. S. & Player, A. Nanotechnology, nanomedicine, and the development of new, effective therapies for cancer. *Nanomedicine Nanotechnology, Biol. Med.* **1,** 101–109 (2005).

218. Theranostics. at <http://www.thno.org/>

219. Koo, O. M., Rubinstein, I. & Onyuksel, H. Role of nanotechnology in targeted drug delivery and imaging: a concise review. *Nanomedicine Nanotechnology, Biol. Med.* **1,** 193–212 (2005).

220. Vaseashta, A. & Dimova-Malinovska, D. Nanostructured and nanoscale devices, sensors and detectors. *Sci. Technol. Adv. Mater.* **6,** 312–318 (2005).

221. Liu, Z., Tabakman, S. M., Chen, Z. & Dai, H. Preparation of carbon nanotubes bioconjugates for biomedical applications. *Nat. Protoc.* **4,** 1372–1381 (2009).

222. Li, Q. S., Zhang, R. Q., Lee, S. T., Niehaus, T. A. & Fauenheim, T. Optimal surface functionalization of silicon quantum dots. *J. Chem. Phys.* **128,** 244714 (2008).

223. Brannon-Peppas, L. & Blanchette, J. O. Nanoparticle and targeted systems for cancer therapy. *Adv. Drug Deliv. Rev.* **64,** 206–212 (2012).

224. Mirkin, C. A., Letsinger, R. L., Mucic, R. C. & Storhoff, J. J. A DNA-based method for rationally assembling nanoparticles into macroscopic materials. *Nature* **382,** 607–609 (1996).

225. He, X. *et al.* In Vivo Study of Biodistribution and Urinary Excretion of Surface-Modified Silica Nanoparticles. *Anal. Chem.* **80,** 9597–9603 (2008).

226. Peer, D. *et al.* Nanocarriers as an emerging platform for cancer therapy. *Nat. Nanotechnol.* **2,** 751–760 (2007).

227. Soussan, E., Cassel, S., Blanzat, M. & Rico-Lattes, I. Drug Delivery by Soft Matter: Matrix and Vesicular Carriers. *Angew. Chemie - Int. Ed.* **48,** 274–288 (2008).

228. Egli, S. *et al.* Biocompatible functionalization of polymersome surfaces: A new approach to surface immobilization and cell targeting using polymersomes. *J. Am. Chem. Soc.* **133,** 4476–4483 (2011).

229. Christian, N. A. *et al.* Tat-functionalized near-infrared emissive polymersomes for dendritic cell labeling. *Bioconjug. Chem.* **18,** 31–40 (2007).

230. Yi, D. K. *et al.* Silica-Coated Nanocomposites of Magnetic Nanoparticles and Quantum Dots. *J. Am. Chem. Soc.* **127,** 4990–4991 (2005).

231. Li, Z., Barnes, J. C., Bosoy, A., Stoddart, J. F. & Zink, J. I. Mesoporous silica nanoparticles in biomedical applications. *Chem. Soc. Rev.* **41,** 2590–2605 (2012).

232. Vaz, A. M. *et al.* Synthesis and characterization of biocatalytic γ-Fe2O3@SiO2 particles as recoverable bioreactors. *Colloids Surfaces B Biointerfaces* **114,** 11–19 (2014).

233. Guerrero-Martinez, A., Perez-Juste, J. & Liz-Marzan, L. M. Recent Progress on Silica Coating of Nanoparticles and Related Nanomaterials. *Adv. Mater.* **22,** 1182–1195 (2010).

234. Han, Y., Jiang, J., Lee, S. S. & Ying, J. Y. Reverse Microemulsion-Mediated Synthesis of Silica-Coated Gold and Silver Nanoparticles. *Langmuir* **24,** 5842–5848 (2008).

235. Yang, Y., Jing, L., Yu, X., Yan, D. & Gao, M. Coating Aqueous Quantum Dots with Silica via Reverse Microemulsion Method: Toward Size-Controllable and Robust Fluorescent Nanoparticles. *Chem. Mater.* **19,** 4123–4128 (2007).

236. Koole, R. *et al.* On the incorporation mechanism of hydrophobic quantum dots in silica spheres by a reverse microemulsion method. *Chem. Mater.* **20,** 2503–2512 (2008).

237. Darbandi, M., Thomann, R. & Nann, T. Article Single Quantum Dots in Silica Spheres by Microemulsion Synthesis Single Quantum Dots in Silica Spheres by Microemulsion Synthesis. *Chem. Mater.* **17,** 5720–5725 (2005).

238. Zhang, Y., Pan, S., Teng, X., Luo, Y. & Li, G. Bifunctional Magnetic-Luminescent Nanocomposites: Y2O3/Tb Nanorods on the Surface of Iron Oxide/Silica Core-Shell Nanostructures. *J. Phys. Chem. C* **112,** 9623–9626 (2008).

239. Zhang, M., Cushing, B. L. & O'Connor, C. J. Synthesis and characterization of monodisperse ultra-thin silica-coated magnetic nanoparticles. *Nanotechnology* **19,** 085601 (2008).

240. Santra, S. *et al*. Synthesis and Characterization of Silica-Coated Iron Oxide Nanoparticles in Microemulsion: The effect of Nonionic Surfactants. *Langmuir* **17,** 2900-2906 (2001).

241. Davila-Ibanez, A. B. *et al.* Magnetic silica nanoparticle cellular uptake and cytotoxicity regulated by electrostatic polyelectrolytes-DNA loading at their surface. *ACS Nano* **6,** 747–759 (2012).

242. Yang, Y., Jing, L., Yu, X., Yan, D. & Gao, M. Coating Aqueous Quantum Dots with Silica via Reverse Microemulsion Method: Toward Size-Controllable and Robust Fluorescent Nanoparticles. *Chem. Mater.* **19,** 4123–4128 (2007).

243. Ding, H. *et al.* Fe3O4@SiO2 core/shell nanoparticles: the silica coating regulations with a single-core for different core sizes and shell thicknesses. *Chem. Mater.* **24,** 4572–4580 (2012).

244. Vogt, C. *et al.* High quality and tuneable silica shell-magnetic core nanoparticles. *J Nanopart Res* **12,** 1137–1147 (2010).

245. Wang, A., Zheng, Y. & Peng, F. Thickness-Controllable Silica Coating of CdTe QDs by Reverse Microemulsion Method for the Application in the Growth of Rice. *J. Spectrosc.* 169245–169250 (2014).

246. Jin, Y. *et al.* Amorphous silica nanohybrids: Synthesis, properties and applications. *Coord. Chem. Rev.* **253,** 2998–3014 (2009).

247. Santra, S., Zhang, P., Wang, K., Tapec, R. & Tan, W. Conjugation of biomolecules with luminophore-doped silica nanoparticles for photostable biomarkers. *Anal. Chem.* **73,** 4988–4993 (2001).

248. Wang, L. & Tan, W. Multicolor FRET silica nanoparticles by single wavelength excitation. *Nano Lett.* **6,** 84–88 (2006).

249. Laurenti, M., Garcia-Blanco, F., Lopez-Cabarcos, E. & Rubio-Retama, J. Detection of heavy metal ions using a water-soluble conjugated polymer based on thiophene and meso-2,3-dimercaptosuccinic acid. *Polym. Int.* **62,** 811–816 (2013).

250. Gonzalez-Sanchez, M. I., Laurenti, M., Rubio-Retama, J., Valero, E. & Lopez-Cabarcos, E. Fluorescence decrease of conjugated polymers by the catalytic activity of

horseradish peroxidase and its application in phenolic compounds detection. *Biomacromolecules* **12,** 1332–1338 (2011).

251. Tardivo, J. P. *et al.* Methylene blue in photodynamic therapy: From basic mechanisms to clinical applications. *Photodiagnosis Photodyn. Ther.* **2,** 175–191 (2005).

252. He, X., Wu, X., Wang, K., Shi, B. & Hai, L. Methylene blue-encapsulated phosphonate-terminated silica nanoparticles for simultaneous in vivo imaging and photodynamic therapy. *Biomaterials* **30,** 5601–5609 (2009).

253. Bagwe, R. P., Yang, C., Hilliard, L. R. & Tan, W. Optimization of dye-doped silica nanoparticles prepared using a reverse microemulsion method. *Langmuir* **20,** 8336–8342 (2004).

254. Hiramatsu, H. & Osterloh, F. E. A Simple Large-Scale Synthesis of Nearly with Exchangeable Surfactants. *Chem. Mater.* **16,** 2509–2511 (2004).

255. Bae, W. K., Char, K., Hur, H. & Lee, S. Single-step synthesis of quantum dots with chemical composition gradients. *Chem. Mater.* **20,** 531–539 (2008).

256. Kumar, A. *et al.* Investigation into the interaction between surface-bound alkylamines and gold nanoparticles. *Langmuir* **19,** 6277–6282 (2003).

257. Slowing, I. I., Trewyn, B. G., Giri, S. & Lin, V. S.-Y. Mesoporous Silica Nanoparticles for Drug Delivery and Biosensing Applications. *Adv. Mater.* **17,** 1225–1236 (2007).

258. Qhobosheane, M., Santra, S., Zhang, P. & Tan, W. Biochemically functionalized silica nanoparticles. *Analyst* **126,** 1274–1278 (2001).

259. Chen, S. *et al.* Novel One-pot Sol-Gel Preparation of Amino-functionalized Silica Nanoparticles. *Chem. Lett.* **37,** 1170–1171 (2008).

260. Rahman, I. A. & Padavettan, V. Synthesis of silica nanoparticles by sol-gel: size-dependent properties, surface modification, and applications in silica-polymer nanocomposites - a review. *J. Nanomater.* **8,** 1–15 (2012).

261. Alonso-Cristobal, P. *et al.* Highly Sensitive DNA Sensor Based on Upconversion Nanoparticles and Graphene Oxide. *ACS Appl. Mater. Interfaces* **23,** 12422–12429 (2015).

262. Wang, S. & Low, P. S. Folate-mediated targeting of antineoplastic drugs, imaging agents, and mucleic acids to cancer cells. *J. Control. Release* **53,** 39–48 (1998).

263. Figueira, F., Cavaleiro, J. A. S. & Tome, J. P. C. Silica nanoparticles functionalized with porphyrins and analogs for biomedical studies. *J. Porphyr. Phthalocyanines* **15,** 517–524 (2011).

264. Milton-Harris, J. *Poly(ethylene glycol) chemistry: biotechnical and biomedical applications*. (Plenum Publishing Group, 1992).

265. Son, Y. J. *et al.* Biodistribution and anti-tumor efficacy of doxorubicin loaded glycol-chitosan nanoaggregates by EPR effect. *J. Control. Release* **91,** 135–145 (2003).

266. Du, J.-Z., Du, X.-J., Mao, C.-Q. & Wang, J. Tailor-Made Dual pH-Sensitive Polymer-Doxorubicin Nanoparticles for Efficient Anticancer Drug Delivery. *J. Am. Chem. Soc.* **133,** 17560–17563 (2011).

267. Danhier, F., Feron, O. & Préat, V. To exploit the tumor microenvironment: Passive and active tumor targeting of nanocarriers for anti-cancer drug delivery. *J. Control. Release* **148,** 135–146 (2010).

268. Dharap, S. S. *et al.* Tumor-specific targeting of an anticancer drug delivery system by LHRH peptide. *Proc. Nat. Acad. Sci.* **102,** 12962–12967 (2005).

269. Sudimack, J. & Lee, R. J. Targeted drug delivery via the folate receptor. *Adv. Drug Deliv. Rev.* **41,** 147–162 (2000).

270. Alley, S. C., Okeley, N. M. & Senter, P. D. Antibody-drug conjugates: Targeted drug delivery for cancer. *Curr. Opin. Chem. Biol.* **14,** 529–537 (2010).

271. Giri, S., Trewyn, B. G., Stellmaker, M. P. & Lin, V. S.-Y. Stimuli-Responsive Controlled-Release Delivery System Based on Mesoporous Silica Nanorods Capped with Magnetic Nanoparticles. *Angew. Chemie - Int. Ed.* **44,** 5038–5044 (2005).

272. Lai, C. Y. *et al.* A mesoporous silica nanosphere-based carrier system with chemically removable CdS nanoparticle caps for stimuli-responsive controlled release of neurotransmitters and drug molecules. *J. Am. Chem. Soc.* **125,** 4451–4459 (2003).

273. Ganta, S., Devalapally, H., Shahiwala, A. & Amiji, M. A review of stimuli-responsive nanocarriers for drug and gene delivery. *J. Control. Release* **126,** 187–204 (2008).

274. Greenfield, R. S. *et al.* Evaluation in Vitro of Adriamycin Immunoconjugates Synthesized Using an Acid-Sensitive Hydrazone Linker Evaluation in Vitro of Adriamycin Immunoconjugates Synthesized Using an Acid-Sensitive Hydrazone Linker. *Cancer Res* **50,** 6600–6607 (1990).

275. Rothemund, P. W. K. Folding DNA to create nanoscale shapes and patterns. *Nature* **440,** 297–302 (2006).

276. He, Y. *et al.* Hierarchical self-assembly of DNA into symmetric supramolecular polyhedra. *Nature* **452,** 198–201 (2008).

277. Yan, H., Zhang, X., Shen, Z. & Seeman, N. C. A robust DNA mechanical device controlled by hybridization topology. *Nature* **415,** 62–65 (2002).

278. Le, J. D. *et al.* DNA-templated self-assembly of metallic nanocomponent arrays on a surface. *Nano Lett.* **4,** 2343–2347 (2004).

279. Zhang, J., Liu, Y., Ke, Y. & Yan, H. Periodic square-like gold nanoparticle arrays templated by self-assembled 2D DNA nanogrids on a surface. *Nano Lett.* **6,** 248–251 (2006).

280. Ding, B. *et al.* Supporting Online Information Gold Nanoparticles Self-similar Chain Structure Organized by DNA Origami. *J. Am. Chem. Soc.* **132,** 3248–3249 (2010).

281. Niemeyer, C. M. & Adler, M. Nanomechanical devices based on DNA. *Angew. Chemie - Int. Ed.* **41,** 3779–3783 (2002).

282. Marrazza, G., Tombelli, S., Mascini, M. & Manzoni, A. Detection of human apolipoprotein E genotypes by DNA biosensors coupled with PCR. *Clin. Chim. Acta* **46,** 31–37 (2000).

283. Wang, J. *et al.* DNA electrochemical biosensor for the detection of short DNA sequences related to the human immunodeficiency virus. *Anal. Chem.* **68,** 2629–2634 (1996).

284. Mao, X., Yang, L., Su, X.-L. & Li, Y. A nanoparticle amplification based quartz crystal microbalance DNA sensor for detection of Escherichia coli O157:H7. *Biosens. Bioelectron.* **21,** 1178–1185 (2006).

285. Liu, G. *et al.* An enzyme-based E-DNA sensor for sequence-specific detection of femtomolar DNA targets. *J. Am. Chem. Soc.* **130,** 6820–6825 (2008).

286. Zhang, X. B., Wang, Z., Xing, H., Xiang, Y. & Lu, Y. Catalytic and molecular beacons for amplified detection of metal ions and organic molecules with high sensitivity. *Anal. Chem.* **82,** 5005–5011 (2010).

287. Liu, X. & Tan, W. A fiber-optic evanescent wave DNA biosensor based on novel molecular beacons. *Anal. Chem.* **71,** 5054–5059 (1999).

288. Nutiu, R. & Li, Y. Structure-switching signaling aptamers. *J. Am. Chem. Soc.* **125,** 4771 (2003).

289. Du, H., Disney, M. D., Miller, B. L. & Krauss, T. D. Hybridization-based unquenching of DNA hairpins on Au surfaces: Prototypical 'molecular beacon' biosensors. *J. Am. Chem. Soc.* **125,** 4012–4013 (2003).

290. Bonnet, G., Krichevsky, O. & Libchaber, A. Kinetics of conformational fluctuations in DNA hairpin-loops. *Proc. Natl. Acad. Sci. USA* **95,** 8602–8606 (1998).

291. Zhang, J. *et al.* Electrogenerated chemiluminescence DNA biosensor based on hairpin DNA probe labeled with ruthenium complex. *Anal. Chem.* **80,** 2888–2894 (2008).

292. Suzuki, M., Husimi, Y., Komatsu, H., Suzuki, K. & Douglas, K. T. Quantum Dot FRET Biosensors that Respond to pH, to Proteolytic or Nucleolytic Cleavage, to DNA Synthesis, or to a Multiplexing Combination. *J. Am. Chem. Soc.* **130,** 5720–5725 (2008).

293. Chen, Z. *et al.* Versatile Synthesis Strategy for Carboxylic Acid–functionalized Upconverting Nanophosphors as Biological Labels. *J. Am. Chem. Soc.* **130,** 3023–3029 (2008).

294. Frangioni, J. V. In vivo near-infrared fluorescence imaging. *Curr. Opin. Chem. Biol.* **7,** 626–634 (2003).

295. Mai, H.-X., Zhang, Y.-W., Sun, L.-D. & Yan, C.-H. Highly Efficient Multicolor Up-Conversion Emissions and Their Mechanisms of Monodisperse NaYF4:Yb,Er Core and Core/Shell-Structured Nanocrystals. *J. Phys. Chem. C* **111,** 13721–13729 (2007).

296. Binnemans, K. Lanthanide-based luminescent hybrid materials. *Chem. Rev.* **109,** 4283–4374 (2009).

297. Idris, N. M. *et al.* In vivo photodynamic therapy using upconversion nanoparticles as remote-controlled nanotransducers. *Nat. Med.* **18,** 1580–1585 (2012).

298. Xu, C. T. *et al.* High-resolution fluorescence diffuse optical tomography developed with nonlinear upconverting nanoparticles. *ACS Nano* **6,** 4788–4795 (2012).

299. Wang, Y.-F. *et al.* Nd^{3+} -Sensitized Upconversion Nanophosphors: Efficient In Vivo Bioimaging Probes with Minimized Heating Effect. *ACS Nano* **7,** 7200–7206 (2013).

300. Yan, B., Boyer, J. C., Habault, D., Branda, N. R. & Zhao, Y. Near infrared light triggered release of biomacromolecules from hydrogels loaded with upconversion nanoparticles. *J. Am. Chem. Soc.* **134,** 16558–16561 (2012).

301. Chen, G., Qiu, H., Prasad, P. N. & Chen, X. Upconversion nanoparticles: Design, nanochemistry, and applications in Theranostics. *Chem. Rev.* **114,** 5161–5214 (2014).

302. Chatterjee, D. K., Rufaihah, A. J. & Zhang, Y. Upconversion fluorescence imaging of cells and small animals using lanthanide doped nanocrystals. *Biomaterials* **29,** 937–943 (2008).

303. Huang, X., El-Sayed, I. H., Qian, W. & El-Sayed, M. A. Cancer cell imaging and photothermal therapy in the near-infrared region by using gold nanorods. *J. Am. Chem. Soc.* **128,** 2115–2120 (2006).

304. Li, Z., Zhang, Y. & Jiang, S. Multicolor core/shell-structured upconversion fluorescent nanoparticles. *Adv. Mater.* **20,** 4765–4769 (2008).

305. Zhang, H. *et al.* Plasmonic modulation of the upconversion fluorescence in NaYF4:Yb/Tm hexaplate nanocrystals using gold nanoparticles or nanoshells. *Angew. Chemie - Int. Ed.* **122,** 2927–2930 (2010).

306. Rantanen, T., Järvenpää, M. L., Vuojola, J., Kuningas, K. & Soukka, T. Fluorescence-quenching-based enzyme-activity assay by using photon upconversion. *Angew. Chemie - Int. Ed.* **47,** 3811–3813 (2008).

307. Li, Z., Wang, L., Wang, Z., Liu, X. & Xiong, Y. Modification of NaYF4:Yb,Er@SiO2 nanoparticles with gold nanocrystals for tunable green-to-red upconversion emissions. *J. Phys. Chem. C* **115,** 3291–3296 (2011).

308. Wu, T., Wilson, D. & Branda, N. R. Fluorescent quenching of lanthanide-doped upconverting nanoparticles by photoresponsive polymer shells. *Chem. Mater.* **26,** 4313–4320 (2014).

309. Wang, Y. *et al.* Aptamer/Graphene Oxide Nanocomplex for in Situ Molecular Probing in Living Cells. *J. Am. Chem. Soc.* **132,** 9274–9276 (2010).

310. Liu, C., Wang, H., Li, X. & Chen, D. Monodisperse, size-tunable and highly efficient NaYF4:Yb,Er(Tm) up-conversion luminescent nanospheres: controllable synthesis and their surface modifications. *J. Mater. Chem.* **19,** 3546–3553 (2009).

311. Yi, G. *et al.* Characterization of High-Efficiency Nanocrystal Up-Conversion Phosphors: Ytterbium and Erbium Codoped Lanthanum Molybdate. *Chem. Mater.* **14,** 2910–2914 (2002).

312. Liu, J. *et al.* Ultrasensitive nanosensors based on upconversion nanoparticles for selective hypoxia imaging in vivo upon near-infrared excitation. *J. Am. Chem. Soc.* **136,** 9701–9709 (2014).

313. Liu, F., Choi, J. Y. & Seo, T. S. Graphene Oxide Arrays for Detecting Specific DNA Hybridization by Fluorescence Resonance Energy Transfer. *Biosens. Bioelectron.* **25,** 2361–2365 (2010).

314. Luo, M. *et al.* Chemiluminescence Biosensors for DNA detection using graphene oxide and a Horseradish Peroxidase-mimicking DNAzyme. *Chem. Commun.* **48,** 1126–1128 (2012).

315. Zhao, H. X., Ma, Q. J., Wu, X. X. & Zhu, Z. Graphene Oxide-based Biosensor for Sensitive Fluorescence Detection of DNA Based on Exonuclease III-Aided Signal Amplification. *Anal. Chim. Acta* **740,** 88–92 (2012).

316. Du, J., Du, X., Mao, C. & Wang, J. Tailor-Made Dual pH-Sensitive Polymer-Doxorubicin Nanoparticles for Efficient Drug Delivery. *J. Am. Chem. Soc.* **133,** 17560–17566 (2011).

317. Dai, Y. *et al.* Up-Conversion Cell Imaging and pH-Induced Thermally Controlled Drug Release from $NaYF_4:Yb^{3+}/Er^{3+}$@Hydrogel Core-Shell Hybrid Microspheres. *ACS Nano* **6,** 3327–3335 (2012).

318. You, J., Zhang, G. & Li, C. Exceptionally High Payload of Doxorubicin in Hollow Gold Nanospheres for Near-Infrared Light-Triggered Drug Release. *ACS Nano* **4,** 1033–1039 (2010).

319. Satarkar, N. S., Biswal, D. & Hilt, J. Z. Hydrogel Nanocomposites: A review of Applications as Remote Controlled Biomaterials. *Soft Matter* **6,** 2364–2412 (2010).

320. Serrano-Ruiz, D., Laurenti, M., Ruiz-Cabello, J., Lopez-Cabarcos, E. & Rubio-Retama, J. Hybrid Microparticles for Drug Delivery and Magnetic Resonance Imaging. *J. Biomed. Mater. Res. B. Appl. Biomater.* **101,** 498–507 (2013).

321. Ruiz-Hernandez, E., Baeza, A. & Vallet-Regí, M. Smart Drug Delivery through DNA/magnetic Nanoparticle Gates. *ACS Nano* **8,** 1259–1267 (2014).

322. Weaver, C., LaRosa, J., Luo, X. & Cui, X. Electrically Controlled Drug Delivery from Graphene Oxide Nanocomposite Films. *ACS Nano* **8,** 1834–1842 (2014).

323. Yuan, Q. *et al.* Photon-Manipulated Drug Release from a Mesoporous Nanocontainer Controlled by Azobenzene-Modified Nucleic Acid. *ACS Nano* **6,** 6337–6342 (2012).

324. Son, S., Shin, E. & Kim, B. S. Light-Responsive Micelles of Spiropyran Initiated Hyperbranched Polyglycerol for Smart Drug Delivery. *Biomacromolecules* **15,** 628–635 (2014).

325. Chien, Y. *et al.* Near-Infrared Light Photocontrolled Chemotherapy with Caged Upconversion Nanoparticles in vitro and in vivo. *ACS Nano* **7,** 8516–8523 (2013).

326. Jayakumar, M. K. G., Idris, N. M. & Zhang, Y. Remote activation of biomolecules in deep tissues using near-infrared-to-UV upconversion nanotransducers. *Proc. Natl. Acad. Sci.* **109,** 8483–8488 (2012).

327. Dai, Y. *et al.* In vivo multi-modality imaging and cancer therapy by near-infrared light triggered trans-platinum pro-drug conjugated upconverison nanoparticles. *J. Am. Chem. Soc.* **135,** 18920–18929 (2013).

328. Luo, Y. L., Shiao, Y. S. & Huang, Y. F. Release of Photoactivable Drugs from Plasmonic Nanoparticles for Targeted Cancer Therapy. *ACS Nano* **5,** 7796–7805 (2011).

329. Liu, J., Bu, W., Pan, L. & Shi, J. NIR-Triggered Anticancer Drug Delivery by Upconverting Nanoparticles with Integrated Azobenzene-Modified Mesoporous Silica. *Angew. Chemie - Int. Ed.* **52,** 4375–4383 (2013).

330. Wang, F. *et al.* Tuning Upconversion through Energy Migration in Core-Shell Nanoparticles. *Nat. Mater.* **10,** 968–976 (2011).

331. Sedlmeier, A., Achatz, D. E., Fischer, L. H., Gorris, H. H. & Wolfbeis, O. S. Photon Upconverting Nanoparticles for Luminescent Sensing of Temperature. *Nanoscale* **4,** 7090–7099 (2012).

332. Cui, S. *et al.* In vivo Targeted Deep-Tissue Photodynamic Therapy Based on Near-Infrared Light Triggered Upconversion Nanoconstruct. *ACS Nano* **7,** 676–688 (2013).

333. Hao, S., Chen, G. & Yang, C. Sensing Using Rare-Earth-Doped Upconversion Nanoparticles. *Theranostics* **3,** 331–357 (2013).

334. Zhao, H., Sterner, E. S., Coughlin, E. B. & Theato, P. O-Nitrobenzyl Alcohol Derivatives: Opportunities in Polymer and Materials Science. *Macromolecules* **45,** 1723–1731 (2012).

335. Pelliccioli, A. P. & Wirz, J. Photoremovable Protecting Groups: Reaction Mechanisms and Applications. *Photochem. Photobiol. Sci.* **1,** 441–492 (2002).

336. Waku, T., Matsusaki, M., Kaneko, T. & Akashi, M. PEG brush peptide nanospheres with stealth properties and chemical functionality. *Macromolecules* **40,** 6385–6392 (2007).

337. Li, G. Z. *et al.* Investigation into Thiol-(meth)acrylate Michael Addition Reactions Using Amine and Phosphine Catalysts. *Polym. Chem.* **1,** 1196–2005 (2010).

338. Park, E. K., Kim, S. Y., Lee, S. B. & Lee, Y. M. Folate-conjugated methoxy poly(ethylene glycol)/poly(caprolactone) amphiphilic block copolymeric micelles for tumor-targeted drug delivery. *J. Control. Release* **109,** 158–168 (2005).

339. Carling, C. J., Nourmohammadian, F., Boyer, J. C. & Branda, N. R. Remote-control photorelease of caged compounds using near-infrared light and upconverting nanoparticles. *Angew. Chemie - Int. Ed.* **49,** 3782–3785 (2010).

340. Veiseh, O., Gunn, J. W. & Zhang, M. Design and fabrication of magnetic nanoparticles for targeted drug delivery and imaging. *Adv. Drug Deliv. Rev.* **62,** 284–304 (2010).

341. Liu, Y., Tu, D., Zhu, H. & Chen, X. Lanthanide-Doped Luminescent Nanoprobes: Controlled Synthesis, Optical Spectroscopy, and Bioapplications. *Chem. Soc. Rev.* **42,** 6924–2958 (2013).

342. Li, W., Wang, J., Ren, J. & Qu, X. Near-Infrared Upconversion Controls Photocaged Cell Adhesion. *J. Am. Chem. Soc.* **136,** 2248–2257 (2014).

10. CONCLUSIONS

1.- The synthesis of a star shaped amphiphilic block copolymer based on biocompatible poly(ε-caprolactone) and poly(ethylene glycol) has been achieved. The self-assembling of this macromolecule in water rendered different structures as a function of the polymer concentration. These polymeric nanoparticles could effectively solubilize in water a highly hydrophobic chlorophenyl carbazole derivate, demonstrating their potential as drug nano-carriers.

2.- A systematic study of the synthesis of core@shell Fe_3O_4@Au nanoparticles was performed. It was demonstrated that the Au:Fe_3O_4 ratio is a key parameter that should be optimized in order to obtain the maximum yield of Fe_3O_4@Au nanoparticles, but it did not affect the Au shell thickness, which could be tuned by varying the reaction temperature. The coprecipitation of the Fe_3O_4@Au nanoparticles with the star shaped amphiphilic block copolymer yielded a magnetic responsive hybrid material with plasmonic properties and a remarkable stability in aqueous solution, which could find potential applications in multimodal contrast imaging and theranostics.

3.- The silica coating of inorganic nanoparticles by the controlled polymerization of TEOS in a reverse microemulsion has been systematically studied. This methodology produced core@shell nanoparticles with a remarkable homogeneity that proved to be very reproducible and versatile: the silica shell thickness could be finely tuned by varying the reaction parameters, it was possible to co-encapsulate different molecules within the silica, and the method could be extended to nanoparticles of different nature. Importantly, the silica shell provided aqueous stability and protected the inorganic cores from the environment without altering their inner properties. In addition, it was demonstrated that the silica surface could be easily modified and functionalized with different functional groups and biomolecules. We conclude that this methodology is very interesting for the construction of multifunctional materials assembled in the nanoscale.

4.- A DNA biosensor platform was prepared by exploiting the FRET pair formed between ssDNA-functionalized upconversion nanoparticles and graphene oxide. In the absence of the cDNA, the fluorescence of the ssDNA-coated UPCNs was quenched. On the contrary, when the cDNA was present, the UCNPs remained fluorescent. The fluorescence intensity was correlated to the concentration of cDNA with a detection limit in the picomolar range. It was demonstrated that this sensor was sequence specific, which could serve as a detector for a variety of diseases with a very low detection limit, by using the appropriate probe sequence.

5.- A NIR-light responsive drug delivery system has been prepared. The system was based on silica coated upconversion nanoparticles and doxorubicin that was covalently attached to a photodegradable linker in the surface of the nanoparticles. Upon the NIR-light stimulus, the UCNPs emitted UV photons that provoked the photodegradation of the linker and consequently the doxorubicin release. The *in vitro* studies with HeLa cells revealed that neither the NIR-light stimulus nor the upconverted UV photons produced any cytotoxic effect. In addition, the doxorubicin was inactive without the NIR stimulus. When the NIR-light was applied, the cell viability decreased as a function of the concentration, which demonstrated that the released doxorubicin retained the cytotoxic activity.

10. CONCLUSIONES

1.- Se ha sintetizado un copolímero anfifílico dibloque en forma de estrella basado en componentes biocompatibles como son poli(ε-caprolactona) y poli(etilén glicol). El auto-ensamblado de esta macromolécula en medio acuoso da lugar a distintas estructuras en función de la concentración de polímero. Estas nanopartículas poliméricas fueron capaces de solubilizar eficazmente en agua una molécula altamente hidrofóbica derivada del clorofenil carbazol, demostrando así su potencial como nano-transportador de fármacos.

2.- Se ha realizado un estudio sistemático sobre la síntesis de nanopartículas de tipo núcleo@corteza de Fe_3O_4@Au. Se ha demostrado que el ratio Au:Fe_3O_4 es un parámetro clave que debe ser optimizado con el fin de obtener el máximo rendimiento de nanopartículas de Fe_3O_4@Au, pero que no afecta al grosor de la capa de oro, la cual pudo ser modificada mediante el control de la temperatura de reacción. La co-precipitación de las nanopartículas de Fe_3O_4@Au con el copolímero anfifílico dibloque en forma de estrella dio lugar a un material híbrido con propiedades magnéticas y plasmónicas y una alta estabilidad en medio acuoso, con potencial aplicación como agentes de contraste en contraste de imagen multimodal y en teranóstica.

3.- Se ha realizado un estudio sistemático sobre el recubrimiento de nanopartículas inorgánicas con sílice mediante la polimerización controlada de TEOS en microemulsión de fase inversa. Esta metodología da lugar a nanopartículas de tipo núcleo@corteza muy homogéneas y se prueba que es muy reproducible y versátil: el grosor de la capa de sílice pudo ser controlado a escala nanométrica con gran precisión variando los parámetros de reacción de forma adecuada; es posible co-encapsular diferentes moléculas dentro de la capa de sílice; el método permite el recubrimiento de nanopartículas inorgánicas de diferente naturaleza. Es importante destacar que la capa de sílice confiere estabilidad al sistema en medio acuoso y permite proteger a los núcleos inorgánicos del medio externo, pero no afecta negativamente a las características propias de dichas nanopartículas. Además, se demuestra que la superficie de las nanopartículas recubiertas con sílice puede ser modificada

con diferentes grupos funcionales y se pueden anclar distintas biomoléculas. Esta metodología, por tanto, se considera de gran interés en la construcción de materiales multifuncionales con estructuración a escala nanométrica.

4.- Se ha preparado un biosensor de ADN que se basa en la pareja FRET formada por óxido de grafeno y nanopartículas con fluorescencia de conversión ascendente funcionalizadas con ADN de hebra simple. En ausencia de la hebra complementaria, la fluorescencia de las nanopartículas se encuentra amortiguada. Por el contrario, en presencia de la hebra de ADN complementaria, las nanopartículas mantienen su fluorescencia. La intensidad de la fluorescencia es proporcional a la concentración de la hebra de ADN complementaria, con un límite de detección en el rango picomolar. Se demuestra que este sensor es específico para la secuencia complementaria por lo cual podría ser empleado como medio de detección de distintas enfermedades con un límite de detección muy bajo, utilizando la secuencia apropiada como sonda.

5.- Se ha preparado un sistema de liberación de fármaco con respuesta a luz NIR. El sistema se basa en nanopartículas con fluorescencia de conversión ascendente (UCNPs) recubiertas con sílice y funcionalizadas con doxorrubicina, la cual se une de forma covalente a un conector fotodegradable basado en un derivado del orto-bencilalcohol presente en la superficie de las nanopartículas. Bajo el estímulo de luz NIR, las UCNPs emiten fotones con longitud de onda en el rango del ultravioleta (UV) que provocan la fotodegradación del conector y la consecuente liberación de la doxorrubicina. Los estudios *in vitro* demostraron que ni el estímulo con luz NIR ni los fotones UV emitidos por las nanopartículas produjeron una reducción significativa de la viabilidad celular. Además, el sistema cargado con doxorrubicina no produjo una actividad citotóxica significativa en ausencia del estímulo con luz NIR. Cuando el sistema se estimuló con luz NIR, la viabilidad celular se redujo en función de la concentración, lo cual demuestra que la doxorrubicina mantenía su actividad citotóxica una vez liberada del sistema.

11. APPENDIX

11.1 PUBLICATIONS FROM THIS THESIS

1) Alonso-Cristóbal, P., Laurenti, M., Sánchez-Muniz, F. J., López-Cabarcos, E., Rubio-Retama, J. Polymeric nanoparticles with tunable architecture formed by biocompatible star shaped block copolymer. *Polymer* **53,** 4569-4578 (2012).

2) Alonso-Cristóbal, P., Laurenti, M., López-Cabarcos, E., Rubio-Retama, J. Efficient synthesis of core@shell Fe_3O_4@Au nanoparticles. *Mater. Res. Express* **2,** 075002 (2015).

3) Vaz, A. M., Serrano-Ruiz, D., Laurenti, M., Alonso-Cristóbal, P., López-Cabarcos, E., Rubio-Retama, J. Synthesis and characterization of biocatalytic γ-Fe_2O_3@SiO_2 particles as recoverable bioreactors. *Colloids and Surfaces B: Biointerfaces* **114,** 11-19 (2014).

4) Serrano-Ruiz, D., Alonso-Cristóbal, P., Méndez-González, D., Laurenti, M., Olivero-David, R., López-Cabarcos, E., Rubio-Retama, J. Nanosegregated polymeric domains on the surface of Fe_3O_4@SiO_2 particles. *Journal of Polymer Science Part A: Polymer Chemistry* **52,** 2966-2975 (2014).

5) Alonso-Cristóbal, P., Vilela, P., El-Shageer, A., López-Cabarcos, E., Brown, T., Muskens, O. L., Rubio-Retama, J. Kanaras, A. G. Highly sensitive DNA sensor based on upconversion nanoparticles and graphene oxide. *ACS Appl. Mater. Interfaces* **7,** 12422-12429 (2015).

6) Alonso-Cristóbal, P., Otón-Fernández, O., Méndez-González, D., López-Cabarcos, E., Barasoain-Blasco, I., Díaz-Pereira, F., Rubio-Retama, J. Synthesis, characterization, and application in HeLa cells of an NIR light responsive Doxorubicin delivery system based on $NaYF_4$:Yb,Tm@SiO_2-PEG nanoparticles . *ACS Appl. Mater. Interfaces* **7,** 14992-14999 (2015).

7) Méndez-González, D. Alonso-Cristóbal, P., López-Cabarcos, E., Rubio-Retama, J. Multi-Responsive Hybrid Janus nanoparticles: Surface functionalization through solvent physisorption. Submitted to *J. Phys. Chem. C* (2015).

8) Laurenti, M. Alonso-Cristóbal, P., López-Cabarcos, E., Rubio-Retama, J. Magnetically recoverable gold clusters and their use as catalyst. Submitted to *ACS Appl. Mater. Interfaces* (2015).

11.2 PARTICIPATION IN OTHER RELATED WORKS

1) Serrano-Ruiz, D., Alonso-Cristóbal, P., Laurenti, M., Frick, B., López-Cabarcos, E., Rubio-Retama, J. Influence of the inter-chain hydrogen bonds on the thermoresponsive swelling behavior of UCST-like microgels. *Polymer* **54,** 4963-4971 (2013).

2) Contreras-Cáceres, R., Alonso-Cristóbal, P., Méndez-González, D., Laurenti, M., Maldonado-Valdivia, A., García-Blanco, F., López-Cabarcos, E. Fernández-Barbero, A., López-Romero, J. M., Rubio-Retama, J. Temperature controlled fluorescence on Au@Ag@PNIPAM-PTEBS microgels: Effect of the metal core size on the MEF extension. *Langmuir* **30,** 15560-15567 (2014).